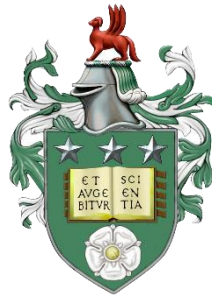# Metastable liquid phase separation in Co – Cu alloys

Oluwatoyin Enitan Jegede

Submitted in accordance with the requirements for the degree of

Doctor of Philosophy

University of Leeds

School of Chemical and Process Engineering

November, 2017

The candidate confirms that the work submitted is his own, except where work which has formed part of jointly-authored publications has been included. The contribution of the candidate and the other authors to this work has been explicitly indicated below. The candidate confirms that appropriate credit has been given within the thesis where reference has been made to the work of others.

Paper

1. Parts of section 5.4 of this thesis is based on a jointly authored paper: Oluwatoyin E. Jegede, Robert F. Cochrane and Andrew M. Mullis, "Metastable monotectic phase separation in Co–Cu alloys". Journal of Material Science, 2017, In Press.

The candidate completed the experiments and analysed the results. The academic supervisors Dr R.F. Cochrane and Professor A.M. Mullis contributed ideas and valuable discussion of the paper.

Acknowledgements

Abstract

Two Co – Cu alloys were studied by drop tube processing technique in a view of investigating the effects of rapid solidification on the phase transformations and microstructural evolution in the metastable alloys.

The as – solidified samples had diameters ranging from 53 – 850+ μm and these were analysed using various characterization techniques such as optical (OM) and scanning electron (SEM) microscopy, x- ray diffraction (XRD) and differential thermal analysis (DTA).

The Cu – 50 at. % Co alloy was observed to experience liquid phase separation at lower undercooling than the Cu – 68.5 at. % Co alloy. This is found to be in accordance to the asymmetrical metastable miscibility gap determined for the alloy system.

Significant number of liquid phase separated structures were observed at cooling rates in excess of 15000 Ks^{-1}, evidenced by a range of microstructural morphologies including stable core shell structures, evolving core shell structures and structures in which the demixed liquid phases were randomly distributed. A large number of these structures experienced multiple liquid phase separation processes.

The configuration of the core shell structures were found to be independent of the composition of phases and their relative abundance, with the core always formed by the higher melting point phase. The optimum production of the core shell structures were found to be a function of cooling rate.

Table of contents

List of figures

List of tables

List of symbols

U	Internal energy
H	Enthalpy
S	Entropy
G	Gibbs free energy
ΔH_f	Heat of fusion
ΔC_p	Change in specific heat capacity
Ω	Interatomic interaction parameter
Z	Number of bonds per atom
ΔG_{mixing}	Change in Gibbs energy on mixing
R	Universal gas constant
n_i	Number of moles of component i,
$\mu_A^\alpha, \mu_A^\beta$	Chemical potential of component A in α and β phase
V^{excess}	Excess volume associated with alloy formation
X_A	Atomic fraction of component A
ρ_m	Density at the melting temperature
T_m	Melting temperature
σαβ	Interfacial tension between α and β phases
σ_{ALLOY}	Interface energy of the alloy
A_X	Surface area of of phase X
N_a	Avogadro's number
V_x	Molar volume of the component x
μ_m	Viscosity of liquid metal at the melting point
D	Diffusion coefficient

D_{AB}	Diffusion coefficient of solute A in solvent B
ΔG_v	Gibbs free energy change per unit volume
ΔT	undercooling
I^{hom}	homogeneous nucleation rate,
I_o	Nucleation pre- factor
Us	Stokes velocity
G	Gravitational acceleration of magnitude 9.8 m/s^2
U_{Mt}	Marangoni velocity
U_{ms}	Solutal Marangoni migration velocity
S_T	Soret coefficient
C	Concentration in mass fraction.

1 Introduction

Immiscible alloys are characterised by large positive enthalpy of mixing due to the large atomic size difference of the different components [1]. This results in small mutual solubility and immiscibility at low temperatures. Immiscible alloys which undergo the monotectic reaction $L_1 \rightarrow \alpha + L_2$ are known as monotectic alloys and this reaction occurs after the alloys have phase separated. Phase separation ($L \rightarrow L_1 + L_2$) is known to occur in monotectic alloys when they are cooled into a region on their phase diagram known as the miscibility gap which is the limit of miscibility above which the alloys are miscible [2]. This dome shaped region spanning over a wide composition range could be stable (e.g. Al-Pb, Cu – Pb, Fe – Ag) or metastable (e.g. Co – Cu, Cu – Fe, Cu – Cr) depending on whether it is above or below the liquidus line on the phase diagram [3]. Monotectic alloys are capable of developing various liquid phase separation patterns during their solidification process and as such can be designed for specific purposes [4], alloys such as Al – Bi, Al – Pb and Cu – Pb with well dispersed Bi or Pb particles are said to have good tribological properties and as such are excellent bearing materials[5–7].

Studies of monotectic systems have gained recent interest due to their potential wide area of utilization especially when undercooled. This is because undercooling of liquid melts can result in the formation of alternate phases as well as cause metastable liquid phase separation[8]. Undercooling is therefore a prerequisite for the non-equilibrium solidification of immiscible alloys to form metastable phases. Large undercooling however is only possible in the absence of heterogeneous nucleation sites. In directional solidification, monotectics are greatly influenced by gravity especially when there is large density difference between the separated liquids due to strong gravity induced convection and sedimentation and the final solidification structure is greatly influenced by these external factors [2,3]. When there is

strong interplay of gravitational forces on the alloy, layered structures are formed with the denser phase occupying the bottom layer. Rapid solidification processes such as the containerless processing techniques are characterised by very high cooling rates which in turn causes appreciable undercooling of the alloy melt. The drop tube method of containerless processing has the combined advantages of rapidly solidifying the melts at high degrees of undercooling and low gravity conditions thereby eliminating gravity induced effects and less contamination due to absence of container walls and as such is commonly used in processing these alloys.

There is extensive literature on alloys with stable miscibility gaps but for those with metastable miscibility gaps literature is sparse due to the transitional state of the metastable phase.

Copper based alloys generally have excellent electrical and thermal conductivity properties making them attractive in many industrial applications. Copper based monotectic alloys may exhibit many microstructural features and solidification characteristics under varied conditions when undercooled which makes them research relevant. Alloys such as $Cu - Cr$ and $Cu - Fe$ are good electrical conductivity and high strength materials [9,10] while $Co - Cu$ alloy with uniformly distributed cobalt particles in high volume fraction is said to be excellent for catalytic reactions [11–14]. Also the alloy has a magnetic transformation temperature that is 573K higher than that of $Cu - Fe$, making $Co - Cu$ possible for magnetic sensor applications [15]. Giant magnetoresistive (GMR) is an interesting property in which electrical resistance changes in response to applied magnetic field. This is an intriguing discovery in thin film magnetism in which stacks of thin films of ferromagnetic materials are separated by stacks of nonmagnetic materials of same magnitude. Alloys exhibiting this phenomenon have a wide range of magnetic, electronic and transport properties. High performance GMR materials can be successfully produced

by rapid solidification from undercooled melts. Studies have shown that Co-Cu possess this property [15–18].

Liquid phase separation has been reported in Co – Cu alloys of different composition upon cooling into the miscibility gap [16,19]. The boundary of the miscibility gap in the system has been of research interest as far back as 1958 when Nakagawa first discovered a near symmetrical metastable miscibility gap in the system at equi – composition [16] during his study on magnetic susceptibility of quenched samples of Co – Cu alloys. So far, rapid solidification studies on the alloy system is yet to report intermediate microstructures at various stages along the solidification process which is what would be expected due to the influence of the rapidity and complex processes happening concurrently during the liquid phase separation of the alloy.

In order to study the metastable phase of the Co – Cu alloy system with desired cobalt inclusions, two undercooled Co – Cu alloys of different composition (50 at. % Co and 68.5 at. % Co) were processed in microgravity environment using the drop tube method of containerless processing. Phase separation was observed in both alloys. The miscibility gap boundary was determined using thermodynamic calculations and was found to have a peak/critical composition at around 58.7 at. % Cu. The choice of alloys was based on of the reported unusual behaviour of the Cu – 50 at. % Co alloy and the Cu - 68.5 at. % Co alloy because it was the furthest away from the cobalt rich side of the critical composition but still within the calculated miscibility gap limits. Based on the constructed metastable phase diagram, the corresponding alloy to the Cu - 68. 5 at. % Co alloy on the copper side of the critical composition would have exact structures to the one on the cobalt rich side but the volume fraction of the cobalt inclusion and of the phases in general would vary. This of course is subject to further research but due to time constraints this study is limited to one side of the critical composition.

The impact of undercooling as well as that of other contributory factors such as composition, cooling rates and volume fraction to the solidification process were examined.

Also documented in this study are the characteristics and mechanism for the formation of the core shell structures observed in the liquid phase separated alloys which is a novel contribution to literature on these microstructural formations in drop tube processed Co – Cu alloys.

1.1   Aim of research

The aim of this PhD research is to study the effects that rapid solidification through containerless processing has on metastable monotectic Co –Cu alloys using a drop tube.

1.2   Research objectives

1.   To determine by thermodynamic calculations and thermal analysis the boundary of the miscibility gap of the Cu-Co system in order to estimate undercooling temperature required for phase separation and the solidification path of alloys on its phase diagram.

2.   To determine how alloy composition and drop tube process environment affects the microstructure and morphology in Cu-Co alloys.

3.   To study the phase separation process and growth mechanism of separated phases in undercooled drop tube Cu-Co samples.

4.   To use quantitative analysis of microstructural features to determine cooling rates and how phase separation and selection is affected by microstructural abundance of phases in droplets of various sizes in drop tube processed Cu-Co alloys.

1.3   Scope

Metastable copper based monotectic alloys (these are copper alloys with their miscibility gaps below the liquidus line) will be studied using drop tube method of containerless processing.

1.4   Thesis outline

The rest of the thesis is divided into five chapters (two to six). Chapter two covers key fundamental knowledge needed for better understanding of the concepts in this research work. Chapter three is literature review of works on (i) monotectics and their solidification, (ii) stable miscibility gap, (iii) metastable miscibility gap alloys, (iv) the Co-Cu alloy system and (v) core shell microstructure in immiscible alloys. Chapter four details the experimental methods and techniques of the research work from alloy production to drop tube processing and characterization techniques. Chapter five contains the results and chapter six is discussion followed lastly by the conclusion.

2 Background knowledge

This section of the chapter is an overview of some relevant background knowledge needed in understanding the concepts of this research. Topics covered in this section include introduction of basic thermodynamic concepts, the thermodynamics of solution and undercooled melts, immiscibility in solutions, immiscible alloy systems, thermophysical properties of melts, nucleation and growth processes.

2.1 Thermodynamics

This section features a brief introduction of basic thermodynamic variables: internal energy (U), enthalpy (H), entropy (S), and the Gibbs free energy (G). Studies of these variables at equilibrium gives an understanding of non-equilibrium situations such as in the formation of metastable phases. The introduction is followed by thermodynamics of undercooled melts and of solutions. In all discussions a hypothetical two phased (α and β) A – B binary system is considered similar to the binary alloy system which is the focus of this research.

2.1.0 Internal energy, enthalpy and entropy

2.1.1 Internal energy (U)

Internal energy of a closed system depends on the properties of the components of the system and its environmental variables. Change in internal energy dU between two states in equilibrium is the difference between the final and initial equilibrium states ($U_2 - U_1$). From the law of conservation of energy [20]:

$$dU = dQ - dW \qquad (2.1)$$

Where Q is heat transferred into the system and W is work done by the system.

At constant pressure, equation (2.1) becomes

dU = dQ – PdV   (2.2)

Where P and V are the pressure and volume of the system.

2.1.2 Enthalpy

Heat energy changes (enthalpy of fusion ΔH_f / latent heat) is associated with solid – liquid transformation. Enthalpy is therefore the total heat content of a system at constant pressure and is given by

H = U + PV   (2.3)

The PV change is negligible and therefore $\Delta H_f \approx \Delta U$. The change in enthalpy due to unit change in temperature (specific heat capacity Cp) at constant pressure is given by

$$\Delta H = \int_{T_1}^{T_2} C_p \, dT$$ (2.4)

The C_p is key in calculating ΔH_f of a phase as the temperature varies.

2.1.3 Entropy (S)

Entropy, thermal energy and heat capacity are as a result of thermal motion in a closed system. It can be explained thermodynamically on the macro and micro scales.

In classical thermodynamics on the macro scale, entropy is concerned with the heat exchanges in or out of the system. It is therefore a measure of the thermal energy distribution in a system [21]. Entropy change in a reversible process is defined as

$$dS = \frac{dQ}{dT}$$ (2.5)

A reaction is therefore thermodynamically spontaneous if it is accomplished by positive entropy change ($\Delta S > 0$). Specific entropy change upon melting a mole of a material at the melting temperature ΔS_{melt} where the process is reversible is

$$\Delta S_{melt} = \frac{\Delta H_{melt}}{T_m} = \frac{L}{T_m} \qquad (2.6)$$

Where ΔH_{melt} is the heat in melting a mole of material at constant pressure, L is the specific latent heat and T_m is the melt temperature. In irreversible reactions such as in undercooling when an alloy solidifies below the equilibrium melting point at $T < Tm$, the entropy change ΔS_u is determined along a pre-defined reversible path between the liquid and solid states i.e.

$$\Delta S_u = \int_T^{T_m} \frac{C_{p,l}}{T} \, dT + \frac{L}{T_m} + \int_{T_m}^T \frac{C_{p,s}}{T} \, dT = \frac{L}{T_m} + \int_T^{T_m} \frac{\Delta C_p}{T} \, dT \qquad (2.7)$$

Where ΔC_p is the difference in the specific heat capacity of the liquid and solid ($\Delta C_p = C_{p,l} - C_{p,s}$). If the specific heat capacities of the two states are equal, the entropy as well as enthalpy will not vary with temperature.

In statistical thermodynamics entropy is related to the randomness of all thermal microstates (ω) in the system and is expressed by the Boltzmann's equation

$$S = k_B \ln \omega \qquad (2.8)$$

Where k_B is the Boltzmann's constant and ω is the interatomic interaction which is a measure of randomness (position and momenta) of the macro states.

2.1.4 Gibbs free energy and equilibrium state

The combined effects of entropy and enthalpy is described by the Gibbs free energy. The relative stability of a closed system at constant temperature and pressure is therefore determined by the Gibbs free energy (G)

$$G = H - TS \qquad (2.9)$$

The free energy change from one state to another is critical in determining whether or not a process is thermodynamically favourable (spontaneous) [22]. At equilibrium a system is at its most stable state, having the lowest overall value of Gibbs free energy

$$dG_{total} = 0 \qquad (2.10)$$

As shown in figure 2.1, A is the stable equilibrium state even though both satisfies equation (2.10). Equation (2.10) is therefore the minimum requirement for equilibrium as the overall free energy change could be below this. B is said to be at metastable state. Metastable states are usually transitional, given time they transform to new stable equilibrium state [22].

Equilibrium
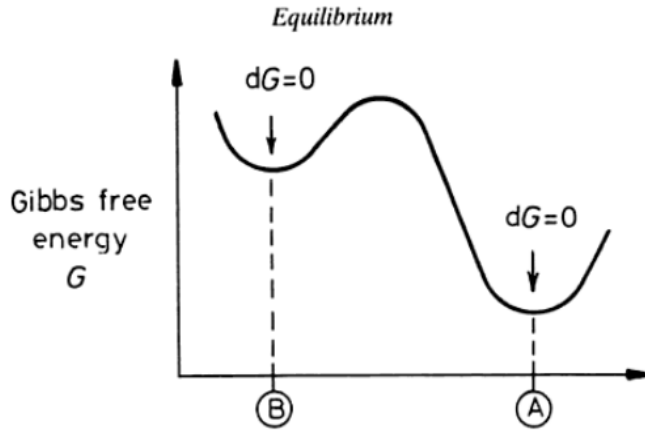
Figure 2.1 Variation of Gibbs free energy with atomic arrangements [22].

Phase transformations are only feasible when they are accomplished with a decrease in the Gibbs free energy.

2.1.5 Undercooled melts

The metastability of a liquid phase terminates by its transformation to a solid phase as the liquid is undercooled below its equilibrium melting temperature. The driving force for this solidification is expressed by the Gibbs energy difference between the solid and liquid states $\Delta G_v = G^L - G^S = \Delta H - T\Delta S$ (after equation 2.9), where G^S and G^L is free energy of solid and liquid respectively. In relation to specific heat capacity, C_p, the enthalpy and entropy term becomes

$$\Delta H = \Delta H_f - \int_{T}^{T_m} \Delta C_p \ dT \tag{2.11}$$

$$\Delta S = \Delta S_f - \int_T^{T_m} \frac{\Delta C_p}{T} \, dT \tag{2.12}$$

$$\Delta H_f = \frac{\Delta S_f}{T_m} \tag{2.13}$$

ΔS_f is the entropy of fusion and T is the temperature of the undercooled melt.

In equations (2.11) to (2.13), it can be seen that the specific heat capacity of the undercooled melt is most critical in its thermodynamic evaluation [23].

Data is sparse on specific heat capacity of undercooled melts, easily available data such as heat capacity difference at melting temperature ΔCp_f, ΔH_f and undercooling level below the eutectic temperature $\Delta T = T_m - T$, have been used in models for ΔG_v calculations [24]. The linear approximation equation by Turnbull [25] assumed the value of the specific heat capacity difference at the melting temperature is zero such that

$$\Delta G_v = \Delta H_f \frac{\Delta T}{T_m} \tag{2.14}$$

The above holds true with experimental data at low undercooling ($\Delta T < 0.2T_m$) [24][26] but at high undercooling (($\Delta T > 0.2T_m$), an experimentally measured specific heat capacity of the undercooled melt is required in calculating ΔG_v and the Dubey and Ramachandrarao [27] equation based on free volume model is most applicable, it is expressed as

$$\Delta G_v = \frac{\Delta H_f \Delta T}{T_m} - \frac{\Delta C_p T_m \Delta T^2}{2T} \left(1 - \frac{\Delta T}{6T}\right) \tag{2.15}$$

Entropy of undercooled liquid decreases faster than that of the stable crystalline phase at reduced temperature [24]. Kauzmann [28] was reported to have shown that at 'ideal glass temperature' (or Kauzmann temperature), T_{og}, the entropy of the undercooled liquid falls below that of the crystalline solid. He was of the opinion that the undercooling of a liquid is ultimately limited by the condition $\Delta S = 0$ [23]. This entropy crisis situation is avoided by the 'Kauzmann paradox', a situation in which the undercooled liquid freezes into a glassy state (glass transition) i.e.

$$\Delta T_{og} = T_m - T_{og} \qquad\qquad (2.16)$$

Fecht [29]and Johnson and Fecht [30] in their study of aluminium, were reported to have said that at above the melting point, a second temperature termed 'instability temperature' of the liquid , $T^S{}_L$, also satisfies the condition $\Delta S = 0$. They reported that at this second temperature, entropy of the liquid is again equal to that of crystalline aluminium.
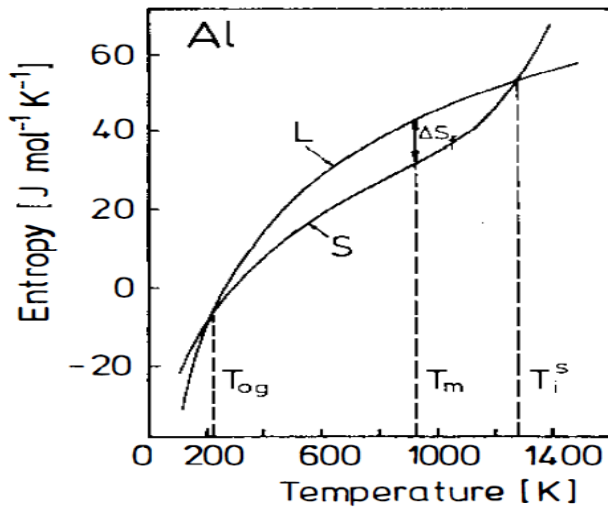
Figure 2.2 Entropy of liquid and crystalline aluminium as a function of temperature. T_m is the melting temperature of pure Al (933 K) and T_{og} is the ideal glass temperature where the entropy of the solid equals the entropy of the undercooled liquid. A similar point is found above the melting point, where solid and liquid entropy coincide at $T^S{}_L$ [22].

Isenthalpic solidification is only possible below a temperature T_{hyp} which marks the beginning of the hyper cooling regime where enthalpy of the undercooled liquid at the solidification temperature is same as the enthalpy of the solid at the melting temperature [24]. The condition $\Delta H = 0$ must be satisfied before this isenthalpic crystallization can occur [23]. The hyper cooling limit is given by

$$\Delta T_{hyp} = T_m - T_{hyp} \qquad\qquad (2.17)$$

Study of the hyper cooling limit is crucial to the preparation of metastable phases from undercooled melts [31] and rapid growth kinetics in undercooled melts [23].

2.1.6 Solutions

The phase behaviour of solutions is determined by their thermodynamic characteristics. Gibbs free energy of pure elements A and B can be determined from the free energies of A and B. The free energy of the mixture of the two components is simply the weighted average

$$G_{(A+B)} = X_A G_A^o + X_B G_B^o. \tag{2.18a}$$

The free energy of the alloy formed is $G_{(ALLOY)} = X_A G_A^o + X_B G_B^o + \Delta G_{mixing}$ i.e.

$$\Delta G_{mixing} = \Delta H_{mixing} - T \Delta S_{mixing} \tag{2.18b}$$

G^O is molar free energy, $X_{A/B}$ is the molar or atomic fractions of components A or B, ΔG_{mixing} is change in Gibbs free energy caused by mixing, ΔH_{mixing} is heat of solution absorbed or evolved during mixing and ΔS_{mixing} is difference in entropy between the mixed and unmixed state.

2.1.6.1 Ideal solution

The simplest type of mixing yields the ideal solution in which $\Delta H_{mixing} = 0$. The free energy change that occurs is due to change in entropy, $\Delta G_{mixing} = -T \Delta S_{mixing}$. The entropy here (configurational entropy) is largely due to the randomness of the atoms arrangement [32]. If $\omega_{conf} = \frac{(n_A + n_B)!}{(n_A)!(n_B)!}$ and $N_a K_B$ = R (universal gas constant), Stirling's approximation of equation (2.12) yields

$$\Delta S_{mixing}^{ideal} = -R(X_A \ln X_A + X_B \ln X_B) \tag{2.19}$$

Therefore for the ideal solution,

$$\Delta G_{mixing}^{ideal} = RT(X_A \ln X_A + X_B \ln X_B) \tag{2.20}$$

The curve of $\Delta G_{mixing}^{ideal}$ is shown in figure 2.3. It shows from the shape of the curve that components A and B are totally miscible.
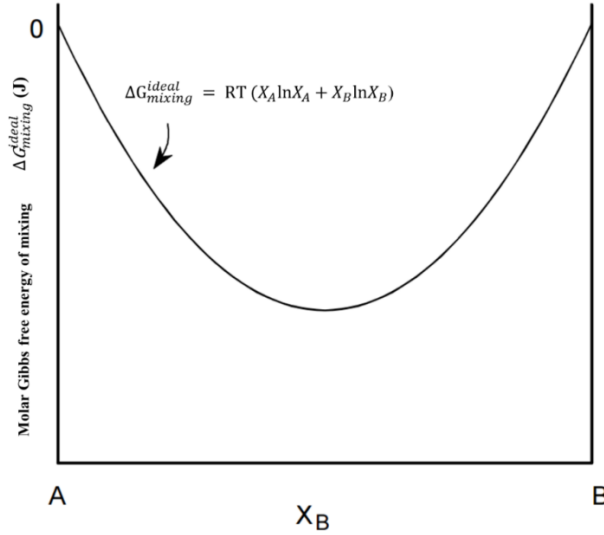
Figure 2.3 Molar Gibbs free energy of mixing curve of an ideal solution of components A and B with complete miscibility.

2.1.6.2 Regular solution

In reality mixing is either endothermic or exothermic. The free energy of the regular solution is determined using atomistic theory based on the assumption of the quasi – chemical model developed by Bhatia and Singh [32] that distance between atoms and their bond energies are independent of composition and so the ΔH_{mixing} is due to bond energies between adjacent atoms. Figure 2.4 shows 3 bond types in A – B system, the internal energy of the system $U = p_{AA}\mathcal{E}_{AA} + p_{BB}\mathcal{E}_{BB} + p_{AB}\mathcal{E}_{AB}$, $\Delta H_{mixing} = p_{AB}\varepsilon$

Where $\varepsilon = \varepsilon_{AB} - \dfrac{(\varepsilon_{AA} + \varepsilon_{BB})}{2}$ $\hfill (2.21)$

Relating equation (2.20) to the mole fractions of A and B and bond energy interatomic interaction parameter, Ω

$\Delta H_{mixing} = \Omega X_A X_B$ $\hfill (2.22)$

Where $\Omega = N_a Z \varepsilon$ $\hfill (2.23)$

Z is the number of bonds per atom and ε is the difference between A-B bond energy and average of the A-A and B-B bond energies.

Gibbs free energy of mixing for the regular solution after equation (2.18b) is then

$$\Delta G_{mixing}^{regular} = \Omega X_A X_B + RT(X_A \ln X_A + X_B \ln X_B) \qquad (2.24)$$

The term $\Omega X_A X_B$ is representative of the solution's deviation from ideal behaviour.

A – A bond (energy E_{AA})

A – B bond (energy E_{AB})

B – B bond (energy E_{BB})
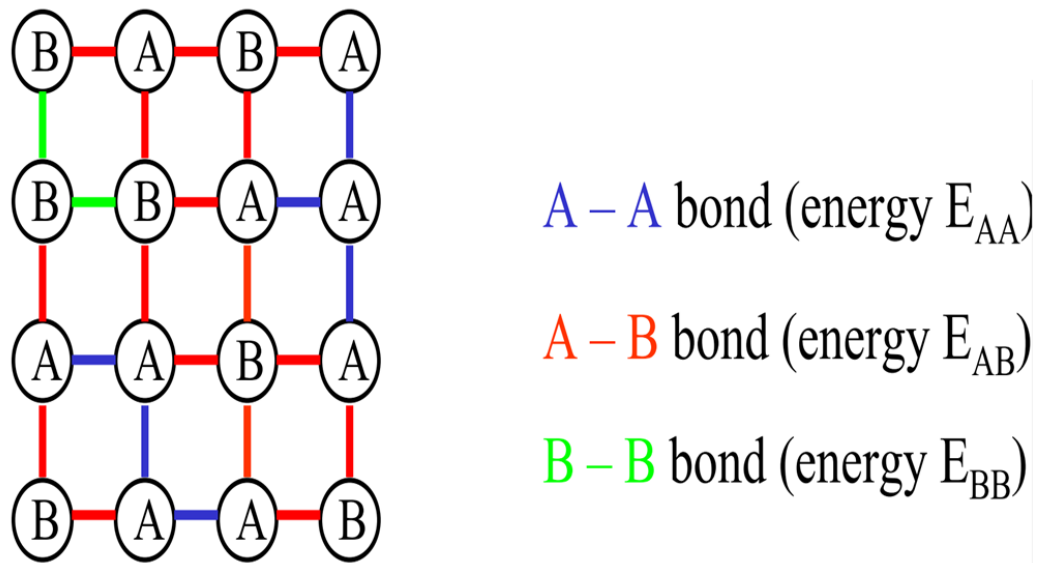
Figure 2.4 Schematic representation of a bond structure in a binary A - B system. The number of each type of bonds are p_{AA}, p_{BB} and p_{AB}.

2.1.7 The Redlich Kister model for excess Gibbs free energy of mixing (ΔG^{excess})

In real alloy systems, excess enthalpy (due to energy change upon new bond formation) and entropy are encountered [33]. The total free energy change is therefore made up of the ideal and excess free energies ($\Delta G = \Delta G^{excess} + \Delta G^{ideal}$) with similar expressions for the entropy and enthalpy changes.

The Redlich Kister model is a power series expansion of the excess quantities in mole fraction of the components. The model is obtained by expanding the infinite series used in representing excess molar Gibbs free energy of a binary

system up to the third term. This infinite series proposed by Guggenheim is given as

$$\Delta G^{excess}/RT = X_A X_B \sum_i A_i (X_A - X_B)^i \qquad (2.25)$$

When expanded this gives the polynomial

$$\Delta G^{excess}/RT = (X_A X_B)[A_0 + A_1(X_A - X_B) + A_2(X_A - X_B)^2 + \cdots] \qquad (2.26)$$

The A constants are determined from experimental data and are at fixed temperature and pressure [34]. The terms $(X_A X_B)$ makes $\Delta G^{excess} = 0$ at the composition $X_A = X_B = 0$.

Series expression for the excess enthalpy and entropy is

$$\Delta H^{excess} = \sum_i A_i X_A X_B (X_A - X_B)^i \qquad (2.27)$$

$$\Delta S^{excess} = \sum_i B_i X_A X_B (X_A - X_B)^i \qquad (2.28)$$

2.2 Immiscibility in solutions

The Gibbs free energy is a function of temperature, pressure and composition i.e. $dG\,(T, P, n_i)$. As already stated at equilibrium the Gibbs free energy is at its lowest:

$$dG\,(T, P, n_i) = \left(\frac{\partial G}{\partial T}\right)_{P,\,n_{i\ldots}} dT + \left(\frac{\partial G}{\partial P}\right)_{T,\,n_i} dP + \left(\frac{\partial G}{\partial n_i}\right)_{T,P,n_{j\ldots}} dn_i = 0 \qquad (2.29)$$

The partial derivative $\left(\frac{\partial G}{\partial n_i}\right)_{T,P,n_{j\ldots}}$ is the chemical potential (μ_i). The chemical potential adjusts a system to equilibrium as components of its phases change. At constant temperature and pressure $dG = \mu_i dn_i + \mu_j dn_j + \cdots = 0$. The fundamental conditions for equilibrium in any system is that the chemical potential be same in the phases present and so in the binary system considered, $\mu_A^\alpha = \mu_A^\beta$ and $\mu_B^\alpha = \mu_B^\beta$.

Where n_i is the number of moles of component i, μ_A^α, μ_A^β represents chemical potential of component A in α and β phase respectively while μ_B^α, μ_B^β represent that of the component B in the α and β phases as well. If one of the chemical potential is less in any of the phase as in non-equilibrium situations, atomic movement is towards phase in which it is lowest.

Molar Gibbs free energy of mixing of the alloy formed becomes

$$G_{ALLOY}^0 = X_A\mu_A + X_B\mu_B \tag{2.30}$$

Total free energy change is

$$\Delta G_{ALLOY}^{total} = X_A\left(\mu_A - G_A^0\right) + X_B\left(\mu_B - G_B^0\right) \tag{2.31}$$

Assuming at a specific temperature an alloy of composition X_B is formed, on the $G^O{}_{ALLOY}$ curve of the phases it is seen that at equilibrium condition the limits of solubility of the phases in the alloy $X^\alpha{}_B$ and $X^\beta{}_B$ falls on a common tangent of the curves of the phases. The solubility of the unstable phase is always greater than that of the stable phase [20]. In a regular solution, if $\Omega > 0$, $\Delta H_{mixing} > 0$, endothermic mixing occurs and atom preference is for like neighbours (immiscibility).
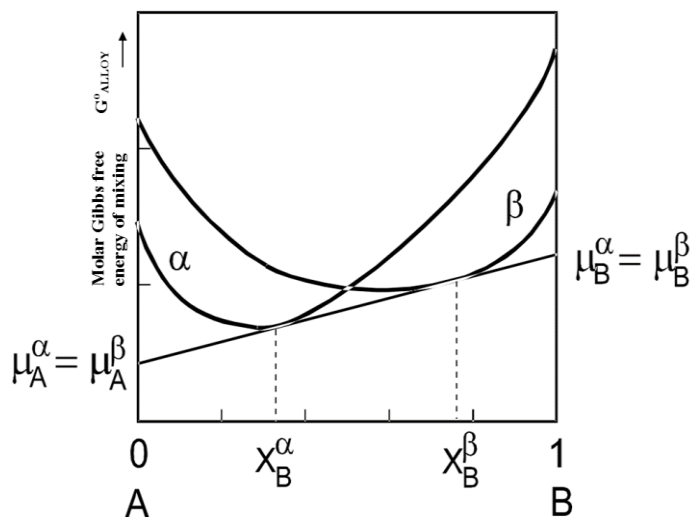
Figure 2.5 Schematic diagram of molar Gibbs free energy of mixing of α and β phases in a binary system showing limited miscibility (immiscibility) using the common tangent method.

If the Gibbs free energy of mixing is symmetrical at mid – composition, the limits of solubility are determined by finding the compositions at which the partial derivative in respect to X_B equals zero i.e. from the regular solution

$$\Delta G_{mixing}^{regular} = \Omega X_A X_B + RT(X_A \ln X_A + X_B \ln X_B)$$

But $X_A = 1 - X_B$

$$\Delta G_{mixing}^{regular} = \Omega(1 - X_B)X_B + RT\big((1 - X_B)\ln(1 - X_B) + X_B \ln X_B\big) \quad (2.32)$$

At the minima

$$\partial \Delta G_{mixing} \Big/ \partial X_B = 0 = \Omega(1\text{-}2X_B) + RT \ln\left(\frac{1 - X_B}{X_B}\right) \quad (2.33)$$

The solution of equation (2.33) plotted against temperature gives the phase diagram of the regular solution which is discussed in details under immiscible alloy systems.

2.2 Immiscible alloy systems

The phase diagram of immiscible alloys have a characteristic dome shaped region known as the miscibility gap within which separation of the initial homogeneous melt occurs [2]. This dome shaped region has a maximum point which is called the critical point, the temperature of which is noted T_c (critical or consolute temperature). Below the T_c is the monotectic temperature T_m where the monotectic reaction $L_1 \rightarrow \alpha + L_2$ occurs.
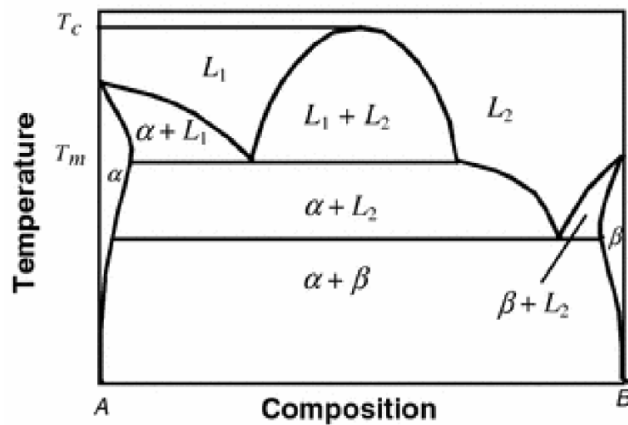
Figure 2.6 Schematic phase diagram of a binary immiscible alloy showing the miscibility gap, critical temperature T_c and monotectic reaction at temperature T_m [35].

The phase separation process in these class of alloy is shown in figure 2.7, on cooling a homogeneous single phase liquid into the miscibility gap, the components lose their miscibility and decompose into liquid phases. This process of decomposition has been said to start with the nucleation of the liquid minority phase in form of droplets, growth of the droplets then occurs through the process of diffusion. These droplets have also been known to migrate due to concentration or temperature gradient or settle due to gravitational forces hence the final solidified microstructure of the undercooled immiscible alloy depends on all these processes [2].
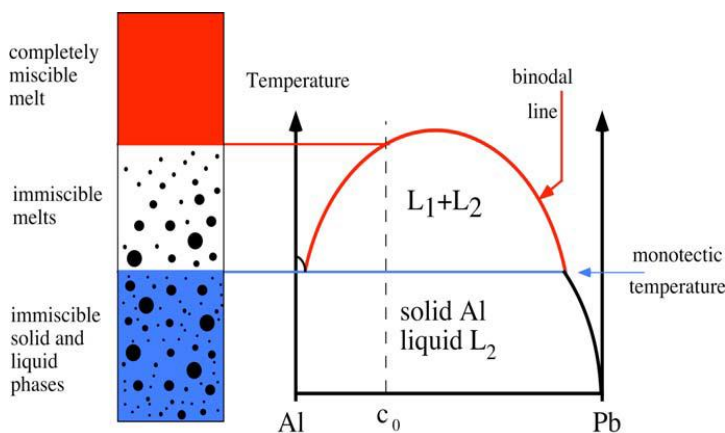
Figure 2.7 Phase separation in immiscible monotectic alloys [36].

Classifications of immiscible alloys have been done according to the stability of their miscibility gaps [36]. Some metallic binary systems under the two classifications are listed below:

1. Stable miscibility gaps

   - Aluminium based (Al - Pb, Al - In, Al - Bi, Al - Cd)

   - Copper based (Cu - Pb)

   - Gallium based (Ga - Bi, Ga - Pb, Ga - Hg)

   - Zinc based (Zn - Pb, Zn - Bi)

   - Silver based (Ag - Fe, Ag - Ni)

2. Metastable miscibility gaps [3]

   - Copper based (Cu - Co, Cu - Fe, Cu - Cr, Cu - Ta)

   - Aluminium based (Al - Be, Al - Ge, Al - Ag)

   - Silver based (Ag - Ge)

2.2.1 Miscibility gap in the liquid state

As already explained under thermodynamics, the origin of immiscibility in the liquid state is traced to the molar Gibbs free energy of mixing of the components. The shape of the Gibbs free energy curve has however been largely attributed to the entropy and enthalpy of mixing [37]. Upon mixing, changes in entropy arise due to ordering changes on alloy formation while changes in enthalpy of mixing is attributed to interatomic interaction parameter (Ω). Phase separation is favoured when the interatomic interaction energy of the alloy formed is weaker than that of its individual constituents. When Ω is positive (which is characteristic of immiscible systems) and at low temperature conditions such as when undercooled, $T\Delta S_{mixing}$ is smaller than ΔG_{mixing} and the resulting Gibbs free energy curve has a negative curvature in the middle [22,37] as shown in figure 2.8. At the composition X_{B0}, a decrease in the free energy from ΔG_0 to ΔG_2^1 occur as the solution transforms into two

phase with compositions X_{B1} and X_{B2} which are also the point of contact on the tangent. The line defined by this double tangent on the curve is known as the binodal line or line of co-existence [33]. The temperature of the co − existing phases is related to their composition using this equation

$$T = \frac{\Omega(1 - 2X_B)}{R(\ln X_A - \ln X_B)} \tag{2.34}$$

Where R is the gas constant.

The points of inflection on the curve $X_B{}'$ and $X_B{}''$ which is where the curvature of the free energy curve is negative and is known as the spinodal line [33]. At this points $\frac{\partial^2 G}{\partial X^2} = 0$, the binodal and spinodal meet at the critical point, marked by temperature T_c (figure 2.8b). For a regular solution, the spinodal line (T_{sp}) and the critical temperature (T_c) of the miscibility gap is given by

$$T_{sp} = \frac{\Omega}{2R} X_A X_B \qquad (2.35) \quad \text{and} \quad T_c = \frac{\Omega}{2R} \tag{2.36}$$

The region between the binodal and spinodal is metastable (at constant temperature) while the region below the spinodal line is unstable. Phase separation occurs below the binodal line through nucleation and growth after overcoming energy barrier but within the spinodal, since the solution is unstable to microscopic perturbations in composition and density and the absence of thermodynamic barriers to the growth of a new phase, A - rich and B -rich regions are formed. This phase transformation that occurred is entirely diffusion controlled and is known as spinodal decomposition [38]. This transformation happens homogeneously all over the alloy through the slow expansion of regions enriched in solute (uphill diffusion) resulting in a two phase modulated structure [39]. The rate of this slow expansion (diffusion) is controlled by the rate of atomic migration as well as the diffusion distance which depends on the scale of undercooling.

The theory of spinodal decomposition has been explained on the basis of small amplitude fluctuations since it entails amplification of elongated wavelengths concentration waves inside a solid solution in a super saturated

state induced by random fluctuations [39]. It was observed that a composition fluctuation that is a function of position in a homogeneous solid solution of composition Co initiates the decomposition process [38]. This sinusoidal composition fluctuation can be represented as

$$C - Co = A \cos \beta x \qquad (2.37)$$

Where A is the amplitude of the sine wave, $\beta = \frac{2\pi}{\lambda}$ is wave number and λ is the wavelength.

If the wavelength is assumed to be independent of time, the time dependence is in the amplitude

$$C(x,t) - Co = A(\beta,t) \cos \beta x \qquad (2.38)$$

But in metastable solutions, minute deviations from the average concentration, Co, decays with time by

$$\Delta C = \Delta Co\, e^{-t/\tau} \qquad (2.39)$$

Where τ is the relaxation time and equals λ^2/D, D is the diffusion coefficient.

In the spinodal, the diffusion coefficient is negative due to the occurrence of backward diffusion from low concentration to high concentration region. In solving the problem posed by a negative diffusion coefficient, the Cahn - Hilliard equation is mostly adopted [40].

The Cahn – Hilliard equation is generally used to model and describe phase separation especially the process of spinodal decomposition. In its simplest form it is a generalisation of the Fick's law of diffusion reflecting the conservation of matter i.e.

$$u_t = -\nabla J \qquad (2.40)$$

Where u_t is assumed to be the concentration of one of the components of the alloy decomposing and J is the mass flux orthogonal to the boundary and satisfies the condition below.

$$J = - M(u) \nabla[f^!(u) - \in^2 \nabla^2 u] \tag{2.41}$$

Where M(u) is the mobility coefficient or internal diffusion (which is always positive), f(u) is the homogeneous free energy and $\in$ is the interaction length of the regions during phase separation.

It then follows that the expression for the Cahn – Hilliard equation describing the evolution of a conserved concentration during liquid phase separation process is

$$\frac{\partial u}{\partial t} = \nabla M(u) \nabla [f^!(u) - \in^2 \nabla^2 u] \tag{2.42}$$

As time progresses after the initial evolution, coarsening occurs and as such the equation is also used to model coarsening of separated phases [40].

From equation (2.43) which is Fick's laws of diffusion [41], the application of the Cahn – Hilliard equation to the expression in (2.39) the rate of growth of the amplitude of the concentration wave is given by the equation in (2.44)

$$D \propto \frac{\partial^2 G}{\partial C^2} \tag{2.43}$$

$$\Delta C = \Delta Co\, e^{(+\mathcal{R}(\beta)t)} \tag{2.44}$$

Which can be re-written after equation (2.38) as

$$C(x,t) - Co = A(\beta,0)e^{(\mathcal{R}(\beta)t)} \cos \beta x \tag{2.45}$$

Where $\mathcal{R}(\beta)$ is the amplification factor and equals

$$-\frac{M}{Na} \cdot \beta^2 \cdot [\frac{\partial^2 G}{\partial C^2} \big| co + 2K\beta^2] \tag{2.46}$$

M is a term derived from the mobilities of the components. The factor $\mathcal{R}(\beta)$ is a maximum for intermediate wavelength. Elongated wavelength fluctuations develop gradually due to the huge diffusion distance, short wavelength fluctuations on the other hand are stifled by the surface energy of the diffuse interface that develop during phase separation. Consequently, the microstructure that develop during spinodal decomposition has a

characteristic periodicity that is usually 2.5 to 10 nm (25 to 100 Å) in metallic systems [38].
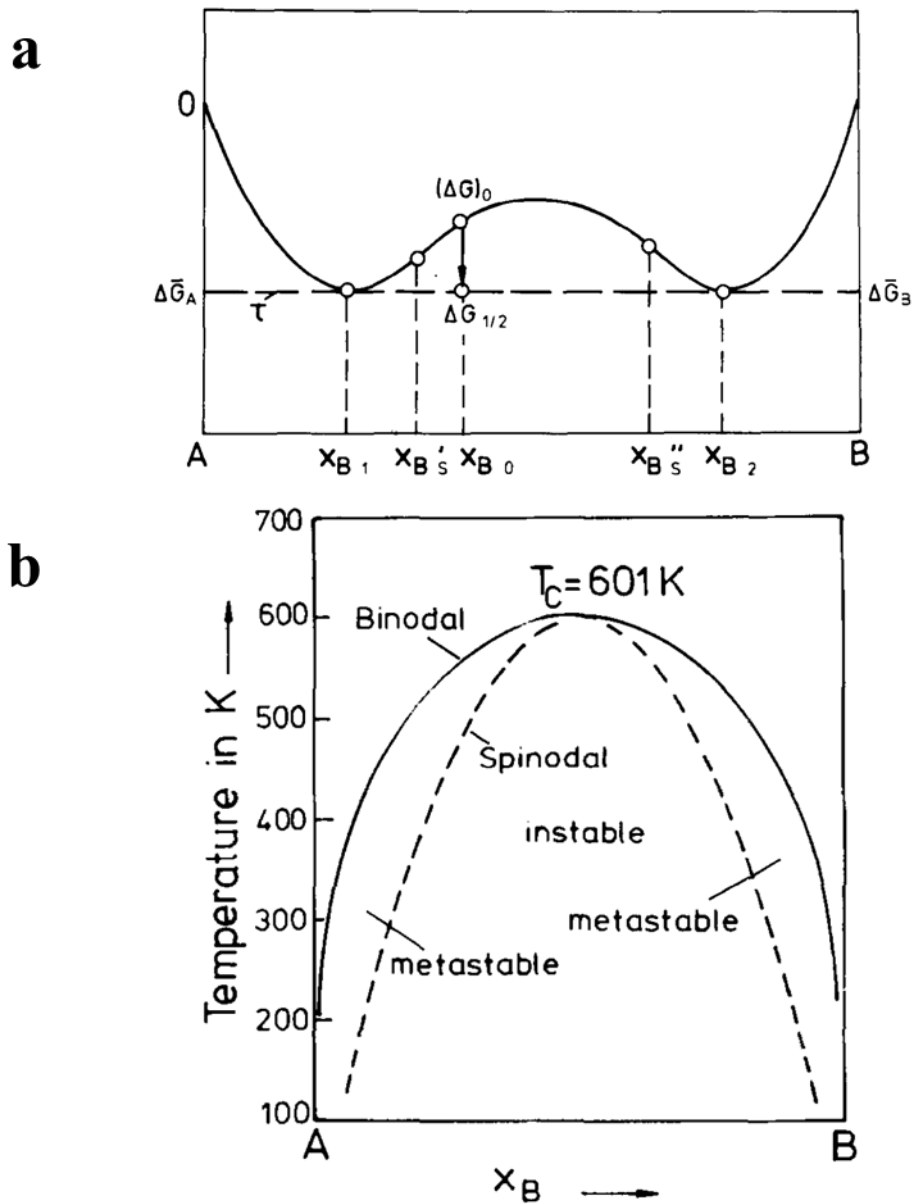
Figure 2.8 Spinodal region explained through (a) free energy diagram of a system with limited miscibility and (b) miscibility gap showing the spinodal line [33].

2.2.2 Types of miscibility gap in the liquid state

1. **Symmetrical binodal:** systems exhibiting this type of miscibility gap can be compared to a regular solution, the T_c is nearly centrally

23

located on the phase diagram and the binodal line is nearly symmetrical around $X = 0.5$. Typical examples of such a system is the Ga - Hg system (figure 2.9a) which has the lowest critical temperature of all binary alloy ($T_c = 477K$) and Al - Pb system (figure 2.9b) [33].
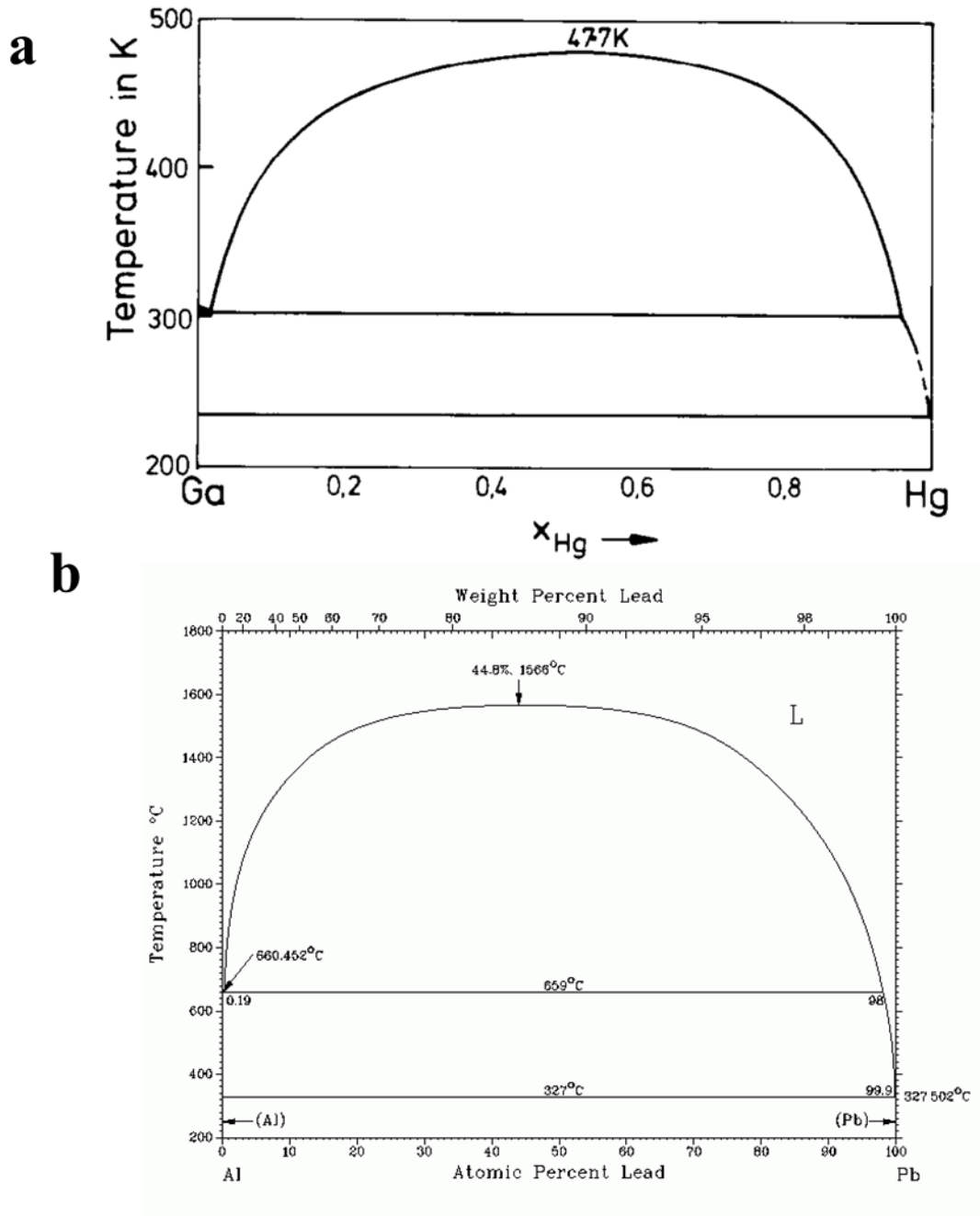
Figure 2.9 Phase diagrams showing symmetrical binodal (a) Ga - Hg system, (b) Al - Pb system [33].

2. **Descending binodal:** In systems exhibiting this type of miscibility gap the T_c is not centrally located on the phase diagram and most times it is lower than the melting point of the higher melting element. Examples of systems in this category include Bi - Zn (figure 2.10a) and Bi - Ga (figure 2.10b). In the Bi-Ga system, T_c is 533K while the melting point of Bi is 544.5K [33]. A gentle descent of the binodal towards the monotectic temperature characterises the miscibility gap of this system while in the Bi - Zn system, a steep descent is noticed with the T_c shifting towards the Zn side. This trend of descending binodal is also seen in the miscibility gap of Cu - Pb (figure 2.10c).
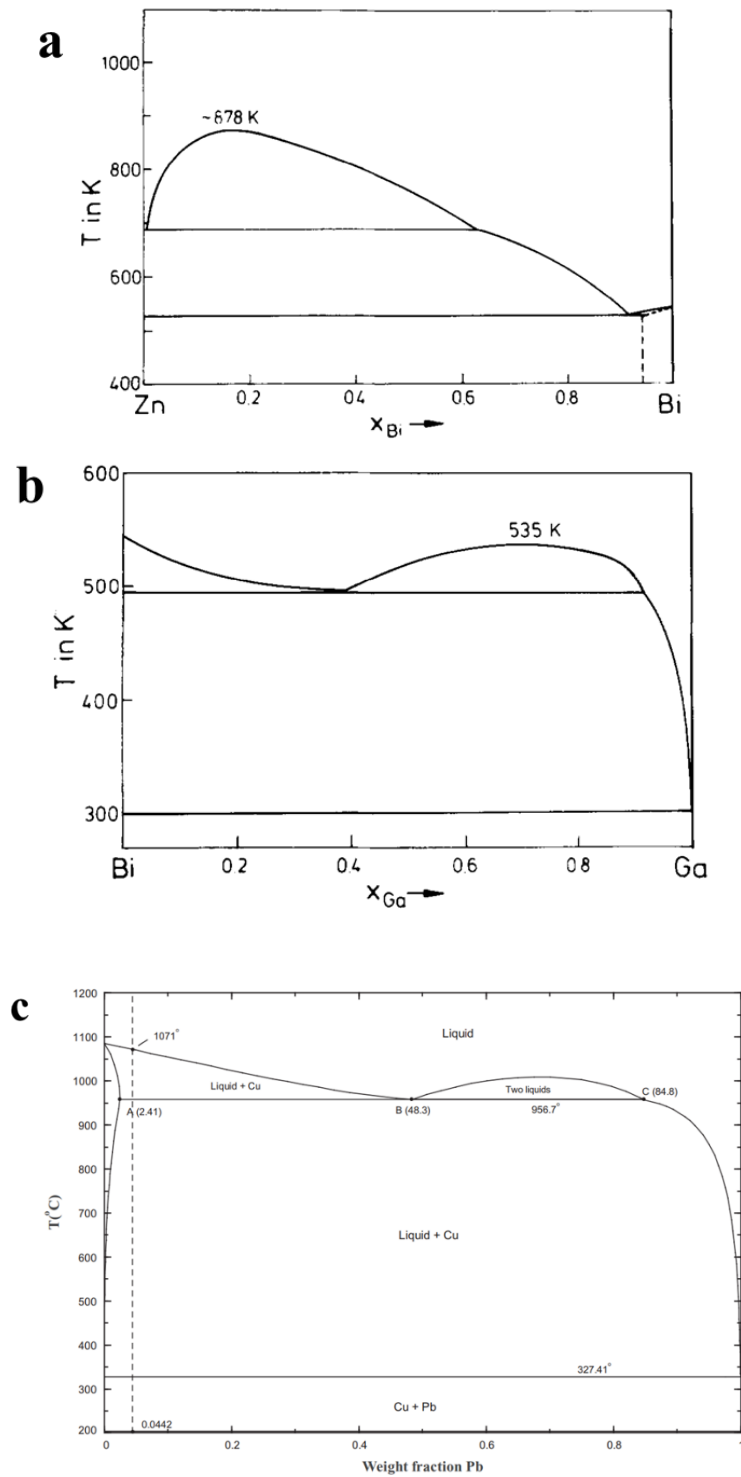
Figure 2.10 Phase diagrams showing (a) Steep descent binodal in Bi - Zn system, (b) gentle descent binodal in Bi - Ga system [33] and (c) descending binodal in Cu - Pb system [42].

3. **Miscibility gaps in systems with similar chemical components:** little is known about the origin of the miscibility gap in these type systems. Under varying bonding conditions, limited solubility in the liquid state is observed e.g. in Li - Na system (figure 2.11c), the cause of immiscibility has been linked to atomic radii difference however, it was reported that Elliot in his research observed a miscibility gap in the Ca - Na (figure 2.11b) and Ca - La (figure 2.11a) systems where there is no difference in atomic radii [33].
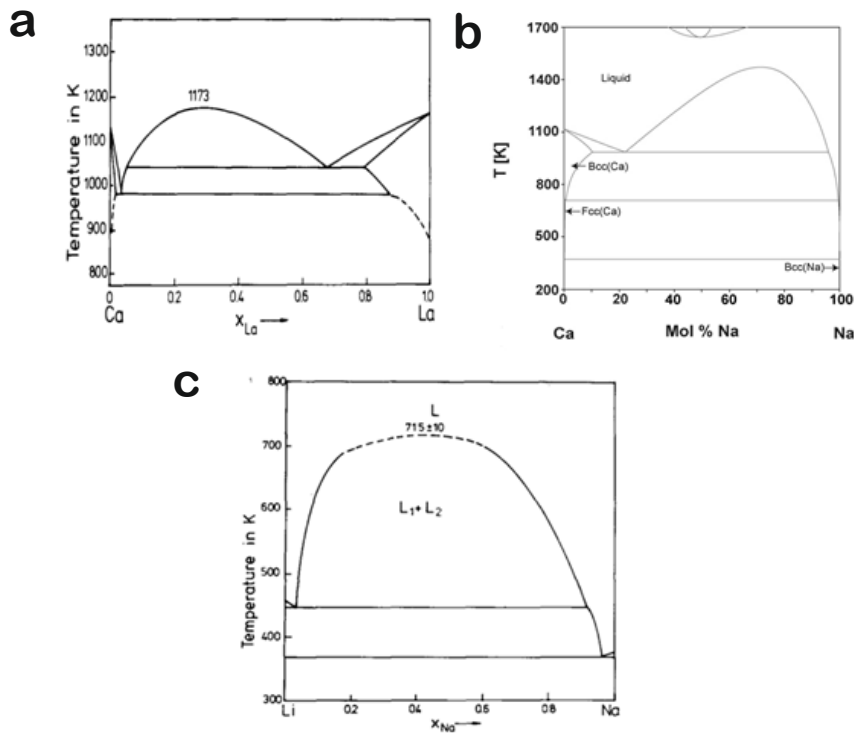
Figure 2.11 Phase diagrams showing miscibility gap in systems with similar chemical composition (a) Ca - La system, (b) Ca - Na system and (c) Li - Na system [42].

Miscibility gaps have also been noticed in some systems with very similar components in terms of chemical properties and atomic size e.g. the rare earth metal combinations. Ratke and Diefenbach [33] in their review cited that a miscibility gap in the liquid state in the rare earth metal combinations Eu - Sm and Eu - La which was absent in La-Sm system. This they attributed to local order and clusters in the melt and they pinned this as the true origin of

phase separation in the systems. They also cited research that was of contrary view in the miscibility gaps in rare earth systems of the type Eu-rare earth metal and Yb-rare earth metal is said to be due to differences in atomic volume. This research was reported to be of the opinion that since Eu and Yb have a 50% larger atomic volume than any other rare earth metal and so the miscibility gap has to be simply as a result of this.

It is however important to state that in some monotectic systems, the equilibrium phase diagram does not exhibit a stable miscibility gap or monotectic reaction as described above. In such systems, the liquidus curve slope towards zero at some point and a metastable miscibility gap is present below this curve. Monotectic reaction in these alloys is also metastable. A typical example is the Co - Cu alloy which is a peritectic alloy system.

2.3   Some thermophysical properties of melts

Thermophysical properties highly impact processes such as nucleation, thermal migration during phase transformation and coarsening during solidification hence their knowledge is very important in understanding the solidification and microstructural behaviour of immiscible alloy systems. There is little accurate and consistent information on the thermophysical properties of systems with miscibility gaps in the liquid state due to the difficulties associated in determining them especially of undercooled liquid metals and at high temperatures due to convection and chemical reactivity influences hence some have been determined in micro gravity conditions [43]. The experimental determination of these properties is beyond the scope of this research, however this section of the chapter reviews available texts and literature on relevant thermophysical properties and how they may be calculated for metastable systems from available data.

2.3.1   Density

The density of a material is defined as its mass per unit volume i.e.

$$\rho = \frac{m}{V} \tag{2.47a}$$

It is a component in calculating other thermophysical properties such as viscosity, surface tension and thermal conductivity as well as in understanding the mass transport, atomic structure and solidification process of liquid alloys.

In theoretical analysis, density is instrumental in determining volume changes associated with melting, alloying and solidification [44]. Similar to solutions, excess volume, V^{excess}, is associated with alloy formation [41] and in a binary alloy

$$V^{excess} = \frac{X_A W_A + X_B W_B}{\rho} - \left(\frac{X_A W_A}{\rho_A} + \frac{X_B W_B}{\rho_A}\right) \tag{2.47b}$$

Where the first expression on the right is the atomic volume of the alloy, V, and the one in bracket is V^{ideal}, A and B are the components and X and W are the atomic fraction and weight respectively.

Crawley [45]and Predel and Emam [46] showed there was no correlation between V^{excess} and the thermodynamic properties (ΔS^{excess}, ΔH^{excess}). Tamaki et al. [47] were however of contrary view in their study on properties of compound forming alloy systems. They showed that negative V^{excess} and ΔH^{excess} values were characteristic of compound forming systems while positive values characterised immiscible systems. In most binary alloys however, V^{excess} is a linear function of composition and is generally within ± 0.02 deviation hence atomic volume of liquid binary alloys is calculated by adding that of its components [41]. Once the atomic volume of the alloy is calculated, the density of the alloy can then be determined using equation (2.47a).

The density of pure liquid metals as a function of temperature is from the Cailletet and Mathias law (rectilinear law) which states that the average density of a liquid varies linearly as the temperature rises to the critical temperature (T_c) [41]. This is usually expressed as

$$\rho_L = \rho_m - b(T - T_m) \tag{2.48}$$

Where ρ_m is density at the melting temperature (T_m), T is absolute temperature in Kelvin and b is dimensionless constant. Values of ρ_m for pure metals and alloys of commercial interest as well as of the constant are available in literature [41,42,45,48,49].

2.3.2   Specific heat capacity

This is the quantity of heat, Q, to change the temperature, T, of a unit mass, m, of a material by one Kelvin. In determining ΔH or ΔS variation with temperature, a knowledge of the temperature dependence of the specific heat is required [20].

The variation of the specific heat as a function of temperature of liquid metals is estimated by

$$C_p = a + bT + cT^{-2} + dT^2 \tag{2.49}$$

Where a, b, c and d are constants.

Excess specific heat capacity C_p^{excess}, is associated with the formation of binary alloys [24] and this excess quantity is given by the expression in [50] as:

$$\Delta C_p^{excess} = -2RT \sum_i x_i \left(\frac{\partial \ln \gamma_i}{\partial T} \right) - RT^2 \sum_i x_i \left(\frac{\partial^2 \ln \gamma_i}{\partial T^2} \right) \tag{2.50}$$

Where γ_i is the activity coefficient of components i and x is the mole fraction.

A positive ΔC_p^{excess} that decreased with temperature was said to have been reported by Chen and Turnbull [24] near the eutectic composition in the Au – Si binary alloy system. Estimates of the specific heat capacity of liquid binary alloys (C_{pL}) is usually calculated by adding the heat capacity of the components according to the Neumann – Kopp rule of mixture [24,44] i.e.

$$C_{pL} = \sum_a^b X_A \left(C_{pL} \right)_A \tag{2.51}$$

Where X_A is atomic fraction of component A in the binary alloy system.

2.3.3 Thermal conductivity

Thermal conductivity, λ, is calculated from its theoretical relationship with electrical conductivity, κ. The theoretical relationship known as the Wiedemann – Franz – Lorenz law [41,44] simply states that the ratio λ/κ is proportional to the absolute temperature, T, with a proportionality constant L which is the Lorenz number i.e.

$$\frac{\lambda}{\kappa_{total}T} \ = \ L = \frac{\pi^2 k^2}{3e^2} \ = \ 2.445 \text{ x } 10^{-8} \text{ (W}\Omega\text{K}^{-2}) \tag{2.52}$$

Where e and k are the electric charge and wave vector constants respectively.

An estimate of the thermal conductivity of liquid alloys is then possible through knowledge of the value of its electrical conductivity. In liquid binary alloy, total electrical conductivity κ_{total} is given by the expression in [41] as

$$\kappa_{total}^{Liq} \ = \ \kappa_A x_A + \ \kappa_B x_B \tag{2.53}$$

The temperature dependence of κ_{total} is given by [44]

$$\kappa_{total} \ = \ \kappa_{total}^{Liq} + \ \kappa_{total}^{Liq} \left(\frac{d\kappa}{dT}\right)_{ALLOY} \tag{2.54}$$

Where $\frac{d\kappa}{dT} \ = \ x_a \left(\frac{d\kappa_a}{dT}\right) + \ x_b \left(\frac{d\kappa_b}{dT}\right)$ (2.55)

The Wiedemann – Franz – Lorenz relationship was reported to have been verified in liquid tin, mercury, and gallium and also in the liquid binary systems Hg - In by Busch et al. and Haller et al. [41], Pb - Bi system by Powell and Tye, and Pashaev was said to have worked on Cd - Sn and Bi - Sn alloys [51].

2.3.4 Surface/ Interfacial tension

An interface is the surface between two phases/ immiscible liquids. An imbalance in the coordination among the surface atoms make it to be at higher energy state than the bulk phase. The surface/ interfacial tension, σ, in liquids is therefore defined as the sum of energies of the surface / interface atoms [20].

The nucleation, growth and migration of nucleated particles in immiscible alloys are greatly influenced by the liquid – liquid interfacial tension and as such knowledge of it and its temperature dependence is key in understanding microstructural evolutions in such alloys [37].

A number of researchers have worked on determining the interfacial tension in immiscible alloys. Kaban and his co – researchers [52–55] worked on binary, ternary and quaternary Al – Bi systems over wide composition and temperature ranges. They used a statistical thermodynamics model based on van der Waals' model of diffusive interfaces proposed by Cahn - Hilliard and came up with an expression for the interfacial tension between α and β phases in [53] as:

$$\sigma_{\alpha\beta} = N_v \int_{-\infty}^{+\infty} \left[\Delta f(c_i) + \mathcal{K} \left(\frac{dc_i}{dx} \right)^2 \right] dx \qquad (2.56)$$

Where N_v is the number of molecules per unit volume, $\Delta f(c_i)$ is the free energy at standard state of equilibrium mixture of α and β, c_i is mole fraction of component i and $\mathcal{K}$ is the coefficient of gradient energy.

Another thermodynamic based model in calculating the surface tension of liquid alloys is one based on the Butler equation [56] in which the surface area and excess Gibbs energy of the liquid metal must be known. In this model proposed by Tanaka and his co – workers [57–59], the liquid surface is considered to be a single layer of atoms in equilibrium with the bulk of the metal. The interface tension is then given as:

$$\sigma_{\text{ALLOY}} = \sigma_A + \frac{RT}{A_A} \ln \left(\frac{1 - x_B^{sur}}{1 - x_B^{blk}} \right) + \frac{1}{A_A} \Delta G_A^{excess,\,sur} - \frac{1}{A_A} \Delta G_A^{excess}$$

$$= \sigma_B + \frac{RT}{A_B} \ln \left(\frac{x_B^{sur}}{x_B^{blk}} \right) + \frac{1}{A_B} \Delta G_B^{excess,\,sur} - \frac{1}{A_B} \Delta G_B^{excess,\,blk}$$

$$(2.57)$$

Where σ_A and σ_B are the surface tension of the pure components, A_A and A_B are the relative surface area in single layer of components and the superscripts sur and blk represents the surface and bulk layer respectively.

The surface area is related to the volumes of the components in the liquid alloy by:

$$A_X = 1.091 N_a^{1/3} V_x^{2/3}$$
(2.58)

Where N_a is the Avogadro's number and V_x is molar volume of the component x which is gotten from the density of its pure component.

Tanaka et al. [58] also established an empirical relationship between the excess Gibbs energy of mixing for the surface and bulk as:

$$\Delta G^{\text{excess, sur}} = \xi \Delta G^{\text{excess, blk}}$$
(2.59)

Where ξ is the parameter that accounts for the reduced coordination number of atoms in the surface layer. 0.83 was suggested for this parameter and is the value widely used for most liquid metals. $G^{\text{excess, blk}}$ is then obtained using the Redlich – Kister polynomial up to the second term [60]

Theoretical models have been developed in calculating the liquid – liquid interfacial tension in immiscible alloys. The Becker model [61] assumes the binary immiscible system is a regular solution possessing a sharp interface between its two liquids and atomic interactions is with nearest neighbour. The interfacial tension is then the energy resulting from the bonds of the pairing atoms across the interface [55,61].

$$\sigma = \frac{N^I}{Z N_a} \Omega (x_{LA} - x_{LB})^2$$
(2.60)

Where N^I is the number of atoms per unit interface area, Z is the coordination number and Ω is the interaction parameter which was related to the T_c in equation (2.36).

The Cahn - Hilliard [62] theoretical model assumes no sharp interface between the separated liquids but rather the interface is viewed as a thin layer

and the interfacial tension is the energy of the layer – like phase [37,55,62]. A continuous change in the concentration profile normal to the interface as well as Gibbs free energy change depending on the resulting composition gradient is assumed in deriving this model which is represented as:

$$\sigma = 2N^v Y k_B T_c \left(1 - {}^T/_{T_c}\right)^{1.5}$$

(2.61)

Where N^v is the number of atoms per unit volume at the interface and Y is the interatomic distance which is given as $r_o/\sqrt{3}$; r_o is the intermolecular distance.

The Chatain and Eustathopoulos model in [63] assumed the liquids in an immiscible system is separated by a coherent interface and the interfacial tension is the difference between the Gibbs free energy of the system and that of a hypothetical homogeneous system formed by the same alloys with same chemical potentials. They also assumed the interface is a (111) plane of a face centered cubic (fcc) lattice. Hoyer et al. [55] reported in their study on aluminium based systems that the Chatain – Eustathopoulos model agrees with the Becker model at low temperatures and with the Cahn – Hilliard's model at high temperatures.

Kaptay [64] in his paper on modelling interfacial energies in metallic systems proposed that the surface tension of liquid metals and the interfacial tension between two immiscible liquids may be calculated from equations (2.62) and (2.63) respectively:

$$\sigma = \frac{0.182\left[qRT_m - C_p(T - T_m)\right] - (2\pm1)T}{1.06V_A^{2/3}N_a^{1/3}}$$

(2.62)

$$\sigma_{AB} = \frac{(6.05 \pm 0.2)T_c + (7 \pm 2)T}{\sqrt{\dot{S}_A - \dot{S}_B}} \left(1 - \frac{T}{T_c}\right)^{1.26}$$

(2.63)

Where q is the enthalpy of melting and $\dot{S}_A$ and $\dot{S}_B$ are molar surface area of liquid A and B respectively.

The temperature dependence of the liquid – liquid interfacial tension has been said to conform to the power function [53,55,63]:

$$\sigma_{\alpha\beta} = c \left(1 - T/T_c\right)^{\delta} \tag{2.64}$$

Where c is a constant and δ is the critical exponent.

Various works have reported on the values of c and δ. The value of $\delta = 1.5$ was proposed by Cahn and Hilliard [62] and classical theory of critical phenomenon by van der Waals while the renormalization theory of critical phenomenon was said to have obtained 1.26 [53]. In a number of systems with miscibility gap the critical exponent has also been determined, 1.36 and 1.19 for the Ga - Pb system by Chatain et al. and Merkwitz et al. respectively [53], 1.3 for Al - Bi system [52] and 1.45 was reported for Al - In in [53]. The constant, c, requires experimental data in order to estimate and since experimental data on surface tension of individual phases as well as that of the interface in immiscible alloy systems are difficult to determine, the theoretical models coupled with the simple Antonow rule that $\sigma_{\alpha\beta} < \sigma_{\alpha} - \sigma_{\beta}$ are mostly used in calculating σ [55].

A much simpler and straightforward model for the temperature dependence of the interfacial tension is one proposed by Rowlinson and Widom [65] which gave the interfacial tension between two immiscible liquids as

$$\sigma_{L1L2} = \sigma_0 \left(1 - \frac{T}{T_c}\right)^{1.26} \tag{2.65}$$

Where σ_o is the value of the interfacial tension extrapolated to 0 K [66].

The temperature dependence coefficient of the interfacial tension $\frac{d\sigma}{dT}$ is then obtained as

$$\frac{d\sigma_{L1L2}}{dT} = -\frac{1.26\sigma_0}{T_c} \left(1 - \frac{T}{T_c}\right)^{0.26} \tag{2.66}$$

2.3.5 Viscosity

The resistance to flow between two adjacent layers in a liquid when subjected to a shear stress τ, is known as the viscosity. The force per unit area (shear stress) between two adjacent liquid layers in relative motion is proportional to the velocity gradient normal to the direction of the applied force $\left(\frac{dV}{dx} \right)$ (Newton's law of viscosity) i.e.

$$\tau = \mu \left(\frac{dV}{dx} \right) \tag{2.67}$$

Where the proportionality constant μ is the dynamic viscosity. The reciprocal of viscosity is fluidity and ratio of viscosity to density is the kinematic viscosity v ($m^2 s^{-1}$).

A number of models have been developed to predict the viscosity of liquid metals. Andrade's 1934 model [67] was based on the assumption that at the melting point, transfer of momentum of atomic vibrations in the liquid state is same as in the solid state and the equation for viscosity of elemental liquid metals at the melting point μ_m was given as:

$$\mu_m = K_{AND} \frac{(MT_m)^{1/2}}{V_m^{2/3}} \tag{2.68}$$

Where V_m is the molar/ atomic volume at the melting point and K_{AND} is the Andrade's proportionality constant which was given as 1.6×10^{-4} (J/ $(Kmol^{1/3})^{1/2}$ but 1.8×10^{-4} (J/ $(Kmol^{1/3})^{1/2}$ is generally used as it is the best empirical value [37,41].

Faber [68] in his book on introduction to the theory of liquid metal gave an expression for the dynamic viscosity in terms of the packing fraction as:

$$\mu = 3.8 \times 10^{-8} \frac{(MT)^{1/2}}{V^{2/3}} \frac{\eta^{3/4}\left(1 - \eta/2\right)}{(1 - \eta)^3} \tag{2.69}$$

He substituted $\eta = 0.45$ at the melting point of liquid metals to give the viscosity at that temperature as:

$$\mu_m = 0.61 \times 10^{-7} \frac{(MT_m)^{1/2}}{V_m^{2/3}} \tag{2.70}$$

Equation (2.70) has been said to underestimate μ_m by a factor of 0.3 [41].

The viscosity of binary liquid alloys μ_{ALLOY} according to Moelwyn – Hughes can be modelled from the expression

$$\mu_{ALLOY} = (x_A\mu_A + x_B\mu_B)\left(1 - 2x_Ax_B\frac{\Delta u}{k_BT}\right) \tag{2.71}$$

Where the interchange energy $\Delta u = \Delta H^{excess}/x_Ax_BN_a$. They also introduced the concept of excess viscosity which they related to the excess enthalpy of mixing by

$$\mu^{excess} = -2(x_A\mu_A + x_B\mu_B)\frac{\Delta H^{excess}}{RT} \tag{2.72}$$

Temperature dependence of viscosity is said to be described by the Arrhenius type equation [37,69].

$$\mu = Ae^{\left(\frac{Q^*}{RT}\right)} \tag{2.73}$$

Where the energy barrier to movement of atoms in liquid is Q^* (the activation energy) and A is a constant said to be viscosity at some reference temperature.

Various expressions have been given for A and Q^*. Eyring et al. [70] gave A $= \dfrac{hN_a}{V}$, where h is the Planck constant (6.626 x 10^{-34} J s) while Grosse [71] gave the constant as A $= \dfrac{5.7\ x\ 10^{-2}\ (MT_m)^{1/2}}{V_m^{2/3}e^{(Q^*/RT_m)}}$. Lida et al. in [41] highlighted the relationship between Q^* for liquid metals and T_m, given as:

$$Q^* = 1.21T_m^{1.2} \qquad\qquad \text{for metals} \tag{2.74}$$

$$Q^* = 0.75T_m^{1.2} \qquad\qquad \text{for semi – metals.} \tag{2.75}$$

The viscosity of a number of immiscible alloy systems has been measured. Vollmann and Riedel [72] measured viscosity of Bi - Ga alloys and found a correlation between Q^* and liquidus temperature. Q^* was also found to

decrease with increasing Ga content and at near the T_c they observed a considerable increase of viscosity. Also in Al - In alloys Guang –Rong et al. [69] observed sharp increase in the viscosity values near the T_c indicating that the temperature dependence follows the Arrhenius relationship. However, in Al - Bi alloys, Wu et al. [73] stated that even though an increase in the viscosity values was observed near the T_c, the temperature dependence deviated from the Arrhenius type relationship. Deviation from the relationship was also observed in Bi – Zn alloys [74]. Plevachuk et al. have also conducted studies on Pb - Zn [75] , In - Se [76] and In – Se - Ti alloys [77].

2.3.6 Diffusion

Diffusion is the mass transport from one region to another in liquid systems. It is a participant to solute redistribution in front of the liquid/ solid interface and as such key in predicting microstructural morphologies during solidification of immiscible alloys [78]. Its measurement in liquid alloys is difficult because of convection effects as a result of uneven composition and temperature gradient on any form of solute transport [24]. Knowledge of self-diffusion in liquid metals is therefore crucial in understanding diffusion in alloys.

Many equations based on different models exist to calculate self-diffusion in liquid metals [37,41], the diffusion flux, *J*, has been related to the continuity equation $\left(\frac{\partial c}{\partial t} = \frac{\partial J}{\partial x} \right)$ to calculate self-diffusion coefficient, D, in liquid metals resulting in Fick's first and second law of diffusion equations given respectively by:

$$J = -D \frac{\partial c}{\partial x} \tag{2.76}$$

$$\frac{\partial c}{\partial t} = \frac{\partial}{\partial x}\left(D \frac{\partial c}{\partial x} \right) \tag{2.77}$$

Einstein [41] proposed his expression for determining the diffusion coefficient by assuming that friction exits between atoms of liquids in random (Brownian) motion to give the Einstein equation:

$$D = \frac{k_B T}{\xi_f} = U_E k_B T \tag{2.78}$$

Where ξ_f is friction coefficient between the atoms and U_E is the motion velocity of the atoms.

Protopapas et al. based their expression for calculating the diffusion coefficient on the hard sphere theory which assumes atoms in metallic systems are surrounded by symmetrical force fields equivalent to hard spheres [41]:

$$D = \eta \sigma K_{AW} \left(\frac{\pi RT}{M}\right)^{1/2} \frac{(1-\eta)^3}{16\eta - 8\eta^2} \tag{2.79}$$

$$\eta = \frac{0.472\rho\sigma^3}{\rho_m \sigma_m^3}; \qquad \sigma = 1.126\sigma_m \left(1 - 0.112 \left(\frac{T}{T_m}\right)^{1/2}\right);$$

$$\sigma_m = 1.41 \left(\frac{M}{\pi \rho_m N_a}\right)^{1/3}$$

Where M is the atomic mass of the metal, η is the atomic packing density and K_{AW} is the Alder − Wainwright correction factor which is obtained from the packing fraction value on the chart in figure 2.12.
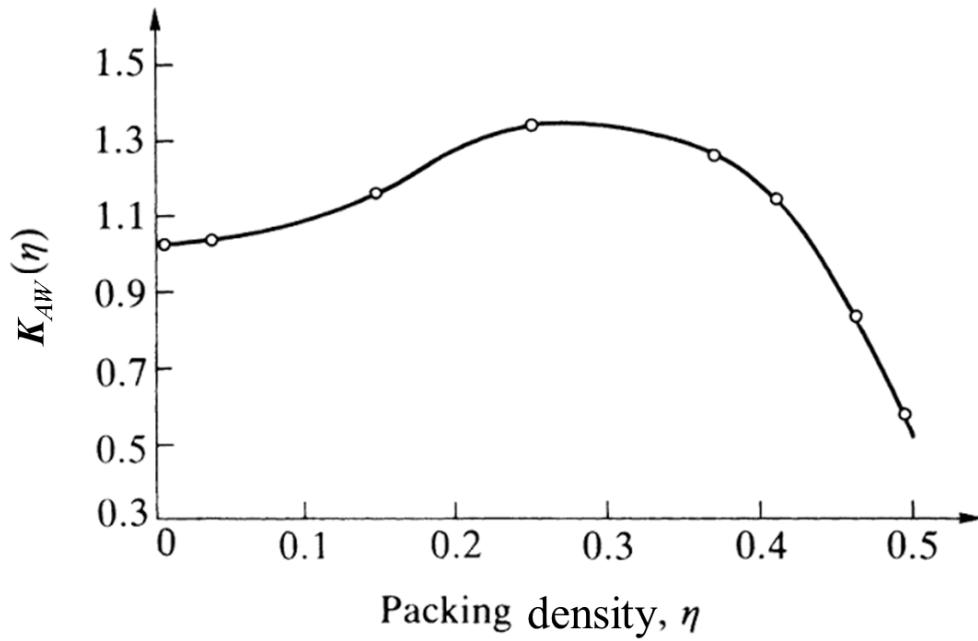
Figure 2.12 The Alder - Wainwright correction factor as a function of packing density [41].

The modified versions of the Einstein relation are both related to the viscosity, μ, of liquid metals. Sutherland proposed a correction to the Einstein equation to give:

$$D = \frac{k_B T}{6\pi v r} \frac{\left(1 + \frac{3\mu}{\mathfrak{B}_s r}\right)}{\left(1 + \frac{2\mu}{\mathfrak{B}_s r}\right)} \qquad (2.80a)$$

Where $\mathfrak{B}_s$ is the sliding friction coefficient between the diffusing particles and the diffusion medium and, r, is the radius of the diffusing particles which could be the Goldschmdt atomic radii if diffusion is on atomic level or Pauling ionic radii if ions. The following situations are possible:

(1) $\mathfrak{B}_s = \infty$ $D = \frac{k_B T}{6\pi\mu r}$;   (2.80b)   r > size of particles of

the diffusion medium

40

(2) $\mathcal{B}_s = 0$ $D = \dfrac{k_B\,T}{4\pi\mu r}$;   (2.80c)   r = size of particles of

the diffusion medium

Equations (2.80b) and (2.80c) are the Stokes – Einstein and Sutherland – Einstein formulae for finding the self-diffusion coefficient in liquid metals.

The modified Stokes – Einstein equation on the other hand is of the form

$$D = \frac{k_B T}{\xi\left(\frac{V}{N_a}\right)^{1/3}\mu} \tag{2.81}$$

Where ξ is a constant having the value of between 5 and 6 in most metals.

The radius of the diffusing particles is obtained on the basis of atomic radii in the hard sphere model [41] using the expression for the packing density $\left(\frac{V}{N_a}\right)^{1/3} = \left(\frac{4\pi}{3\mu}\right)^{1/3} = 2.1r$. It then follows that

$$\frac{k_B T}{12.6\mu r} \leq D \leq \frac{k_B T}{10.5\mu r} \tag{2.82}$$

Roy and Chhabra [79] worked on predicting solute diffusion coefficient in liquid alloys. Their model was based on the simple fact that diffusion in liquid binary alloy involves two species of different size and valence. They focused on the size effect to come up with an expression which they claim allows prediction of solute diffusion in molten alloys:

$$D_{AB} = \frac{d_B}{d_A} D_{BB} \tag{2.83}$$

Where D_{AB} is diffusion coefficient of solute A in solvent B, D_{BB} is self-diffusion coefficient of B and d_A and d_B are the Goldschmidt diameters of A and B. They further gave the temperature dependence of the solute diffusion as:

$$D_{AB} = \frac{0.2\mathfrak{b}Rd_B^3}{d_A}\left[\frac{T}{V}\left(\frac{V - \Omega_0}{\Omega_0}\right)\right]_B \tag{2.84}$$

Where Б and Ω_0 are independent of temperature and are the characteristic constants of the liquid metal, table 2.1 lists some values of some metals.

Table 2.1 Value of characteristic constants of some liquid metals [71]

Metal	Ω_0 x 10^3 (m^3/kg atom)	Б (Pa/s)
Co	6.80	1860
Fe	7.05	2040
Cu	7.10	2300
Ag	11.00	3900
Zn	9.50	5700
Pb	18.80	8800
Al	10.70	11000

While most of the immiscible alloys discussed so far have been those with stable miscibility gaps only a handful of researchers have worked on metastable systems. There are few mentions of investigations of thermophysical properties of the Co - Cu alloy system. Watanabe et al. [80], Watanabe and Saito [81], Egry et al. [82–85] have all worked on determining the density and surface tension of the liquid alloy. The alloy was reported to have positive excess volume [85] and temperature dependence of the density of liquid cobalt and copper was reported to be given by the expressions below in [80,81] as:

$$\rho_{co}(T) = 9.71 - 1.11 \text{ x } 10^{-3}(T) \tag{2.85}$$

$$\rho_{cu}(T) = 8.75 - 0.675 \text{ x } 10^{-3}(T) \tag{2.86}$$

The relationship was verified by Egry et al. [82] who came up with the expression for the density of liquid Co - Cu alloy as:

$$\rho_{cocu}(T) = X_{co}\rho_{co}(T) + X_{cu}\rho_{cu}(T) \tag{2.87}$$

Surface tension in the $Cu_{70}Co_{30}$ alloy was found by Eichel and Egry [83] to vary with temperature according to equation (2.88) while Egry et al. [82] got very close results using oscillating drop technique on levitated samples of $Cu_{75}Co_{25}$ and gave the temperature variation as equation (2.89)

$$\sigma(T) \ = \ 1.22 - 0.29 \times 10^{-3}(T - 1638K) \qquad (2.88)$$

$$\sigma(T) \ = \ 1.29 - 0.28 \times 10^{-3}(T - 1630K) \qquad (2.89)$$

The interfacial tension in the alloy was represented by equation (2.90) [82] which was subsequently verified in $Cu_{15}Co_{85}$ and $Cu_{90}Co_{10}$ alloys.

$$\sigma_{L1L2} \ = \ \sigma_{L1} - \sigma_{L2} (T - T_L) \qquad (2.90)$$

Where L_1 and L_2 are the demixed liquids rich in components 1 and 2, T_L is the liquidus temperature of the alloy in degree Kelvin.

The diffusion coefficient of cobalt in the Co - Cu system at various temperature has been calculated [79], table 2.2 gives a comparison of the calculated and experimental values.

Table 2.2 Diffusion coefficient of Co - Cu system at various temperatures [78]

Solute	Solvent	T (K)	Diffusion Coefficient x 10^{-9} (m^2/s)	
			Experimental	Calculated
		1373	3.61	6.04
		1423	4.18	6.44
Co	Cu	1473	4.80	6.86
		1523	5.45	7.30
		1573	6.14	7.74

Roy and Chhabra placed the divergence between the calculated and experimented values to the uncertainties and errors from varying

experimental methods. They postulated an agreement between the two results as temperature increases.

2.4 Nucleation and growth of particles in undercooled immiscible alloys

As already discussed, upon encountering the binodal curve, phase separation in the immiscible alloy occurs through decomposition of the parent melt in the form of spherical particles (droplets) of one phase (here referred to as higher phase droplets, HPD) in a continuous liquid phase of another phase of different composition from the parent phase (here referred to as the matrix). This phase separation mechanism occurs through the process of nucleation and growth (coarsening) of the HPDs.

Nucleation, the formation of a nucleus (group of atoms or molecules of a new phase) is governed by three categories of theories: those which study the nucleation rates and do not consider the cluster formation energy (kinetic theories), those that study cluster structure as well as free energy of cluster formation (molecular theories) and lastly those like the classical nucleation theory which relates the free energy of cluster formations to macroscopic quantities such as density and surface tension (phenomenological theories).

Most commonly observed heterogeneous nucleation process start on some surface e.g. structural impurities or container walls while the less observed homogeneous nucleation process occurs within a pure phase. Homogeneous nucleation is more likely in undercooled melts where the nucleation process is the crystallisation rate determining step hence the nucleation rate is also the crystallisation rate [24]. The nucleation rate of these HPDs is generally calculated using classical homogeneous nucleation theory hence discussion is limited to this type of nucleation.

The total Gibbs free energy change upon the formation of a spherical HPD of radius r, (ΔG_r) in the matrix is made up of the interfacial free energy (surface

tension) which is created upon the formation of nucleus and the decreasing free energy of the system i.e.:

$$\Delta G_r = 4\pi r^2 \sigma_{nm} + \frac{4}{3}\pi r^3 \Delta G_v \qquad (2.91)$$

Where ΔG_v is the Gibbs free energy change per unit volume and depends on undercooling. The expression for ΔG_v has already been given in equation (2.14) which can also be represented by equation (2.92) in terms of melting temperature as:

$$\Delta G_v = \frac{1}{V}\frac{L}{T_m}(T - T_m) = \frac{L\Delta T}{T_m} \qquad (2.92)$$

Where ΔT is the undercooling.

As the HPD grows, the competition between the decreasing free energy of the bulk and the increasing interfacial free energy results in a maximum on the plot of ΔGr against r which corresponds to the critical radius (r*) of a HPD in the matrix and the corresponding free energy at this point which is the activation threshold for its formation (nucleation barrier) is ΔG^* [24]. Expressions for both are given in equations (2.93) and (2.94) respectively.

$$r^* = \frac{2\sigma_{nm}}{\Delta G_v} \qquad (2.93)$$

$$\Delta G^* = \frac{16}{3}\pi\frac{\sigma_{nm}^3}{\Delta G_v^2} \qquad (2.94)$$

Where σ_{nm} the interfacial energy between the nucleus and the melt can be determined from the model proposed by Thompson and Spaepen [86] relating it to entropy and crystal structure of the nucleus by the expression

$$\sigma_{nm} = T\alpha\frac{\Delta S_f}{N_a^{1/3}V^{2/3}} \qquad (2.95)$$

Where α is nucleus structural factor with value of 0.86 for fcc and hcp structures and 0.71 for bcc structures.

The nucleation process is dynamic in the sense that the nuclei aggregate to form clusters and as such when $r \geq r^*$, the HPD is viable and continues to grow but a sub-critical nuclei having $r < r^*$ is at the surface and the total free energy of the bulk is dominated by the interfacial free energy. Sub-critical particles therefore dissolves into the matrix since they are not thermodynamically favourable. Both r^* and G^* will decrease with increasing undercooling.

The homogeneous nucleation rate, I^{hom} which is the total number of clusters per unit time which grows larger than the critical size is then given by:

$$I^{\text{hom}} = I_o e^{\left(-\frac{16\pi\sigma^3 T_L^2}{3\Delta H_f^2 \Delta T^2 k_B T}\right)} e^{\left(\frac{-\Delta G^*}{k_B T}\right)}$$ (2.96)

Where I_o is the nucleation pre-factor with is said to have values typically between $10^{25} - 10^{30} \, \text{m}^{-3} \, \text{s}^{-1}$ for homogeneous nucleation [24]. However, under the assumption that nucleation is a diffusion process and using the Stokes – Einstein relation for the diffusion coefficient, Turnbull was able to approximate the nucleation rate from an undercooled melt using (2.97) with a pre-factor value of 10^{39} [23].

$$I^{\text{hom}} = 10^{39} e^{\left(\frac{-\Delta G^*}{k_B T}\right)}$$ (2.97)

Classical homogeneous nucleation theory has been used to study the nucleation rate of dispersed particles in undercooled immiscible alloys. In the Ga – Bi system, Perepezko et al. using differential thermal analysis (DTA) was reported to have observed that the nucleation of the dispersed particles was characterised by low values of ΔG^* hence at very little undercooling the dispersed particles were formed. They also stipulated that the binodal of the system was non symmetrical stemming from variation of the undercooling with composition on both sides of the miscibility gap [37]. Undercooling values from the homogeneous nucleation rate has also been compared with those determined experimentally in hypermonotectic Zn - Pb alloys. There was agreement between both undercooling values and it was found to be strongly dependent on Pb content on both sides of the miscibility gap [87,88].

Nucleation studies have also been carried out on the Co - Cu system. Zhang et al. [89] studied the undercooling values associated with 120 nucleation events in Co – rich dispersed particles of Cu - 30 at. % Co alloys of different mass. The undercooling which was found to increase with decreasing sample mass was related to the liquidus temperature and was said to be approximately $0.2T_L$. The homogeneous nucleation rate was also found to increase continuously with increasing undercooling in all samples.

Even though the classical homogeneous nucleation theory is widely used to study the kinetics of phase transitions due to its simplicity, some of its assumptions have been questioned. The model assumes that nuclei are spherical while this might be a valid argument in that it is the geometry that minimizes surface free energy the most, there are reports in literature where non spherical nuclei have been observed [90]. Also the assumptions that nucleus are formed one at a time (which means that clusters are ignored), nucleus /clusters of the new phase are stationary droplets at equilibrium concentrations have all been questioned leading to various modifications and extensions to address issues such as binary multicomponent nucleation [86,91]. One of such modifications to the classical homogeneous nucleation rate is the introduction of the Zeldovich factor which gives steady state concentration instead of equilibrium concentrations and accounts for cluster formation around the critical size.

2.4.1 Growth and coarsening

As a result of various forces, the nucleated liquid HPDs are constantly moving relative to the matrix and other droplets. Growth / coarsening of these HPDs may occur via a diffusion based mechanism known as Ostwald ripening process in which larger droplets are formed at the expense of smaller ones. The ripening process is due to the dependence of solubility on the radius of curvature of droplets. Droplets with small radii have higher curvature and solubility and as such shrink at the expense of the growing larger ones hence

the ripening process is intense at the early stages of nucleation when the nuclei have large curvatures. Another mechanism of droplet growth which is as a result of their relative motion leading to coalescence is collision and coagulation process in which the moving droplets collide to form larger ones [92]. The coagulation process occurs as a result of reduction of interfacial tension between colliding droplets within capture radius of each other. This results in the formation of a liquid bridge through which the bigger droplet absorbs the smaller one (figure 2.13 and 2.14). The process leads to the formation of droplets of larger volume.
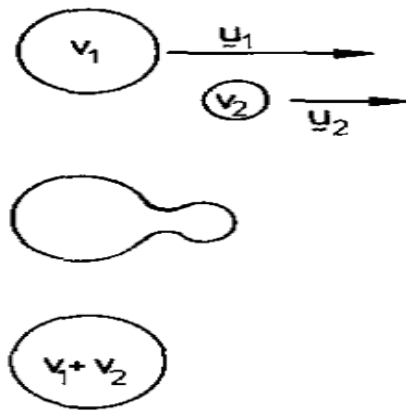
Figure 2.13 Schematic diagram showing the coagulation process of two droplets of different velocities (a) before collision, (b) during collision and (c) after collision [92].
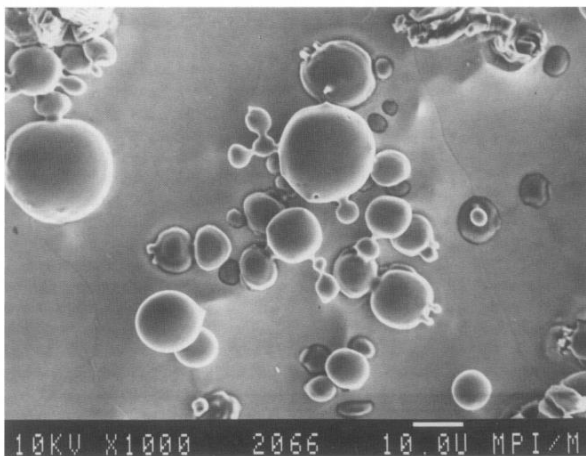
Figure 2.14 SEM micrograph of immiscible Al - In alloy showing coagulation of In – rich droplets in Al- rich matrix [92].

Collision and coagulation may be brought about by action of 4 different motions namely: velocity induced by gravity (Stokes motion), thermal molecular motion (Brownian motion), motion induced by thermo – capillary forces as a result of interfacial stress (Marangoni motion) and convection induced motion. In the case of high convection, dispersed particles are strongly influenced by coagulation which if high enough can result in few dispersions in the microstructure [93]. This is undesirable and also does not give useful information about the droplet growth. Deviation from spherical shape has also been said to be indicative of high convection influences [94].

In drop tube experiments, convection induced flow are usually discounted due to the higher cooling rates which result in short solidification time. Agreed there is relative motion of the dispersed spherical particles but the decreasing natural convection in the drop tube enables Marangoni motion play a pivotal role in the solidification process [95].

In this research, only the first 3 motions are relevant. The 3 are briefly discussed below:

2.4.1.1   Stokes motion

When coalescence is aided by gravitational force, Stokes motion becomes relevant. Assuming the density of the HPDs is higher than that of the parent melt, sedimentation occurs but if not floatation of the HPDs in the parent droplet is observed. An example is shown in figure 2.15 which shows the micrograph of DTA processed Co - Cu droplet in which the large Cu – rich droplet is situated at the top of the parent droplet while the denser Co – rich ones were observed at the lower part [96].
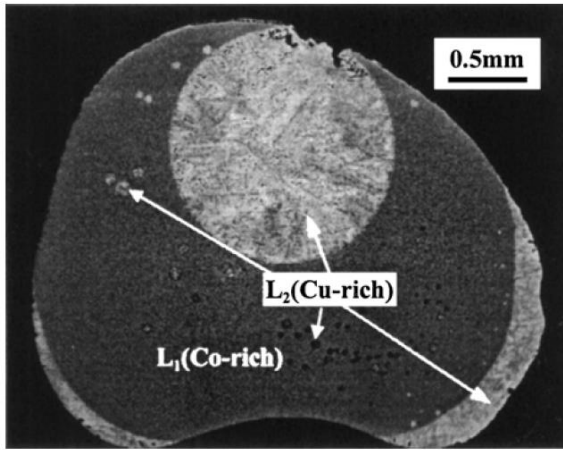
Figure 2.15 SEM micrograph of DTA processed Co - Cu droplet showing Cu – rich particles at the top of the parent droplet [96].

The gravitational force is an increasing function of the droplet diameter and inverse to its viscosity. The velocity of single droplets in the matrix induced by this gravitational force, U_s (velocity of Stokes motion) is described by the Hadamard – Rybczynski relation in [97] as:

$$U_s = \frac{2\dot{g}(\rho_d - \rho_m)}{3\eta_m} \frac{(\eta_d + \eta_m)}{3\eta_d + 2\eta_m} r_d^2 \qquad (2.98)$$

Where the subscripts d and m refer to the droplet and matrix phase respectively and $\dot{g}$ is the residual acceleration which is estimated to be 10^{-3}g (g is the gravitational acceleration of magnitude 9.8 m/s^2). The relation is only valid for very small Reynolds number as seen in materials with high viscosity and in microgravity conditions.

The collision and coagulation process progress very rapidly such that within a few seconds a dispersed structure may convert into a layered one.

2.4.1.2   Brownian motion

In contrast to the Stokes motion is the Brownian motion which is the constant random thermally driven movement of droplets which in time can cause even

distribution to occur. Brownian motion is a diffusion process and is mostly effective on very small particles with radii less than 1 μm.

Zhao et al. [98] studied the effect of Brownian motion induced coagulation on microstructural evolution in rapidly solidified Al - Pb alloys and found that the effects of Brownian coagulation decreases with droplet size and increases with cooling rate which makes sense since higher cooling rates causes higher nucleation and consequently finer dispersions which in turn favours Brownian motion. They also found that the coagulation favours a wider size distribution of dispersed droplets.

In microgravity environment, U_s and Brownian motion are of the same magnitude for liquid droplets and as such Stokes sedimentation is usually supressed.

2.4.1.3 Marangoni motion

Surface tension as already discussed is a function of composition and temperature. Temperature and /or concentration gradients therefore causes gradient of surface tension. Droplet motion as a result of this surface tension gradient is Marangoni motion. The surface tension gradient causes a tangential stress at the droplet surface which in turn drags the neighbouring phase fluid towards the surface and the overall reaction on the parent droplet is in the opposite direction where the surface tension is lower.

 In the presence of a temperature gradient, movement is in the direction of region of higher temperature and the droplet Marangoni migration velocity (U_{Mt}) is described by the equation of Young et al. in [97] as:

$$U_{Mt} = -\frac{2r}{\left(2+\frac{\lambda_d}{\lambda_m}\right)(3\eta_d + 2\eta_m)}\frac{d\sigma}{dT}\nabla T \qquad (2.99)$$

Where the product $\frac{d\sigma}{dT}\nabla T$ is the interfacial tension gradient due to temperature and $\frac{d\sigma}{dT}$ is the temperature dependent coefficient of the interfacial tension

between the liquid droplet and the liquid matrix. The ratio ${}^{\lambda_d}/_{\lambda_m}$ is estimated to be unity for liquid alloys.

When Marangoni migration is due to the variation of the interfacial solute concentration, the resultant solutal Marangoni migration velocity (U_{ms}) is described by:

$$U_{Ms} = - \frac{2r}{\left(2+\frac{D_d}{D_m}\right)(3\eta_d+2\eta_m)} \frac{d\sigma}{dC} \nabla C \qquad (2.100)$$

Where $\frac{d\sigma}{dC}\nabla C$ is the interfacial tension gradient due to concentration and $\frac{d\sigma}{dC}$ is the concentration dependent coefficient of the interfacial tension.

Marangoni velocity is thought to be the chief mechanism for microstructural formations in phase separated alloys observed in microgravity unlike in terrestrial environment where it is over shadowed by Stokes sedimentation. Ahlborn and his co-workers [99,100] worked on the influence of Marangoni motion on the migration of nucleated droplets in binary and ternary monotectics alloys under microgravity. They observed that nucleated droplets in Zn - Bi, Zn - Pb and Zn – Bi - Pb in the presence of temperature gradient translated towards part of the parent droplet where the temperature was highest [99]. However, in Al – Si - Bi ternary alloy they observed that calculated mean particle radius upon collision and coagulation was far lesser than that in the experiment and concluded that other processes responsible for particle growth were active [100].

2.4.2 Thermophoresis / thermal diffusion / Soret effect

In addition to the Marangoni movement, the temperature gradient could cause one of the components to diffuse. This effect occurs when a concentration gradient is induced in order to balance the effect of a constant temperature gradient imposed across the parent droplet [101]. Thermophoresis / thermal diffusion / Soret effect is therefore an additional particle transport mechanism in the presence of a temperature gradient. The effect has been attributed to

Brownian motion as it is caused by variations of the intensity of particle motion between the hotter and colder regions of the droplet.

Motion of particles occur at higher intensity in hotter part than in the colder part hence higher collision is observed due to the higher kinetic energy. As a result, there is accelerated particle migration against the temperature gradient (i.e. towards the colder side) [102]. Being as a consequence of Brownian motion, the effect is more pronounced on very small particles (in nanometres) and as such more likely at the earliest stage of particle nucleation.

Since thermophoresis can modify the concentration gradient in the liquid near the liquid – solid interface and can lead to large concentration gradients [103], it follows that the concentration fluctuations $\left(\frac{\nabla C}{C}\right)$ is proportional to the temperature gradient (∇T) i.e.

$$\frac{\nabla C}{C} = -S_T \nabla T \tag{2.101}$$

Where S_T, the Soret coefficient is a measure for the degree / effectiveness of separation of particles and also shows the magnitude and sign of the concentration gradient. S_T has been reported to be sensitive to some factors [104] such as particle size, thermodynamic variables and temperature.

The Soret coefficient is then expressed as the ratio of the thermal diffusion coefficient (D_T) to the normal / chemical diffusion coefficient (D) i.e.

$$S_T = \frac{D_T}{D} = -\frac{1}{C(1-C)}\frac{\nabla C}{\nabla T} \tag{2.102}$$

Where C is the concentration in mass fraction.

In solid metals and alloys, thermophoresis / Soret effect is rarely considered principally because its effect on the concentration gradient is very small as $D_T < D$ by several orders of magnitude [105]. There are presently no theoretical models for Soret effect prediction in liquid alloys even after over 150 years since it was first mentioned. This is worth considering due to the faster rate of diffusion in liquids in general and the possibility that the thermal diffusion process may proceed at faster rate than chemical diffusion and may

even lead to compositional inhomogeneity [105] as shown by Lu et al [106] in Al - Bi alloys where Soret effect was said to provide driving force for solute segregation.

Currently there is not a great deal of information on thermophoresis in immiscible alloys, values of S_T and the correct sign are elusive in literature. The concept would however be used for explanatory purposes in this research.

3 Literature review

This chapter is a review of selected works on immiscible alloy systems with miscibility gaps in the liquid state with bias for those rapidly solidified and / processed under micro gravity conditions since under normal ground conditions these tend to solidify into layered structures which limits their applications.

The chapter is divided into five sections; the first section discusses monotectics and their solidification features. The second and third sections examine the characteristics of the liquid phase separation, growth of separated phases and microstructural formations in alloys with stable and metastable miscibility gap respectively. The fourth section focuses on the Co − Cu system with emphasis on its miscibility gap estimation, liquid phase separation pattern and microstructural morphologies. The last section is on core shell microstructures which are reported to be characteristic of rapidly solidified immiscible alloys in micro gravity environment.

3.1   Monotectics

Monotectic alloys are immiscible alloys. They are characterised by limited mutual solubility in the liquid state and have a miscibility gap in their equilibrium phase diagram. The phase diagram (figure 3.1) has the same terminology as that of the immiscible alloy system i.e. has a dome shaped region within which two liquid phases of different compositions from the parent melt co-exist, critical temperature T_c which is the maximum temperature of the dome shaped region and 'limit of immiscibility' which is the boundary of the $L_1 + L_2$ field. Metastable monotectic alloys like the Co-Cu system have their miscibility gaps below the liquidus line. Alloys to the right of the monotectic composition X_m in figure 3.1 are hypo-monotectic; those up to the composition of liquid L_2 at the monotectic temperature ($X^m L_2$) are hyper-monotectic alloys. Those alloys of composition greater than that of the hyper-monotectics are known as super-monotectic alloys. Below T_m is the

eutectic temperature T_e where the eutectic reaction occurs and final solidification takes place.

The monotectic reaction is such that at the monotectic temperature T_m, liquid of component L_1 (which is A – rich) decomposes into solid phase S_1 (figure 3.1) and another liquid phase L_2 (which is B- rich). In most monotectic systems, S_1 is a continuous solid matrix wherein the liquid phase L_2 which characteristically has a low volume fraction is dispersed [107].
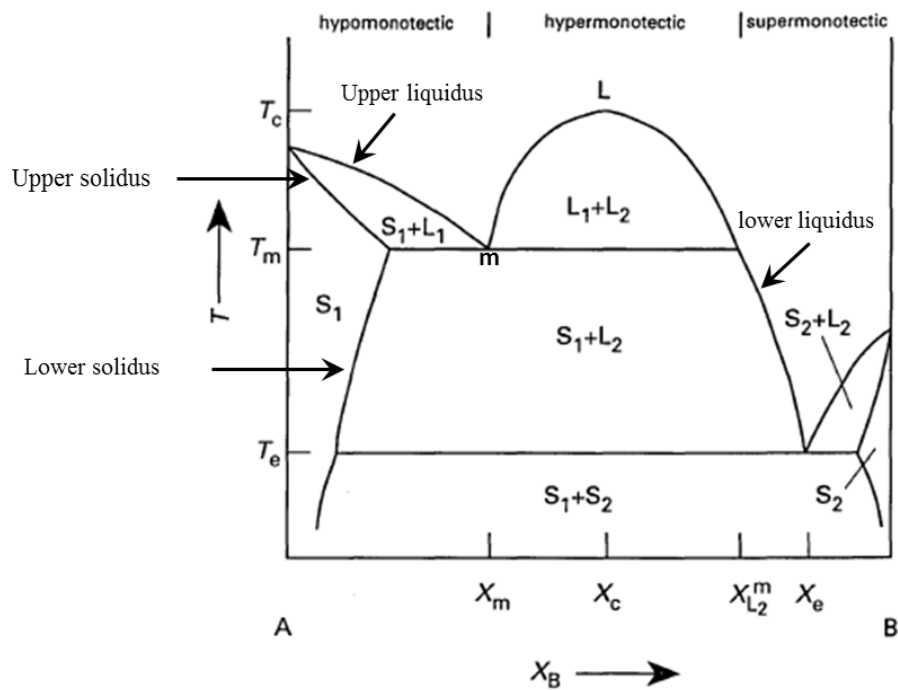
Figure 3.1 Schematic phase diagram of a monotectic system with a stable miscibility gap showing the invariant point, m, where L_1 of alloy of monotectics composition transforms to form a two phase structure comprising L_2 and solid S_1 [107].

3.1.1 Solidification of monotectic alloys

The solidification mechanism generally is quite complicated owing to concurrent effect of various factors such as solidification velocity, temperature gradient ahead of solid –liquid interface [108,109], composition [110], degree of undercooling [111], cooling rate [112] and alloying additions

[10,54,111]which all affects the type of microstructure of immiscible alloys in general.

The monotectic solidification is characterised by these two equations:

$$L \rightarrow L_1 + L_2 \qquad\qquad (3.1)$$

$$L \rightarrow S_1 + L_2 \qquad\qquad (3.2)$$

Herlach et al. [24] explains further that the first reaction is mainly phase separation as the liquid is cooled below the critical temperature T_c into the two phase $L_1 + L_2$ region. The second reaction is similar to a eutectic reaction except that one of the phases produced is a liquid.

The alloy of exact monotectics composition in figure 3.1 above undergoes the monotectics reaction $L_1 \rightarrow S_1 + L_2$ upon solidification. In directional solidification, composite growth similar to the rod – like and lamellar microstructures in eutectic systems are observed (figure 3.2a). These regularly observed composite growth are usually rod – like structures of L_2 in the S_1 matrix. The rod – like appearance of the L_2 phase is to minimize interfacial energy and its presence has been said to be dependent on the solidification velocity, v, and diffusion due to the high atomic mobility between the liquid phases (L_1 and L_2). These regularly observed rod-like microstructures have however been noticed to break down into droplets/ irregular structures (figure 3.2b) leading to the classification of monotectic growth as either regular or irregular [107]. In regular monotectic growth the rod-like structures grow in the matrix but break down at high cooling rates while in irregular growth the opposite holds as the rod-like structures are only observed at high cooling rates.
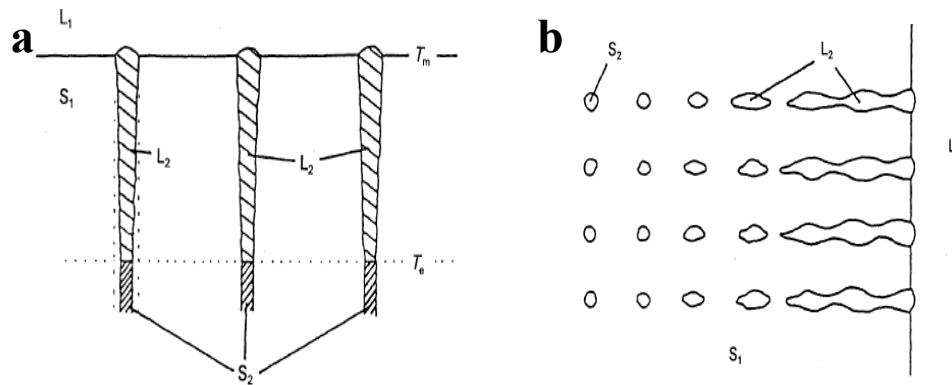
Figure 3.2 Schematic diagram diagrams showing (a) the process of monotectic growth and (b) breakdown of regular rod-like microstructures to irregular droplets [107].

These two types of growth in directional solidification have been linked to the interfacial energies between the phases, aligned structures are said to be formed when the condition $\sigma(S_1L_2) < \sigma(S_1L_1) + \sigma(L_1L_2)$ is satisfied otherwise irregular structures are formed [113].

The solidification microstructure present has been linked to the ratio of the temperature gradient G_T and growth rate R^* [114] and the ratio of the critical temperature T_c and monotectic temperature T_m [115,116]. Regular structures are said to be formed at high G/R^* ratio while at low ratios, rows or string of spheres are formed [115]. In organic and metallic monotectic systems, Grugel and his co-workers [115,116] concluded that at $T_m/T_c > 0.9$, irregular growth occurs while at $T_m/T_c < 0.9$ regular growth occurs.

Monotectics are therefore generally classified on two criteria: the ratio of the monotectic temperature T_m to the critical temperature T_c (T_m/T_c) and the difference between the T_c and T_m ($T_c - T_m$) [2].

1. High dome alloys: in this type of alloys, the ratio T_m/T_c is less than 0.9 and the difference in $T_c - T_m$ is large, usually in hundreds of degree Kelvin (K). Alloys in this category includes Al - Pb, Ga – Hg, Al - Bi

(600°C), and Al - In (206°C). These category of alloys are said to satisfy the interfacial energy condition for formation of aligned composite growth [2].

2. Low dome alloys: T_m/T_c ratio is greater than 0.9 and the difference between T_c and T_m ($T_c - T_m$) is small (in tens of degree Celsius ($^{\circ}$C). Examples of alloy systems in this group include Cd - Ga (13°C) and Cu - Pb (35°C) (figure 2.10c).

The solidification of hypo-monotectic alloys start with the precipitation of S_1 which is dendritic in nature for metallic systems. The monotectic reaction then occurs at T_m yielding S_1 and L_2. When the system is subjected to undercooling, as the temperature decreases more precipitate is formed and at T_e the last liquid undergoes the eutectic reaction and solidifies as S_2 [107]. Hyper-monotectic alloys on the other hand enter the miscibility gap where separation into L_1 and L_2 liquid phases occur. Liquid phase L_1 subsequently undergoes the monotectic reaction while L_2 solidifies through the eutectic reaction. Due to surface tension effects which increase as the system is undercooled, nucleation of the second liquid phase occurs. Usually this would be of L_2 within an L_1 matrix for alloys to the left of the T_c and of L_1 in L_2 matrix for those to the right [107].

3.2   Monotectic systems with stable miscibility gap in the liquid state
The binodal curve of these alloy is part of their equilibrium phase diagrams.

A number of researchers have worked on aluminium based monotectics [110,112,117–125]. These alloys are desirable for their low friction and wear properties as well as for their good load bearing capabilities. They are also sought after in light weight applications owing to the light weight of aluminium which has a density of about a third of that of copper [54].

Dai et al. and Lu et al. worked on the Al – Bi alloy system [110,112,117,118]. Lu et al. [117] used the process of aerodynamic levitation to rapidly solidify

alloys of Al − 10wt. % Bi (1.4 at. %) and Al − 90 wt. % Bi (53.7 at. %). Phase separation was reported in both alloys and core shell microstructures were observed. The authors reported that the minority phase droplet type depends on the volume fraction of the phases. In the alloy with 10 wt. % Bi composition, the minority phase was Bi − rich while in the 90 wt. % Bi alloy the minority phase droplets was Al − rich. Irrespective of the configuration, the reported core shell microstructures in both alloys were said to be uniform (Al − core, Bi − shell).

A probable explanation would be that the Bi −rich phase has lower surface energy hence has affinity for surface segregation. The higher surface energy phase (here referred to as higher phase droplets, HPD) then migrates under Marangoni towards the centre. Even though the author gave a lot of explanation, it is thought that the basic preference for the alloy was that irrespective of the separation pattern, the HPD will still form the core. However no microstructural evidence were presented for these structures as the authors only used sketches.

Dai et al. [112] rapidly solidified Al − 65.5 wt. % Bi alloy (19.7 at. %) by force ejecting liquid melts of the alloy into silicon oil of different temperatures. Same microstructural morphology as [117] was observed. It is inferred from the authors' microstructural evidence and explanation that Bi − rich minority phase droplets (MPD) was formed as well as Al − rich droplets. The authors also suggested that segregation occurs before phase separation. If the two phases are nucleated and segregation occurred before phase separation, an explanation for the uniformity of core shell structures in both [112,117] studies is then possible in that surface segregation of Bi occurred on cooling into the miscibility gap (MG) of the alloy. This segregation in turn led to a layer deficient in Bi, this created a concentration gradient which made it possible for Al − rich MPD to form and these subsequently formed the Al − rich core as earlier explained.

Another study by Lu et al. [118] also investigated the Al − 10 wt. % Bi alloy using synchrotron radiography and favours the views of [112] that surface

segregation of Bi occurs before phase separation and that the segregation is always in the direction of the temperature gradient (which was from bottom to the top in their research). Just as in [117], they observed that the MPD was Bi – rich and always at the location of advancing interface. They listed five forces acting on the dispersed Bi – rich droplets; a repulsive force between the Bi droplets and the advancing interface, Marangoni force, buoyancy force, stokes force and gravitational force. The repulsive force was said to be much more dominant at the early stage of the solidification than the Marangoni force hence core shell microstructures were not observed in the study. The alloy was however not rapidly solidified.

Liu et al. [119] studied Al – 17.5 wt. % In (4.8 at. %) alloy using melt spinning. They observed that as – solidified microstructures had dispersed nano – sized In - rich particles which increased in size with increasing distance from the chill surface. This suggests that cooling rate had a refining effect on the In - rich particles. This microstructural morphology and phase separation pattern is corroborated by the study of Potard [120] on samples raging from monotectic to hyper monotectic compositions and [122] on Al – 10 at. % In (2.5 at. %) alloys both which were conducted under microgravity in a space shuttle simulation. However in another space study on Al - 40 wt. % In (13.5 at. %) and Al - 70 wt. % In (35.4 at. %) alloys, a different structure comprising Al - rich centre surrounded by In – rich phase was observed [121]. The reason for the opposite phase separation pattern in these space studies is not elucidated in the papers however, Potard [120] stated that indium was not observed to have surface segregation tendencies.

Kim et al. [126] worked on melt spun hypo monotectic alloy of composition Al – 7 wt. % In (1.74 at. % In). Monotectic solidification was said to have occurred in the alloy and they observed that microstructural variation depended on the solidification rate with nano – size dispersed indium particles

observed close to the chilled ribbon surface. They identified four stages of solidification in the alloy:

a. Heterogeneous nucleation of primary aluminium grains on the chilled surface which causes an enrichment of L_1 phase ahead of the solidifying growth front.

b. When the MG is encountered, L_2 phase is nucleated either homogeneously or heterogeneously through contact with the aluminium growth front.

c. In a bid to minimise their surface energies, the growing L_2 droplets adjust their shape thereby resulting in faceting.

d. The alloy finally solidifies after passing through the eutectic point.

Even though the authors stated that droplet migration occurred in the liquid phase, the mechanism by which these occurs were not discussed. The paper was more focused on the monotectic solidification.

The alloys in studies of Liu et al. and Potard [119,120] also experienced the monotectic reaction but Liu et al. [119] concluded that phase separation dominated the non – equilibrium solidification of the Al – 17.5 wt. % In alloy. This was inferred from the bimodal size distribution of the In - rich particles in the Al - rich matrix; bigger particles being dominant at liquid phase separation (LPS) stage and smaller particles during monotectics solidification. In their study, the larger particles far outweigh the smaller one hence the conclusion.

Studies have been reported on hyper monotectic [123] and monotectic [124,125] Al - Pb alloys. Ozawa and Motegi [123] studied the effect of microgravity on the alloy using a 1000 m drop shaft. They observe the homogeneous dispersion of Pb – rich phase at lower cooling rates compared to the control experiment under normal gravity (70 Ks^{-1} to 130 Ks^{-1} respectively). The study seems to suggest that higher cooling rates do not

favour phase separation / nucleation / growth of the dispersed phase. A probable explanation for this observation in their study is that since their experiment was not done in a containerless environment, heterogeneous nucleation facilitated the phase separation and as such even at lower cooling rates dispersed structures were formed. Also, undercooling effects aided it. A layered structure was observed in samples processed under normal gravity.

Moore et al. [124] and Luo and Chen [125] both worked on Al – 5 wt. % Pb (0.7 at. %) alloy. Moore et al. used chill casting and melt spinning methods to rapidly solidify the alloy and observed bimodal size distribution of Pb – rich particles of nano size for melt spun samples and micron sized particles for the chill cast ones. If the argument from the works of Ozawa and Motegi [123] is adopted, it means the chill cast samples were at the LPS stage while the melt spun ones had progressed out of the MG and gone beyond the monotectic point.

A rather interesting set up was employed by Luo and Chen [125] in investigating the effects of microgravity on Al – 5 wt. % Pb monotectics alloy. It involved electromagnetic levitation (EML) of the alloy sample above the drop tube, dropping of the levitated droplets into the drop tube and allowing the processed droplet to drop containerlessly down the tube into bath of silicon oil at the bottom of the tube. The samples were compared with those processed by drop tube processing (DTP) alone. Their observation was that microgravity environment had a refining effect on the size of Pb – rich particles dispersed. This is expected due to the higher cooling rates and higher undercooling in the droplets via the EML route since the parent droplets and dispersions will be smaller than those via DTP alone.

The Cu - Pb alloy system was also reported to have been studied using DTP by Wang et al. [127], glass fluxing method by Dong and Wei [128] and melt

spinning method by Kim and Cantor [129]. In the 3 m drop tube experiment, Wang et al. [127] observed core shell microstructures of different configurations. The range of composition for the formation of the structures were in doubt but they stated it has to be at close proximity to the critical composition (X_c). Only few portions of alloys on the opposite side of the X_c with respect to the alloy they studied were deemed able to form core shell structures. The paper is discussed in detail under core shell microstructure formation.

Dong and Wei [128] worked on undercooled Cu – 20 wt. % Pb (7.1 at. %) hypo monotectic alloy. Phase diagram estimates predict the solidification of the alloy outside the MG range but close to its monotectics composition of 37.4 wt. % Pb (66.1 at. %). Dendritic structure is expected and was observed with volume fraction of dendrites increasing rapidly after monotectic reaction. Kim and Cantor [129] also worked on another hypo monotectic alloy having composition of 5 wt. % Pb (1.6 at. %). LPS did not occur even though dispersed Pb – rich particles were observed in the Cu – rich matrix. This is thought to be due to dendritic solidification suppression as a result of monotectics reaction.

The Fe – Sn alloy system has also been well researched. Wang and Wei [130] studied phase separation and microstructural evolution in undercooled Fe – 48.8 wt. % Sn (31 at. %) monotectic alloy using drop tube and glass fluxing methods. For the drop tube experiment, they calculated the miscibility gap and concluded that the undercooling required for the spinodal decomposition of the alloy was too large (387 K) to attain in the 3 m drop tube for droplets with d > 100 µm. The alloy however experienced binodal decomposition. In larger particles (800 µm), nucleation was said to initiate at the parent droplet surface due to lower temperature there as a result of contact with inert gas. This is however hard to deduce from the image the authors presented. In smaller droplets (160 µm droplet was presented) multiple nucleation of the

L$_2$ phase was said to occur and the microstructure is said to contain these dispersed uniformly. Again this is not clearly shown in the image presented (figure 3.3) but it is observed in the image that surface segregation of the Sn – rich phase occurred since it has lower surface tension than the Fe – rich phase. In samples that progressed to the monotectic point, oriented structures said to be as result of negative temperature gradient in the droplet was observed. In the glass fluxing experiment, maximum undercooling of 172 K was attained and the observed microstructure were very different from the drop tube ones. Microstructural transformation from dendritic at very small undercooling to disperse Sn – rich droplets at larger undercooling was observed. The dendritic structures were observed to be very branched due to longer solidification time.
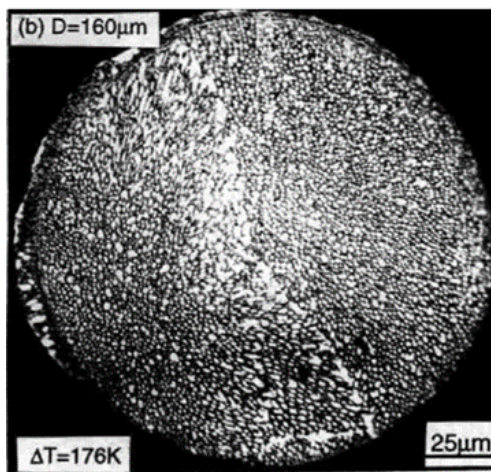
Figure 3.3 Microstructure of Fe – 48.8 wt. % Sn droplet [130].

Luo et al. [131] also using a 3 m drop tube studied Fe – 50 at. % Sn (68 wt. %) alloy and obtained multi layered core shell microstructures. It was observed that the phase diagram presented had the X_c at around 52 at. % Sn (69.7 wt. %) unlike the diagram presented in [130] which had X_c at around 50 at. % Sn (68.5 wt. %). Luo et al. however assumed a symmetrical MG making their alloy of the critical composition. In the figures presented, Sn – rich phase always segregated at the surface.

Liu et al. [132] also using a 3 m drop tube examined Fe – Sn alloys ranging from monotectics to hyper monotectics compositions. Droplet sizes ranged from 100 to 1000 µm. The maximum undercooling in the studied alloys were found to vary with composition departure from the critical composition with 270 K, 282 K and 288 K estimated for Fe – 48.8 wt. % Sn, Fe – 40 wt. % Sn and Fe – 58.8 wt. % Sn alloys respectively.

In the Fe – 48.8 wt. % Sn alloy, the nucleation and growth of structures varied with droplet size. In larger droplets a 1:1 ratio of spherical and fibrous structure was observed while in smaller droplets, the spherical structures become more dominant. Droplets with complete fibrous structure were also presented. Just as observed in [130], the fibrous/ eutectic like structures were aligned. Their alignment is said to be as a result of origin of nucleation. In figures 3.4a and 3.4b shown below, the fibrous structure are said to have originated from nucleation sites in the centre and at the droplet surface respectively.
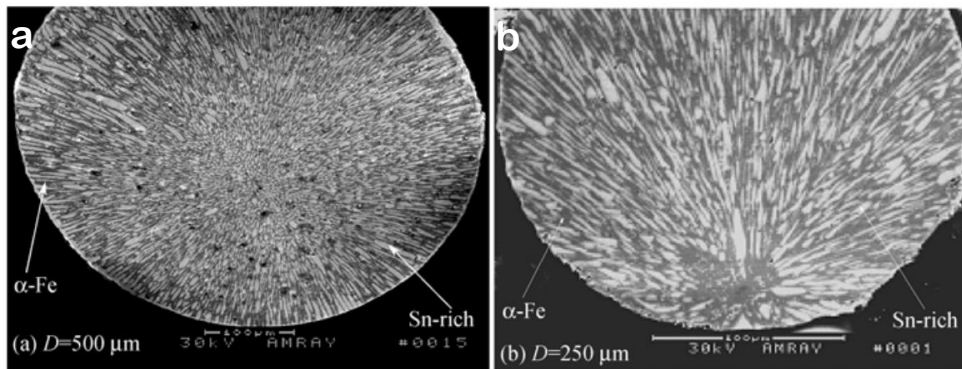
Figure 3.4 Microstructure of Fe – 48.8 wt. % Sn alloy showing dendritic growth nucleating from (a) centre of droplet and (b) droplet surface [132].

The Fe – 40 wt. % Sn (23.9 at. %) alloy had two types of morphology; (i) α – Fe dendrites in Sn – rich matrix of larger droplets and (ii) α – Fe particles in

smaller droplets. The particles structure is said to be as a result of faster growth velocity brought about by higher undercooling.

In the Fe − 58 wt. % Sn (39.4 at. %) alloy, a combined structure comprising dendrites and concentric spheres was observed (figure 3.5). The spheres had a Fe − rich outer shell while the core had the fibrous growth. This is quite unique as in all the core shell structures examined in the course of this research none displayed a eutectic like structure in the core. The authors did not give an explanation how this might have happened. The structures are however noticed to have protrusions which might be growing dendrites.
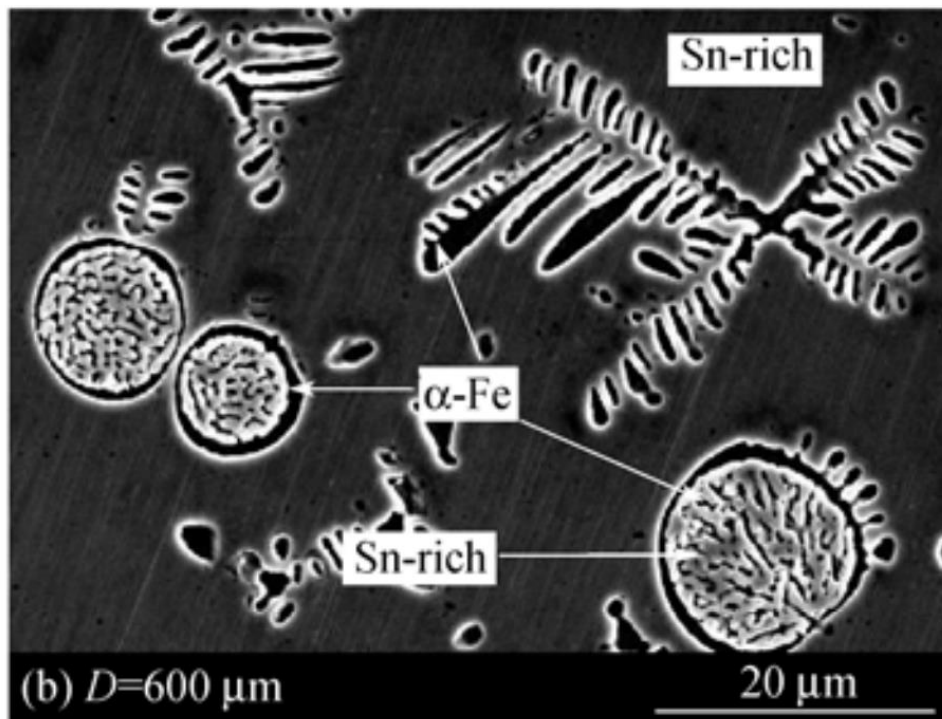
Figure 3.5 SEM image showing dendritic and concentric circle structures of Fe − 58 wt. % Sn alloy processed in a drop tube [132].

3.3   Monotectic systems with metastable miscibility gap in the liquid state

In comparison with the stable MG systems literature is sparse on monotectic systems with metastable MG owing to the transitional nature of the metastable phases. There has also been disparity in the actual type of phase

diagram of some of these systems due to the high melting point and strong oxidation tendencies of some of the constituents of the system. Experimental conditions of researches on these alloys are subject of debate and as such continue to be of research interest.

Metastable liquid phase separation has been predicted for binary alloy systems with evenly sloping/ flat liquidus on their equilibrium phase diagrams [133] as observed in systems such as Ag - Pb, Cu - Ta, Co - Cu, Cu - Fe, Cu - Cr and Cu - Nb. Studies of such binary systems is therefore necessary to verify the existence of the metastable phases and if present detailed investigation of the phase separation mechanism, microstructural morphology and phase transition behaviour is also essential. Thermal analysis is also needed to address the phase equilibrium debate.

This section of the chapter is a focused review of studies on three binary systems (Cu - Nb, Cu - Cr and Cu - Fe) predicted to possess a metastable miscibility gap and in which metastable liquid phase separation is envisaged. The alloy systems are selected due to the shared characteristics of their equilibrium phase diagram with the alloy of interest in this research. This is in order to establish (or not) similarities in their phase separation patterns and behaviour under rapid cooling.

3.3.1   Cu - Nb system

The Cu - Nb alloy system alloy possess high mechanical strength and has excellent thermal and electrical conductivity. The alloy has also been shown to have less damage to radiations and as such been tipped for future applications in nuclear energy [134]. The very strong affinity for oxygen and carbon and the high melting point of Nb makes temperature measurements and homogenisation of melt very difficult for Nb containing alloys [135].

A number of systems have been proposed for the alloy by various researchers. A peritectic system was proposed by Chakrabarti and Laughlin [136] and Smith et al [137], a eutectic system by Petrenko et al, Somov et al and Sinibaldi was cited in the work of Hamalainen et al. [138]. A stable liquid

state MG was reported for the system by Li et al. [135], Leonov et al, Petrenko et al and Popov and Shirjaeva [138].

Presently, two phase diagrams are accepted for the system namely: a stable liquid MG phase diagram proposed by Popov and Shirjaeva in 1961 and the generally accepted as the more accurate phase diagram with a near horizontal liquidus (figure 3.6) proposed by Allibert et al. in 1969 [139].

Li et al. [135] observed liquid phase separation in alloys of 5 – 35 wt. % Nb (3.5 – 26.9 at. %) upon cooling into the stable MG and this was attributed to oxygen impurities as the stable MG is said to be induced in the presence of oxygen in slowly cooled alloys. The presence of a nearly flat liquidus; an indication of a possible metastable liquid MG which was confirmed in another study by Li et al. [140] as evidenced by the microstructure of a droplet processed in 105 m drop tube. In order to verify this, electromagnetic levitation was used by Munitz et al. [141] in 2009 on the alloy containing 5 – 70 wt. % Nb (3.5 61.5 at. %) and contrary to the earlier reports liquid phase separation was only observed for alloy of concentration of 20 wt. % Nb (14.6 at. %). Fihey et al. [142] however, observed dispersed Nb – rich particles in an alloy of Cu – 7 wt. % Nb (5 at. %) and suggested that the distribution, size and shape of the Nb – rich particles is dependent on the cooling rate. They observed Nb – rich flowers at very low cooling rates which they attribute to the connection of spheres of different sizes while at higher cooling rates the dispersed spheres were observed.

Zhang et al. [134] however in 2013, published a paper in which experimental phase diagram of the Cu - Nb system was reproduced using embedded atom model interatomic potentials (EAM). They reported that no evidence of a metastable MG exists in the Cu - Nb system.
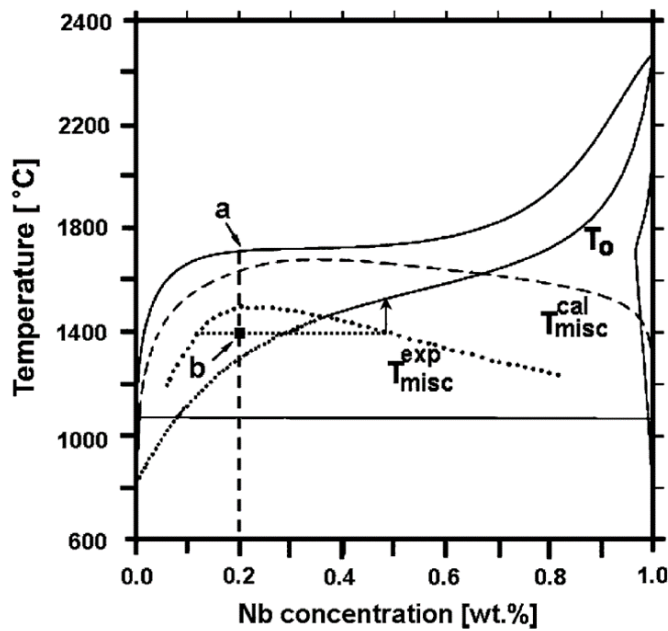
Figure 3.6 Accepted phase diagram of the Cu - Nb system with super
imposed calculated and experimental metastable miscibility gap by Munitz
et al. [141].

3.3.2   Cu - Cr system

Cu - Cr alloys possess a unique combination of high mechanical strength with
thermal and electrical conductivities making it attractive in many industrial
applications especially in high voltage vacuum interrupters [9].

Hindrichs and other scholars proposed a monotectic type phase diagram with
a stable miscibility gap in Cr-rich compositions [2,143–146]. However, this
type of phase diagram has been constantly challenged and has been said to be
an effect of impurity in raw materials used or contamination of melt
[138,147–150].

The currently accepted phase diagram for the Cu - Cr system is of the eutectic
type with a flat liquidus and complete miscibility in the liquid state. This was
proposed by Jacob et al. [149] based on a thermodynamic study of the system
using mass spectrometry. This phase diagram shows a metastable miscibility
gap in undercooled liquid with critical point (T_c, X_c) at 1787K and 43.6 at.%
Cr respectively on the Cu-rich side.

70

The credentials of this phase diagram by Jacob et al. has also been challenged in some studies. Li et al. [140]and Zhou et al. [2] argued that the phase diagram proposed by Jacob et al. had underestimated liquidus temperatures and that the miscibility gap lies on the Cr-rich side from splat quenching experiments.

The existence of this metastable miscibility gap in the Cu- Cr system makes phase separation studies possible in the alloy, however, its boundary as well as phase separation in Cr - rich alloy compositions have not been fully explored as most rapid solidification experiments have been on Cu - rich compositions.

Melt spinning [151,152] as well as EML in combination with spat quenching [153] have been used in studying the alloy system.
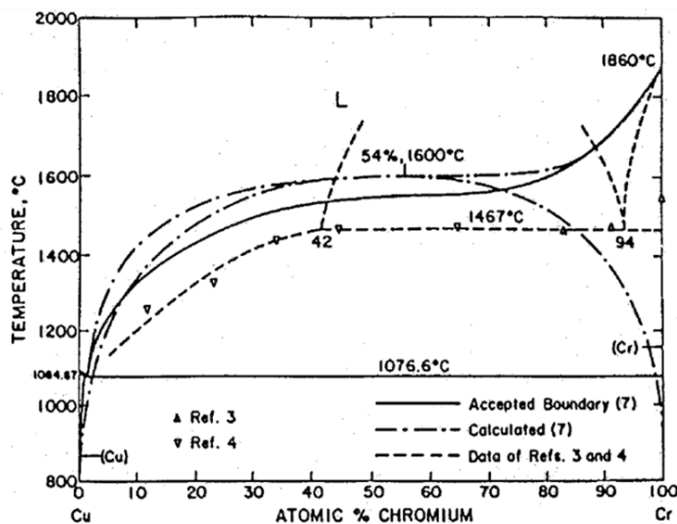
Figure 3.7 Calculated liquidus and miscibility gap for the Cu - Cr system [148].

Wang et al. [151] studied Cu – 35 at. % Cr alloy under various cooling rates by controlling the speed of the cooling roller in melt spinning experiment and observed the variance of microstructure. At zones near the chill surface, nano sized Cr – rich nodular particles were observed in comparison to dendrites formed at the free surface farthest form the chill. Further increase in the cooling rate (up to magnitude of 10^6 Ks^{-1}) was reported to produce more

refined Cr – rich particles (< 300 nm). Secondary liquid phase separation was inferred by the authors due to presence of Cu – rich phase in the nodular structures. They reported that arc melt samples at cooling rate of 10^4 Ks^{-1} were only dendritic.

Sun et al. [152] also used the melt spinning method to study Cu – 25 wt. % Cr (29 at. %) alloy and noted that liquid phase separation occurred at cooling rate of about 10^4 Ks^{-1}. This is contrary to what was reported by Wang et al. [151]. At cooling rate of 10^5 Ks^{-1} the Cr – rich particles had reduced to 100 – 500 nm while at 10^6 Ks^{-1} further refinement was observed. However, at the cooling rate of magnitude of 10^7 Ks^{-1} the LPS was not retained. The same trend was observed in Cu – 15 wt. % Cr (18 at. %) and Cu – 35 wt. % Cr (40 at. %) alloys. Size of the Cr – rich particles were also found to increase with Cr – content when it is between 15 to 35 wt. % Cr.

Gao et al. [153] on the other hand studied Cu – 25 wt. % Cr alloy. In their control experiment using only EML, coarse dendritic structures were observed even though their phase diagram estimate puts the critical undercooling required for LPS at just 27K. A suppression of the LPS by heterogeneous nucleation at the surface by a layer of chromium oxide was cited as being responsible for this. However, in the EML plus splat quenched samples Cr – rich spheres on which dendrites were observed to be nucleating were noticed (figure 3.8). The undercooling for these samples was estimated to be 210 K.
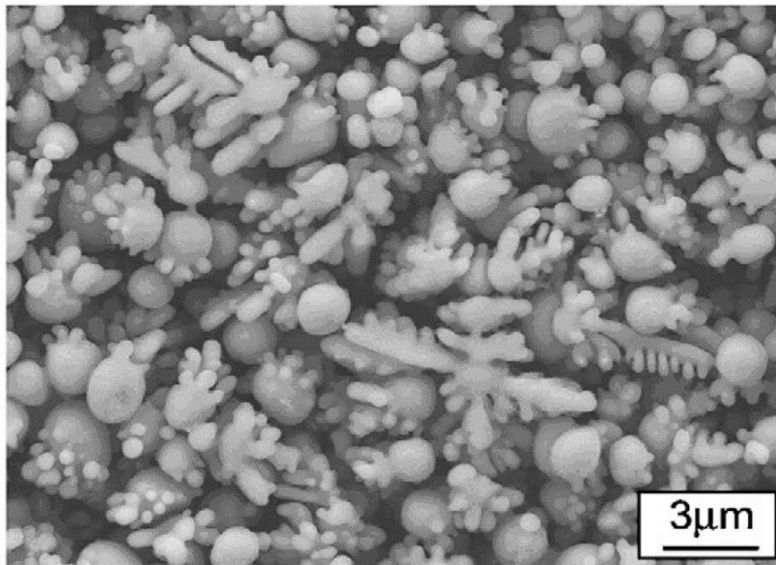
Figure 3.8 SEM image of levitated and quenched sample showing dendrites nucleating from Cr – rich spheres [153].

3.3.3 Cu - Fe system

Cu - rich compositions of this alloy system possess high strength and electrical conductivity properties and have also been said to have giant magnetoresistance properties like the Co – Cu alloy system [154]. This binary system consists of three condensed phases [155] liquid, face centered cubic (fcc) and body centered cubic (bcc). The Fe-rich fcc phase is denoted γ, Cu-rich fcc is ε, the high temperature bcc is δ and low temperature bcc is α. One eutectoid ($\gamma \leftrightarrow \varepsilon + \alpha$) and two peritectic ($L + \delta \leftrightarrow \gamma$), ($L + \gamma \leftrightarrow \varepsilon$) transformations are also present on the phase diagram.

The Cu - Fe and Co –Cu have similarly shaped MG (figure 3.9) but the MG of Cu – Fe system is said to be about 20 K below the liquidus hence it demixes more readily than Co – Cu (90 K) [16]. Nakagawa [16] placed the critical points of the MG observed in the system at 1696 K and 56 at.% Fe, however, Wilde et al. [156,157] using fluxing technique placed the critical point at 1704 K and 53 at.% Fe with undercooling up to 250 K achieved. He was also said to have reported the occurrence of other processes in the system (synthetic reaction at 1405 K ($L_1 + L_2 \leftrightarrow \varepsilon$) and metastable solidification ($L \rightarrow \delta$). The

liquidus temperature T_L, critical phase separation temperature T_{sep} and critical undercooling for phase separation ΔT_{sep} of the Cu - Fe system are available in literature.
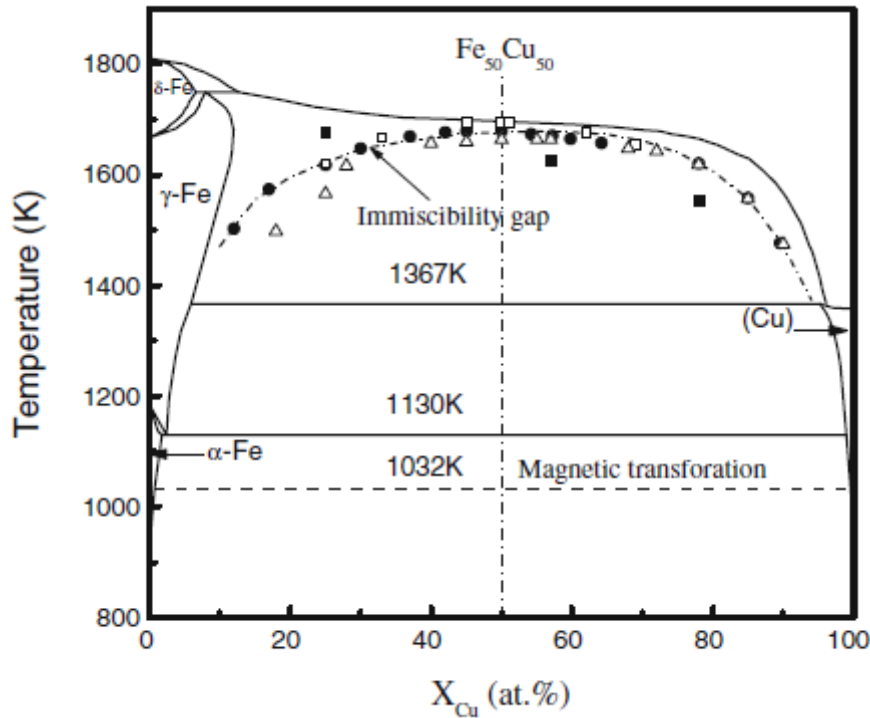
Figure 3.9 Equilibrium phase diagram of Fe - Cu alloy system showing the position of the Cu – 50 at. % Fe alloy with calculated and measured metastable MG boundary from various studies [158].

Liu [159] and Luo et al. [160] studied the Cu - 50 at. % Fe alloy. Luo et al. obtained a critical undercooling of 7 K to bring about LPS. This value is much lower than the estimates of Nakagawa (20 K) [16] and Wilde (55 K) [156,157]. Micrographs in support of this were presented showing LPS structures at undercooling of 20 K and 261 K (which was the maximum undercooling attained in their glass fluxing experiment). Microstructural features exhibited at both undercooling were the same; a crescent shaped Cu – rich region (L_2) surrounding a Fe – rich region (L_1) that is not fully enveloped around it. The Cu – rich region contained Fe – rich dendrites and spherical particles while the Fe – rich region also contained dendrites and Cu

– rich particles. However, Liu [159] in his own study concluded that at undercooling less than 46 K, the alloy solidifies under equilibrium condition with Fe – rich dendrites in a Cu – rich matrix. The reason for the divergence of microstructural features in these two similar studies is not clear but a reasonable hypothesis after comparison with other studies on the alloy system is that calculations in [160] were wrong or the LPS was aided by heterogeneous nucleation.

The LPS pattern was also found to depend on the degree of undercooling. [159] observed that microstructure at undercooling of 65 K was the same as that observed by [160] at undercooling of 20 K and 261 K. However, at undercooling of 173 K, dispersed droplets of the minority phase in the Fe – rich region were observed by Liu [159]. The observed change in the structure of the Fe – rich region is an indication that a secondary LPS occurred in the region. The crescent shaped Cu – rich region however remained dendritic. Growth of the dispersed particles were said to be by coagulation which is influenced by Stokes motion but the Stokes effect was more visible in the micrographs presented by [160] with the Fe – rich phase floating to the top due to the density difference between Fe and Cu (7.87 and 8.96 (g/cm^3) respectively).

It is evident from these two studies that the higher the degree of undercooling, the longer the phase separation time.

Chen et al. [161] and He and Zhao [154] also studied Cu- Fe alloys. In Cu – 30 at. % Fe alloy, [161] obtained a critical undercooling of 56 K which was much higher than the values in [16] and [160] but quite similar to that of Wilde [156,157]. The LPS pattern was consistent with [159] and [160] with secondary phase separation also observed in the Fe – rich phase with the presence of L_2 spherical particles. Just as in [159], the phase separation pattern was observed to vary with degree of undercooling with the L_1 phase said to possess higher undercooling than the L_2 phase. This can be explained by the phase diagram of the system (figure 3.10).

The size of the dispersed L_1 spheres increased with increasing undercooling [161] probably due to accelerated coalescence rate. Their growth rate occurred in three stages:

a. Steadily increasing L_1 sphere at slow growth rate when undercooling is between 56 K and 79 K.
b. Drastic growth rate stage at which Ostwald ripening is said to be very dominant. Occurs when undercooling is between 79 K and 142 K.
c. Saturated stage when the increase in the size of the L_1 sphere is said to be negligible. Occurs at undercooling in excess of 142 K.

These 3 stages of growth of the dispersed droplets was said to have also been observed in an entirely different alloy system (Cu – 30 wt. % Co (31.6 at. %) alloy) [161]. It would be expected that the microstructure at the different stages be different, the authors however did not highlight how these would vary with droplet size and cooling rate.

The study of the size effect was attempted in gas atomized Cu – 15 at. % Fe alloy by He and Zhao [154]. They found that the size of the L_1 spheres decreased as the parent droplet size decreased but their number density increased. They went further using numerical simulation to establish a relationship between the radius, (r), of the L_1 spheres and the diameter, (D) of the parent droplet as

$$r = 49D^{0.437} \tag{3.3}$$

The critical undercooling was put at 71 K and the undercooling generally was found to increase as the droplet size decreased.
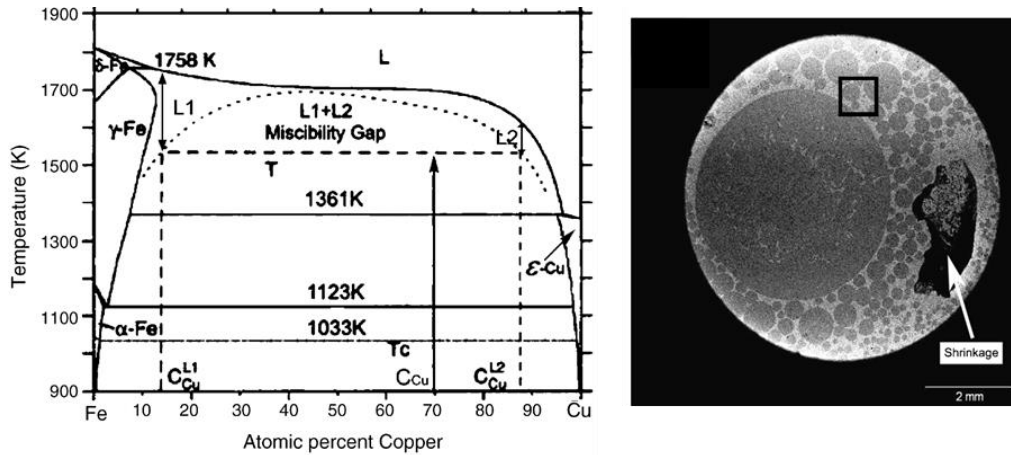
Figure 3.10 Phase diagram estimates of Chen et al. and back scattered SEM image of a Cu – 30 at. % Fe alloy showing L_1 phase (Fe – rich) in a L_2 matrix (Cu – rich) [161].

3.4   The miscibility gap in the Co – Cu system

A nearly symmetrical miscibility gap at equi – atomic composition was first reported for the system in 1958 by Nakagawa [16] in his study on high temperature magnetic susceptibility and microscopic examination of quenched samples of Cu-Co and Cu-Fe alloys in the liquid state. He noticed LPS occurred more easily in undercooled samples of Cu-Fe alloys as higher minimum undercooling was observed for the Cu-Co system. The observed critical undercooling was said to be about 90 K below the equilibrium liquidus. Nakagawa's experiment was however flawed in terms of the sensitivity of the technique used, oxygen impurities were said to be the source of the liquid phase separation observed [133] a claim verified by the study of Verhoeven and Gibson [162] in their observation of oxygen effects in Cu - Nb alloys under chill casting technique.

Robinson et al. [133] and Elder et al. [163] directly determined the position of the submerged binodal line which is the boundary of the miscibility gap by measuring the LPS temperature in Co – Cu alloys of different compositions. Robinson et al. [133] roughly determined the boundary of a symmetrical metastable miscibility gap by plotting measured values of T_{sep} (temperature

at which liquid phase separation begins) in samples processed by fluxing onto the phase diagram. The critical undercooling at the equi – atomic composition was put at 80 K below the equilibrium liquidus which is close to the result of Nakagawa [16], they also confirmed that the peritectic reaction occurred in the system at temperature (T_p) of 1385 K. The directly determined MG by Robinson et al. was said to be in agreement with that determined from composition analysis of quenched samples by Munitz and Abbaschian [8] even though their own MG was asymmetrical.

Cao et al. [164] using differential thermal analysis and glass fluxing was able to directly measure the T_{sep} and T_L in undercooled Cu-Co alloys of composition Cu- 16 at. % Co – Cu- 87.2 at. % Co. Their miscibility gap (figure 3.11) had a binodal boundary in the composition range of 16 – 89.3 at. % Cu with the curve slightly symmetrical around 53 at. % Cu, the LPS temperature was 1547 K which was 108 K below its equilibrium liquidus temperature. Their observed T_{sep} was 30 K lower than that of Nakagawa and Robinson et al. They placed the deviation to the use of T_p as calibration for experiment by Robinson et al. and to the responsiveness of the magnetic susceptibility of the alloy to fluctuations in concentration in Nakagawa's experiment.

Yamauchi et al. [165] also in a flux experiment used thermal analysis in studying the undercooling behaviour of Cu - Co alloys during solidification and effect on their solidification structure. They reported that minimum undercooling for LPS to occur decreased on the addition of boron and as such boron could facilitate LPS in the alloy. They observed T_p of 1360 K which was lower than the equilibrium value of 1385 K verified by [133], the reason for the low value was not given. The critical undercooling at the equi - atomic composition was put at 96 K.

Palumbo et al. [166] using calculation of phase diagram (CALPHAD) method, stated that the critical point of the metastable miscibility gap of the system occurs at 58.5 at. % Cu with a corresponding temperature of 1556 K.
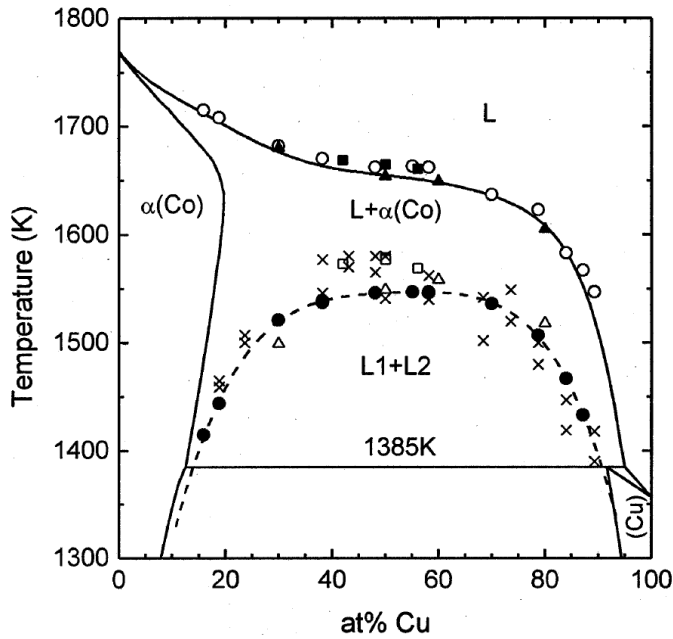
Figure 3.11 Phase diagram of the Co – Cu alloy system showing results from various studies of the measurement of (a) T_L (■ - Nakagawa [16], ▲ – Yamauchi et al. [165] and ○ – Cao et al. [164]), (b) miscibility gap boundary (□ – Nakagawa, Δ - Yamauchi et al., ● – Cao et al. and X – Robinson et al. [133]) [164].

3.4.1 Liquid phase separation and microstructural morphology in undercooled Co - Cu system

Generally the Cu - Co alloy undergoes metastable liquid phase separation into L_1 (cobalt rich) and L_2 (copper rich) liquid phases when undercooled beyond a certain temperature limit (T_{sep}) which is composition dependent [8,165,167]. The solidification path of the two liquids when traced on the metastable phase diagram will be different to each other and to the parent melt. This is because each liquid will have a different undercooling. Secondary liquid phase separation of one liquid phase inside the other has also been said to occur in the alloy at high undercooling due to incomplete diffusion [8].

Munitz and Abbaschian [8] studied Co – Cu alloys of composition 10 – 67 at. % Co using EML and splat quenching. They observed L_1 – rich spherulites (spherical particles arranged radially about a point) in a L_2 rich matrix in

alloys with composition < 40 wt. % Co (42 at. %) (figure 3.12a). Their spherulites consisted of equi axed structures while the matrix contained $\alpha -$ Cu dendrites surrounded by peritectic $\varepsilon -$ Cu phase (figure 3.12c). In contrast, alloys with composition > 55 wt. % Co (57 at. %) were observed to have microstructures of $L_2 -$ rich spherulits in a $L_1 -$ rich matrix (figure 3.12b). They noticed that the structure of the spherulites in both alloy were the same and concluded that they were from the same melt. This implies that the $L_1 -$ rich spheres in the alloy < 40 wt. % Co nucleated from a Co – rich melt. This contradicts literature findings that when immiscible alloys are rapidly solidified, the minority phase in the melt nucleates. An explanation for why the spheres are not formed by the minority phase is already offered under the section on stable miscibility gap alloys.
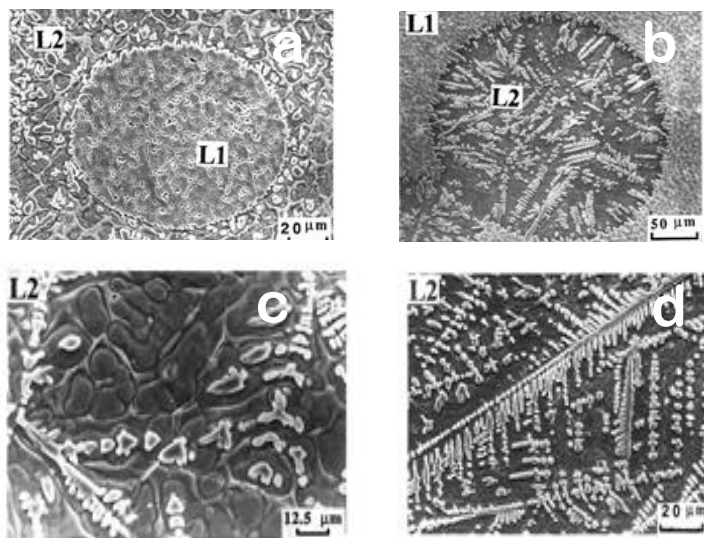
Figure 3.12 SEM images showing spherulite structures in (a) Cu-30 wt. % Co undercooled at 210K, (b) Cu-55 wt. % Co undercooled at 150 K, microstructure of (c) spherulite ($L_1 -$ rich) region in (a) and (d) spherulite ($L_2 -$ rich) region in (b) [8].

Zhang et al. [168] in their study of alloy of composition 75 at. % Cu also agreed with [8] that alloys with Co > 41.6 at. % (which is the critical composition on the metastable phase diagram estimates by [164]) would disperse Cu – rich particles while Co – rich particles are dispersed in those

with Co < 41.6 at. %. They observed Co – rich particles in L_2 matrix (figure 3.13a). Alloy of composition 28.4 at. % Cu processed by fluxing also reported a LPS pattern supporting the rule [135]. At undercooling of 228 K, Cu – rich spheres were observed dispersed in the matrix (figure 3.13b) while at lower undercooling (130 K), dendritic structures were reported. However, this rule seemed not applicable in some alloys especially in the Cu – 50 at. % Co alloy which will be discussed in detail in the next section.

Different structures have been reported in alloys processed by drop tube. Luo et al. [125] examined alloy of composition 89.3 at. % Cu processed in a 50 m drop tube and thereafter quenched. They reported a dual structure comprising α – Co dendrites at the surface of the droplet (said to be due to quenching induced temperature gradient) and L_1 - rich spheres towards the centre (figure 3.13c). EDX analysis however revealed that the Cu content of these spheres were high (up to 48 at. %).

Cao et al. [169] examined samples of composition 70 at. % Cu processed in a 3 m drop tube. Large droplets (500 μm) were also reported to be characterised by α – Co dendrites with well-defined secondary and tertiary arm spacing. These were said to have also originated from the surface, they occur alongside with fragmented dendrites at the centre (figure 3.13d). LPS structures in smaller particles (150 μm) were uniformly dispersed Co – rich spheres of different sizes. Identical dispersed particles were also reported in Cu – 16 at. % Co [94,170] and Cu – 41.8 at. % Co [170] alloys processed in an 8 m drop tube.

Due to the fact that the secondary dendrite arm spacing (SDAS) is formed during coarsening, it serves as a measure of the cooling rate of the solidification process [171]. The relationship between the secondary dendrite arm spacing (λ_{SDAS}) and the cooling rate ($\dot{T}$) is of the form

$$\lambda_{SDAS} = \Lambda(\dot{T})^{-n} \tag{3.4}$$

Where Λ is a material dependent constant and n is between 0.333 and 0.5 [171]. No literature was found in the course of this research validating this relationship in rapidly solidified droplets that have undergone metastable liquid phase separation (for obvious reasons) even though it is possible for dendritic formation to exist in such droplets. All droplets used in validating the relationship in this research are assumed not to have undergone the metastable liquid phase separation.
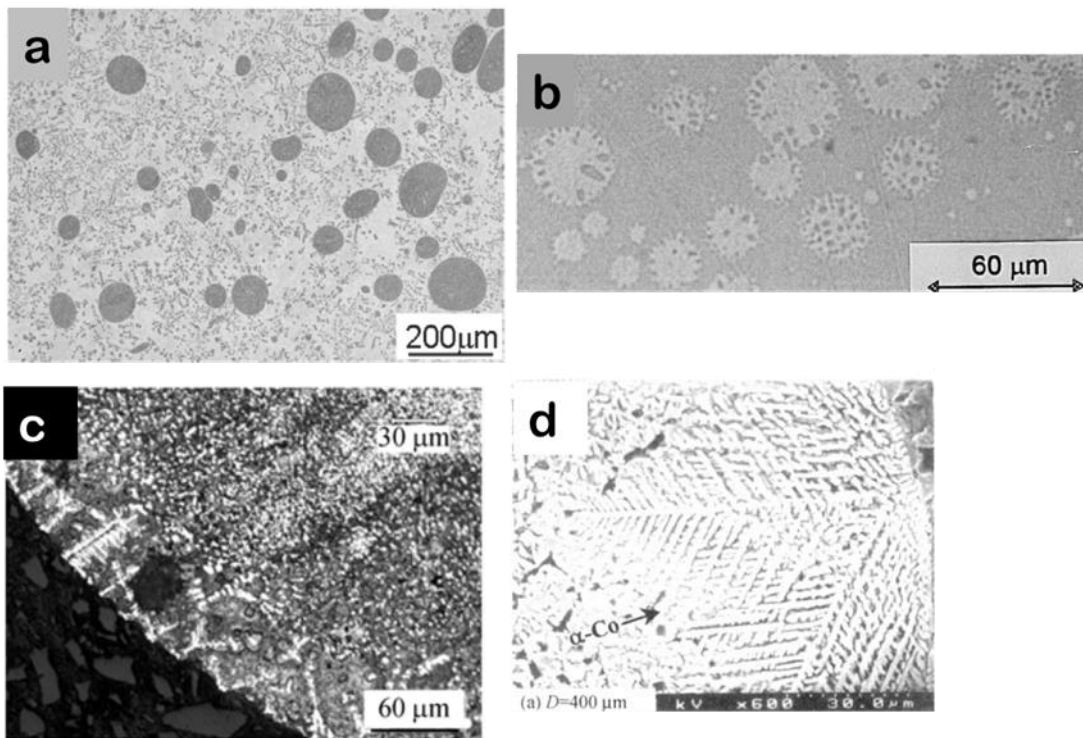
Figure 3.13 SEM images showing structures in Co – Cu alloys: (a) Co – rich particles dispersed in L_2 – rich matrix [168], (b) Cu – rich particles dispersed in L_1 – rich matrix [135], (c) α – Co dendrites at the periphery of a droplet and L1 – rich spheres towards the centre [125] and (d) dual structure of α – Co dendrites and fragmented dendrites [169].

3.4.2 The Cu - 50 at. % Co alloy

The alloy containing equal parts of copper and cobalt ($Co_{50}Cu_{50}$) has been extensively researched. Based on the generally accepted metastable miscibility gap of the system by Cao et al. [164], this alloy is close to the critical composition and its liquidus temperature is put at 1655 K with critical

undercooling for LPS estimated to be 106 K. Munitz and Abbaschian [8] concluded that liquid phase separation does not occur in the alloy of Cu – 50 wt. % Co (52 at. %) even though experimental result from various researches say otherwise. Table 3.1 lists values of T_L, T_{sep} and critical undercooling for LPS (ΔT_c) for the Cu – 50 at. % Co alloy extracted from various studies.

Table 3.1 Experimental results of the liquidus temperature (T_L), liquid phase separation temperature (T_{sep}) corresponding to the T_c and the critical undercooling (ΔT_c) below the equilibrium liquidus for the Cu – 50 at. % Co alloy using different methods: DSC differential scanning calorimetry, MAG magnetic susceptibility and DTA differential thermal analysis [158].

Composition (at. % Co)	T_L (K)	T_{sep} (K)	ΔT_c	Experimental method	Ref
50	1666	1538	128	DSC	[172]
50	1665	1579 / 1577	86 / 88	MAG	[16]
50	1654	1549	105	DTA	[165]
50	1664	1544	120	DSC	[173]
50	-	1541 /1580	-	DTA	[133]

In their EML experiment [8] undercooled the alloy to above 110 K. LPS was not observed instead the micrograph showed zones of fine and coarse dendrites (figure 3.14a); distinction between the dendritic zones became blurry with increase in undercooling and at undercooling of 200 K the coarse dendrites penetrated into the fine dendritic zone (figure 3.14b).   In compositions that showed evidence of LPS, the spherulites were said to become distorted as the undercooling increased. This is not expected to be observed in drop tube processed samples as the distortion is caused by

convective flow induced by the electromagnetic stirring. Convective flow is also said to affect the size distribution of dispersed spherical particles in EML samples as it influences coalescence of smaller particles to form larger ones or cause larger particles to collide and break into smaller ones.

Appearance of spherical structures which were aligned perpendicular to plane of sectioning and coarse dendrites was observed at undercooling of 250K and above (figure 3.14c).
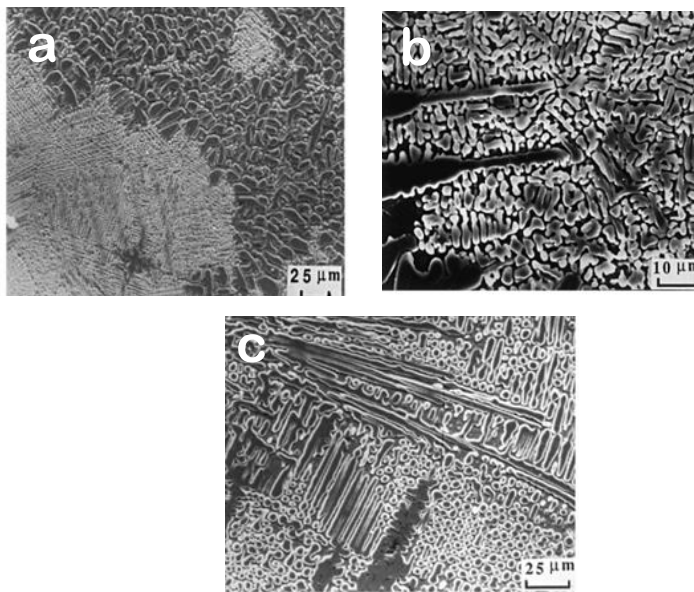
Figure 3.14 SEM microstructure of Cu -50 wt. % Co (52 at. %) undercooled at (a) 180K: zones of fine and coarse dendrites, (b) 200K: penetration of the coarse dendrites into the fine dendritic zone and (c) 250K: aligned spherical structures [8].

Dendrites were also observed in samples processed by electron beam surface melt [174], drop tube (figure 3.15a) [167] and fluxing [133]. The researchers all reported that phase separation occurs at this composition only with increased undercooling. In electron beam surface melted samples, structures close to the fusion line were cellular and at about 50 to 70µm away from it dendritic. As the distance increased from the fusion line, a mixed cellular / dendritic structure was observed. This was in contrast to alloys in the composition range of 10 – 30 wt. % Co (11 – 32 at. %) which showed

evidence of LPS at 100 μm from the fusion line [174]. Similar to the dual dendritic structure in [8], the mixed structure is due to increased undercooling as distance increases from the fusion line.

In [167] levitated samples of the alloy were dropped into a 105 m drop tube and a variation of microstructures as the undercooling increased during the free fall were observed. Structure ranged from coarse Co – rich dendrites (Figure 3.15a) of composition 81 wt. % Co (82 at. %) to spherical particles (Figure 3.15b) in the composition range 76 – 80 wt. % Co (77 – 81 at. %). The LPS structures were however said to occur at undercooling of 300 K which far exceeds metastable phase diagram estimates for an alloy of this bulk composition.

A structure of primary α-Co dendrites and peritectic copper was seen in sample undercooled by fluxing technique, a large cobalt droplet in the middle of the specimen was noticed in the microstructure as well [133].
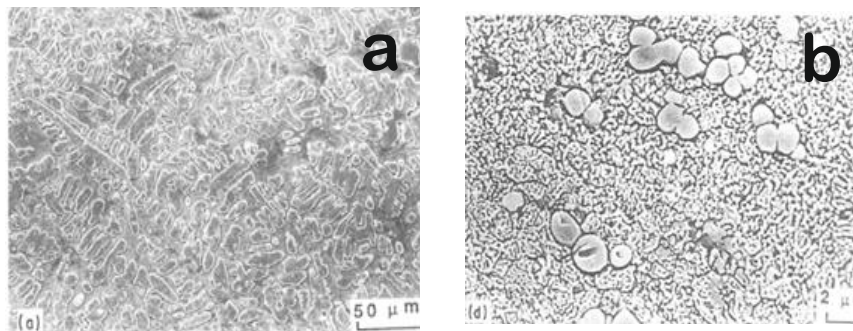
Figure 3.15 SEM images showing microstructure of drop tube processed Cu- 50 wt. % Co (a) Co dendrites in a Cu rich matrix and (b) undercooled at 300K showing spherical shaped L_1 surrounded by tiny precipitates of L_2 [167].

Yamauchi et al. [165] subjected the Cu – 50 at. % Co alloy to cyclic heating and cooling in a high frequency induction experiment and observed that at undercooling of 65 K there were no evidence of LPS but rather Co – rich dendrites (Figure 3.16a). When the undercooling increased to 123 K, Cu – rich spherical particles were observed in a Co – rich matrix (Figure 3.16b). This separation pattern was different from studies discussed earlier. Also contrary to earlier findings, peritectic structures and features suggesting dual dendritic zones were not observed in their research. They suggested the dual dendritic structure could be obtained by rapid cooling of the melt at the start of liquid separation. The spherical particles occurred alongside Co – rich dendrites an indication that two melts of different composition was solidifying. When the undercooling increased to 196 K, samples that phase separated after recalescence were noticed to have two distinct melt layers L_1 (cobalt rich) in upper part and L_2 (copper rich) in lower part, both layer contained spherical particles. Clearly phase separation occurred here however, it took longer and as such particles failed to coalesce and coupled with gravitational influence the somewhat layered structure was formed. At the interface of the layers droplets of the different phases were seen (figure 3.16c) but further away from the interface dendritic structure dominated suggesting that the phase separation only occurred at and close to the interface, the dendritic structure being a product of solidification of the two different phases.
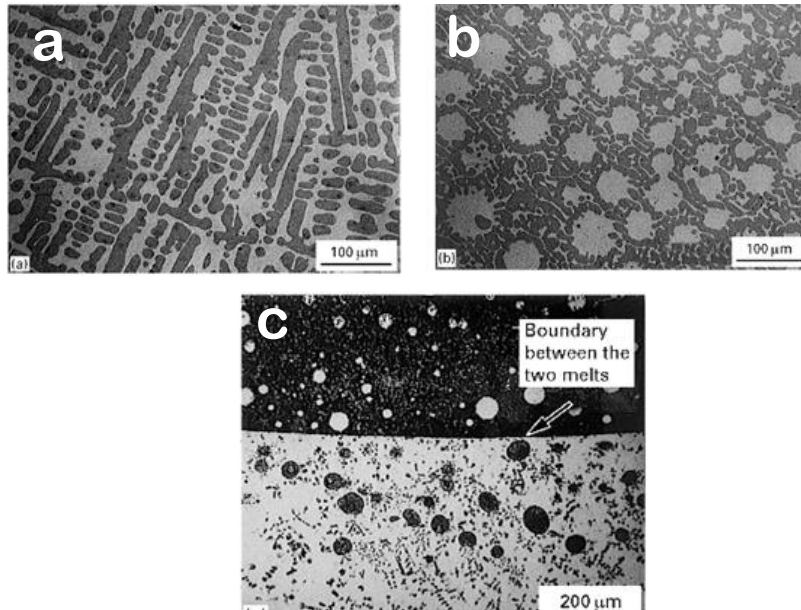
Figure 3.16 SEM images showing microstructure of Cu - 50 at. % Co alloy (a) undercooled at 65K: dark primary Co dendrites in copper rich inter dendritic white phase, (b) phase separated structure showing Cu rich spherical structures in dark Co rich matrix and (c) 2 melt layer showing droplets of L_1 and L_2 phases at and close to the interface [165].

Zhang et al. [175] and Davidoff et al. [176] also obtained a separation pattern identical to that of Yamauchi et al. [165]. Zhang et al. [175] used EML under static magnetic field while Davidoff et al. [176] examined rapidly quenched samples of Cu – 50 at. % Co alloy using EML and splat quenching. In samples processed by EML alone at undercooling in excess of 120 K, they placed the observed structure within the binodal region and the large spherical / distorted L_2 particles were found to be almost pure copper with composition 96 at. % Cu while the L_1 – rich matrix had a composition of 84 at. % Co [176]. The interface between the two liquids just as in [165] had dendrites but in this case protruding from the L_1 phase into the L_2 phase implying that they were formed after the solidification of the Co – rich phase. In samples quenched on a Pb – coated copper substrate, undercooling of 220 K was achieved with cooling rate magnitude estimated at 10^4 Ks^{-1}. LPS also occurred and the micrograph presented (figure 3.17a) like in [96] contained a large coagulated Co – rich

87

phase containing L_2 droplets indicating further LPS occurred. The L_2 droplets did not contain dendrites as in the EML samples but rather Co – rich dots (figure 3.17b). Explanation was not offered on how the structure in figure 3.17a was formed. It is thought that the presented micrograph showed evidence of surface segregation of copper which in turn depleted the bulk of the parent droplet in copper making it rich in cobalt. Upon cooling into the binodal, Cu – rich MPD were formed (explains the presence of the L_2 droplets in the bulk Co – rich region). Simultaneously in the segregated region, Co – rich MPD were formed but because this side is far from the chill surface, the degree of undercooling and cooling rate is slightly less and as such LPS takes longer to occur. This explains the absence of further LPS artefacts in the distorted L_1 rich particles observed in this region. In splat quenched samples with estimated cooling rates of order $10^6 - 10^7$ Ks^{-1}, spinodal decomposition structures were observed (figure 3.17c).
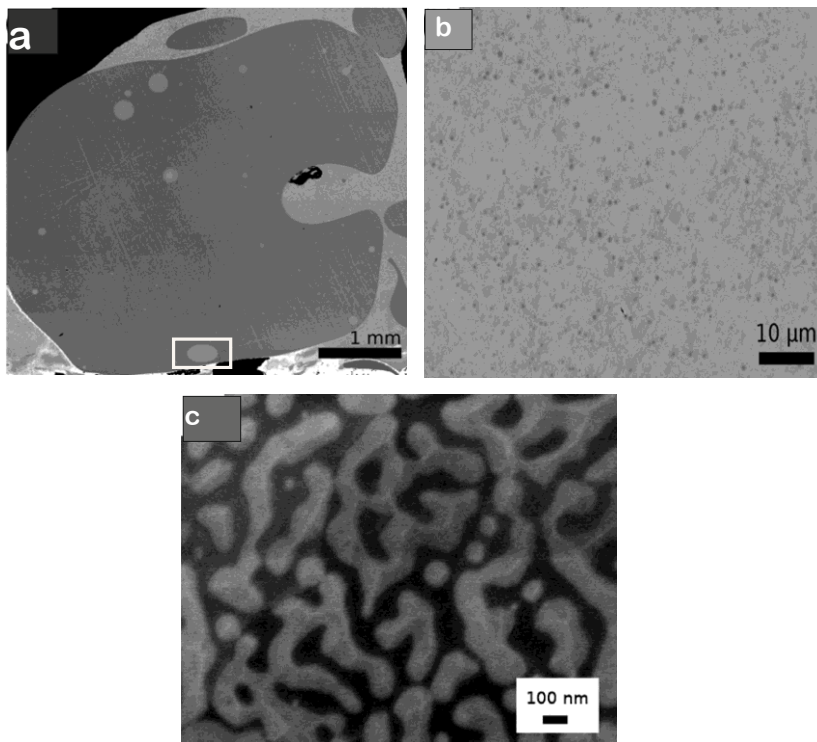
Figure 3.17 SEM images showing microstructure of electromagnetic levitated Cu - 50 at. % Co alloy (a) quenched on a Pb – coated copper substrate (b) magnified view of highlighted L_2 – rich droplet and (c) spinodal structure in splat quenched samples [176].

Clearly, a significant knowledge gap exists regarding phase selection, liquid phase separation and microstructure formation mechanism in metastable immiscible alloys. The findings of some of the research on the Co – Cu alloy system is debateable. The boundary of the miscibility gap in the alloy is subject to the accuracy of the experimental technique adopted by the various researchers. In view of this, an attempt is made in estimating the miscibility gap in the system using thermodynamic calculations.

The dispersion of the L_1 or L_2 phase in demixed alloys does not conform to the phase diagram rule mentioned in [8] and [168]. A typical alloy not conforming to the rule is the Cu – 50 at. % Co alloy. Liquid phase separation in this alloy is said to only occur at high undercooling which contradicts phase diagram prediction that the alloy should easily phase separate due to its proximity to the critical composition and little gap between its equilibrium liquidus and the binodal curve of the miscibility gap. Also in all the reviewed literature, there is only one mention of successful spinodal decomposition in the alloy which was by Davidoff et al. [176] (with evidence at very high cooling rate of order $10^6 – 10^7$ Ks^{-1}). This is unusual as there is little or no gap between the binodal and spinodal curves of the alloy, so it should easily spinodally decompose.

The Cu – 50 at. % Co alloy is therefore the interest in this research as well as Cu – 68.5 at. % Co alloy. The Cu – 68.5 at. % Co alloy is not expected to spinodally decompose because the estimated undercooling to cool into the spinodal region of the miscibility gap is rather high.

3.5   Core shell microstructures in monotectic systems

Core shell structures may be formed when immiscible alloys are processed in microgravity environment as a direct consequence of thermal and / or composition gradient coupled with high cooling rates. This microstructure is

characterised by droplets of a phase (reported in many literature as the minority phase droplets) (which coalesce to form the core) being enclosed in the liquid matrix of the major phase (the shell) [177]. These structures are highly desirable in monotectic systems due to the enormous possibility of properties that may be induced by varying the size and composition of the core and shell materials [178]. Figure 3.18 shows a schematic representation of potential core shell structures in binary monotectic alloys.
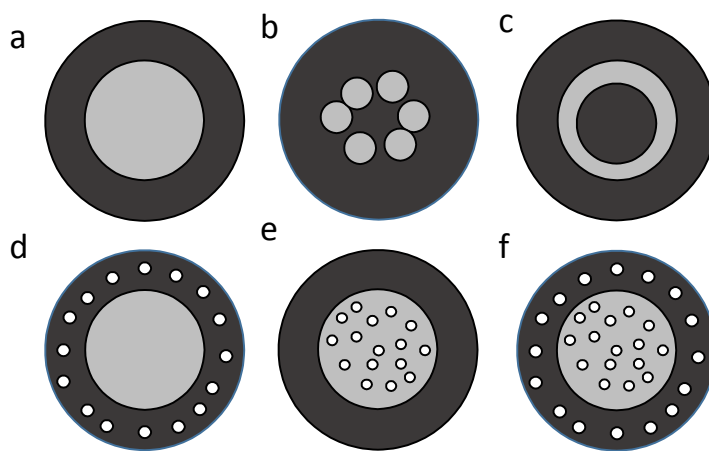
Figure 3.18 Different core shell structure configurations likely in a binary monotectic system, a – spherical core shell [112], b – core shell particle with multiple cores, c- multiple shell /matryoshka / onion like core shell particle [179], d – core shell particle with embedded multiple spherical particles in the shell, e – core shell particle with inclusions in the core and f – core shell particle with embedded multiple spherical particles in both the core and shell [127].

The strong interplay of interfacial energies and temperature and or composition gradient in micro- gravity environment leading to Marangoni motion has been used to explain the formation mechanism of core shell microstructures [103,111,112,127,177,180–184]. During free fall, a temperature gradient between the surface and centre of falling droplets may be developed. If the droplets are cooled into the miscibility gap, spherical particles of minor phase are said to be formed close to the surface of the falling parent droplets. The temperature gradient causes Marangoni motion to

occur leading to the migration of these minority phase particles to higher temperature zone within the parent droplets [177]. The migrating particles eventually coalesce by collision to form the core.

It is important to state that although Marangoni motion offers basic explanation for the formation of these structures, it does not fully account for the whole solidification features of metastable immiscible alloys. Possible contributions of other factors such as composition, cooling rates, degree of undercooling, collision and volume fraction of phases are still not fully explored [178].

Wang et al. [185] and Luo et al. [131] studied phase selection characteristics of core shell microstructures in two stable miscibility gap systems. Wang et al. [185] observed that in Fe - Sn and Cu - Pb alloys, the surface energy of the phases was crucial in determining which phase becomes the core and which becomes the shell and also whether a double or triple layer core shell structure is formed. They reasoned that the phase with the lower volume fraction forming the minority phase droplets also has the lower surface energy and as such spreads into the periphery of the parent droplet thus forming an outer shell. This is because at the early stage of nucleation of the droplets, the particles are too small for Marangoni to be effective hence they do not migrate to the centre. They were of the opinion that if the reverse were the case (minority phase having higher surface energy), the particles of the minority phase will fail to spread even though a thermal gradient exists and the resulting structure would not be a core shell structure but rather one in which these particles are randomly dispersed. Their argument most likely favours formation of a matryoshka type core shell structure since upon attaining a critical size the minority phase droplets are picked by Marangoni and then depleting the immediate surrounding liquid of this phase subsequently resulting in core shell setup where the core is the same phase as the outer most shell (figure 3.19a). The migration capability of particles was said to be dependent on the cooling rate and miscibility gap temperature interval. Luo

et al. [131] also in the Fe - Sn alloy reported multi layered core shell structures with 2, 3 and 5 layers (figures 3.19b, c and d). The authors went further to propose that nth layer core shell structures are possible however the actual mechanism for the formation of these structures are not clear from the write up, phase field simulation was however used to predict how the structures may have formed. However, the micrographs presented show that segregation was very active in the alloy (Fe − 50 at. % Sn) and the growth mechanism seems more likely due to collision as merging droplets are perfectly spherical (figure 3.19b, c and d). They also calculated that the Marangoni velocity was very high this probably increased the rate of movement of particles which in turn could explain the why the phases alternate.

However, in a metastable Cu - Fe based alloy system (Cu − Fe − Si - C) Wang and his co − workers maintained that even though the lower volume phase formed the core, there were instances where this was not the case [186]. Dai et al. [110,112] also reported that in Al - Bi alloy system, Al always formed the core even when Bi phase had the lower volume fraction (figure 3.20).

Additions to binary immiscible alloy systems have also been reported to have effect on volume fraction of phases present. The addition of Ni to the Co - Cu system was reported to significantly decrease the volume fraction of cobalt rich droplets [187], however, in Cu - Sn - Bi [184] the addition of the rare earth metal Ce was only stated to have had effect on Marangoni velocity and no link to the volume fraction.

Cooling rate has also been reported to have effect on Marangoni velocity [110,112] and core shell microstructures were said to be readily formed at high cooling rates in Al-Si-Zr alloys [188].
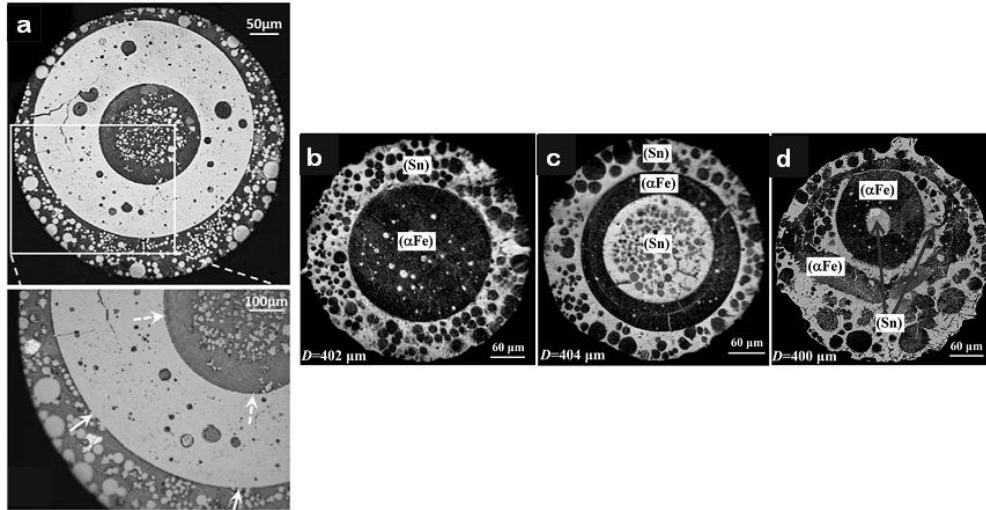
Figure 3.19 SEM images showing (a) core shell microstructure in Fe – 68 wt. % Sn alloy processed in a drop tube [127] and (b – d) double, triple and five layer core shell microstructure in drop tube processed Fe – 50 at. % Sn alloy [131].

N. Wang et al. and C.P Wang [127,186], Dai et al. [180], Ma et al. [111] and Li et al. [184] studied the effects of alloy composition on the formation of core shell microstructures. Wang et al. [127] in their 3 m drop tube experiment discovered that the migration period of the dispersed particles in monotectic alloys was composition dependent. In alloys near the critical composition and where the gap between the binode and the spinode is relatively small, spinodal decomposition occurs at less undercooling. The spinodal decomposition process is very fast and once the new phase attains a critical size it migrates to the centre if a temperature gradient exists. However, as the alloy composition departs from that of the critical composition, nucleation becomes more dominant obviously due to the higher undercooling needed to reach the spinodal region hence LPS occurs only in the binode. LPS via this route would normally need to overcome an energy barrier and also droplets of the new phase would need to attain a critical size in order to migrate. This would take some time to occur therefore the formation of core shell microstructures via this mechanism is likely not be completed before solidification. Hence alloys near the critical composition have a longer period for migration of

dispersed droplets and most likely to form stable core shell structures before solidification since they have enough time to coagulate. In comparison, alloys far from the critical composition are expected to have less stable core shell structures but more of structures en – route into forming stable core shell microstructure.

The migration period was also said to be dependent upon particle size, smaller droplets possessing higher cooling rate and therefore shorter migration periods hence core shell structures are not easily formed in them.

They also found that the composition affects the phase separation characteristics. As cooling occurred, marginal variation in composition also occurred which in turn altered the volume fraction of phases. This in turn led to changes in the viscosity (since different phases have different viscosities) and surface energies which are both crucial in determining the Marangoni velocity and ultimately the prospects of forming core shell structures is affected. They proposed that alloys towards the low melting point component, LMP, have larger Marangoni velocity and as such are able to form core shell structures than those on its left (where the higher melting point phase, HMP is). They cited that HMP alloys have higher thermal conductivities and as such the ratio λ_d / λ_m and viscosity is larger and the value of the denominator $(3\mu_d + 2\mu_m)$ used in calculating the Marangoni velocity is substantially increased. This results in smaller values of the Marangoni velocity and as such the dispersed droplets cannot aggregate to form the core.
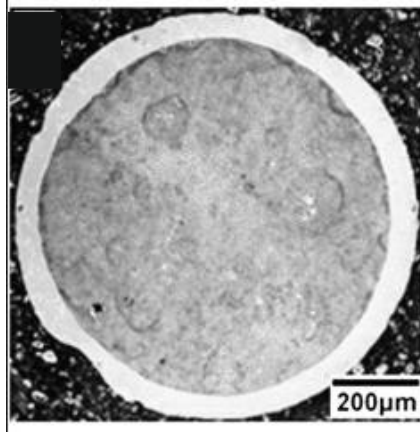
Figure 3.20 A stable core shell microstructure in the hyper monotectic Al – 65.5 wt. % Bi alloy [112].

Models have also been used by a number of researchers to simulate the formation of core shell microstructures [127,131,177,179,183,188–192]. Xu et al. [188] and Wang et al. [191] used mathematical models to calculate the formation of the shell in Al – Si - Zr and Al – Ti - B - Re grain refiner alloy respectively, both models were based on diffusion kinetics in the core shell structure but were dissimilar in that Wang et al. [191] assumed continuous diffusion in their model while Xu et al. made no such assumption and were able to link the formation rate of the shell to the cooling rate.

Phase field simulation had also been used to predict core shell microstructure formation [131,177,183,192]. In the work carried out by Shi et al. [177] on gas atomised Cu - Fe alloy, the inter dependency of factors affecting formation and characteristics of core shell microstructures were highlighted. A spherical core was said to be centrally located in the structure if spinodal decomposition occurred concurrently with fluid flow and Marangoni motion while an offset core was said to be a result of diffusion alone or phase separation with fluid flow. They predicted that the product of spinodal decomposition would be a bi – continuous structure similar to that obtained by Davidoff et al. [176] but proposes that it fragments into spherical particles

95

with time and if equal volume fraction of the phases are present, these would eventually converge at the right part of the parent droplet giving rise to a two phased structure different from a core shell microstructure (figure 3.21a). In the absence of equal volume fractions of the phases, the minority phase is predicted to always form the core Timing for the formation of core shell structures was also said to be influenced by the processes at play; phase separation coupled with Marangoni motion was said to have faster rate of coagulation. The phase field predictions of Luo et al. [131] for the formation of n – layer core shell structure is shown in figure 3.21b.

) $X_0=0.5$

(e) t = 3.6e-8s   (f) t=4.8e-8s   (g) t=4.44e-7s   (h) t=7.2e-6s

(a) initial state   (b) C_f=1000   (c) C_f=5   (d) C_f=0.05

a

(e) C_f=0.02   (f) C_f=0.012   (g) C_f=0.011   (h) C_f=0.01

b
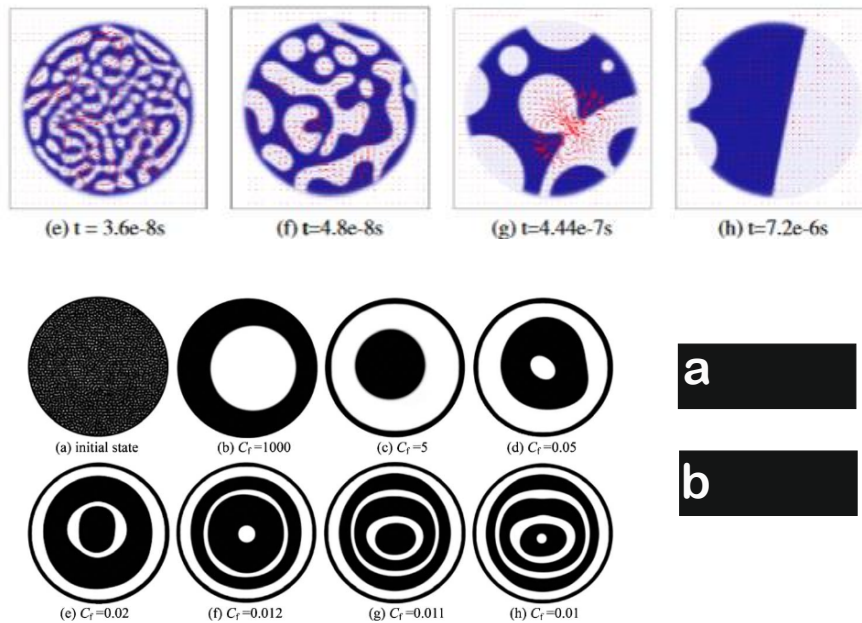
Figure 3.21 Phase field simulation by (a) Shi et al. detailing the evolution of a spinodally decomposed droplet [177] and (b) evolution of different layered core shell structures according to Luo et al. [131].

The scope of this research work is on the rapid solidification of metastable alloys. Desired phase separation patterns or microstructures are those with finely dispersed particles of one phase in the matrix of the other or core shell structures where one phase is enveloped by the other phase with distinct boundaries. Such microstructural configurations have been known to improve

96

the plastic deformation resistance of alloys since the dispersed phase acts as barriers to dislocation flow. There are no real evidence of core shell structures in Co - Cu alloy system as at the time of writing this report, these structures in principle could drastically improve the strength of the alloy. The evidence, solidification and formation of these structures in Co - Cu alloys is presented and discussed in detail later on.

4 Experimental techniques and methodology

It has already been established from the literature review that in order for liquid phase separation to occur in the Co – Cu alloys, they have to be undercooled into the miscibility gap region which lies below the liquidus. Containerless processing techniques have also been stated as most effective in achieving this undercooling status since it eliminates the effects of sites which could aid nucleation making undercooling of the liquid phase almost impossible.

This chapter covers the calculation of the miscibility gap region of the phase diagram, preparatory methods prior to undercooling in a 6.5m drop tube, a detailed description of the drop tube processing procedure and basics of post processing techniques used in characterising the specimens as well as the methodology employed.

4.1   Thermodynamic calculations

The limits of the metastable miscibility gap of the Co-Cu alloy was determined using thermodynamic calculations. The calculations were based on the regular solution model and the free energy (G) of the system was determined from the sum of the molar free energies of the elemental components in liquid state (G_L) (A= Co and B= Cu) after equation (2.18a), the molar Gibbs free energy of mixing using equation (2.24) and the excess Gibbs energy of mixing (using the Redlich – Kister model) i.e.

$$G = [X_A G_L^A + (1 - X_A)G_L^B] + \frac{RT}{v_m}[X_A \ln X_A + (1 - X_A)\ln(1 - X_A)] + G_L^{xs}$$

(4.1)

Free energy of elemental component A, G_L^A is given by the expression in equation (4.2) with similar expression for component B

$$G_L^A = a^A + b^A T + c^A T \ln T + d^A T^2 + e^A T^3 + f^A T^{-1} + g^A T^7 + h^A T^{-9}$$

(4.2)

Where T is absolute temperature and the coefficients of the powers of T, *a-h*, are extracted from the SGTE solution database.

Excess Gibbs energy of mixing is obtained after equation (2.25) using the expression below

$$G_L^{xs} = X_A(1 - X_A) \sum_{i=0}^{m}(a_i + b_i T)\left((1 - 2X_A)^i\right)$$

(4.3)

Where X is the mole fraction of component B, m is equal to 2 for the Co-Cu system and coefficients a_i and b_i are also extracted from SGTE solution database.

The free energy was then plotted against composition and the binodal limits determined by constructing a common tangent to the free energy curve with the linear component removed. Figure 4.1 shows an example calculated at 1500K with binodal limits at 30.5 at. % Co and 82.2 at. % Cu.

The second differential $d^2 G/dc^2$ was also determined to find the points of inflection which correspond to the composition limits of the spinodal. Again as an example at 1500K the calculated spinodal limits was 42.3 at. % Co and 73.3 at. % Cu. The critical point of the miscibility gap corresponds to where the plotted curve has only one point of inflection and this was found to be at 1623K and 58.7 at. % Co. The spinodal and binodal limits were calculated for different temperatures and then superimposed on the equilibrium phase diagram of the alloy to get the metastable phase diagram of the system.
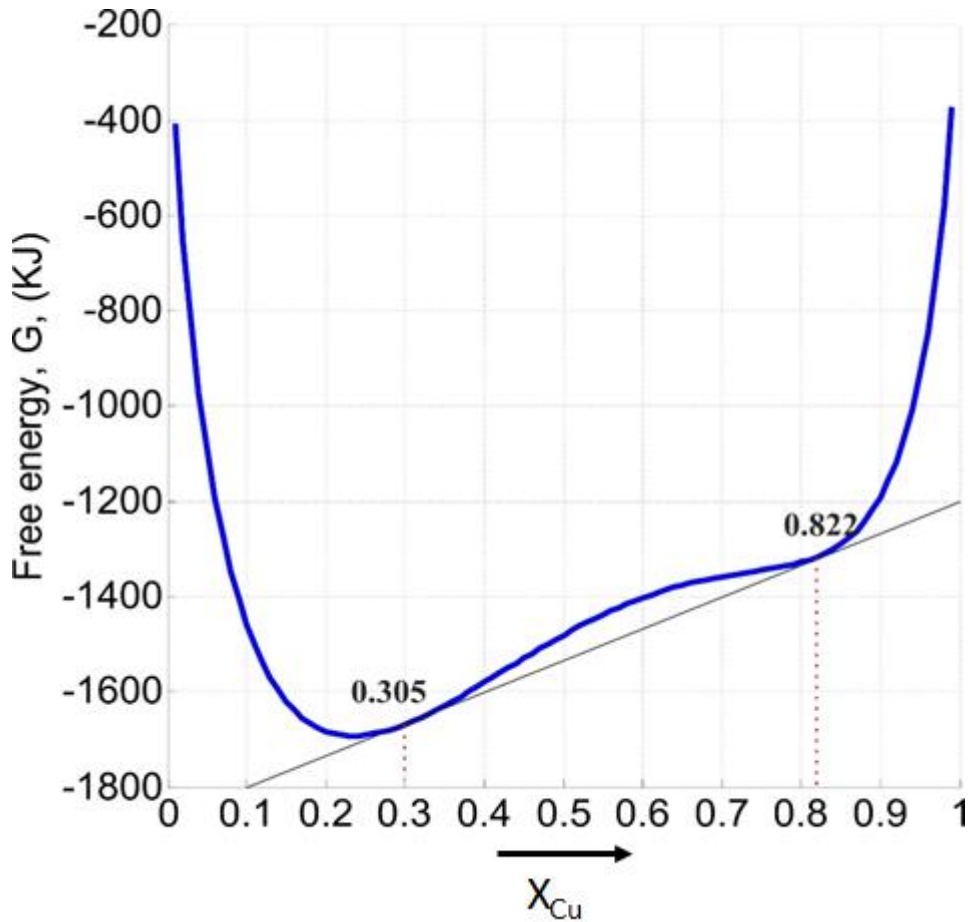
Figure 4.1 Free energy curve (without linear component) showing binodal limits at 1500 K.

4.2 Selection of alloys

Based on the calculated miscibility gap on the metastable phase diagram of the Co-Cu system, the alloys with 50 at. % Co and 68.5 at. % Co were selected for research. Even though the 50 at. % Co alloy has been extensively researched there has been little report of phase separation in the alloy but according to the calculations made in this research it should be able to phase separate both spinodally and by binodal phase separation after the critical alloy because of the minimal undercooling estimated to be required to get the alloy into the miscibility gap. The 68.5 at. % Co alloy on the other hand is the furthest from the critical composition on the cobalt rich side but still within

the limits of the miscibility gap regions. This alloy is also expected to show two separation mechanism i.e. spinodal and binodal phase separation.

4.3   Alloy production (arc melting)

The master alloys used to produce the drop tube samples were prepared at the University of Leeds from high purity solids of Alfa Aesar™ Cu (99.999%) and Co (99.99%) using IDEALARC™ R3R – 400 arc melter furnace operated at 225 Amps. The arc melt equipment consists of the furnace chamber (which is made up of a water cooled copper mould and tungsten electrode), vacuum pumps and power supply unit (figure 4.2a and b).

Solid chunks of Cu and Co were weighed using ADAM™ PW 124 analytical balance and were placed together in the small copper hearth. Weighted amounts of titanium which acts as oxygen scavenger was placed in a separate small hearth of the arc melter furnace. The furnace chamber was closed, evacuated and back filled with argon 5 times to reduce oxidation during the melt arc process. An arc was struck with the electrode on a tungsten striker stub and the titanium was melted first to reduce partial pressure of oxygen. After this, the samples were melted by moving the electrode tips over them uniformly. Care was taken not to touch the samples with the electrode tip while melting so as not to contaminate the melt. Melting time was 30 seconds after which the samples were allowed to cool for 10 minutes. After each melt process, the sample and the titanium getter were weighed.

After the first melt, the copper and cobalt were yet again placed together (copper below, cobalt on top) in the large copper hearth, the chamber was again evacuated and back filled with argon 5 times and then melted. The samples were flipped after each melting process so as to alternate the surface exposed to the water cooled hearth and arc. The melt process was repeated several times in order to have homogeneity of the specimen. Mass changes after each melt process were noted (table 4.1). The last melt process was done in the narrow through of the copper hearth to give the produced specimen a

cylindrical shape to make slicing easier later on. Slices from the produced ingots were subsequently used in producing the drop tube samples.

Table 4.1 Mass changes during arc melt process of two Co - Cu alloys.

Start/melt cycle	Mass change in 50 at. % Co alloy (mg)			Mass change in 68.5 at. % Co alloy (mg)		
	Co	Cu	Ti	Co	Cu	Ti
start	12.2659	15.4745	4.0711	17.0511	9.8934	5.9428
1	27.3551		4.0723	26.6385		5.9442
2	27.0359		4.0730	26.1427		5.9454
3	26.7258		4.0751	25.4861		5.9467
4	26.2217		4.0759	24.3656		5.9478
5	26.0183		4.0761	24.3910		5.9508
6	25.5856		4.0772			
7	25.3374		4.0778			
8	25.1068		4.0788			
9	24.9978		4.0796			
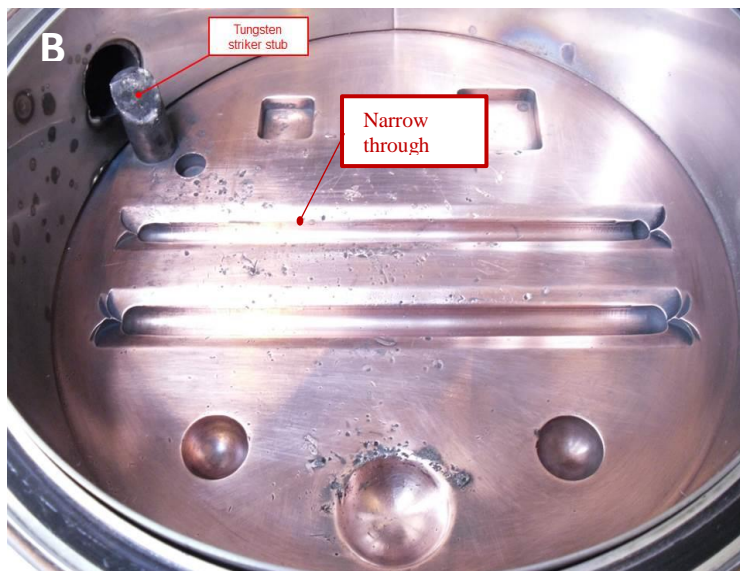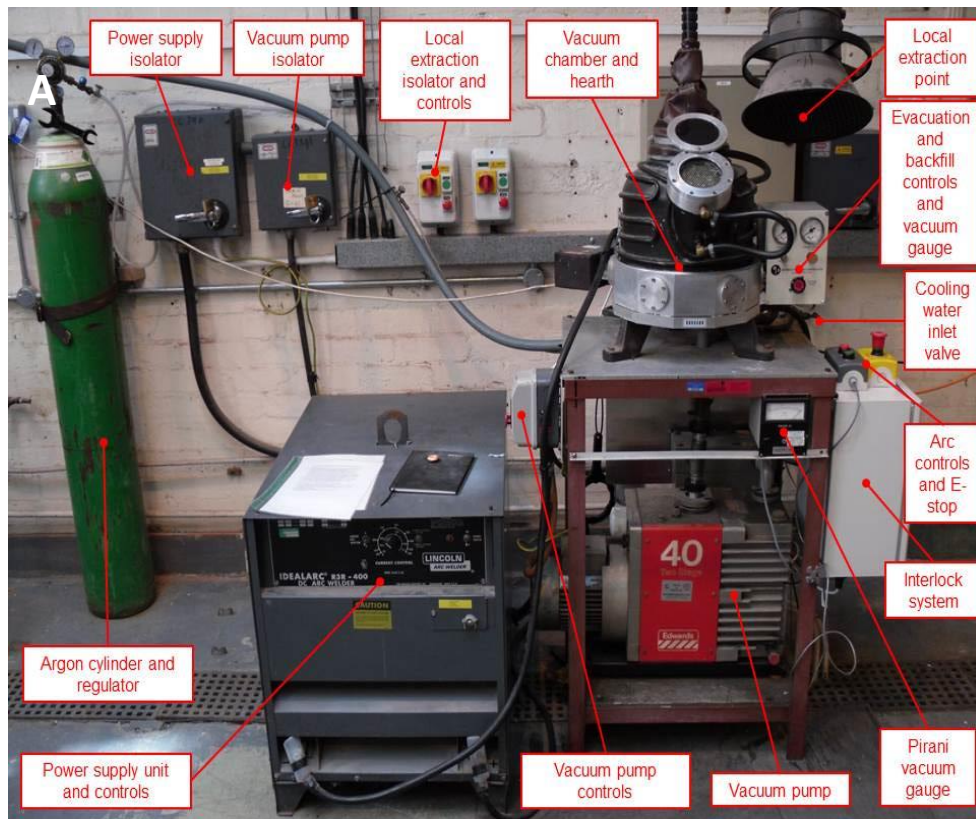
Figure 4.2 Arc melter furnace showing (a) arc melter furnace setup and (b) copper hearth with the cups and the narrow through.

4.4   Drop tube method of containerless processing

Containerless processing is effective in undercooling alloy melts below their equilibrium melting temperature. These methods eliminate the effect of contaminants that may be introduced by the container, making it possible to undercool alloy melts before solidification which would have been impossible due to container wall induced heterogeneous nucleation [23]. There are basically two techniques of containerless processing; (1) levitation in which the sample is suspended using non − contacting forces such as electric forces from an electromagnetic field or gas pressure and (2) free fall technique in which small droplets of the alloy melt falls without the use of any container down a tube that is usually evacuated and backfilled with gas [193].

DTP is employed in this research because it offers the unique advantage of a simulated space environment by combining rapid cooling with containerless state at low gravity [193].

DTP entails sub dividing the melt into fine droplets and allowing droplets to cool and solidify while falling freely down a tube within which there is a controlled atmosphere [24]. This subsequently ensures (1) high cooling rates and (2) less chances of nucleation in the small droplets. These two effects enhance the degree of undercooling.

There are basically two types of drop tubes reflecting the type of method of droplet production in them:

4.4.1   Long drop tube (in excess of 50 m high)

In long drop tubes unlike in the short ones, individual drops are processed [193]. It is used mainly to study microgravity effects on solidification in earthbound laboratories at relatively low costs by exploiting the fact that a falling body in vacuo has zero gravity. Pendant drop technique is used in melting single droplet (1 − 5mm diameter) which is then released into the evacuated drop tube. Si or InSb photodiodes along the length of the tube then monitors the droplet during free fall. In this way, recalescence is detected

[193]. Undercooling achieved at nucleation ΔT cannot be measured directly from this type of drop tube but can be inferred from a heat flow model using the time of flight of the droplet and initial droplet temperature [24].

4.1.2 Short drop tubes (less than 50 m high, usually in the range of 1.2 to 6.5 m)

These type of drop tubes are mainly used for statistical analysis of solidification behaviour of droplets in range of 0.1 to 1 mm diameter. Here, the melt is dispersed into many small droplets by forcing through a thin nozzle (Rayleigh instability of thin liquid jet) at the base of crucible used in melting using Argon (Ar), Helium (He) or Nitrogen (N_2) gas pressure [23]. The droplets subsequently cool, undercool and solidify during free fall in the tube under microgravity conditions. The free fall length of droplets is readily available here but the characteristics of the individual droplets during free fall are impossible to determine [193]. Nucleation temperature determination using this type of drop tube is almost impossible due to inability to detect recalescence [24].

Drop tubes are used to study evolution of grain refined microstructures, produce metallic glasses and metastable crystalline materials. The technique is also used to study the process of phase selection in immiscible alloys and owing to the fact that the droplet diameter scales with the cooling rate of the droplet during free fall down the tube, it is then possible to investigate temperature time transformation behaviour [193].

Determination of the cooling rate in short drop tubes can be made by taking a balance of the heat flux of individual free falling droplet i.e.

Heat balance of a falling droplet is

$$\Delta H + \Delta Q_{ENV} = 0 \tag{4.4}$$

If no first order phase transformation occurs the heat content of the droplet ΔH is given by [193] as

$$\Delta H = \rho_m C_{pm} V_D \delta T \tag{4.5}$$

Where ρ_m and C_{pm} is the density and specific heat capacity of the alloy melt, V_D is the volume of the droplet of diameter D $\left(\pi D^3 / 6\right)$ and δT is temperature difference. ΔQ_{ENV} is heat transfer to the environment.

Heat flow through the surface of the droplet $\dot{Q}$ with surface area $A_{surf} = \pi D^2$ is given by equations (4.6)

$$\dot{Q} = A_{surf} \left[h_d (T_D - T_R) + \varepsilon \sigma_{SB} (T_D^4 - T_R^4) \right] \tag{4.6}$$

Where h_d is heat transfer coefficient of the droplet falling through the gas used, T_D and T_R is droplet temperature during free fall and room/ ambient temperature respectively, ε is the total surface emissivity and σ_{SB} is the Stefan – Boltzmann's constant.

From the time of the formation of the droplet (t = 0) to time nucleation starts (t = t_n), heat transferred to the environment is given by

$$\Delta Q_{ENV} = \int_0^{t_n} \dot{Q} dt \tag{4.7}$$

But prior to crystallization, cooling rate $\dot{T} = - DT/dt$ $\qquad$ (4.8)

Substituting into equation (4.7) then gives

$$\Delta Q_{ENV} = \frac{1}{\dot{T}} \int_{T_0}^{T_n} \dot{Q} dT \tag{4.9}$$

Where $\dot{T}$ is the constant cooling rate of the droplet from initial temperature T_0 to temperature T_n.

An estimate of the cooling rate is then made by substituting equations (4.5) and (4.8) into (4.4) and the resulting differential equation governs heat transfer of a falling droplet [194].

$$\rho_m C_{pm} V_D \frac{dT}{dt} = - A_{surf} \left[h_d (T_D - T_R) + \varepsilon \sigma_{SB} (T_D^4 - T_R^4) \right] \tag{4.10}$$

Substituting equation (4.8) into (4.10) and re arranging gives an expression for the cooling rate as a function of droplet size.

$$\dot{T} = \frac{6}{\rho_m C_{pm} D} [h_d(T_D - T_R) + \varepsilon \sigma_{SB}(T_D^4 - T_R^4)]$$ (4.11)

The heat transfer coefficient for spheres falling through a gas can be deduced from the Nusselt number (N_u) [195]

$$h_d = \frac{N_u \lambda_{gas}}{D}$$ (4.12)

N_u is dimensionless and combines the characteristic properties of the environment gas by the expression

$$N_u = 2.0 + 0.6 R_e^{1/2} Pr^{1/3}$$ (4.13)

Where Reynolds number (R_e) = $\frac{U_{term} \rho_{gas} D}{v_{gas}}$ and Prandtl number (Pr) = $\frac{C_{pgas} v_{gas}}{\rho_{gas} \lambda_{gas}}$, properties of the gas used are v_{gas} is kinematic viscosity, λ_{gas} is thermal conductivity, ρ_{gas} is density, C_{pgas} is specific heat and U_{term} is the terminal velocity which is the differential velocity between the droplet particle and gas. For a spherical droplet in a drop tube, U_{term} is given by the expression:

$$U_{term} = \sqrt{\frac{4gD}{3C_d}\left(\frac{\rho_L - \rho_{gas}}{\rho_{gas}}\right)}$$ (4.14)

Where ρ_L is the density of the liquid melt, g is acceleration due to gravity and C_d is the coefficient of drag exerted on the falling droplet. C_d is dependent on the Reynolds number and is determined from Stokes' flow by the expression

$$C_d Re^2 = \frac{4mg}{\Pi \rho_{gas} v_{gas}^2}$$ (4.15)

The heat transfer coefficient is then determined using equations (4.16a) or (4.16b)

$$h_d = \frac{\lambda_{gas}}{D}\left(2 + 0.6\sqrt{Re}\sqrt[3]{Pr}\right)$$ (4.16a)

$$h_d = \frac{2.0\lambda_{gas}}{D} + \frac{0.6\lambda_{gas}}{\sqrt{D}} \left(\frac{U_{term}\rho_{gas}}{v_{gas}}\right)^{1/2} \left(\frac{C_{pgas}v_{gas}}{\lambda_{gas}}\right)^{1/3} \qquad (4.16b)$$

Short drop tubes (< 10 m) have very little drag force compared with gravitational force. At a falling distance of L = 6.5 m, final velocity of a droplet of 850 µm diameter is calculated to be 15.2 m/s dropping to 2.1 m/s for droplet of 38 µm diameter.

Slices from the ingots from the arc melt process were processed in a 6.5 m drop tube by placing the sample in a ceramic crucible with 3 laser drilled holes of about 0.3 mm each at its base. The crucible was then installed in a graphite susceptor encased in an aluminium shield (which prevents thermal radiation heat loss in the susceptor) surrounded by copper induction coils at the top of the drop tube. The drop tube was evacuated and backfilled with nitrogen gas thrice in order to purge the system prior to the melt process. Melting of the sample occurred by induction heating of the susceptor after the drop tube was evacuated and backfilled a final time with nitrogen gas at 40 kPa. The melt was superheated and a stream of nitrogen gas at 400 kPa was forced into the crucible causing the molten metal to be ejected through the crucible orifices. The ejected melt dispersed into drops of various sizes which rapidly solidified down the tube. The solidified droplets after being allowed to cool were collected at the bottom of the drop tube and sorted using different sized wire mesh sieves. The schematic diagram of the overall drop tube configuration used in this research is shown in figure 4.3.
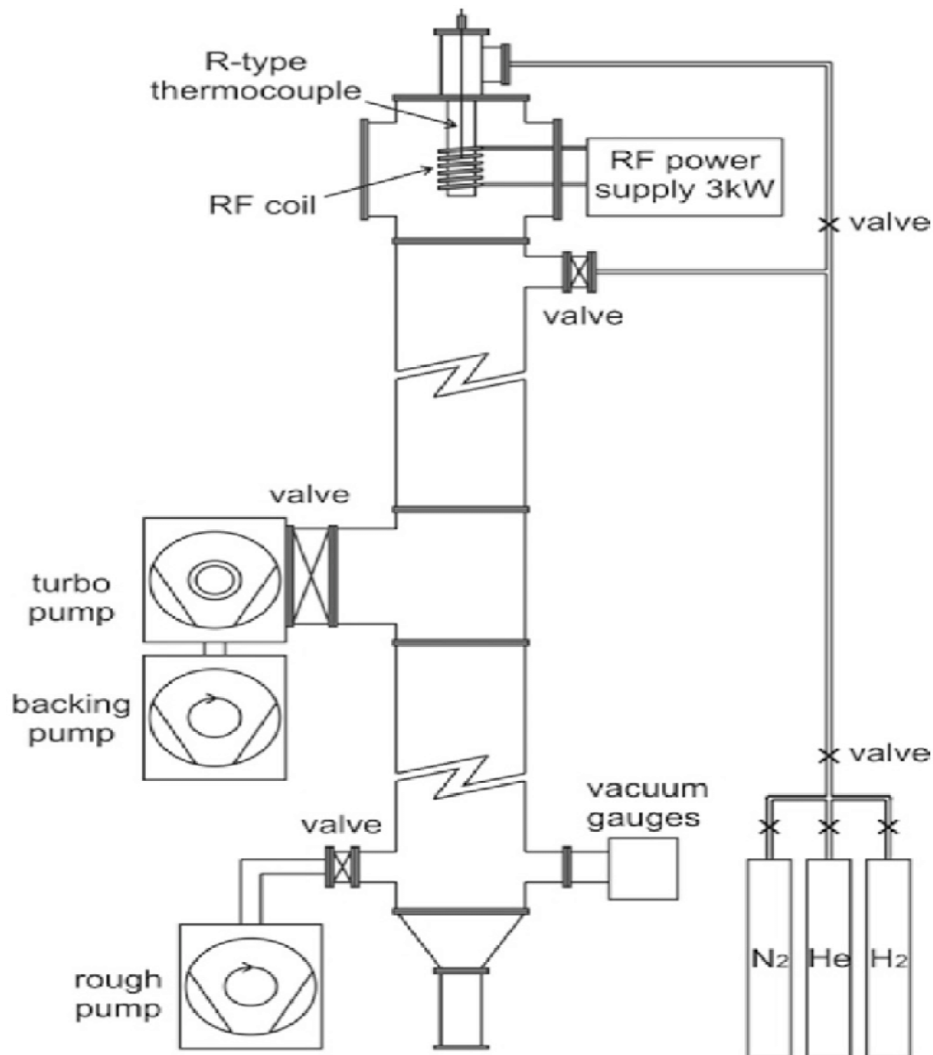
Figure 4.3 Schematic diagram of the 6.5 m drop tube utilised in this research.

4.5   Metallographic preparation and etching

The drop tube powders of the two alloy compositions were sorted into ten different sieve size fractions (850+, 850 – 500, 500 – 300, 300 – 212, 212 – 150, 150 – 106, 106 – 75, 75 – 53, 53 – 38 and < 38) µm. In order to carry out compositional and microstructural analysis on the different sized drop tube powders as well as the arc melt samples (for comparative study of rapid solidification effects), they were prepared for optical and scanning electron microscopy (SEM) using standard metallographic methods.

4.5.1 Mounting

Hot mounting was done using the Buehler SimpliMet ™ 1000 automatic mounting press (figure 4.4a). Transoptic resin was poured into the mounting cup of the press and then the drop tube powder was sprinkled onto the resin. The powder sank into the resin, the cylinder of the press was lowered and the piston applied. The resin melted and enveloped the powder when heat and pressure was applied.

4.5.2 Grinding and polishing

In the arc melt samples debris grounded off were constantly entrapped in pores which in turn made grinding and polishing difficult because the hard phase continually scratches the softer phase. After several attempts at grinding and polishing of this sample, the procedure in table 4.2 was found to produce good samples.

In the drop tube powders of the Cu - 50 at. % Co alloy, manual grinding with a Buehler MetaServ ™ grinder - polisher machine (figure 4.4b) using a P1200 SiC paper at 250 rpm was employed. This is due to the limited amount of powder of this composition available for analysis, care was taken not to lose the powder during the whole process. Total grinding time was one minute and the samples were constantly checked using a Nikon Optiphot optical microscope. After the droplets were exposed in the resin from the grinding process, the samples were polished on a Buehler Beta ™ grinder – polisher machine using progressively finer polishing clothes (6, 3, 1 and 0.25 µm) smeared with abrasive diamond particle pastes. At the end of each polishing stage steps a,c and d in table 4.2 were carried out.
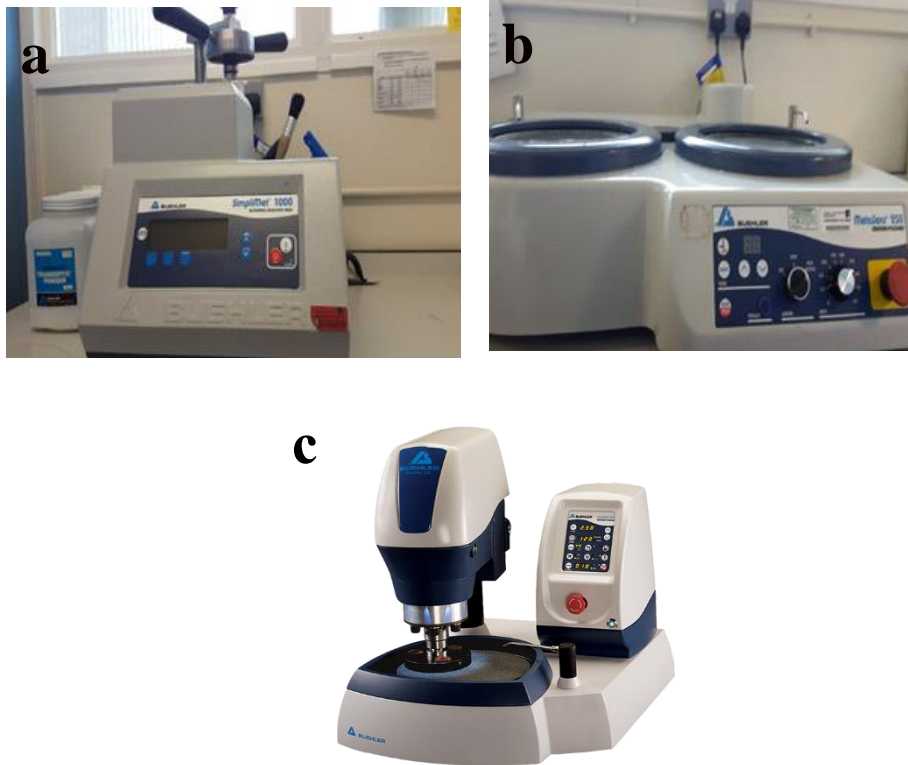
Figure 4.4 Equipment used for metallography preparation of samples, (a) compression mounting press, (b) grinding station, (c) semi – automatic grinder – polisher.

Checking under the optical microscope was important at the end of each grinding and polishing stage before deciding to proceed to the next stage or not to avoid over grinding and check for scratches. Non-alcoholic polishing lubricant was used for the polishing process; bubbles were noticed on the alloy surfaces when an alcoholic one was used.

Table 4.2 Preparation route for Co - Cu solid samples.

Grinding (at 450 rpm)	Polishing (at 450 rpm)	Cleaning steps
Grinding on P1200 for 15 seconds per section. Rotate 4 times (4 sections). Total grinding time 1 minute.		a) Clean with dilute soap and water. b) Put in ultrasonic cleaner for 5 minutes. Agitate tray every minute to dislodge trapped particles. c) Blast with water to dislodge any debris still left in pores. d) Spray with methanol to dry excess water, dab with tissue and dry under fan heater for 1 minute.
	6 micron cloth. Total time 6 minutes.	Repeat steps (a) – (d).
	3 micron cloth. Total time 5 minutes.	Repeat steps (a) – (d).
	1 micron cloth. Total time 3 minutes.	Repeat steps (a) – (d).
	¼ micron cloth. Total time 2 minutes.	Repeat steps (a) – (d).

The powders of the 68.5 at. % Co alloys were processed using semi-automatic machine (figure 4.4c). The samples were simply loaded onto the machine and the route that was finally adopted is listed in table 4.3.

Table 4.3 Preparation route for Co - Cu powder samples using automatic grinder – polisher.

Paper/ Cloth	Force (Newton)	Speed (RPM)	Direction on machine	Process time / Notes
P2500.	20	250	>>	Until exposed. Change paper after 1 minute of use.
6 µm Ultrapad.	25	150	><	5 minutes.
3 µm Trident.	25	150	>>	4 minutes.
0.06 µm colloidal silica (chemomet).	20	150	><	2 minutes. Flush pad with water the last 15 seconds of polishing.

4.5.3 Etching

Colour contrast was observed between the phases in the alloy samples (figure 4.5a) (lighter and darker phase) but in order to identify and analyse the microstructural features present, better image contrasting was required.

After good polishing quality had been confirmed in the samples, etching was done in order to have better contrast in the microstructure. A selection of etchants were considered and the most suitable one was selected.

Ferric chloride was found to have aggressive effect on the alloys with the lighter phase observed to have been completely eroded to the extent that the outline of the unetched phase was completely visible (figure 4.5b). In samples etched with ammonium persulphate grain contrast etching was observed in the region containing only the darker phase. Faceting which is etchant attack on differently oriented grains causing grain contrast etching usually occurs due to the variation of the dissolution rate of differently oriented grains. This causes light reflection to produce the observed grey level contrast (figure 4.5c). Nital solution (2% nitric acid, 98% propan – 2- ol) was observed to

cause a colour change of the darker phase from grey to black when viewed under the optical microscope as seen in figure 4.5d (comparing the unetched micrograph in figure 4.5a to natal etched one in figure 4.5d). It had a preferential dissolution effect on the darker phase and was found most suitable and adopted. The samples were submerged in the solution for 10 seconds (smaller particles, diameter < 75 µm) and 20 seconds (larger particles, diameter > 150 µm). The etching time for the samples polished with colloidal silica was however slightly less because it was observed to have a slight topographic effect on the alloys. They were all etched for 7 seconds. Table 4.4 shows the composition of the various etchants. All polished and etched samples were subsequently examined using optical (OM) and electron (SEM) microscopes.

Table 4.4 Etchant composition and techniques.

Etchant name	Etchant composition	Technique
Nital.	2% Nitric acid, 98% Propan-2-ol.	Submerged.
Ammonium persulphate $(NH_4)_2SO_2O_8$	10g of salt in 100ml of warm water.	Submerged and swabbed.
Ferric Chloride ($FeCl_3$).	5g $FeCl_3$, 100ml ethanol and 10ml HCl.	Submerged.
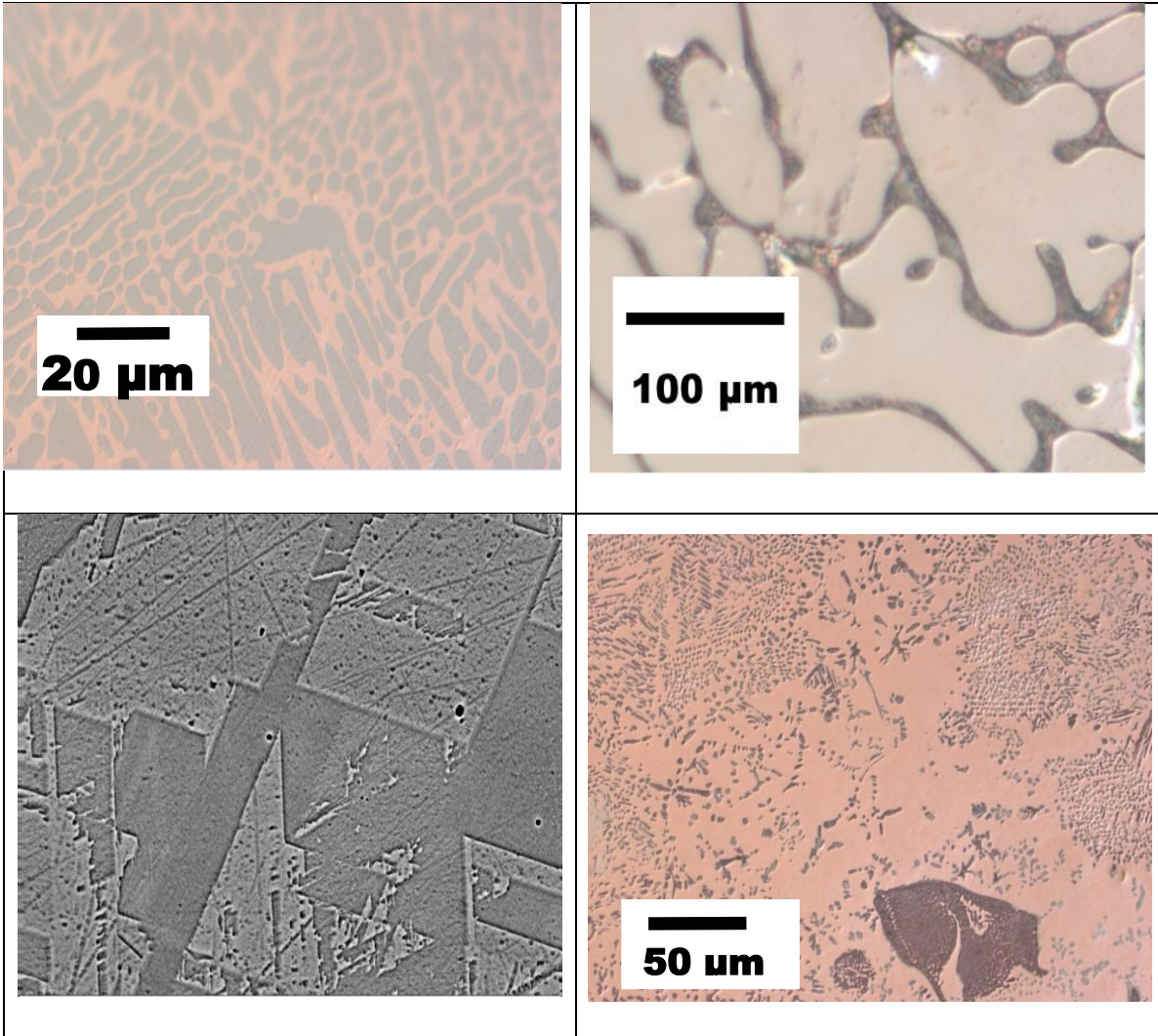
Figure 4.5 Micrographs showing effects of different etchants on arc melted samples of Co – Cu alloys: (a) is OM image of unetched sample, (b) OM image of sample etched in ferric chloride, (c) SEM image of sample etched in ammonium persulphate (this was not visible under OM) and (d) OM image of sample etched in natal solution.

4.6   Characterisation

4.6.1   Microscopy

4.6.1.1 Optical microscopy (OM)

Optical microscopy uses light and a combination of lenses in establishing an interaction with the specimen being examined and the eye – brain coordination of the microscope user [196]. Figure 4.6 shows a typical compound optical microscope with its various components labelled. Basically, the specimen is mounted on the specimen stage (which controls the coordinates of the area under observation) after which it is illuminated by the illuminating system made up of the light source and condenser lenses. The condenser aperture controls the amount of light allowed into the microscope. Light from the specimen is then reflected into the objective lens which magnifies the real image of the specimen while the ocular lenses (eye piece) made up of the field lens and eye lens further magnifies the image by the objective [197]. Lens magnification, M, is given by

$$M = \frac{u}{v} = \frac{v}{f} - 1 \tag{4.17}$$

Where f is the focal length of the lens $\left(\frac{1}{f} = \frac{1}{u} + \frac{1}{v}\right)$ and u and v represents the object and image distance respectively [198]. Magnification depends on the focal length of the lenses [197] and would normally be specified on the various lens mount on the microscope.

In order to get optimum imaging quality from the OM, adequate resolution (ability of the microscope to see minute details) of the desired details by the lens system of the microscope is necessary. Resolution is the minimum distance between two points on a specimen at which they are identified as being separate. It is not dependent on the magnification of the image as empty magnification occurs when an image is magnified to the extent that further resolution is no longer visible. The resolving power, r, of the optical microscope is given by

$$r = \frac{1.22\lambda}{NA_{\text{obj}} + NA_{\text{cond}}} \qquad\qquad (4.18)$$

Where λ is the wavelength of the illuminating light and NA_{obj} and NA_{cond} represents the numerical aperture of the objective and condenser lens respectively. Numerical aperture describes the quality of lenses and would normally be stated on the barrel of the objective lens. It follows from equation (4.18) that the shorter the wavelength, the better the ability of the microscope to resolve finer details.

Image quality is also greatly affected by the depth of field. The depth of field describes the range of distance a specimen can move and its image is still in acceptable focus. It can be defined as the difference between the distance of the nearest object focus plane and the farthest focus plane. Areas within the depth of field appears sharp while areas beyond it appears out of focus (blurry) (figure 4.7). The depth of field is dependent on the resolution of the microscope. Closely related to the depth of field is the range of acceptable focus of a specimen's image (depth of focus). The depth of focus however, unlike the depth of field is dependent on the magnification.

Individual features of the specimen are distinguished from its surrounding background through image contrast. It is the ratio of the light intensity of the image and adjacent background to the overall background. Contrast is not an intrinsic specimen property but rather a consequence of interaction with light. This interaction with light subsequently results in colour and / or intensity differences.

It is essential to manipulate the optical microscope in order to get the best image quality. For instance, higher magnification will cause low depth of field and higher depth of focus. Higher resolution also causes shorter depth of field and the more the need for contrast enhancing.
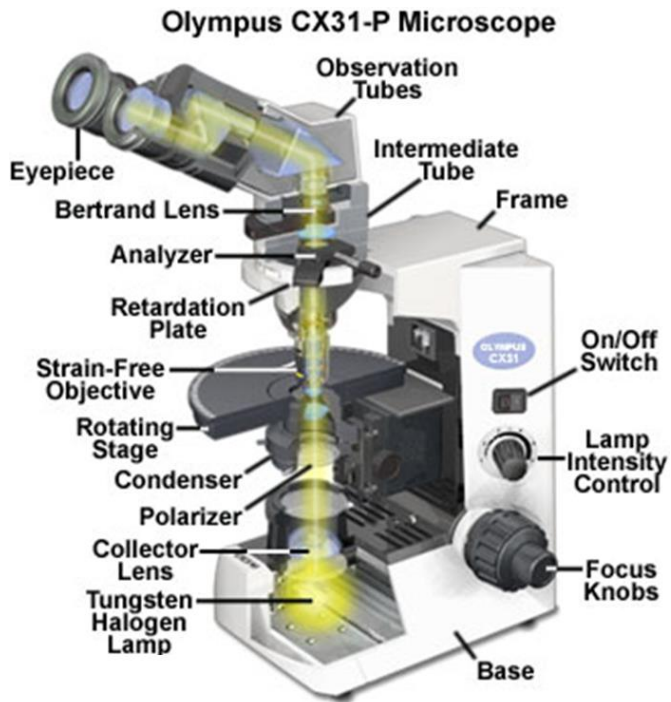
Figure 4.6 Diagram of an optical microscope (sourced from Olympus microscopes www.olympusmicro.com).
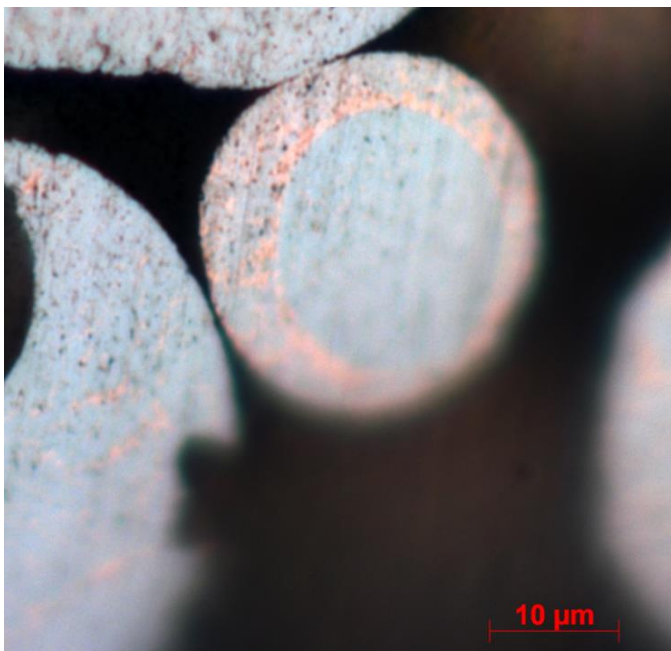
Figure 4.7 OM micrograph showing out of focus core shell microstructure in Cu – 68.5 at. % Co alloy.

Two optical microscopes are utilised in the course of this research. One was a Nikon Optiphot microscope used for checking the grinding and polishing quality. The second one used was a BX51 Olympus optical microscope fitted with a Zeiss AxioCam™ MRc5 camera for imaging.

4.6.1.2 Scanning electron microscopy (SEM)

In scanning electron microscopy, imaging is obtained by scanning focussed beam of electrons across the sample surface in a line along the $x - axis$. At the end of each line the beam returns to the position at $x = 0$ and the y coordinate is increased by Δy [196]. As a result of the impingement of the focused beam, electrons are scattered/ deflected in the sample. Scattering of electrons by gases is much stronger than by light hence the SEM chamber operates under vacuum. The effective diameter of the beam in the sample is larger than that of the incident beam, this is known as the interactive volume (figure 4.8). The size and shape of this interactive volume varies with the energy of the primary electrons and on the elemental composition of the specimen.
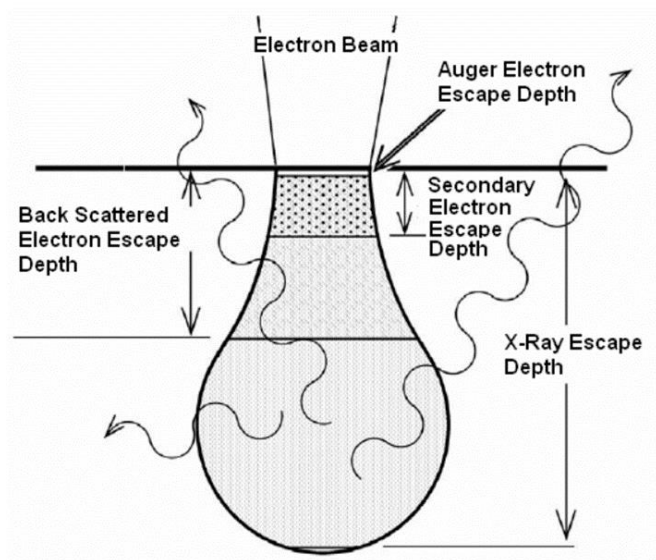
Figure 4.8 Interactive volume of different signals from the interaction of an electron beam with a sample.

The interaction of the electron beam with the sample results in (1) inelastic scattering which occurs as a result of the interaction of the electrons primary beam with the atom of the specimen. This results in the knocking off of electrons (secondary electrons, SE) from close to the surface of the sample (say an escape depth of about 5 nm). (2) Elastic scattering which is as a result of interaction of electrons of the primary beam with the nucleus of the atom of the specimen. This causes a reverse in the direction of the electrons of the incident beam. If the resulting scattered electrons are deflected out of the sample, back scattered electrons (BSE) are generated at escape depth of about 0.5 μm and as such information about the bulk properties of the sample are revealed. The tendency for back scattering increases with atomic number. (3) X–rays are also generated as Bremsstrahlung x–rays which are continuous x–ray spectrum generated due to loss of energy of the incident beam as a result of interaction with loosely bound electrons. Characteristic x–rays are also generated as a result of excitation of inner shell electrons of the sample by the incident beam (figure 4.9).
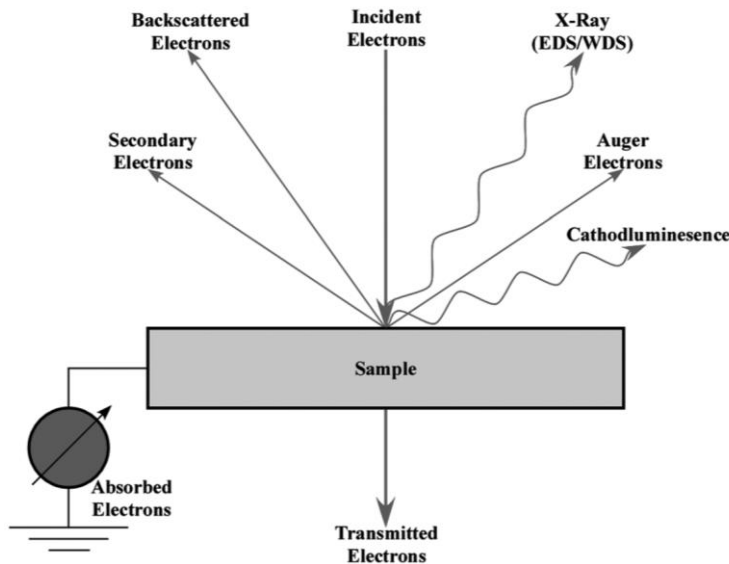
Figure 4.9 Beam interaction showing some signals used in SEM [196].

The SEM is fitted with detectors to detect SE, BSE and characteristic x − rays (EDX).

Secondary electrons can also be generated by back scattered electrons (as illustrated in figure 4.10). Secondary electrons generated this way have larger interaction volume and resolution compared with those excited by the primary beam. Generally, the resolving power of the SEM is orders of magnitude better than the optical microscope due to the fact that wavelength of the probe electrons is smaller. Compared to optical microscope limit of resolution for OM is 150 nm (green light $\lambda = 400$ nm) while 20 kV electrons can achieve a resolution of about 50 nm ($\lambda = 0.0037$ nm).

Backscattered Electron
BSE
SE_{II}
B
Beam Electron
SE_I
5λ
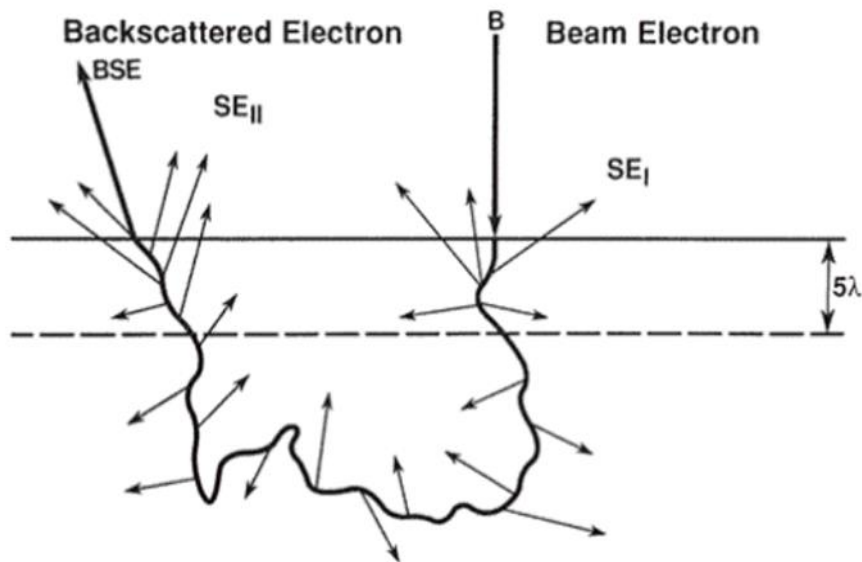
Figure 4.10 Diagram showing 2 modes of generating secondary electrons as a result of beam interaction with a sample (sourced from http://slideplayer.com/slide/5317298/).

The SEM unlike the optical microscope has capabilities for energy dispersive x–ray spectroscopy (EDX) which is a technique for determining chemical composition of a sample using information from the generated characteristic x–rays. Vacancy generated by excited inner shell electrons is filled by higher energy outer shell electrons. The difference in energy between these shells result in the characteristic x–rays. An energy dispersive detector then

measures the spectrum of the photon intensity which are atomic number specific therefore making it possible to determine the elemental composition of the specimen or excited region [196].

In preparing the polished and etched samples for SEM, they were first cleaned by submerging them in an ultrasonic bath of methanol for 2 minutes and subsequently drying them under a fan heater. SEM stubs were attached to them and they were coated with carbon paint in order to make the resin conductive taking care to avoid the powders. The powder samples themselves were made conductive by coating with vacuum evaporated carbon fibres (~ 10 nm) using Emscope TB500™ carbon coater machine. A Carl Zeiss Evo MA15 tungsten system scanning electron microscope in SE and BSE modes was then subsequently used in examining the alloys at a working distance of 8.5 mm and accelerating voltage of 20 kV. Elemental analysis of the observed regions in the alloy was done using energy dispersive x-ray (EDX) by focussing beam of electrons over the samples to get point chemical analysis. The line intensities in the x-ray spectrum emitted upon bombardment with the electron beam is measured for each element in the sample.

4.6.1.3 Quantitative metallography

Quantitative analysis of the microscope images were carried out using the image processing software ImageJ. Volume fraction V_f of phases present in the droplets, particles distribution λ_p as well as secondary dendrite arm spacing (SDAS) were calculated.

The volume fraction of the phase of interest is determined using

$$Vf = \frac{V_i}{V_T} = \frac{A_i}{A_T} = \frac{d}{D} \tag{4.19}$$

Where V_i, V_T, are the volume fractions of phase, i, and total volume fraction, A_i, A_T represents the area of phase i and total area while d and D is the

diameter of the region of phase of interest and total diameter of the droplet respectively.

But in calculating the core shell volume fraction, bias in measurement of the diameters arise due to sectioning effects as sections off the equatorial axis will give over / under estimated values. This error is particularly larger in the core as illustrated in figure 4.11a. In order to correct this, a statistical programme based on Monte Carlo technique which subjects the droplet to random sectioning and takes measurement of the diameter from random distances from the sectioning plane was adopted.

In figure 4.11b, a true shell volume fraction f_{sh} on sectioning through the equatorial axis is first randomly selected within the interval a $= \frac{2}{(1 + \sqrt{2})}$ and b $= \frac{2\sqrt{2}}{(1 + \sqrt{2})}$ (based on the knowledge that sieves vary by a factor of $\sqrt{2}$ between adjacent sizes). A sectioning height h is then set which determines distance from the equatorial axis. A large number of trials is then performed (in this case 500) in which the droplet is sectioned at random heights above the equatorial line. The shell volume F_{sh} is then estimated. If h = 0, all sectioning occurs at the equatorial plane and the input value of f_{sh} is returned for all volume fractions, if $h > 0$, $F_{sh} > f_{sh}$. The mean measurement was then determined for increasing sample size which also correlates to cooling rate.

The distribution of dendrites and secondary dendrite arm spacing were estimated using equations (4.20) and (4.21) respectively

$$\lambda_p = \frac{1 - V_{particles}}{N_{particles}} \qquad (4.20)$$

$$SDAS = \frac{L}{n} \qquad (4.21)$$

Where L, is the length of dendrite spline, n, is the number of side arms, $V_{particles}$ is the volume fraction of particles and $N_{particles}$ is the number of particles interception per unit length of region of interest.
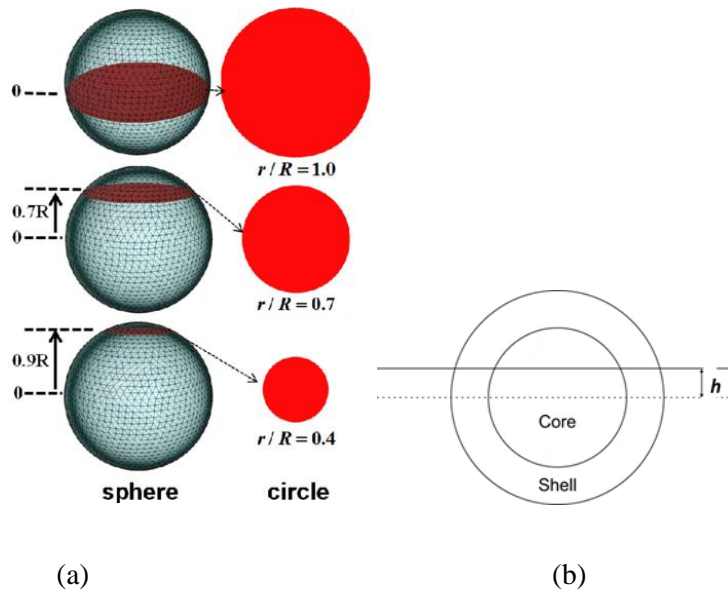
Figure 4.11 Sectioning effects on (a) core diameter [199]and (b) shell volume faction.

4.6.2 X- ray diffraction (XRD)

X-ray diffraction, XRD, is an analytical technique in which x - rays produced by electrons in an x – ray tube are used to study the internal structures of specimen.

Characteristic x-rays are generated when energised electrons create vacancies in the inner shells of the target atom, which is subsequently filled by electrons from higher energy outer shells. The energy difference between the shells in play determines the characteristic wavelength [200]. This manifest as distinct peaks of different intensities against the continuous spectrum [201].

The intensity of total x-rays emitted across the continuous spectrum ($I_{cont.\ spect}$) is proportional to the applied voltage (V) and atomic number (Z) of the target metal [202];

$$I_{cont.\ spect} = AZV^2 \tag{4.22}$$

A is the proportionality constant. Efficiency of getting x-ray therefore depends on the target material and increases as atomic number of the target and applied voltage increases.

124

The characteristic x-rays are classified as lines of increasing wavelengths, K line when vacancy was in the K shell (innermost shell closet to the nucleus) which is filled by either L or M shell. In x-ray diffraction, only the K lines are used since its wavelength is within the range mostly used for diffraction (0.5 – 2.5 Å). K also has different lines but the three strongest are mostly used in diffraction studies i.e. α1, α2 and β. Kα1 intensity is twice as strong as Kα2 and six times that of Kβ. Kα1 and Kα2 are usually so close that they do not show as separate lines and in instances where they do, they are referred to as the Kα doublet.
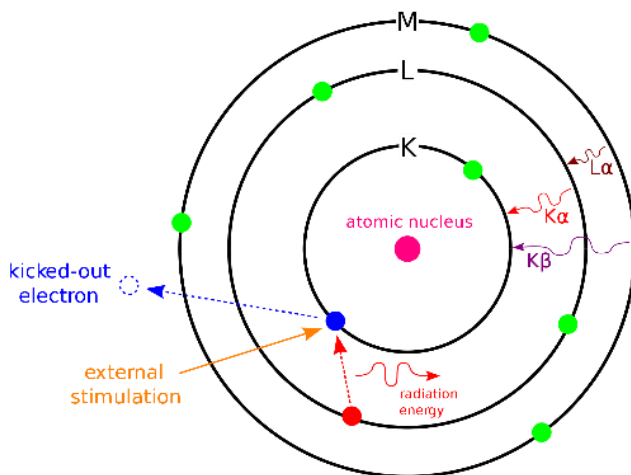
Figure 4.12 Schematic diagram of electronic transitions in an atom showing x-ray emissions (sourced from https://commons.wikimedia.org/wiki/File:EDX-scheme.svg).

Diffraction occurs when wave motion encounters evenly spaced scattering objects, the wavelength of the wave motion and the distances between the scattering points being of same magnitude [202]. This phenomenon was first observed in light and is the principle upon which Max Laue based diffraction of x - ray by crystals size, crystals contain regularly arranged lattice points which acts as scattering centres. His work was further simplified by the Braggs who proposed that for diffraction to occur, the condition expressed by the Bragg's law must be satisfied:

$$n\lambda = 2d \sin \theta \qquad (4.23)$$

λ is the wavelength of the diffracted beam, d is the spacing of the planes of atoms and θ is the incidence beam angle. The angle between the incident beam and the diffracted beam is 2θ. Diffraction is therefore a scattering event and a diffracted beam is one made up of various scattered rays reinforcing one another [202].

There are basically three methods of carrying out diffraction analysis; (1) Laue method in which the angle of scattering is fixed and wavelength of radiation varied. This method is specifically useful for studying crystal orientation and quality. (2) Rotating crystal method in which beam of fixed wavelength and variable scattering angles are employed. Mostly used for detecting unknown crystal structure. (3) The most common method which is employed in this study is the powder method and is useful for phase identification and lattice parameter determination. In this method, the scattering angles are also varied. Powdered form of specimen is placed in a beam of monochromatic x-ray and due to the random orientation of the crystals of the fine powder, every set of lattice plane is capable of diffraction.

XRD analysis was done to determine the phase and phase fractions in the drop tube processed monotectic alloys. Also quantitative study of the lattice parameter variation as composition and cooling rate of the specimen varied was carried out. A Bruker D8 Advance Diffractometer with Cu Kα radiation of wavelength 1.5408 Å at 40kV was used to carry out the diffraction analysis.

Three forms of the alloys were analysed:

1. Arc melt ingots used to produce the drop tube powders.
2. Loose drop tube powders.
3. Drop tube powders mounted in transoptic resin, metallographic prepared by grinding and polishing to expose the cross section of the droplets.

The total number of samples per alloy form is listed in table 4.5.

Table 4.5 Number of each alloy set analysed by XRD.

Alloy form	Total samples Cu – 50 at. % Co alloy	Total samples of Cu – 68.5 at. % Co alloy
1	1	1
2	5	5
3	5	5
Total number of samples examined	22	

The spherical nature of the drop tube powders and low quantity available made it challenging in collecting their diffraction patterns and coupled with the demand on equipment, a number of options were tried before settling for method that worked best for each set of samples.

Series of quick scans and different sample holders were tried and a scan range of 2θ from 40° to 80°, step size 0.025 degree for 120 minutes was adopted for all samples.
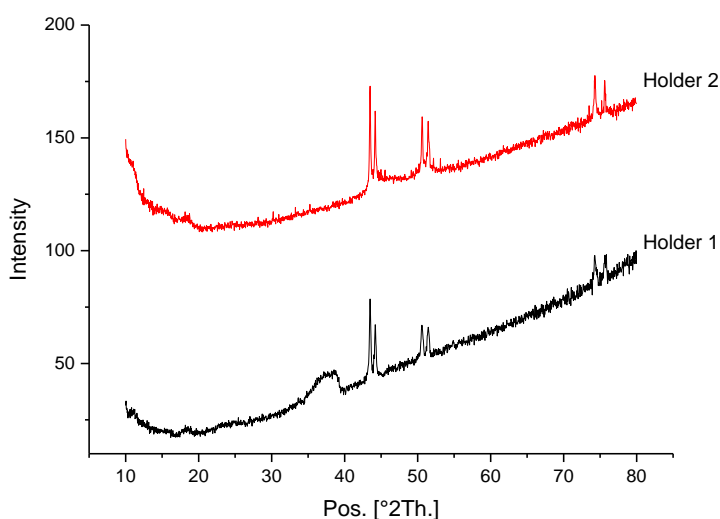
Figure 4.13 Sample holder effects on 500-300 micron drop tube powders.
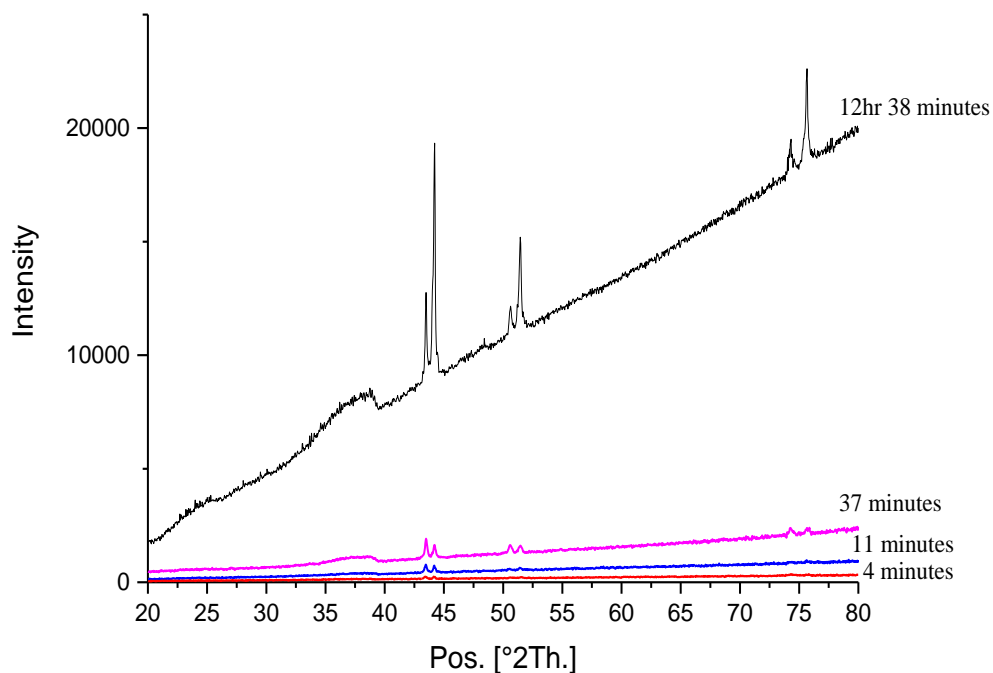
Figure 4.14 Scan time and rate effect on 500-300 micron drop tube powders.

Figure 4.15 Adopted sample set up for mounting the drop tube powders in the diffractometer. The single crystal silicon holder was mounted on plasticine so that the XRD pattern could be recorded without extra X-ray intensity attributed to the sample holder. The sample could then be placed on the stage at the correct vertical height in order to satisfy the Bragg condition, making it possible to obtain maximum diffraction intensity from very small amounts of powders.

The powders mounted in resin were simply put in a holder and mounted on the instrument stage. The powders were mounted in the middle of the resin and in instances where this was not so, the resin block was manipulated to get the colony of powders in focus as much as possible to the beam.

Figure 4.16 Holder cup used for the polished powders mounted in transoptic resin.

In order to maximise intensity of diffracted peaks, a divergence slit of 1 mm was deemed adequate and was used for all scans. A 0.5 mm slit was tried but the signal to noise ratio was not high enough.

The diffracted peaks were indexed by assigning Miller indices to each peak and identified by comparing with JCPDS files in X'Pert Highscore software after which the (. raw) files were all converted to DAT file extension and quantitative analysis carried out using the Rietveld analysis software, General Structure Analysis System, GSAS [203] with its graphical user interface package EXPGUI. The parameters refined in the Rietveld analysis included the global parameters 2θ zero, peak profile parameters, and 20 background parameters in a shifted Chebyschey model. Phase specific parameters that were refined include the scale factor, lattice parameter, and the isotropic displacement parameters. All profile parameters were constrained between the two phases and refined at the same time. The space group and atomic

positions of the two identified phases in the drop tube powders were obtained from crystallography.net. The least squares method was used to check the fit of all refinements

$$R= \frac{\sum[W| I_o - I_c|]_p}{\sum[WI_o]_p} \qquad (4.24)$$

Here p is the individual experimental points, I_o observed intensity, I_c is calculated intensity and W is the statistical weight [204].

Quantitative phase analysis was done using the Hill and Howard method [204] expressed by the relation

$$X_p = \frac{S_p (ZMV)_P}{\sum_i^n S_i (ZMV)_i} \qquad (4.25)$$

X_p is the relative weight fraction of phases p in a mixture of n phases, S_p is the Rietveld scale factor of phase p, Z is the number of formula units per cell and M is mass of the formula units (atomic mass unit) and V is the unit cell volume in $Å^3$.

Estimates of the composition of the alloys was subsequently determined from the phase fractions, lattice parameter was estimated for the alloy using Vegard rule which relates composition of a binary alloy to its lattice parameter gotten from the diffraction study and is given by the simple mathematical expression

$$a_{ab} = a_a^o (1 - X_b) + a_b^o (X_b) \qquad (4.26)$$

Where a_{ab} is the lattice parameter of the binary alloy of components *a* and *b*, a^o_a and a^o_b are the lattice parameters of the pure components of the alloy and X_b is the mole fraction of component b.

4.6.3   Differential thermal analysis (DTA)

Differential thermal analysis (DTA) is a method of thermal analysis in which temperature difference between a sample and a reference is measured. The sample and reference is subjected to heating or cooling at the same rate and the temperature difference as a result of changes in the sample relative to the reference is recorded. The sample and reference are both connected to

thermocouples and are simultaneously subjected to the same condition in the furnace having a linear temperature increase. Voltage difference between the thermocouples is correlated to temperature differences between the sample and reference. As long as no heat is absorbed or evolved, temperature differences between the sample T_S and reference T_{REF} is $\Delta T = 0$.

As a result of physical, structural, chemical or microstructural changes which may occur in the sample as the heating or cooling process happens, heat interaction between sample and reference occurs. If there is heat absorption, there is endothermic reaction in the sample and the temperature of the sample lags behind that of the reference ($T_S < T_{REF}$) and the differential temperature $\Delta T = T_S - T_{REF}$ is negative. In an exothermic reaction, the sample temperature exceeds that of the reference and the temperature difference $\Delta T = T_S - T_{REF}$ is positive.

The result of the DTA is displayed as a plot of the differential temperature ΔT against temperature or time. An endothermic event displays as a minimum on the curve while an exothermic event is observed as a maximum on the DTA curve.
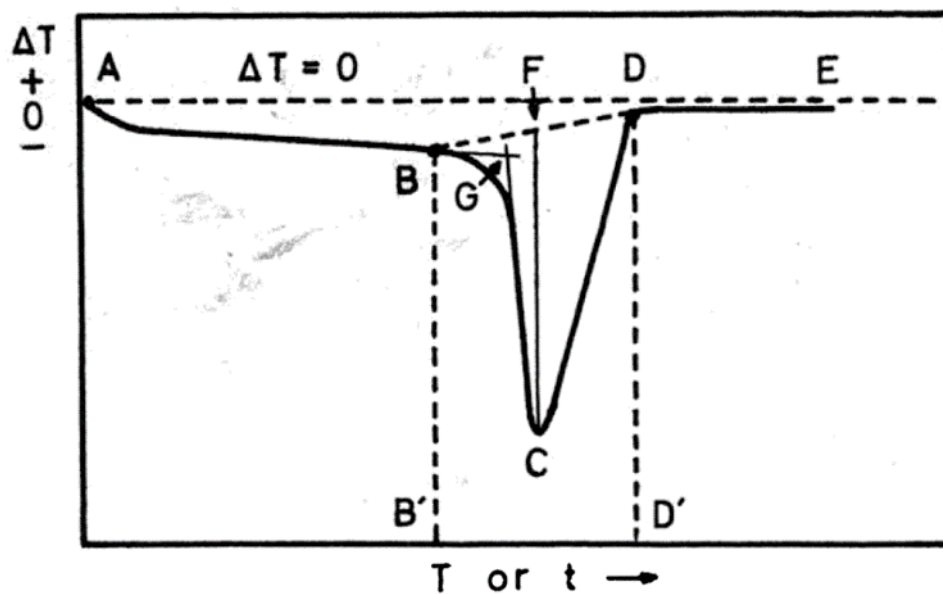
Figure 4.17 Typical DTA curve [205].

A simple DTA curve is shown above in figure 4.17. AB, DE is the baseline of the DTA curve at which ΔT is zero, BCD is the peak it departs and returns to the baseline, BCDB is the peak area surrounded by the peak and baseline, CF is the peak height and is the vertical distance to the abscissa between the baseline and peak tip, B'D' is the peak width and is the points of departure and return to the baseline on the abscissa, G is the onset and is the extrapolated point of intersection of tangent at point where peak is steepest (BC) with the baseline.

The peak area *Ap* as far back as 1930 has been shown to be related to the enthalpy change ΔH of the reaction that caused the thermal event [114,206–208].

$$\Delta H = \alpha A_p = \alpha \int \Delta T \, dt \qquad (4.27)$$

α is the proportionality constant and is related to the thermal property of the sample and is temperature dependent.

Due to the non-identical thermal conductivity and heat capacity of the sample being studied and reference sample, displacement is observed in the linear portions of the DTA curve. Detecting phase transition temperatures using DTA therefore has a slight degree of difficulty. The onset of the DTA peak in principle indicates the start temperature of phase transition but due to likelihood of temperature lag as a result of the thermocouple location with respect to the sample and reference or heating block, shifts from actual values are likely to occur. This necessitates the calibration of the DTA equipment with standards of known melting points.

Speil [209] took the issue above into consideration and deduced that

$$A = \frac{qM}{g_s \, K} \qquad (4.28)$$

Where q is the enthalpy change per unit mass, M is the total mass of the sample, g_s is the geometric shape factor and K is the thermal conductivity of the sample. The fraction $M/g_s \, K$ is the calibration constant (α) of the DTA equipment.

Speil in deriving equation (4.28) assumed that the value of the geometric shape factor was constant all through the process which is not what is observed in reality.

In order to know the thermal transitions and temperatures in the Co - Cu alloys, DTA was carried out using a PerkinElmer™ STA 8000 simultaneous thermal analyser. A pair of Al_2O_3 crucibles were used as sample and reference. The purge gas was nitrogen. Alumina powder was used in-order to act as a layer in preventing the Co - Cu powders from sticking to the inside of the sample crucible.

Alumina powder was put in both the sample and reference crucibles and weighed. This was done by placing both crucibles on the holder assembly in the furnace and zeroing the weight on the Pyris software used in running the equipment. Once the weight was zeroed, the baseline experiment was done with the empty crucibles (by empty, it is meant without the Co - Cu powders) by running the Pyris software with the pre- determined programme loaded.

After getting the baseline, the sample crucible was removed from the furnace and the Co - Cu samples were put into it. This was then covered with the crucible lid again to trap any evolved gas during the process. The whole assembly was then gently placed in the furnace and the weight retaken so the amount of Co - Cu alloy used was determined. Pyris was then run to start the experiment after which the results were viewed and analysed to determine the transition temperatures. The process was repeated for different sizes of alloys. The programme run is shown in table 3.6.

Table 4.6 Computer programme sequence for DTA.

Action	Temperature range ($^{\circ}$C)	Duration (minutes)	Steps/min ($^{\circ}$C)
Hold	50	1	
Heat	50-1450		15
Hold	1450	2	
Cool	1450- 50		15
Hold	50	2	
Heat	50-1450		15
Hold	1450	2	
Cool	1450-50		15

5 Experimental results

5.1   Metastable phase diagram and miscibility gap

The calculated binodal and spinodal limits are shown in table 5.1.

Table 5.1 Calculated binodal and spinodal limits.

Temperature (K)	Binodal composition boundary (mole fraction)		Spinodal composition boundary (mole fraction)	
1350	0.122	0.917	0.267	0.822
1375	0.138	0.906	0.278	0.811
1400	0.172	0.883	0.317	0.799
1425	0.200	0.875	0.348	0.788
1450	0.199	0.856	0.370	0.775
1475	0.238	0.825	0.400	0.756
1500	0.305	0.822	0.423	0.733
1525	0.325	0.775	0.440	0.728
1550	0.425	0.760	0.468	0.700
1575	0.424	0.761	0.499	0.675
1600	0.467	0.700	0.520	0.640
1623	0.587			

The phase diagram for the Co-Cu system with calculated metastable binodal and spinodal lines is shown in figure 5.1. The outer curve is the binodal curve while the inner one is the spinodal curve. T_c and $T_{liquidus}$ are the temperatures of the critical point and that of the liquidus at the critical composition

respectively. The two vertical lines show the composition of the Cu-50 at. % Co and the Cu - 68.5 at. % Co alloys that are the focus of this study.
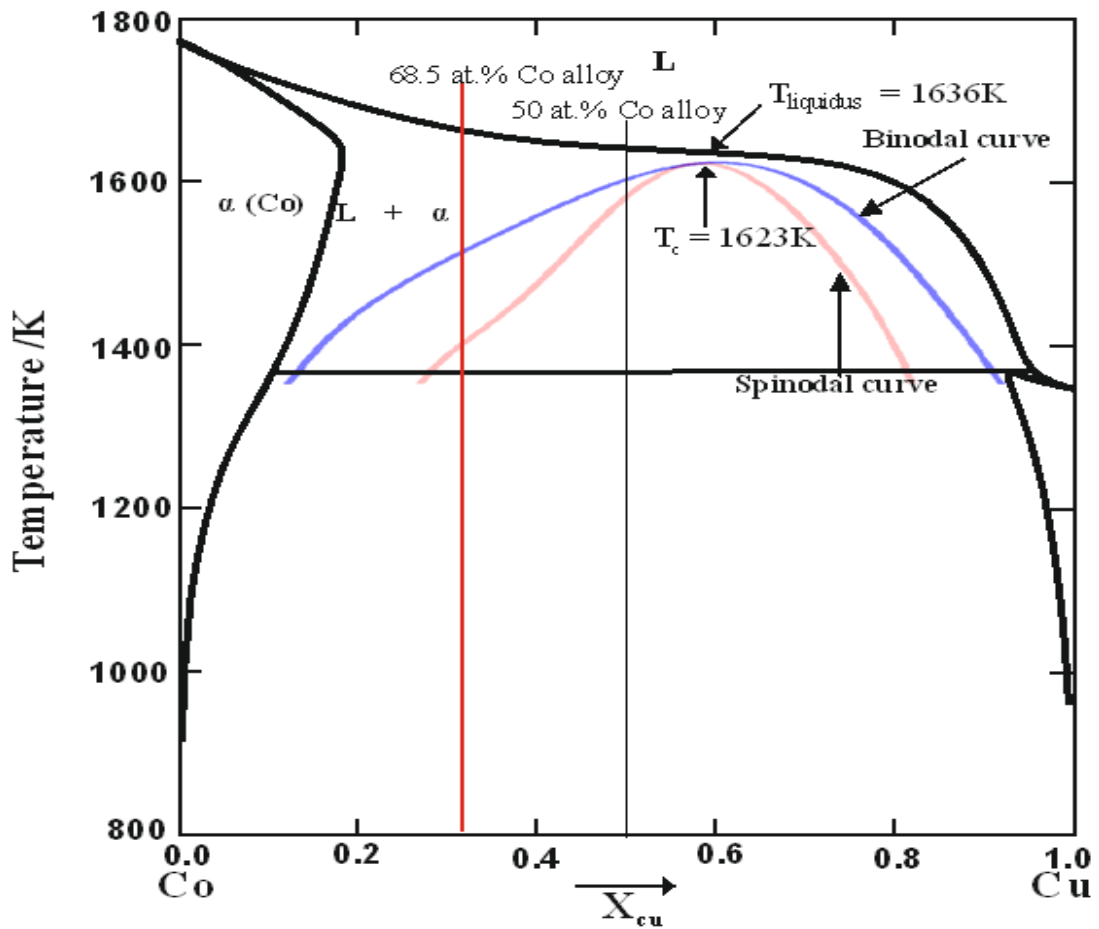
Figure 5.1 Metastable phase diagram of the Cu-Co alloy system with calculated miscibility gap. In the binodal, the alloy is metastable and phase separation would occur by nucleation while in the spinodal region, the alloy is unstable and separation occurs by mechanism of spontaneous fluctuation.

It is seen from figure 5.1 that the calculated critical point occurs at the composition Cu - 41.3 at. % Co and 1623 K. The liquidus at this point was 1636 K, giving the minimum undercooling for LPS to occur either by nucleation in the binodal or spinodally within the spinode of just 13 K. The liquidus of the Cu - 50 at. % Co alloy is 1639K with a required undercooling of 41 K for binodal decomposition and undercooling of 52 K to decompose via spinodal route. In comparison, the Cu - 68.5 at. % Co

alloy has a liquidus of 1662K and an estimated undercooling of 143 K and 256 K for binodal and spinodal decomposition respectively.

5.2 Elemental analysis.

Table 5.2 Elemental analysis of drop tube processed Co - Cu alloy.

Element	Alloy		
	Cu - 50 at. % Co (wt. %)	Cu - 68.5 at. % Co (wt. %)	
Cu	55.90	Cu	35.44
Fe	< 0.02	Fe	< 0.02
Sn	< 0.02	Sn	< 0.02
Mg	< 0.02	Mg	< 0.02
Pb	< 0.02	Pb	< 0.02
Ti	< 0.02	Ti	< 0.02
Zr	< 0.02	Zr	< 0.02
P	< 0.02	P	< 0.02
Al	< 0.02	Al	< 0.02
Ni	< 0.02	Ni	< 0.02
Cr	< 0.02	Cr	< 0.02
Mn	< 0.02	Mn	< 0.02
Zn	< 0.02	Zn	< 0.02
V	< 0.02	V	< 0.02
B	< 0.005	B	< 0.005
Co	44.24	Co	62.76
O	0.044	O	0.024

Table 5.2 shows the compositional analysis for the alloys obtained by inductively coupled plasma mass spectrometry (ICP-MS). The samples were digested with concentrated nitric acid (HNO_3) using microwave heating after which they were cooled and filtered. The samples are then refluxed using hydrochloric acid (HCl) before finally being diluted with deionized water. The samples were then nebulized and the aerosol generated transferred to the plasma torch where element specific emissions are detected by photomultiplier tubes.

The powders were quite segregated hence two separate analysis were done i.e. Co (trace) and Cu (ICP shifts) and the chances that the two elements will add up was very unlikely due to the segregation. There was insufficient samples to do a large weight dissolution to overcome the segregation.

5.3   Cooling rate estimates in drop tube powders

Estimates of the cooling rate as a function of droplet diameter in the drop tube powders are made using reference equations in chapter four. In doing this, the determined liquidus of the alloys from the phase diagram is chosen as their melting temperature. Estimates have also been made for the largest droplet diameter of 850 μm and smallest droplet diameter of 38 μm. Thermophysical properties of the gas and melt used in the calculation are listed in tables 5.3 and 5.4 respectively.

The calculated results for the two alloys are very similar with the cooling rate in the Cu - 50 at. % Co alloy shown in figure 5.2, varying from 8.66×10^2 K s^{-1} to 8.47×10^4 K s^{-1} as the droplet diameter decreases from 850 μm to 38 μm. In the Cu - 68.5 at. % Co alloy the variation is between 8.52×10^2 K s^{-1} and 8.08×10^4 K s^{-1} for 850 μm and 38 μm diameter particles respectively. The cooling rate estimates are lower than the values quoted by Kolbe and Gao (by one order of magnitude) [94] who worked on drop tube processed Cu – 16 at. % Co alloy. The variance in the cooling rates could be due to the differences in the cobalt content of the alloys (i.e. that the cooling rate

decrease with increasing cobalt content) which is explainable by the asymmetrical nature of the miscibility gap or due to the drop tube processing environment. They used helium as their drop tube gas which has a considerably higher thermal conductivity than nitrogen gas used in this study. The estimated cooling rates may be approximated by power law relationships of the form $(1.815 \times 10^7)\,(d/\mu m)^{-1.476}$ and $(1.687 \times 10^7)\,(d/\mu m)^{-1.469}$ for the Cu - 50 at. % Co and Cu - 68.5 at. % Co alloys respectively.
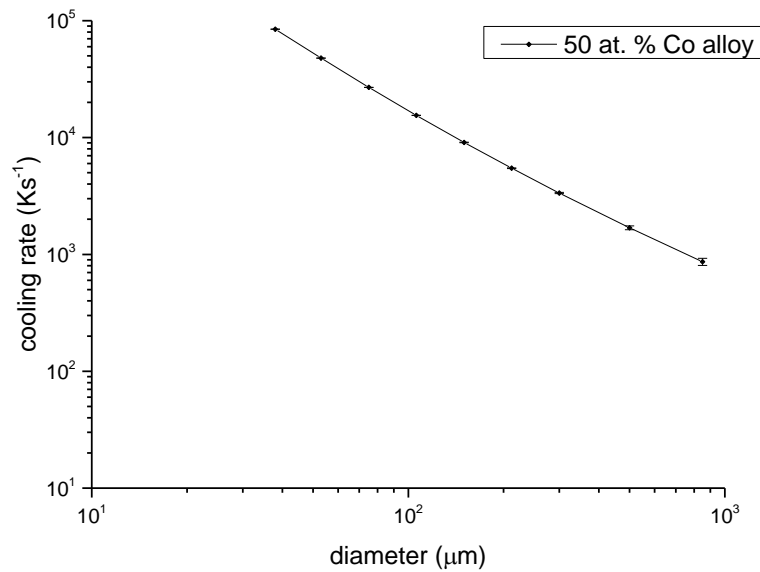
Figure 5.2 Calculated cooling rate as a function of droplet diameter in the Cu - 50 at. % Co alloy.

Table 5.3 Thermophysical properties of nitrogen gas at room temperature.

C_g, Specific heat capacity, J kg^{-1} K^{-1}	1039
λ_g, Thermal conductivity, W m^{-1} K^{-1}	2.4×10^{-2}
μ_g, Dynamic viscosity, N s m^{-2}	1.76×10^{-5}
Pr, Prandt number	0.7619

Table 5.4 Thermophysical properties of Co - Cu melts.

Specific heat capacity, C_m, J kg^{-1} K^{-1}	(50% Co)	590 [a]
Specific heat capacity, C_m, J kg^{-1} K^{-1}	(68.5% Co)	627 [a]
Density of melt, ρ_m, kg m^{-3}	(50% Co)	7885 [a]
Density of melt, ρ_m, kg m^{-3}	(68.5% Co)	7835 [a]
Latent heat of melting, L, J kg^{-1}		0
Emmisivity of melt, ε		0.3007 [a]
Stefan Boltzmann constant, σ_B, W m^{-2} K^{-4}		5.67×10^{-8}

5.4   X-ray diffraction results

5.4.1   Identification and indexing of diffraction pattern

In all the diffraction data, first, second and third order peaks were observed in pair suggesting there were two major phases in the alloys. In order to index the peaks, the Miller indices of each of the observed peaks was calculated and assigned. This was compared and found to be same as index assigned by the GSAS software. An example indexing calculation done for 300–212-micron polished powder sample in the 50 at. % Co alloy is shown in table 5.5 below.

Table 5.5 XRD peaks indexing for 300 - 212 μm drop tube powders.

Phase	Peak position 2θ (± 0.02)	θ (radians)	sinθ	$\sin^2\theta$	1 X ($\sin^2\theta / \sin^2\theta_{Min}$)	2 X ($\sin^2\theta / \sin^2\theta_{Min}$)	3 X ($\sin^2\theta / \sin^2\theta_{Min}$)	$h^2+k^2+l^2$	hkl
1	43	0.38	0.37	0.14	1.0	2.0	3.0	3	111
2	44	0.38	0.38	0.14	1.0	2.1	3.1	3	111
1	50	0.44	0.43	0.18	1.3	2.7	4.0	4	200
2	51	0.45	0.43	0.19	1.4	2.8	4.1	4	200
1	74	0.65	0.60	0.36	2.7	5.3	8.0	8	220
2	76	0.66	0.61	0.37	2.8	5.5	8.3	8	220

The 2θ values of the indexed peaks corresponded to that of (111), (200) and (220) planes of copper (phase one) and cobalt (phase two). Subsequent comparison with ICDD standard powder diffraction data (table 5.6) confirmed that the phases were (fcc) copper and (fcc) cobalt. The angles were however observed to vary slightly as the sieve fraction size of the alloys changed.

Figures 5.3 – 5.6 show the x-ray diffraction patterns of polished (figures 5.3 and 5.4) and powder (figure 5.5c and 5.6) samples of the Cu – 50 at. % Co alloy and Cu – 68.5 at. % Co alloy respectively. Both types of sample were analysed based on the assumption that the powder samples would reveal surface information due to the penetration depth of the x-ray beam while more detailed information from within the droplets are expected from the exposed cross section of the polished samples.

In all the samples, the higher angle peaks in the drop tube samples were observed to be very low and in some cases undetectable (the 850 – 500 µm and 300 – 212 µm diffraction pattern of the powder and polished samples in the Cu – 68.5 at. % Co alloy is an example in which only the Co peak was detected in the latter (figure 5.4 and 5.6).

Some of the peaks had shoulders which could be an indication of segregation, this would however have to be verified by microstructural evidence.
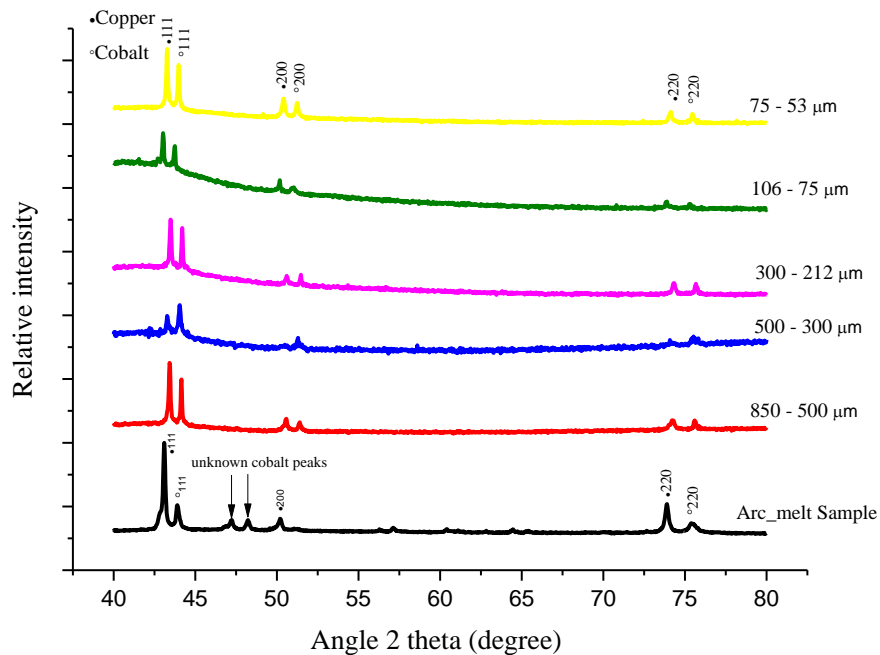
Figure 5.3 X-ray diffraction pattern of polished arc melt and drop tube powders of Cu - 50 at. % Co alloy. The unknown peaks are unindexed cobalt peaks from the ICCD reference.
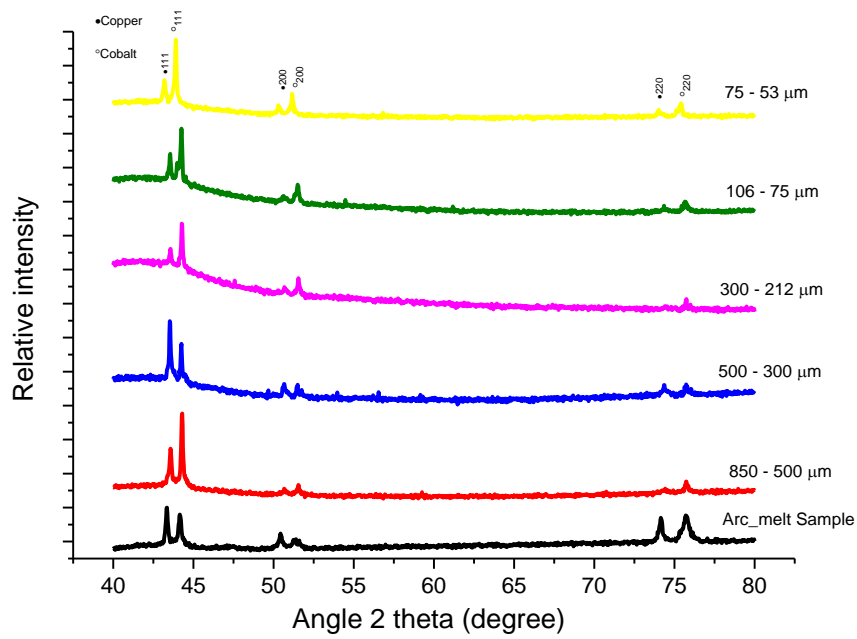
Figure 5.4 X-ray diffraction pattern of polished arc melt and drop tube powders of Cu - 68.5 at. % Co alloy.
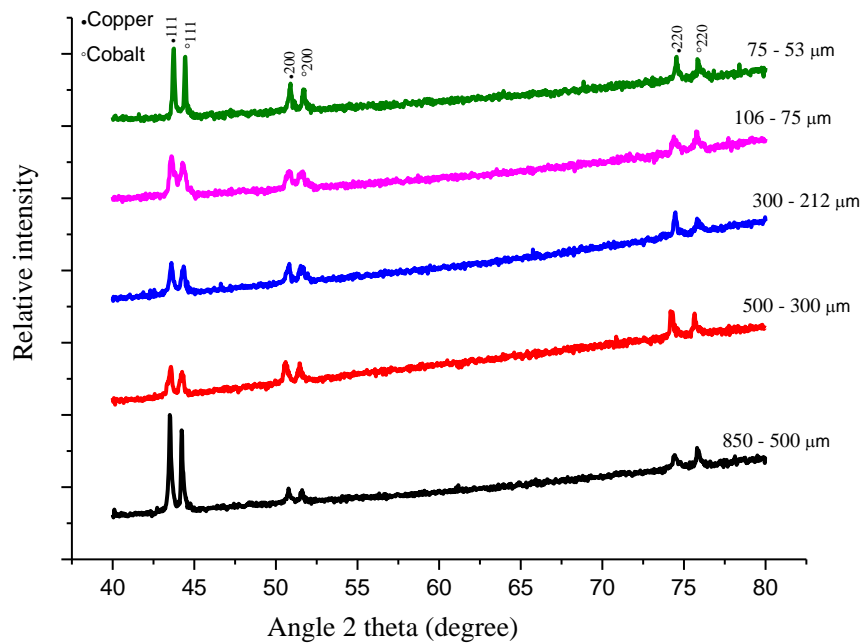
Figure 5.5 X-ray diffraction pattern of drop tube powders of Cu - 50 at. % Co alloy.
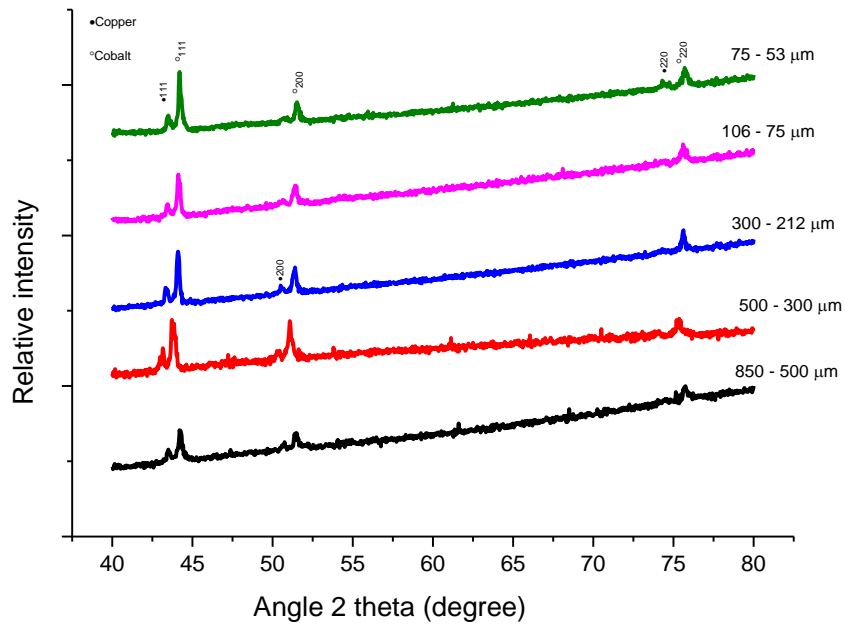
Figure 5.6 X-ray diffraction pattern of drop tube powders of Cu - 68.5 at. % Co alloy.

Table 5.6 Comparing experimental diffraction angles with that of standard specimen.

Phase	Diffraction angles 2θ (degrees) (± 0.02)		File No
	Experimental	ICDD standard specimen	
1	43	43	01-071-4610
	50	50	
	74	74	
2	44	44	01-071-4651
	51	51	
	76	76	

5.4.2 Rietveld refinement

The calculated peaks from the Rietveld refinement indicates peak ratio is fairly consistent with relative phase abundance. This is especially true in powder samples as shown in figures 5.7 and 5.8 below.
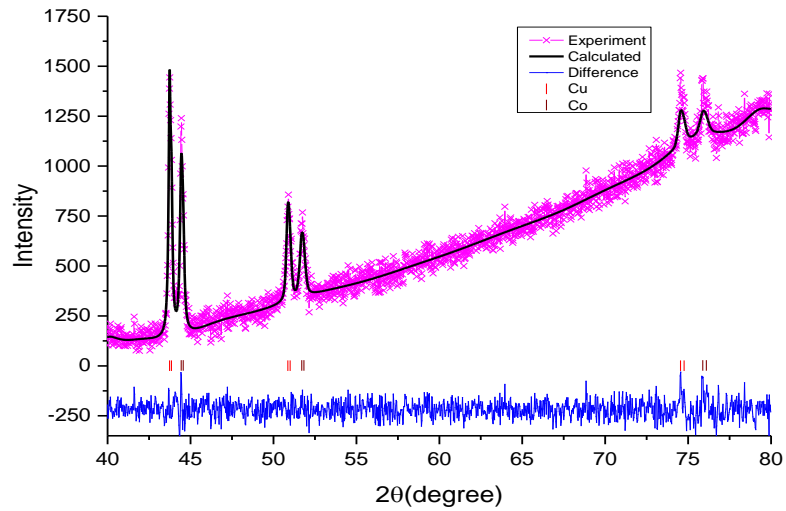
Figure 5.7 Diffraction pattern and Rietveld refinement of 75-53 micron powder of the 50 at. % Co alloy.
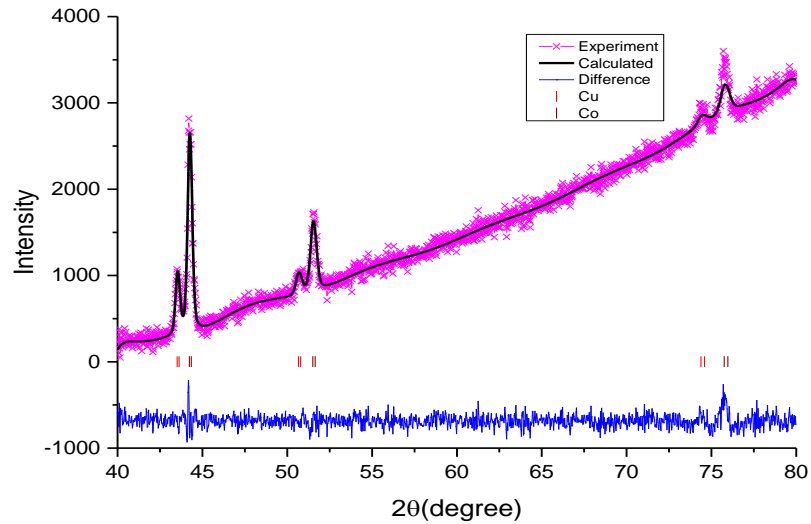
Figure 5.8 Diffraction pattern and Rietveld refinement 75 –53 micron powder of the 68.5 at. % Co alloy.

The amount of powder produced from the drop tube run was very small (58 mg for the Cu - 50 at. % Co alloy and 56.8 mg for the Cu - 68.5 at. % Co alloy). This limited the amount of powder available for analysis after sorting into the different sieve size range. This is thought to be responsible for the significant background effect on the diffraction pattern of the powder samples when compared with the polished samples (figures 5.3 to 5.8). Background was subtracted from all the diffraction patterns. Due to the uneven background, higher angle peaks were disproportionally large and difficult to fit and so were excluded from the final refinement of the powdered samples (figure 5.9).
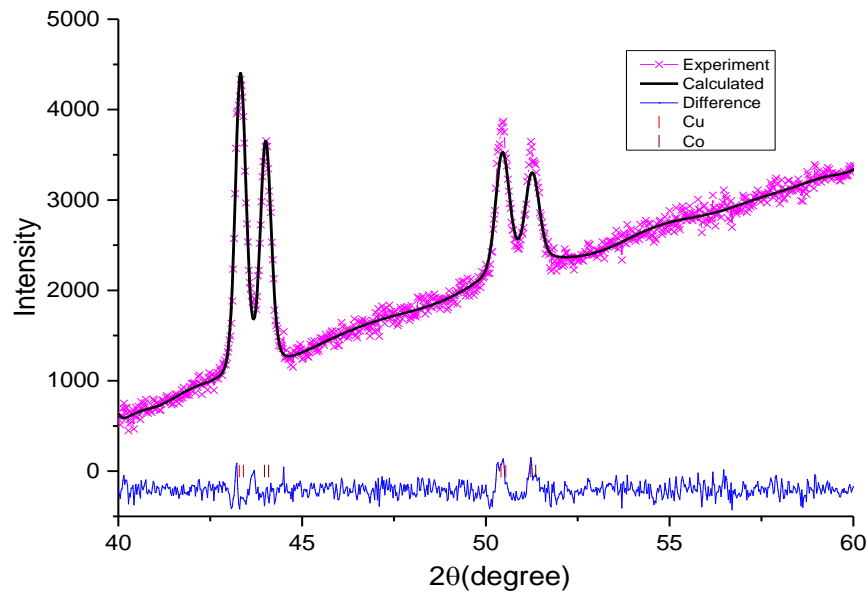
Figure 5.9 Diffraction pattern and Rietveld refinement of 300-212 micron powder of the 50 at. % Co alloy with the higher angle peaks excluded.

5.4.2.1 Phase fraction and composition variation in drop tube powders.

In order to distinguish between the polished and powder samples, the sieve size range in the polished samples have been given alphanumeric notation: AB2, AB3, AB4, AB7 and AB8 represents $850 - 500$ μm, $500 - 300$ μm, $300 - 212$ μm, $106 - 75$ μm and $75 - 53$ μm sieve size range respectively in the Cu - 50 at. % Co alloy while the same sieve size range is represented using CD2, CD3, CD4, CD7 and CD8 for the Cu − 68.5 at. % Co alloy.

Table 5.7 and 5.8 presents phase fractions and lattice parameter of phases directly obtained from the Rietveld analysis software for the Cu − 50 at. % Co alloy and Cu − 68.5 at. % Co alloy respectively. The lattice parameter were obtained by the unit cell refinement in the GSAS software using least square fitting method. Also listed on the tables are the residual errors, %Rp and %WRp, of the refinement processes (these are observed to be < 10% in both alloys) and the composition of the phases estimated using Vegard's law.

In comparison, table 5.9 and 5.10 lists phase fractions calculated from the refined scale factors from the refinement process using equation (4.25), the lattice parameters as well as the compositions of the Cu and Co – rich phases which were calculated from the angles of reflection. Only the first order diffraction peaks (which was uniform across the whole sieve size range in both alloy) in combination with Vegard's law was used in estimating the composition. Table 5.9 is for the Cu – 50 at. % Co alloy while table 5.10 is for Cu – 68.5 at. % Co alloy.

Table 5.7 Rietveld analysis for the Cu - 50 at. % Co alloy.

Size range (μm)	Phase fraction Cu at. %	%Rp	%WRp	lattice parameter (Å)		Composition (at. %)	
				Cu	Co	Xco	Xcu
AB2	55.45	8.53	11.6	3.62	3.56	77.32	100.0
AB3	28.25	5.94	8.08	3.62	3.56	78.87	100.0
AB4	50.22	5.81	9.59	3.61	3.56	80.00	98.73
AB7	45.58	2.82	3.98	3.61	3.56	78.03	96.34
AB8	51.91	4.98	7.56	3.61	3.56	81.13	96.06
850	50.62	4.36	6.78	3.60	3.54	100.0	73.66
500	50.02	5.68	9.69	3.64	3.59	40.85	100.0
300	50.72	2.74	3.76	3.64	3.586	40.85	100.0
106	48.82	4.27	6.34	3.61	3.56	75.07	98.17
75	49.42	5.27	7.56	3.62	3.56	76.34	100.00

Table 5.8 Rietveld analysis for the Cu - 68.5 at. % Co alloy.

Size range (μm)	Phase fraction Cu at. %	%Rp	%WRp	lattice parameter (Å)		Composition (at. %)	
				Cu	Co	Xco	Xcu
CD2	29.31	4.16	5.37	3.62	3.56	73.38	100.0
CD3	31.45	4.46	6.40	3.61	3.56	84.37	94.93
CD4	17.68	4.39	6.69	3.62	3.56	77.46	100.0
CD7	24.58	4.85	6.90	3.61	3.56	76.48	99.44
CD8	22.66	3.94	3.94	3.61	3.56	79.01	97.75
850	21.02	2.53	3.66	3.62	3.56	76.34	100.0
500	20.35	4.54	6.44	3.61	3.56	81.69	93.94
300	19.39	2.79	4.71	3.61	3.56	81.83	98.17
106	18.73	2.97	4.59	3.62	3.56	73.80	100.0
75	19.2	3.47	5.44	3.61	3.55	85.92	92.68

Table 5.9 Phase fraction from refined scale factor, lattice parameter and composition from first order diffraction peaks for the Cu - 50 at. % Co alloy.

Size range (μm)	Phase fraction Cu at. %	lattice parameter (Å)		Composition (at. %)	
		Cu	Co	Xco	Xcu
AB2	56.67	3.61	3.55	92.89	85.32
AB3	29.23	3.61	3.56	82.08	100.0
AB4	51.4	3.60	3.55	98.08	79.09
AB7	46.67	3.63	3.58	48.81	100.0
AB8	53.06	3.62	3.56	75.30	100.0
850	51.47	3.60	3.54	100.0	76.96
500	51.14	3.60	3.55	100.0	68.77
300	51.65	3.59	3.54	100.0	68.50
106	49.88	3.59	3.54	100.0	63.02
75	50.54	3.59	3.55	100.0	52.66

Table 5.10 Phase fraction from refined scale factor, lattice parameter and composition from first order diffraction peaks for the Cu - 68.5 at. % Co alloy.

Size range (μm)	Phase fraction Cu at. %	lattice parameter (Å)		Composition (at. %)	
		Cu	Co	Xco	Xcu
CD2	30.33	3.60	3.54	100.0	69.17
CD3	32.48	3.60	3.55	100.0	73.99
CD4	24.1	3.59	3.54	100.0	69.39
CD7	25.41	3.60	3.55	75.51	71.89
CD8	23.47	3.62	3.56	66.70	100.0
850	21.78	3.60	3.55	100.0	77.43
500	21.06	3.61	3.57	60.78	100.0
300	20.12	3.61	3.55	90.30	97.31
106	19.39	3.60	3.55	88.65	85.70
75	19.91	3.60	3.55	97.57	81.18

It is seen from figures 5.10 and 5.11 that in polished (mounted) and powdered samples respectively that there is general agreement between the calculated phase fraction and the Rietveld estimates although the calculated values are generally slightly higher. It is also observed from the figures that the phase

148

fractions of the Cu – rich phase are lower in the Cu – 68.5 at. % Co alloy (in the range of about 15 to 33 at. % in polished samples and a maximum of about 21 % in the powdered samples) than in the Cu – 50 at. % Co alloy across the sieve size range.
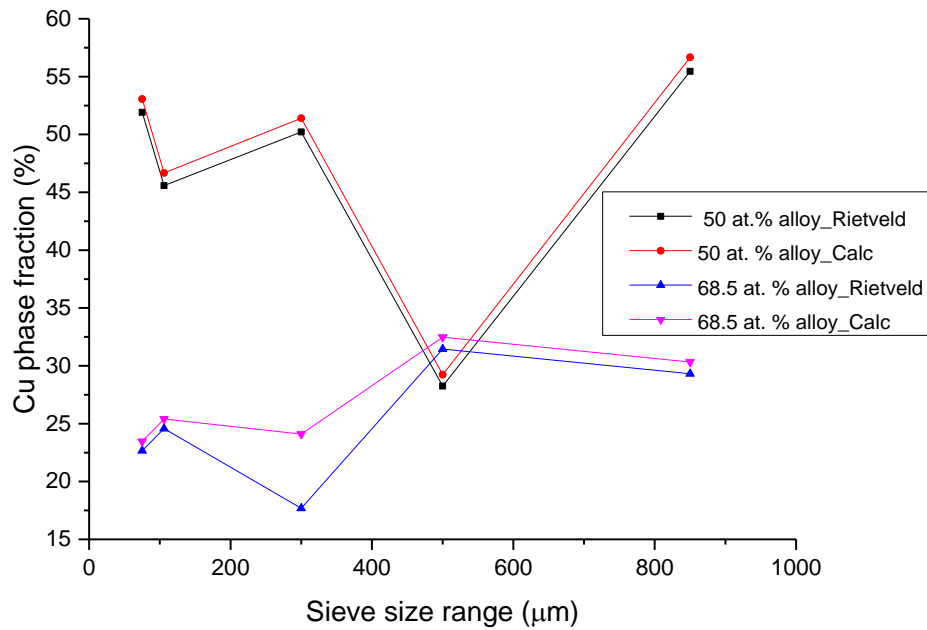
Figure 5.10 Variation of Cu rich phase fraction with droplet size in mounted and polished samples. The calculated values are those estimated using the scale factor from the refinement process.
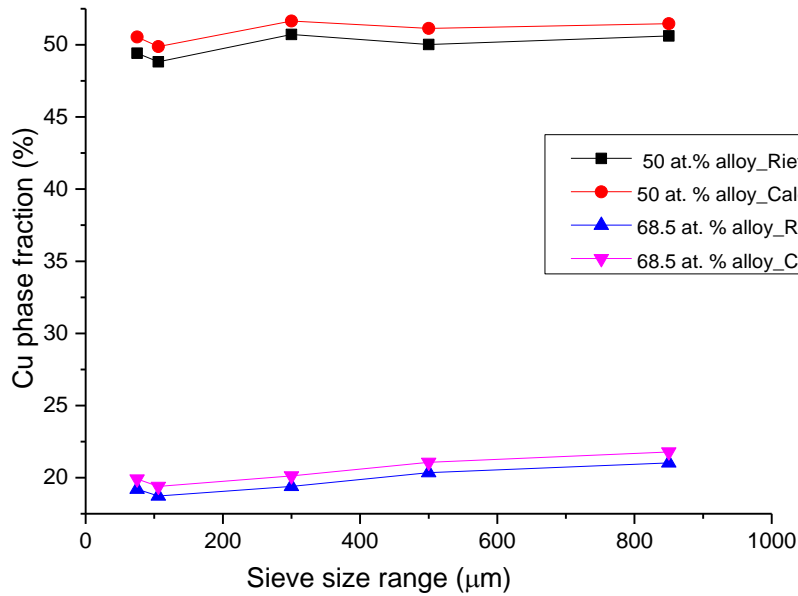
Figure 5.11 Variation of Cu rich phase fraction with droplet size in unmounted powder samples of the Cu – 50 at. % Co and Cu – 68.5 at. % Co alloys. The calculated values are those estimated using the scale factor from the refinement process.

In the plot of the powder samples of the Cu – 50 at. % Co alloy shown in figure 5.12, the points cluster around the 50% marker suggesting that the phases are in near equal volume of abundance. The copper composition however varies, with slight shifts noticed in the phase fractions. This figure suggests the composition of copper increases as the phase fraction of the Cu – rich phase up to a point and then starts to decrease.

In the polished samples however, the phase fraction of the Cu – rich phase spreads from 28 to about 56% which would be expected in the case of a segregated structure. Most of the readings however, appear to be within regions with high fraction of the Cu – rich phase. It is also observed that the highest copper composition occurred where the phase fraction of the Cu – rich phase is lowest. This suggests Cu – rich region exists within regions where the other phase (Co – rich) is the majority phase.

The Rietveld details of the Cu – 68.5 at. % Co alloy are shown in figure 5.13 wherein the Cu – rich phase fraction of the powder sample also appears to converge around the 20% marker. The highest phase fraction is 21% which coincidentally also has the highest Cu composition.

In the polished samples just as in the Cu – 50 at. % Co alloy, the phase fraction is widely spread. As said earlier, the phase fractions in this alloy are generally low confirming that the alloy is Co – rich. It is however noticed in this set of samples that the highest phase fraction occurred with lowest composition.
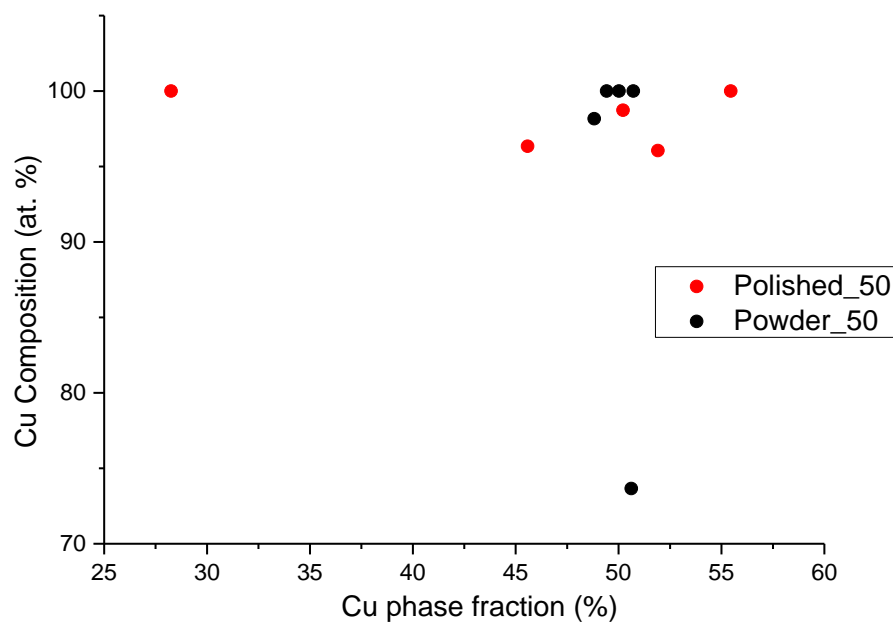
Figure 5.12 Rietveld estimates of the variation of Cu concentration with phase fraction in samples of Cu – 50 at. % Co alloy.
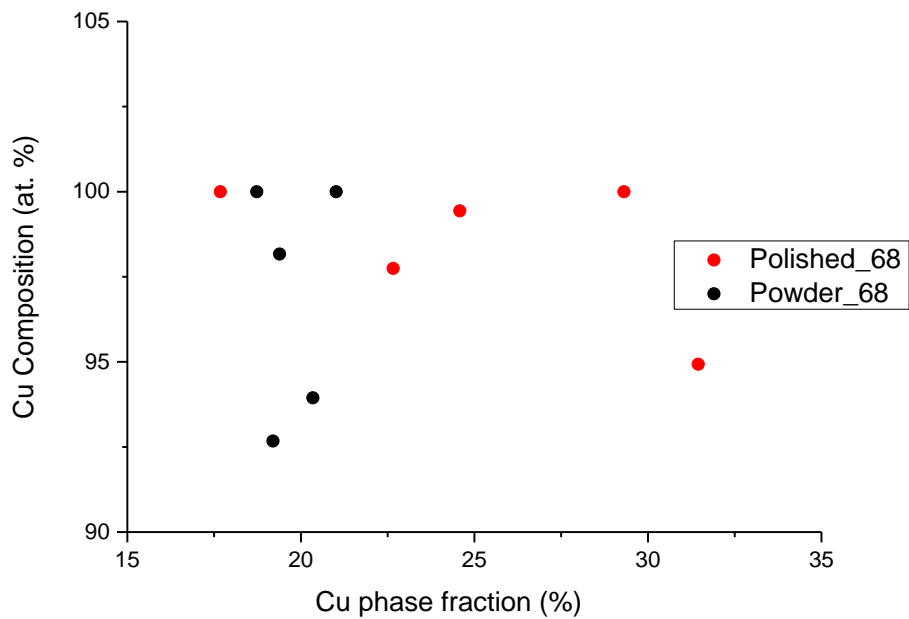
Figure 5.13 Rietveld estimates of the variation of Cu concentration with phase fraction in samples of Cu – 68.5 at. % Co alloy.

In the experimental data of the Cu – 50 at. % Co alloy shown in figure 5.14 it is also observed that the points of the powder samples cluster around the 50% phase fraction marker. The polished samples here also show variations in the phase fractions. It is thought that as the amount of the Cu – rich phase increases, the Cu composition gradually starts to reduce.

Figure 5.15 is plotted from the calculated data of the Cu – 68.5 at. % Co alloy. The points of the powder samples seems to form a C – curve that had a peak at about 18% Cu phase fraction and composition of about 85 at. % Cu. This implies the presence of features that are very rich in copper within a region that is predominantly Co – rich (similar to what exists in a core shell microstructure).
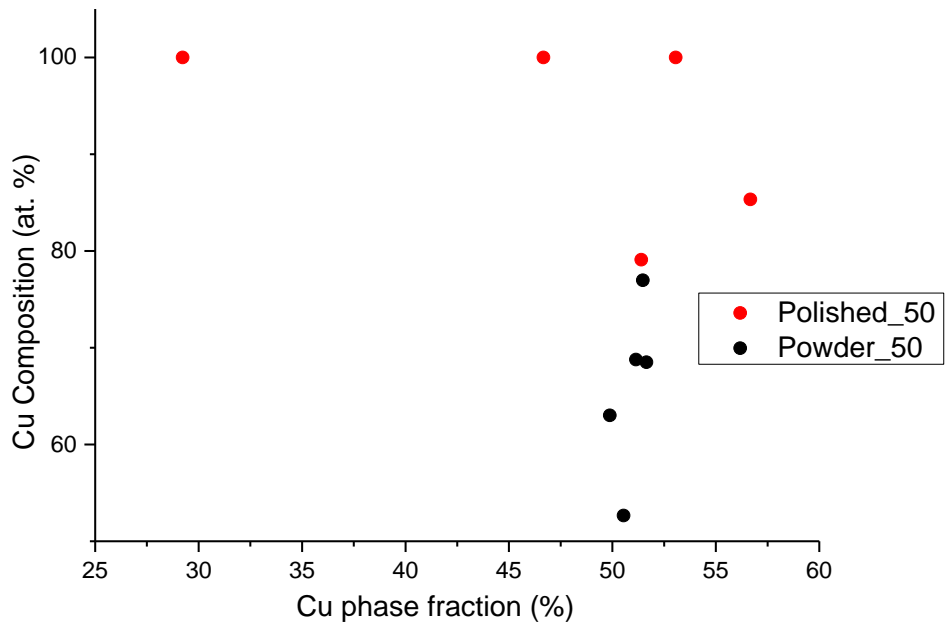
Figure 5.14 Estimates from diffraction data of the variation of Cu
concentration from with phase fraction in samples of Cu – 50 at. % Co
alloy.
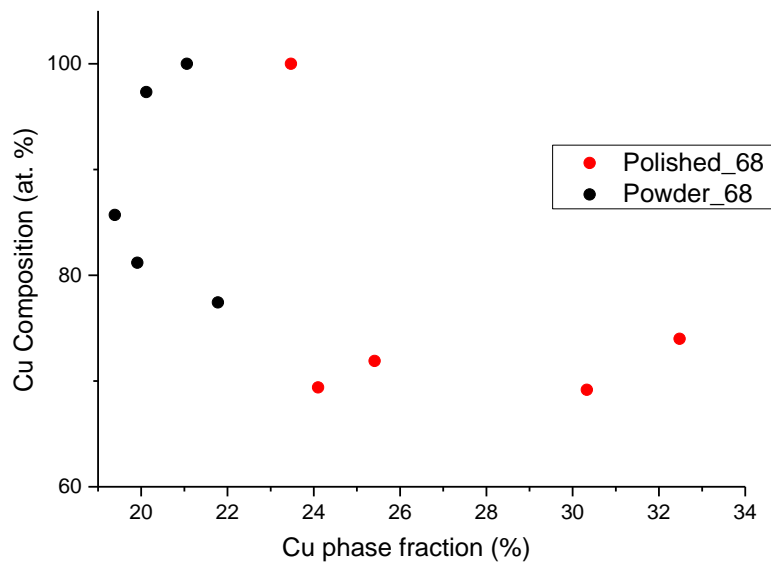
Figure 5.15 Estimates from diffraction data of the variation of Cu
concentration from with phase fraction in samples of Cu – 68.5 at. % Co
alloy.

A comparison of the Cu composition estimated from diffraction peaks and that derived from the lattice parameter measured by the Rietveld analysis software in unmounted powder samples of the Cu – 50 at. % Co alloy is shown below in figure 5.16.

Figure 5.16 Measured and estimated composition variation with droplet size for unmounted powder samples of Cu – 50 at. % Co alloy.

It is seen that the Rietveld estimates are generally higher than the calculated values. Also, the Rietveld curve suggests that as the undercooling increases (droplets get smaller) the Cu composition increases (in droplets with d > 500 μm) after which a marginal decrease in the Cu composition occurs with undercooling and finally increases again in droplets with d < 100 μm.

The calculated curve of the alloy however suggests that as the droplet size decreases in all size fractions, the Cu composition gradually decreases. A steep drop is first observed in the Cu composition (region 1), followed by a period of slow decrease (marked by region 2 on the curve) and then another period of slow decline finally followed by a sharp drop in the Cu composition.

This pattern is expected if LPS occurred as at the initial stage cobalt rich phase is nucleated which explains the first steep decline in the Cu composition (region 1). It then takes a while for the nucleated phase to attain a critical size, at this stage the decline in the Cu composition will be very little. It is believed this is what causes the region 2 to appear like there was no change in the composition. It is a slow process. Once the nucleated Co – rich phase attains a critical size, growth processes are initiated and with more and more cobalt rich phase being formed the Cu composition starts to drop gradually again. This would explain region 3 of the curve. With further undercooling however, the solidification process proceeds and Co – rich dendrites / dispersed particles are formed which might explain the sharp drop in Cu composition observed in droplets with d < 100 μm.

In the mounted powder samples (figure 5.17), the first striking thing observed is that the Rietveld and calculated estimates are the same at the 500 μm sieve size range and it indicates that the droplets in this range are Cu – rich. The values were not noticed to converge in the unmounted samples (figure 5.16) although it also shows that the droplets in this range are Cu – rich. However, from figure 5.10 it is seen that the phase fraction of the Cu – rich phase is actually low (about 28%). These results again shows that in a Co – rich region there exists spots of almost pre Cu – phase.
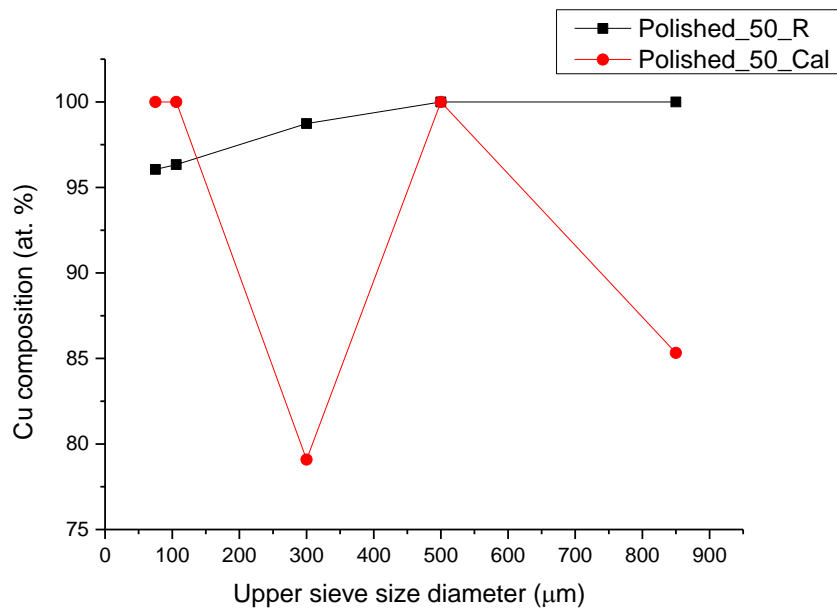
Figure 5.17 Measured and estimated composition variation with droplet size for polished samples of Cu – 50 at. % Co alloy.

Figure 5.18 shows the corresponding results for the unmounted samples of the Cu – 68.5 at. % Co alloy in which the Rietveld are noticed to be higher than the calculated ones as well.

The trend of the Rietveld line is that as droplet size decreases, Cu composition in the alloy sharply drops (d > 500 µm) and then increases sharply at first then gradually in droplets f diameter 500 µm < d > 100 µm. The Cu composition is then observed to drop slightly with increased undercooling (d < 100 µm).

The calculated line however shows opposite trend in droplets of d > 500 µm. It shows that the Cu composition in such droplets sharply increases after which it drops and keeps on dropping as undercooling increases further. It can be seen from this line that the final Cu composition approaches that of the starting value.
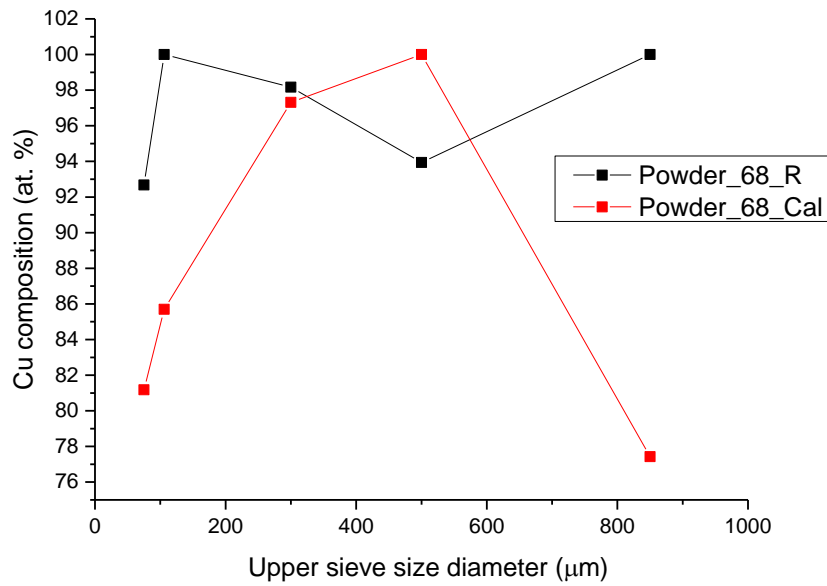
Figure 5.18 Measured and estimated composition variation with droplet size for unmounted powder samples of Cu – 68.5 at. % Co alloy.

In comparison in the mounted samples (figure 5.19), the calculated line shows a different trend in droplets with d < 300 µm. The Cu composition in these were observed to steadily rise in droplets up to 100 µm after which the increase appears to be constant (d < 100 µm). This implies with further undercooling the Cu composition in small droplets approaches pure copper which is contrary to what was observed in the unmounted powder samples.

The fraction of the Cu – rich phase is however small in this alloy (figure 5.10) and so it is most likely the XRD analysis is reflecting aggregate composition of Cu – rich inclusions in a cobalt majority region.
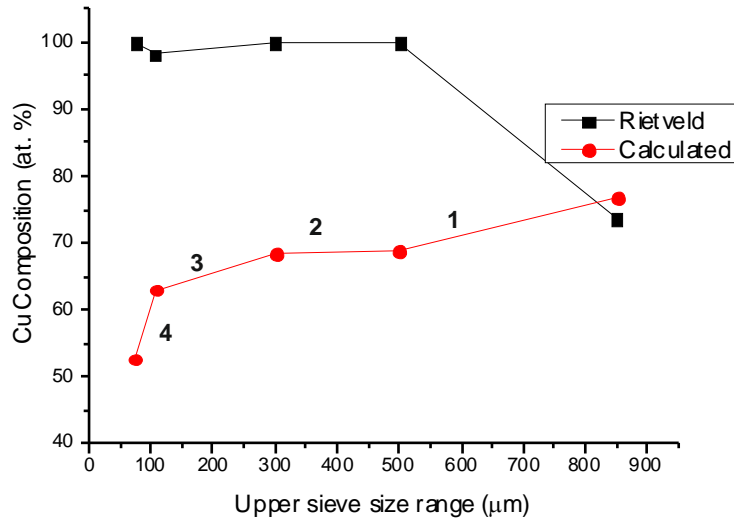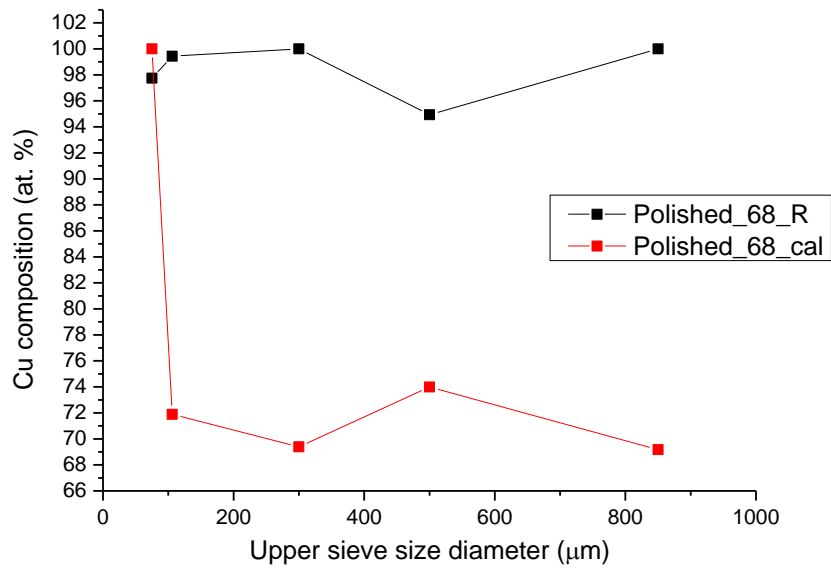
Figure 5.19 Measured and estimated composition variation with droplet size for polished samples of Cu – 68.5 at. % Co alloy.

The composition determined from XRD diffraction angles using Vegard's law has been said to represent the binodal boundaries in a miscibility gap system. It is however uncertain if such a binodal estimate would be accurate due to the fact that miscibility gap systems are expected to show positive deviations from Vegard's law. The estimated Co and Cu compositions are traced out on the calculated metastable phase diagram (example shown in figure 5.20 below) where it is observed that none of the points coincide with the binodal boundaries.
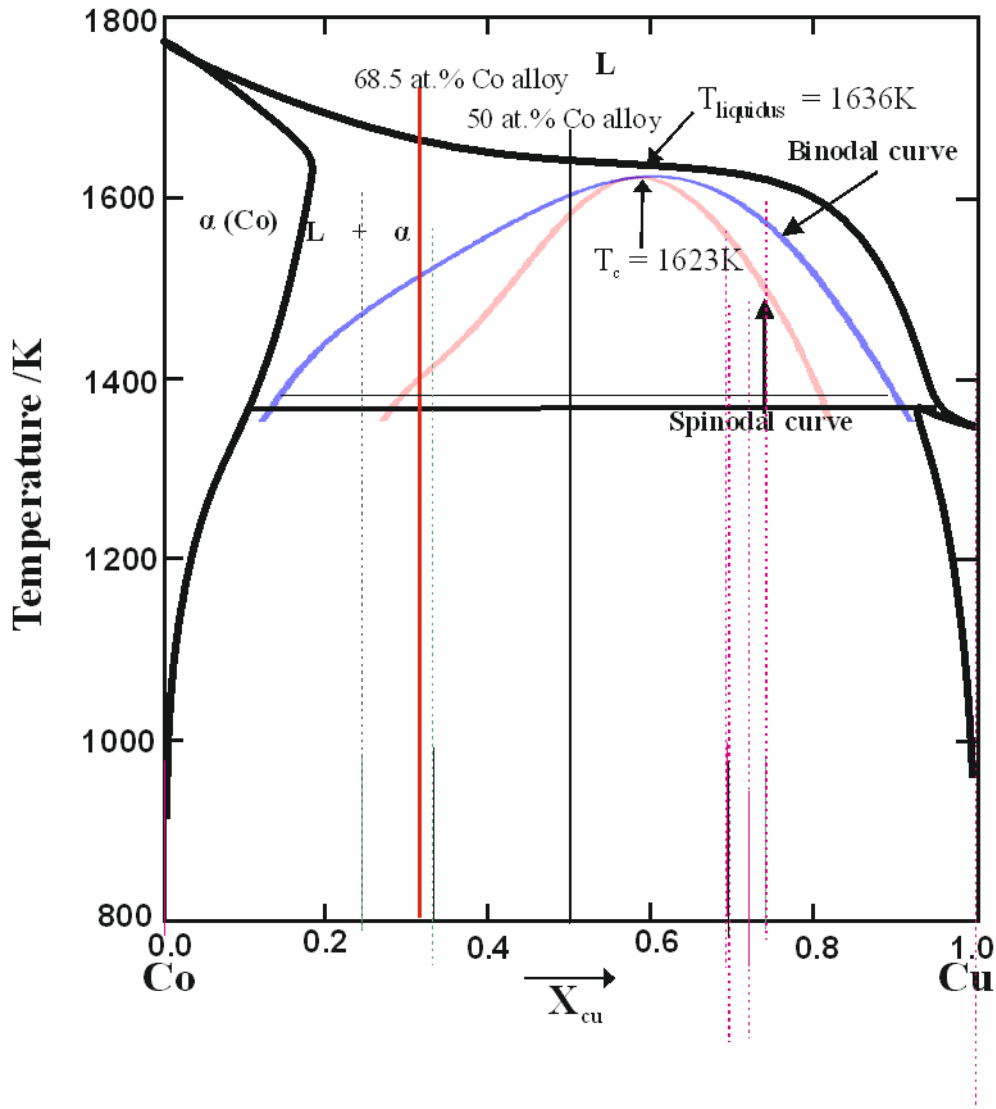
Figure 5.20 Trace of compositions estimated from XRD on the metastable phase diagram of the Co – Cu system.

5.4.2.2   Lattice parameter

The Bragg reflexes from the experimental diffraction pattern was used to calculate the mean lattice parameter of the Cu – rich and Co – rich phases, this was then compared with the standard lattice parameter for the pure fcc crystal structure of Cu (3.615 Å) and Co (3.544 Å).

The pattern of the variation of the lattice parameter of both the Cu – rich and Co – rich phases with droplet size was the same in powder and polished samples of the Cu – 50 at. % Co alloy (figure 5.21).

In the Cu – 68.5 at. % Co alloy on the other hand, the lattice parameter of the Co – rich phase seems to experience growth sprout as cooling rate increased (i.e. droplet size decreased) in the powder sample (figure 5.22). Apart from the lattice parameter of the Cu – rich phase being higher, there is no difference in the trend of the Cu and Co lattice parameters across the sieve size range in the polished samples (figure 5.23).
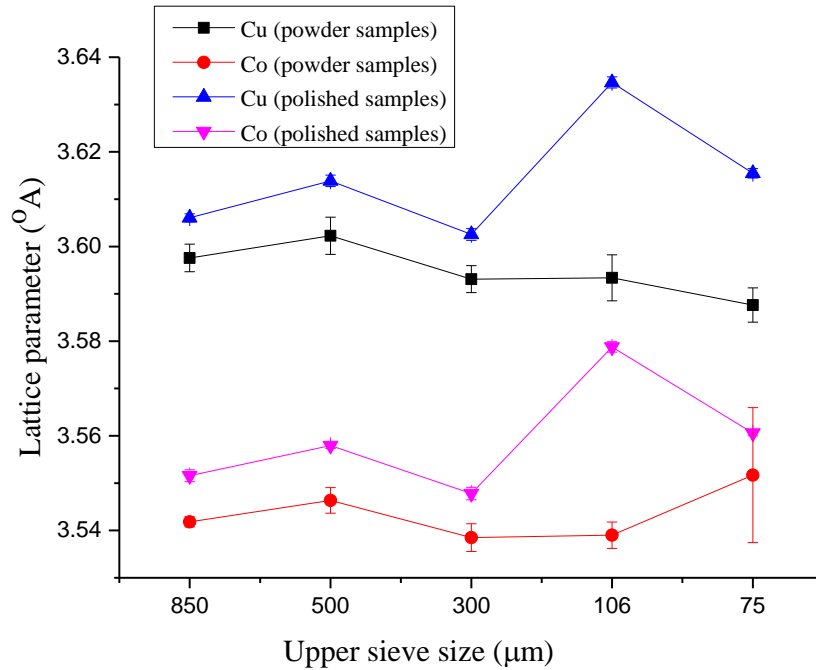
Figure 5.21 Variation of lattice parameter from x – ray diffraction pattern in powder and polished samples of the Cu – 50 at. % Co alloy.
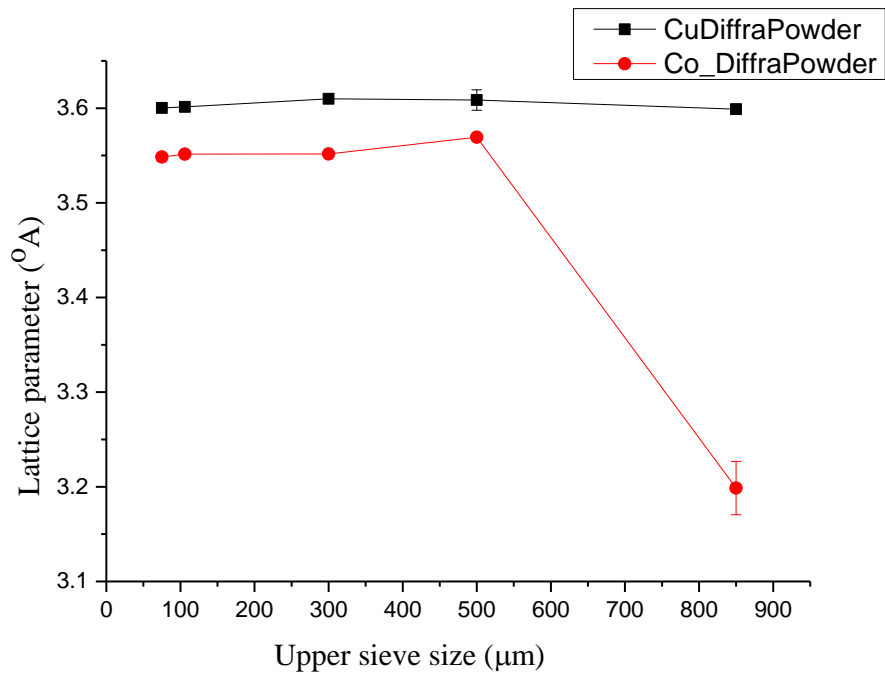
Figure 5.22 Variation of lattice parameter from x – ray diffraction pattern in powder samples of the Cu – 68.5 at. % Co alloy.
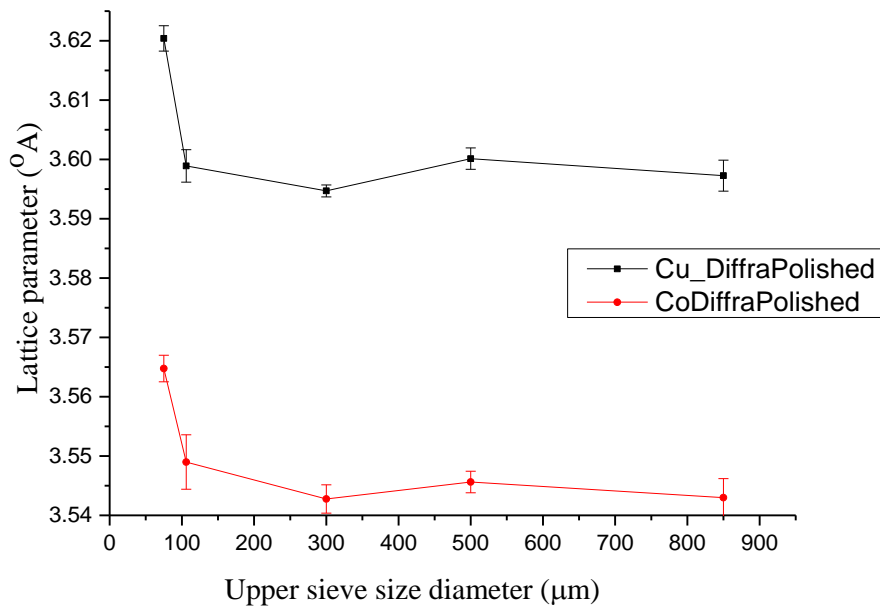
Figure 5.23 Variation of lattice parameter from x – ray diffraction pattern in polished samples of the Cu – 68.5 at. % Co alloy.

161

The lattice parameter of the Cu – rich phase in the Cu – 50 at. % Co alloy was found to be 0.3% lower (3.605 Å) than that of pure fcc Cu while the lattice parameter of the Co – rich phase was higher by 0.19 % (3.551 Å). The overall increase in the lattice parameter of the Co – rich phase might be due to increase in its solubility resulting from higher cooling rates.

Similar trend was observed in the Cu – 68.5 at. % Co alloy with lower values recorded for the Cu – rich phase (3.603 Å) and same value for the Co – rich phase (3.551 Å).

Rietveld estimates puts the lattice parameter in the Cu – 50 at. % Co alloy at 3.618 Å and 3.563 Å for the Cu - rich and Co -rich phase respectively. The estimates from this research are not far off from the values cited in literature for rapidly solidified Cu – 50 at. % Co alloy. Davidoff et al. [176] using diffraction data reported lattice parameter of 3.615 Å and 3.559 Å for the Cu and Co – rich phases. Rietveld estimates of 3.612 Å and 3.560 Å for the Cu – rich and Co – rich phases were also cited [176].

Using Vegard's law, the estimate of lattice parameter for the Cu – 50 at. % Co alloy was 3.561 ± 0.0001 Å while that of the Cu – 68.5 at. % Co alloy was 3.549 ± 0.0001 Å.

These result suggests both alloys are Co – rich.

5.5   Microstructural characterisation
5.5.1   Arc melt samples
The microstructure of the arc melt Cu – 68.5 at. % Co alloy is shown in figure 5.24 below. The microstructure as expected is dendritic with no evidence of LPS. EDX gave the average composition of the dendrites as 84.27 at. % Co (± 0.02).
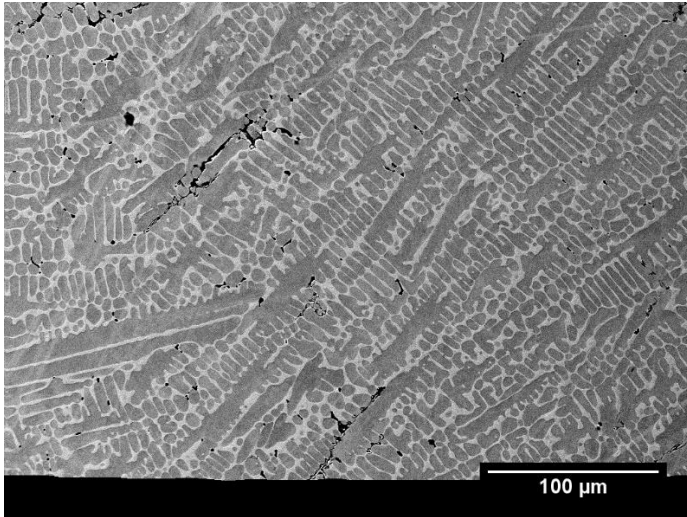
Figure 5.24 SEM backscatter image showing microstructure of arc melt sample of Cu – 68.5 at. % Co alloy.

The optical micrograph of some of the slices of the Cu – 50 at. % Co alloy ingot is shown in figure 5.25. The micrographs revealed in slices closest to the copper hearth dark structures in a light matrix (figure 5.25a - c). Some of the dark structures clustered together while some were not. The clustered particles were thought to be dendrites but higher magnification revealed these were spherical and spheroidised particles (figure 5.25b). The EDX analysis (shown in figures 5.25d - e) revealed the dark structures were Co - rich particles (average composition of 87.65 at. % Co ($\pm$ 0.02)) and the matrix was Cu - rich.

The un-clustered structures seems to divide or section into clustered spherical particles and particle free zones are observed in the microstructure (figure 5.25c). The existence of the particle free zones indicates that the volume fraction of the dispersed Co -rich phases in the matrix is low.

The clustering nature of the spherical particles mean that their rate of transport is high which in turn is expected to lead to coarsening effect but the spherical

particles appear to be of uniform size. Figures 5.25a – c seems to suggest the Cu – 50 at. % Co alloy had undergone LPS during the arc melting process.

Element	At %	
	Spectrum 6	Spectrum 7
Co	4.59	70.28
Cu	95.41	29.72
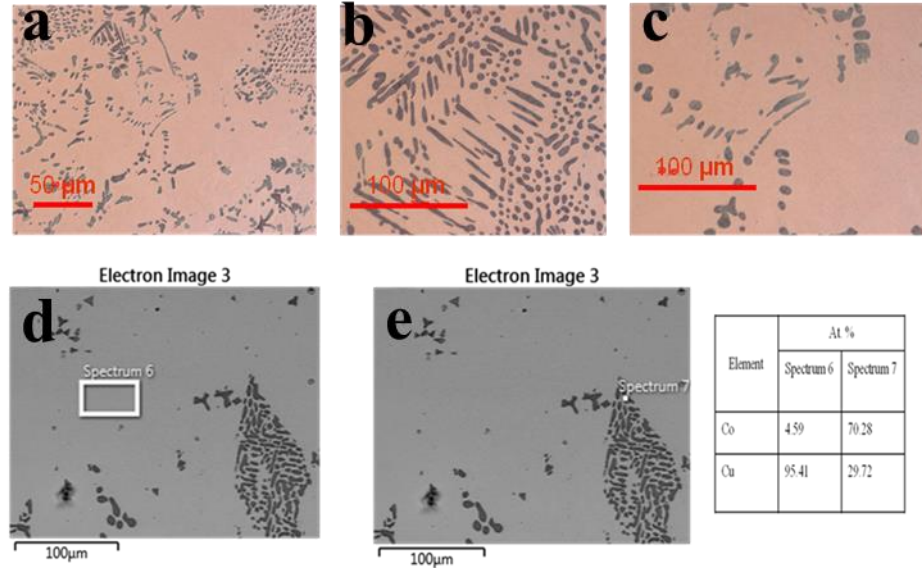
Figure 5.25 Optical microscopy images of arc melt sample of Cu – 50 at. % Co alloy (a) clustered structures, (b) higher magnification of (a) showing phase separated microstructure (c) particle free zones in the microstructure (d) and (e) showing EDX spectrum taken in the matrix and of the dark inclusions respectively.

5.5.2   Drop tube powders

In order to avoid ambiguity, a classification convention was adopted in naming the structures observed in the drop tube processed powders. The classification scheme is applicable to both alloys as there are no features unique to just one composition.

The structures are classified into two broad categories namely: (1) the non-liquid phase separated structures (NLPS) and (2) the liquid phase separated structures (LPS). These two categories are further divided into sub divisions, figure 5.26 below is the organogram of the classification system employed. The notations NLPS_D, NLPS_F, CS, DP, MS, SCS and ECS represents dendritic (which entails dendrites with visible secondary arm), fragmented dendrites (with no visible secondary dendrite arm), core shell

(entails all structures with two clearly defined phases), distributed phases (structures predominantly containing dispersed particles), mixed structures (shows characteristics of LPS and NLPS), stable core shell (comprises structures which have perfect or near perfect spherical core and shell), evolving core shell (which comprises of all coalescing structures with distinct regions in them, could be in form of loops, globules or non-perfectly formed SCS).

The LPS structures are observed to contain dispersed spherical structures, these are referred to as spherical particles in this write up. The spherical particles are either Co or Cu – rich.

Judging from the calculated phase diagram, the structures in the Cu – 50 at. % Co alloy are likely to have experienced spinodal decomposition due to the little or no gap between its binodal and spinodal curves while the structures in the Cu – 68.5 at. % Co alloy are expected to have only undergone binodal decomposition due to the high undercooling estimated to get it into the spinodal. A selection of these structures is presented in image 5.27.
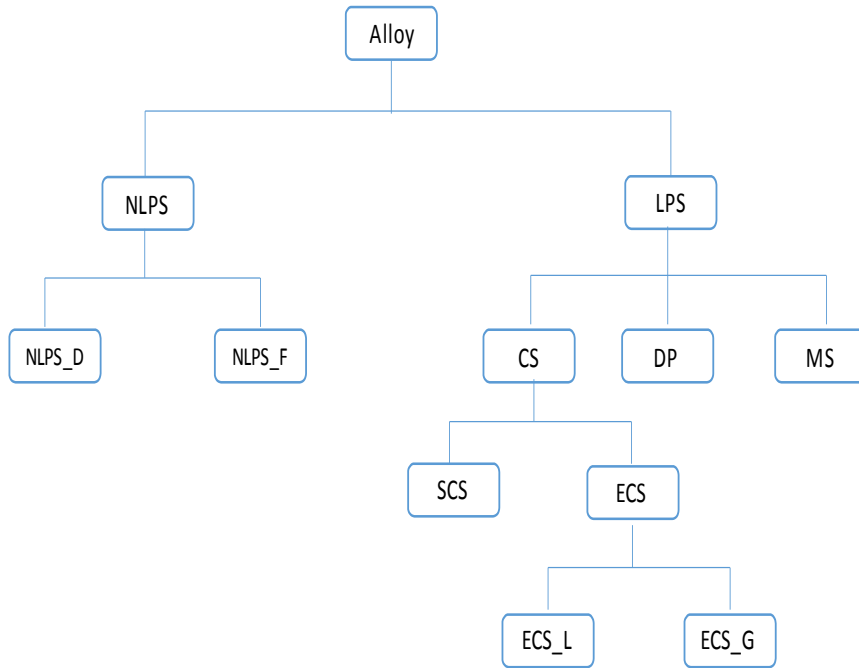
Figure 5.26 Organogram of structures in drop tube processed Co- Cu alloys. Observed structures are non-liquid phase separated (NLPS), liquid phase separated (LPS), non-liquid phase separated dendrites (NLPS_D), non-liquid phase separated fragmented dendrites (NLPS_F), core shell (CS), dispersed particles (DP), mixed structures (MS), stable sore shell (SCS), evolving core shell (ECS), evolving core shell loops (ECS_L) and evolving core shell globules (ECS_G).
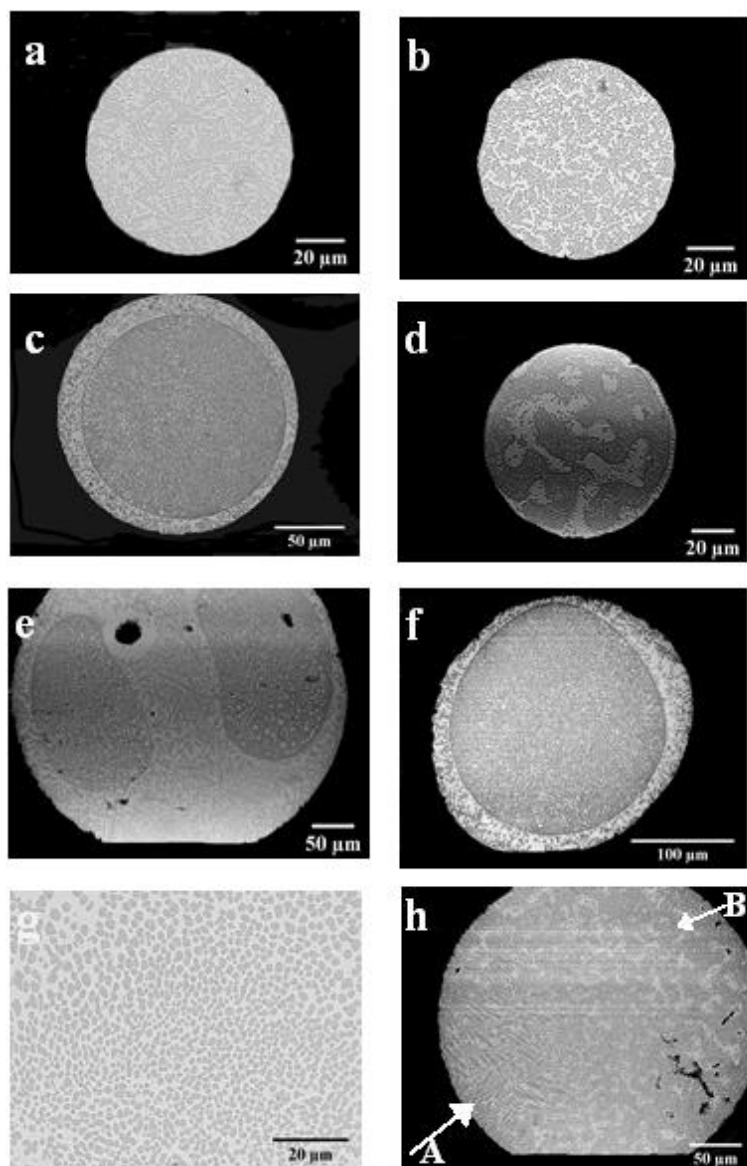
Figure 5.27 SEM back scattered images showing representative microstructures in drop-tube processed Co-Cu alloys: (a) and (b) show NLPS structures: dendritic, fragmented dendrites respectively. (c) is a typical SCS structure while (d) – (f) are ECS structures (d- loops, e-globules and f- non-perfectly formed SCS), (g) is high magnification micrograph of a droplet with dispersed particles and (h) is a droplet showing mixed structure (A is dendritic part, B is spherical particles region).

The dendritic structures in the Cu – 50 at. % Co alloy are observed to be much larger/ coarse and not as densely packed as those in the Cu – 68.5 at. % Co alloy an indication that the dendrite fraction is higher in the later alloy.

It was also noticed that the NLPS_D type structures in the Cu – 50 at. % Co alloy experienced hot tears (figure 5.28) which usually occurs as a result of resistance to liquid metal flow through the emerging inter – dendritic network. Hot tears are known to occur in alloys with high solid fraction towards the end of the solidification process and as such would be expected to occur in the Cu – 68.5 at. % Co alloy in which the volume fraction of α – Co dendrites was higher. However, this was not the case as they were predominant in the Cu – 50 at. % Co alloy. The reason for this is not known.
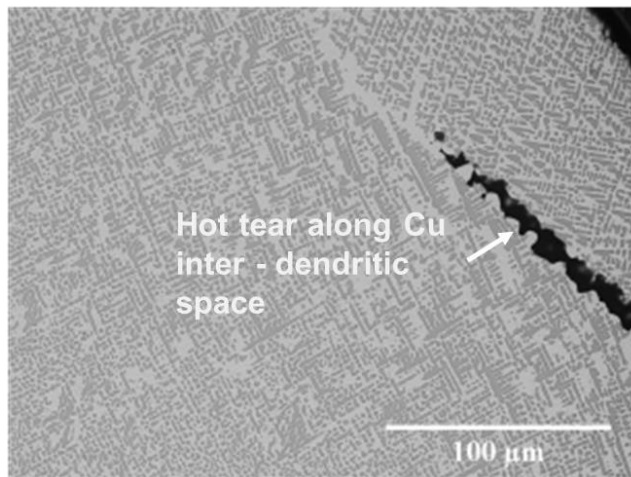
Figure 5.28 SEM Micrograph showing hot tears in droplet of the Cu – 50 at. % Co alloy.

The distributed phase separated structures (DP) is made up of all non-coalesced, non-dendritic, uniformly/ patterned distributed particles. These distributed particles are mostly spherical but there are instances where they are not. Droplets in which the distributed particles are spherical are assumed to have been frozen just after LPS occurred. Figure 5.27g is an example of a droplet in which spherical particles are dispersed while figure 5.29a and b shows magnified images thought to be good examples in which the types of dispersed structures are depicted. The dispersed non spherical particles (figure 5.29a) are believed to be formed from dendrites that are remelting

(which might explain the sequential arrangements noticed in some), so technically they are fragmented dendrites.
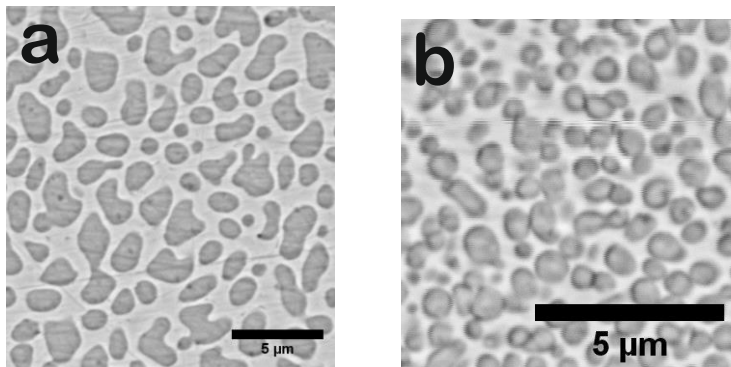
Figure 5.29 Magnified SEM images showing two types of distributed phases in the Co – Cu alloys (a) non spherical and (b) spherical distributed phases.

The group of droplets observed to contain regions believed to have undergone liquid phase separation and regions containing either NLPS_D or NLPS_F type structures are classified as mixed structures (MS). A magnified image of a typical structure in this category is shown in figure 5.30 in which spherical particles indicative of LPS are observed at the edges of the droplet and dendritic structures observed inwards. This image suggests that nucleation of the LPS structures occur at the edge of the droplets. This is discussed in detail later on.
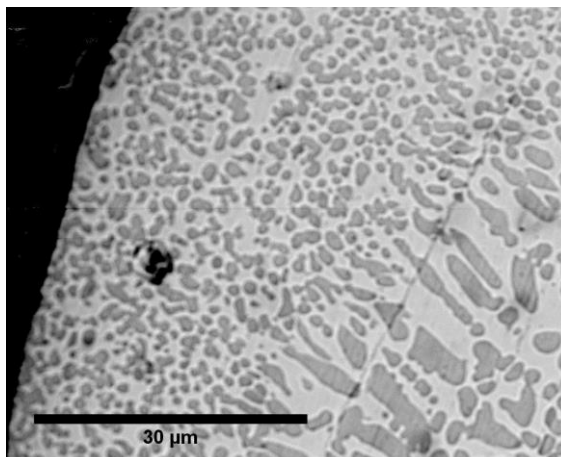
Figure 5.30 SEM image of a mixed droplet showing regions with LPS structures and NLPS structures.

The category CS is made up of stable (SCS) and evolving (ECS) core shell structures. A typical two-layer SCS structure produced in this study is shown in figure 5.27c. These are characterised by a darker L_1 phase (Co-rich) as the core at the centre of the droplet surrounded by a lighter coloured Cu-rich shell.

Higher magnification of these (figure 5.31) reveal that both the core and shell contain inclusions. The core contains many small Cu – rich particles dispersed in it while the shell is observed to contain either Co – rich spherical particles or dendrites and in some instances a mixture of both as inclusions.
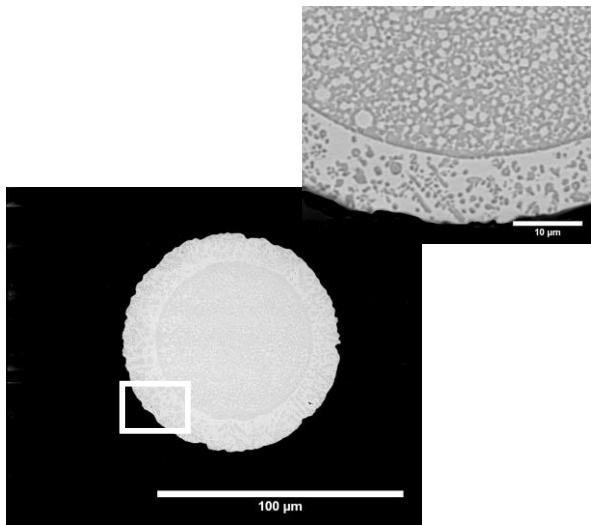
Figure 5.31 SEM micrograph of a typical stable core shell microstructure exhibiting mixed shell and a core with Cu – rich inclusions. The insert is magnified view of the portion in the rectangle.

All the SCS type structures had in common two rings around the core while the ECS type structures display only a single ring. The two ring configuration is typically an outer copper ring and an inner cobalt ring separating the main core and shell structures. These rings are thought to be segregation boundaries on the copper and cobalt rich sides of the core shell interface respectively. Figure 5.32a clearly shows the two distinctive rings in a typical SCS structure while the section in rectangle in 5.32b Cu – rich ring devoid of Co – rich inclusions since such can easily migrate into the Co – rich core.
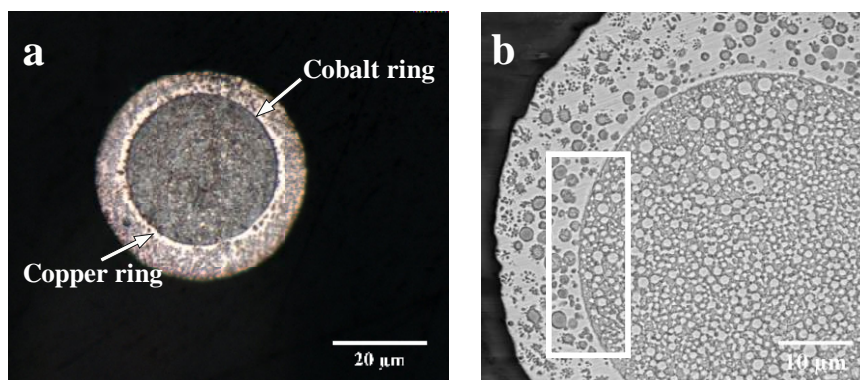
Figure 5.32 Images of (a) optical micrograph showing segregation rings in a SCS structure and (b) SEM magnified view of an SCS structure in which rectangular highlight show spherical particles at very close proximity to the copper and cobalt rings.

The structures shown in figure 5.27d – f are three different ECS type microstructures. A somewhat bi- continuous structure is shown in figure 5.27d. The figure clearly shows that the liquid phase separated Co and Cu – rich regions are coagulated but the complete migration of the Co – rich region to the centre has not yet occurred. As already stated, the Co – rich region contains Cu – rich spherical inclusions. The Cu – rich region on the other hand contains Co – rich inclusions but these are very few with those that are present being close to the boundary with the bulk Co-rich region, suggesting that migration was in progress when freezing occurred. It can be seen on the image the clear outline for the formation of a bulk, Cu-rich shell. Figure 5.27e shows another ECS type droplet in which the coagulation process is assumed to have progressed further than that in 5.27d as there are now two well developed, bulk Co-rich regions. The bulk Cu-rich region of this droplet contains Co - rich dendrites while the bulk Co-rich region contains numerous spherical Cu-rich particles. The Cu-rich particles were noticed to have filament like tails which suggest that the region is in motion. The non-spherical core-shell morphology in figure 5.27f is thought to be the final stage in the evolution towards the formation of a SCS structure.

A very small number of droplets appeared to have three layers, these could erroneously be classified as core-shell-corona or matryoshka type structures. However, given the low numbers of such structures occurring it was concluded that this is most likely a sectioning effect. A good example to demonstrate this is a spherical droplet with a structure as shown in figure 5.33a, when sectioned along the line 'X – X', would erroneously produce a core-shell-corona type structure, as shown in figure 5.33b.
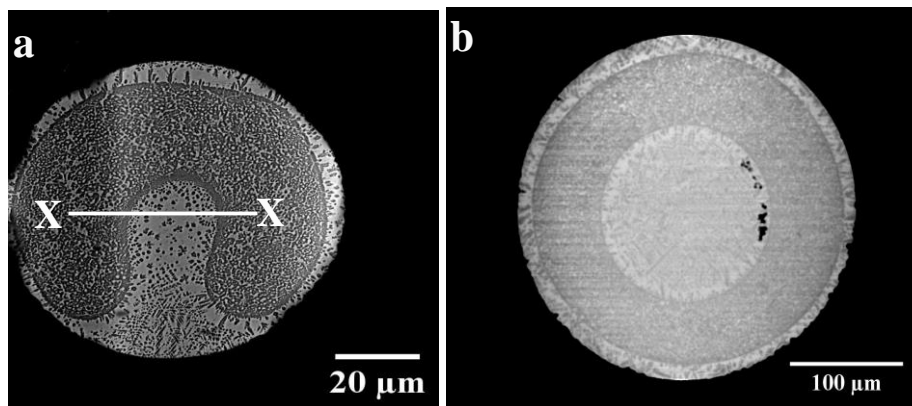
Figure 5.33 SEM images illustrating sectioning effect (along the line X-X in (a)) could be identified as a core-shell-corona structure (b).

5.6 Microstructure variation in rapidly solidified metastable Co – Cu drop tube powders

The frequency of the distribution of the LPS and NLPS structures in the two alloys as a function of sieve size fraction is shown in figure 5.34. Two observations are very clear from the figure (1) larger droplets with D > 106 μm consists mainly of the NLPS structures in both alloys and (2) LPS structures are more common in the Cu-50 at.% Co alloy than in the 68.5 at.% Co alloy. Both observations are to be expected as higher undercooling is estimated for the 68.5 at. % Co alloy to access the binodal and spinodal transition than would be the case for the 50 at. % Co alloy, with these higher undercooling being more likely in the smaller sieve fractions.

Lower limits of sieve droplet size (µm)	850	500	300	212	150	106	75	53	38	<38
NLPS%_Co50	106	95	138	211	108	195	142	120	77	60
LPS%_Co50	13	6	27	72	31	47	114	127	56	143
NLPS%_Co68.5	93	85	98	98	88	91	97	82	70	70
LPS%_Co68.5	7	15	2	2	12	9	3	18	30	30
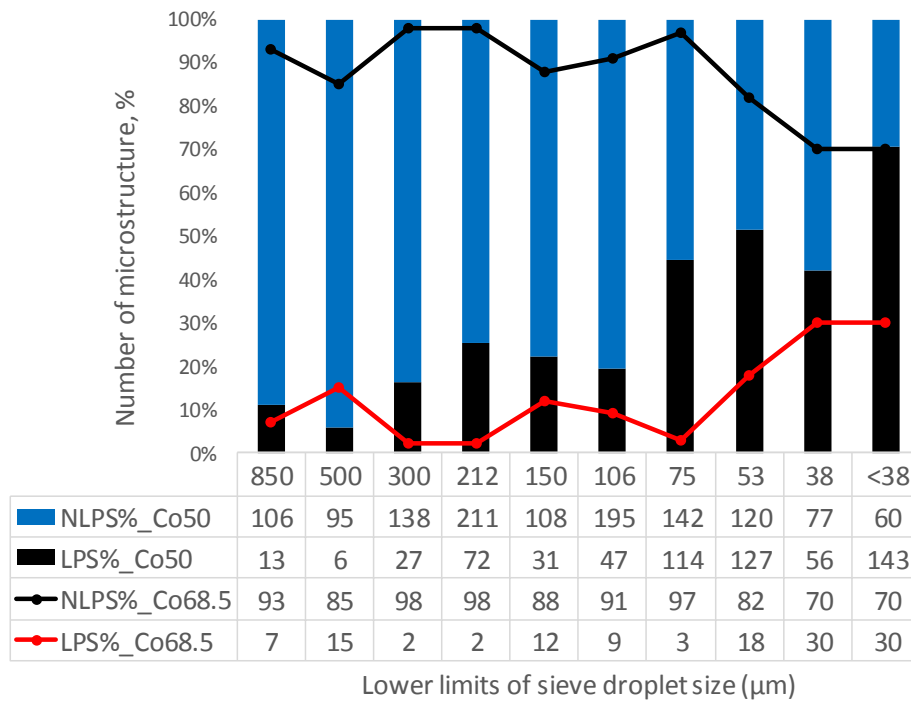
Figure 5.34 Distribution of microstructural types as a function of droplet diameter in drop-tube processed Co-Cu alloys. More LPS structures were observed in the Cu-50 at. % Co alloy. The last four rows of the table on the x-axis show the actual number of observation of the microstructures.

A pattern is observed in the distribution of the NLPS microstructures. In figure 5.35 the percentage of the structures in the NLPS_D category is observed to decrease as the droplet size reduces while the percentage of NLPS_F structures increases. Additionally in the plot of the Cu – 68.5 at. % Co alloy it is observed that the percentage of NLPS_F structures in smaller droplets (d < 53 µm) is almost constant. Generally, there are more NLPS_F structures than NLPS_D and is the dominant structure in this alloy. In both alloys there seems to be preferential nucleation of dendrites from clusters of spherical particles and similar to the findings of Wang and Wei [130] and Liu et al. [132], most of the dendrites (NLPS_D) were aligned. Figures 5.36a and b show dendrites growing outwards (from clusters within the droplet) and inwards (from clusters at edge of droplets) respectively.
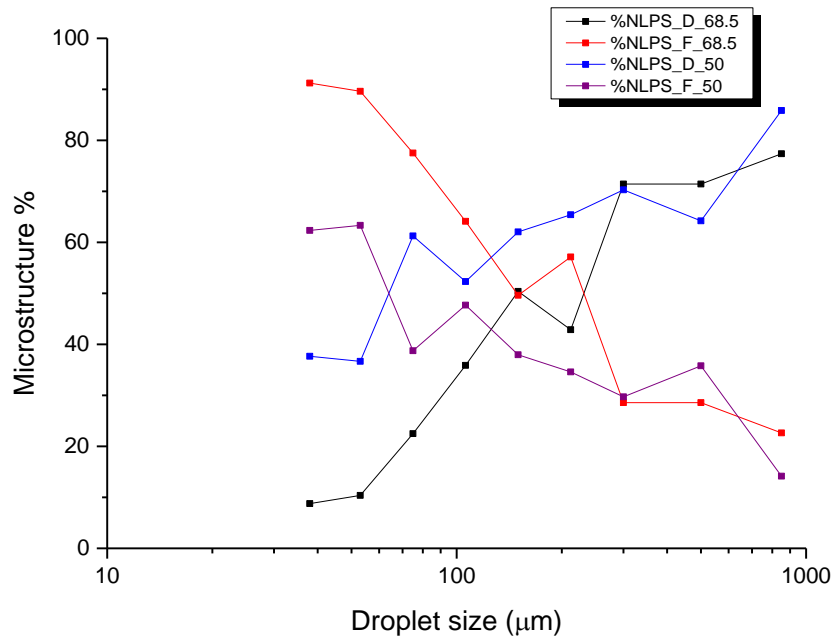
Figure 5.35 Distribution of dendritic (NLPS_D) and fragmented dendrites (NLPS_F) structures in drop tube powder of the Cu – 50 at. % Co alloy and Cu – 68.5 at. % Co alloys.
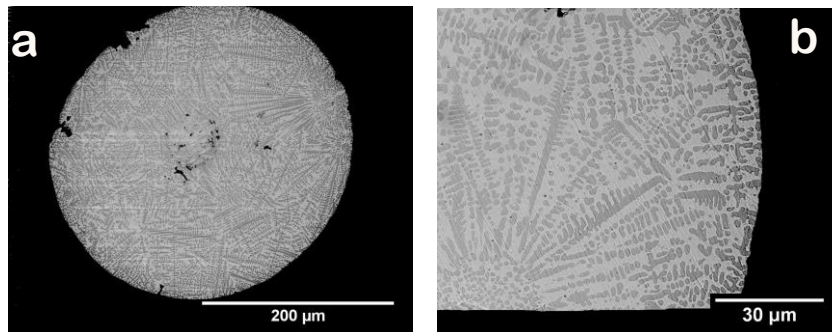
Figure 5.36 SEM micrograph showing (a) dendrites nucleating from clusters of spherical particles at the tip of the droplet and (b) nucleating dendrites growing outwards.

A further breakdown of the LPS structures for both alloys is shown in figure 5.37 and figure 5.38 for the 50 at. % Co and 68.5 at. % Co alloys respectively. With reference to figure 5.37 it can be seen that for cooling rates in the range of 10^3 K s^{-1} to 10^4 K s^{-1} (corresponding to droplets in the sieve fractions from 300 μm down to < 38 μm) the whole range of LPS microstructures were

observed. Also observed is the steady increase in the percentage of SCS type microstructures as the droplet diameter decreases and the cooling rate increases, with a maximum occurring at 2.7 x 10^4 K s^{-1} (75 μm diameter), at which 87% of the sampled structures were of the SCS type. With further increase in the cooling rates a steep decline in the percentage of SCS type structures is observed. This behaviour reflects the influence of the cooling rate and undercooling on the time available for coalescence after liquid phase separation.

At low cooling rates, low undercooling will be achieved so relatively little time will be available after liquid phase separation for coalescence. At increased cooling rate the undercooling is also increased and LPS occurs much quickly thereby giving longer time for coalescence to occur. However, at very high cooling rates, despite large undercooling presumably being attained, the rapid extraction of heat means that the time available for coalescence again decreases, leading to an increase in partly coalesced (ECS) or non-coalesced (category DP and MS) structures.

In figure 5.38, it is seen that in the 68.5 at. % Co alloy at cooling rates below 5000 K s^{-1} ($d > 212$ μm) due to the higher undercooling required to initiate liquid phase separation there is very little time available for coalescence hence DP and MS type structures dominate. In contrast at cooling rates in excess of 5000 K s^{-1} ($d < 212$ μm) there is sufficient time after liquid phase separation for coalescence to occur, leading to an increase in SCS and ECS type structures. This results in a maximum occurrence of SCS structures (85%) at cooling rate of 1.5 x 10^4 K s^{-1} (106 μm diameter). These results implies that LPS structures in metastable monotectics are mainly dependent on the cooling rate and undercooling and not on the Marangoni velocity alone at portrayed in most literature.

The results also show a distinctly different trend for metastable monotectic alloys to that found by Wang et al. [127] for stable monotectics, with the difference being explainable in terms of the cooling rate and undercooling required to initiate metastable liquid phase separation and as such possible at all compositions with the miscibility gap.
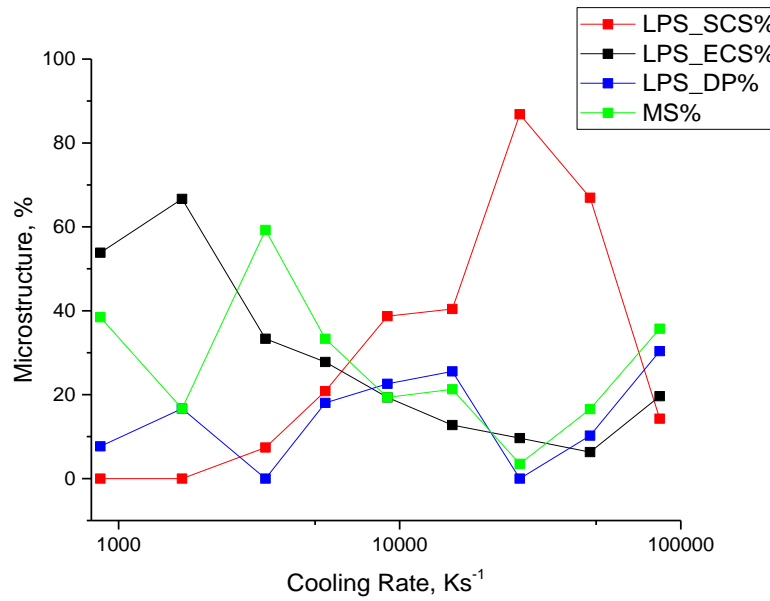
Figure 5.37 Variation of phase separated structures with cooling rate in the Cu-50 at. % Co alloy.
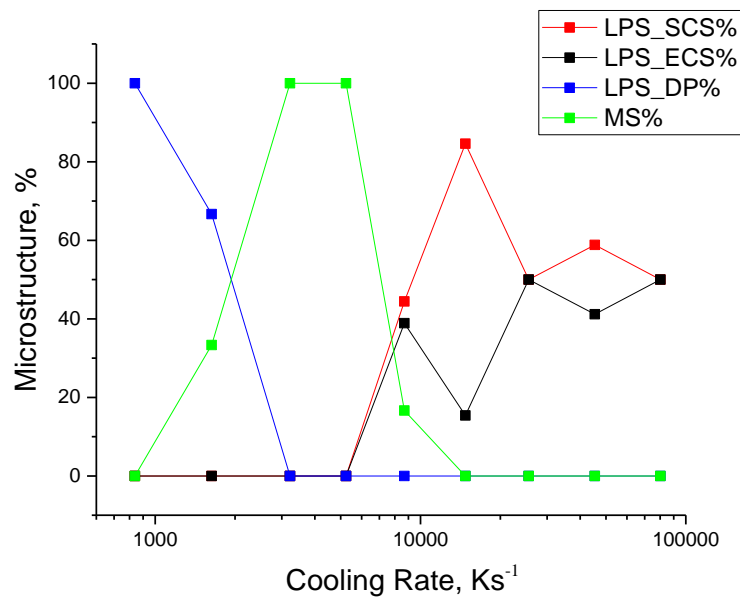
Figure 5.38 Variation of phase separated structures with cooling rate in the Cu - 68.5 at. % Co alloy.

An attempt is made to find the size distribution of the dispersed Cu – rich particles in the core of the Cu – 50 at. % Co alloy because it is most prevalent in this alloy in comparison to the Cu – 68.5 at. % Co alloy. SCS structures were randomly selected from three sieve size range (300 – 212, 150 – 106 and 106 – 75 µm). The frequencies of the apparent radius of these particles were normalised with respect to the overall particle population per size. Figure 5.39 shows the frequency distribution of the Cu – rich inclusions in the samples.

A bimodal distribution of the Cu – rich inclusions is observed in the three sieve fractions. A primary peak is observed to occur at ln (r) < 3 and a secondary peak at ln (r) > 3. In the 300 – 212 µm samples, the primary peak is centred at ln (r) = 2.8 with frequency of 7 % while the secondary peak is centred at ln (r) = 4.67 with frequency of 42 %.

In the 150 – 106 µm samples, the primary peak is centred at ln (r) = 2.35 and has a frequency of 34 % while the secondary peak is at ln (r) = 3.25 with frequency of 90 %.

In the 106 – 75 µm droplet category, the peak of the smallest Cu – rich inclusions was centred at ln (r) = 0.2 and has a frequency of 85 % while the larger particles with a frequency of 19 % were centred at ln (r) = 3.2.
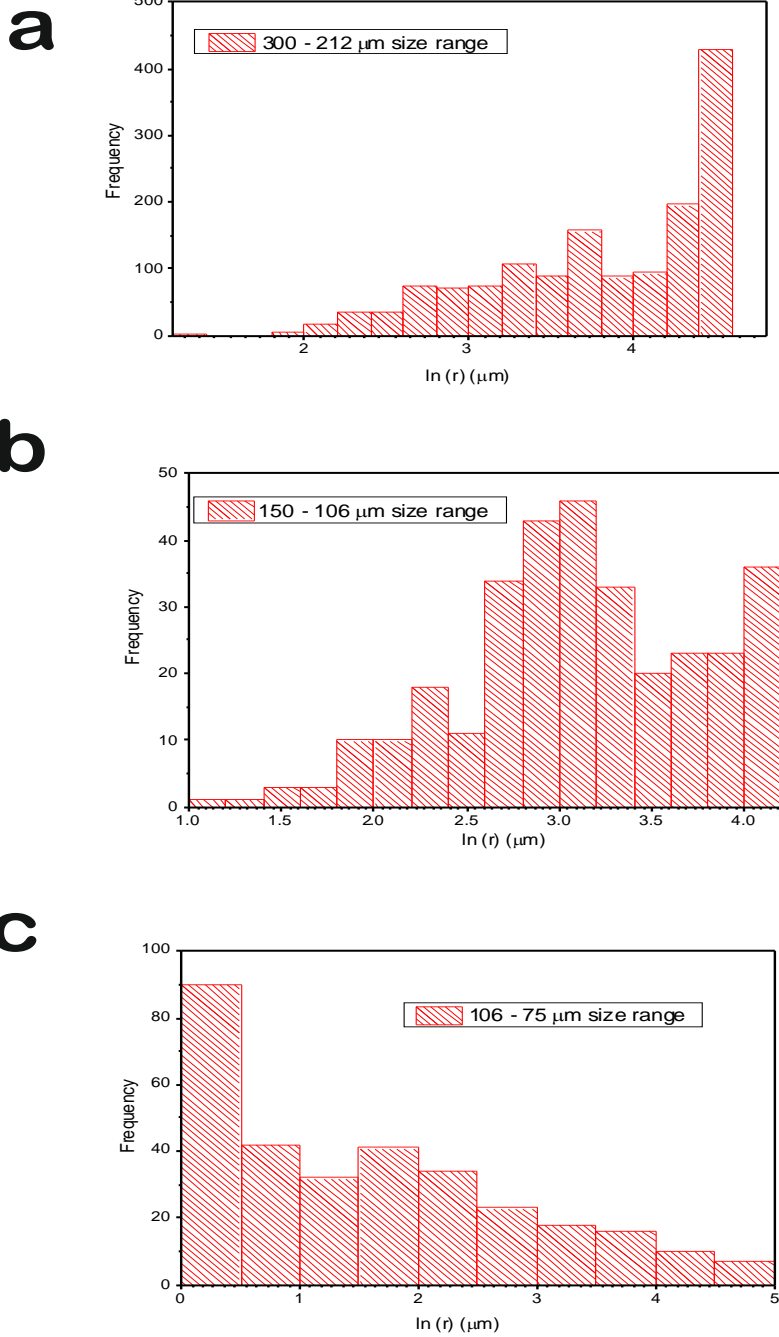
Figure 5.39 Distribution of Cu – rich inclusions in the core region of stable core shell structures in Cu – 50 at. % Co alloy.

These results imply that as the undercooling increases, the dispersed Cu – rich inclusions in the core region reduces. This is reasonably so as undercooling is generally higher in smaller droplets due to higher cooling rates.

Also, from the bimodal size distribution of the inclusions, the bigger particles are much more frequent in the various size range (except in the last category) further proving that LPS occurred in the alloy and in the sizes considered. It is rather interesting that in the 106 – 75 μm size range, the smaller inclusions showed dominance which might suggest that monotectic solidification occurred in the droplets in this range. However, there were no microstructural evidence in support of this though the size range is made up of about 60 % of NLPS structures.

5.7 Volume fraction and surface tension effects on core shell microstructure formation

The analysis in this section is also limited to the Cu – 50 at. % Co alloy due to the very low number of SCS structures in the Cu – 68.5 at. % Co alloy. Most of the literature on core shell microstructure stated that the core was formed by the phase with the lower volume fraction [110,117,185,186].

Figure 5.40 shows the experimental results of the volume fraction of the shell (L$_2$) phase in the Cu – 50 at. % Co alloy. It is observed that the shell phase varied from 10 to 82 %. However, in contradiction to the earlier reports, the morphology of the SCS structure in both the alloys were identical (figure 5.42). This is consistent with literature in that the core was always formed by the higher melting point phase irrespective of its volume fraction. If this were not the case a reversal of the core and shell materials would be expected from one alloy to the other and this was never observed. The implication of this is that the impact of volume fraction on phase selection in the metastable Co-Cu alloys was minimal. An explanation for this is that the higher melting point phase (here the Co – rich phase) has the higher surface tension which in turn drives inward migration. This is in line with the observation that in Co - Cu alloys surface segregation arises due to the phase with the lower surface tension completely wetting the higher energy phase and adheres to the surface of the parent droplet in order to minimise its free energy [84,103].
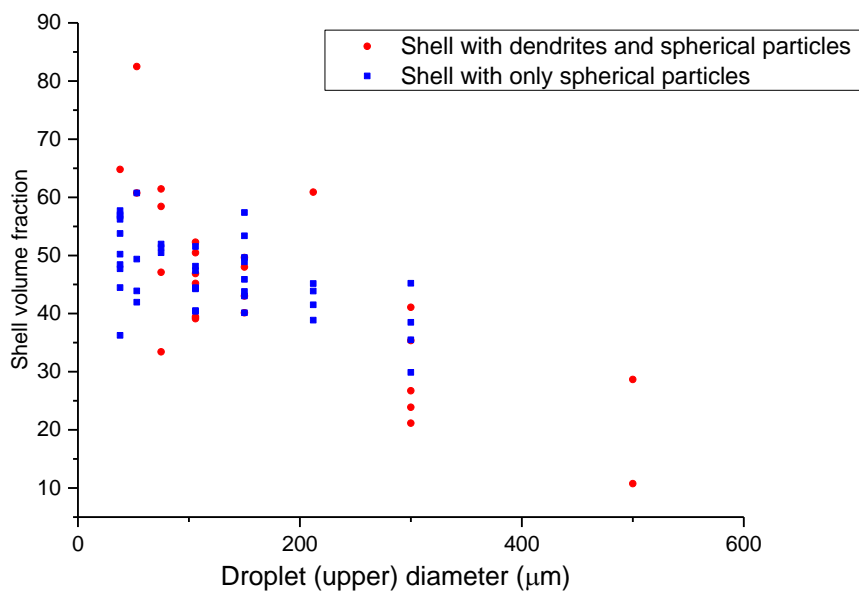
Figure 5.40 As – measured volume fraction of the shell (L$_2$ phase) in Cu – 50 at. % Co alloy.

The spread of the L$_2$ volume fraction can however not be inferred from figure 5.40 due to statistical errors arising from the sectioning. To overcome this, Monte Carlo simulation was done in order to predict the true shell volume fraction with the result presented in figure 5.41. It can be seen from the simulation result that the actual variation is from around 8 to 75 % and as the droplet diameter decreases (increased undercooling) dendritic shells become more prevalent. This is due to the constantly adjusting composition as the undercooling increases and as such the phases solidify at different rates.
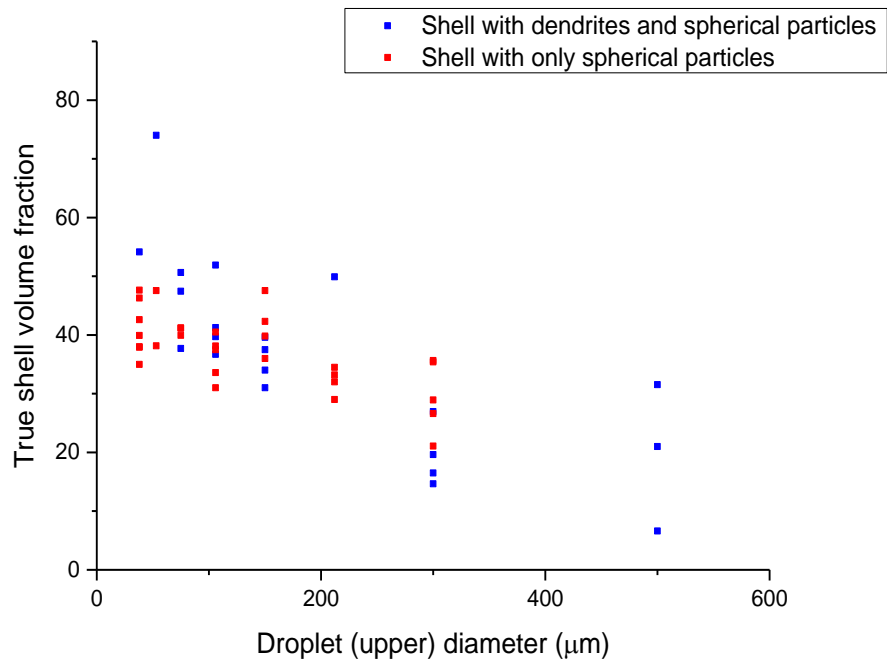
Figure 5.41 Monte Carlo simulation for the shell volume fraction in Cu – 50 at. % Co alloy.
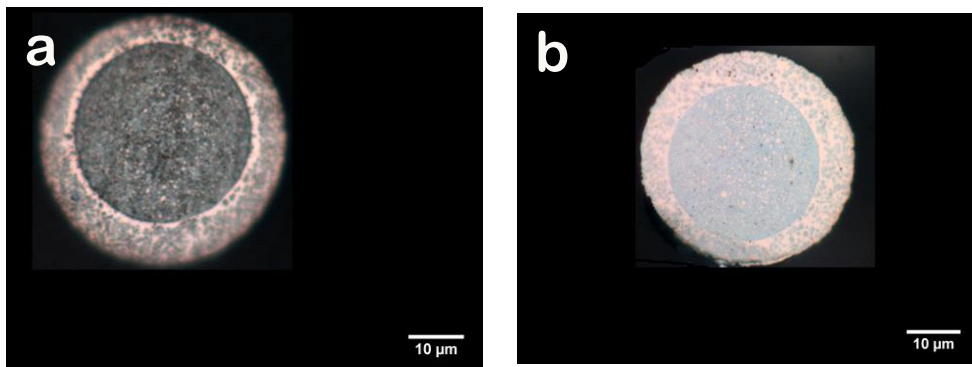
Figure 5.42 Optical micrograph of stable core shell microstructures from the (a) Cu – 50 at. % Co (etched in Nital) and (b) Cu – 68.5 at. % Co alloys (unetched). Both images are from the 53 – 38 μm sieve fraction size.

5.8 Cooling rates from secondary dendrite arm spacing

As earlier mentioned in section 3.4.1, the cooling rate can also be determined from experimental data by measuring the secondary dendrite arm spacing, SDAS.

The approach is to use estimated cooling rates from heat balance as a function of droplet size as reference for establishing a relationship between the cooling rate and the SDAS.

SDAS measurements were then taken from SEM images. Figures 5.43 and 5.44 shows two methods of taking such measurements. In the example shown in figure 5.43, the SDAS is measured by measuring the distance between the dendrite arms while in figure 5.44, the SDAS is determined by taking the length of the trunk and dividing by the number of visible arms.

Figure 5.45 shows an example of the frequency distribution of the SDAS in the $500 - 300$ µm range of the $Cu - 50$ at. % Co alloy.

The average per size range was tabulated (table 5.11) and then plotted against the estimated cooling rate, this is shown in figures 5.46 and 5.47 for the $Cu - 50$ at. % Co and $Cu - 68.5$ at. % Co alloys respectively. Each SDAS point on the plot represents an average value of 54 measurements in the $Cu - 50$ at. % Co alloy. Due to the fact that most of the dendrites in the $Cu - 68.5$ at. % Co alloy were fragmented, the sample size was relatively low.
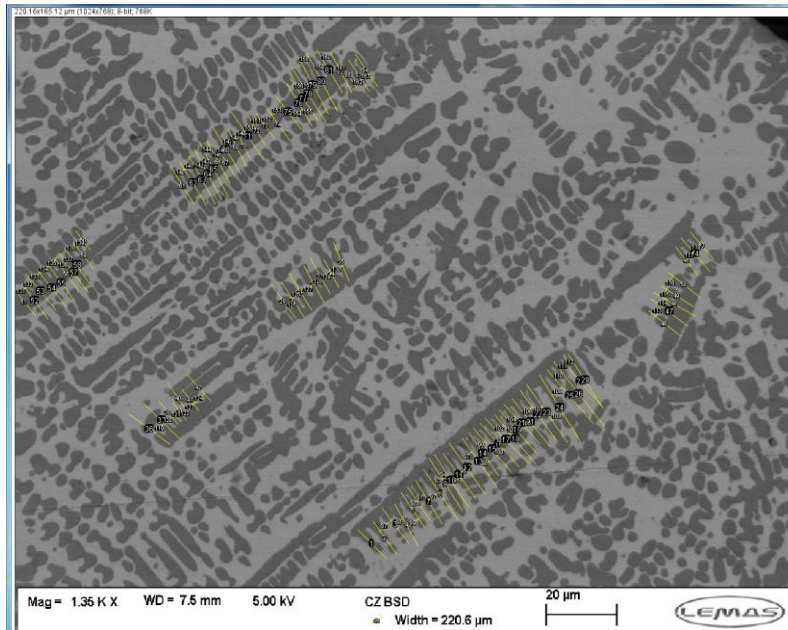
Figure 5.43 Sample measurements of SDAS in Cu – 50 at. % Co alloy by measuring the mid-point of adjacent dendrite arms.
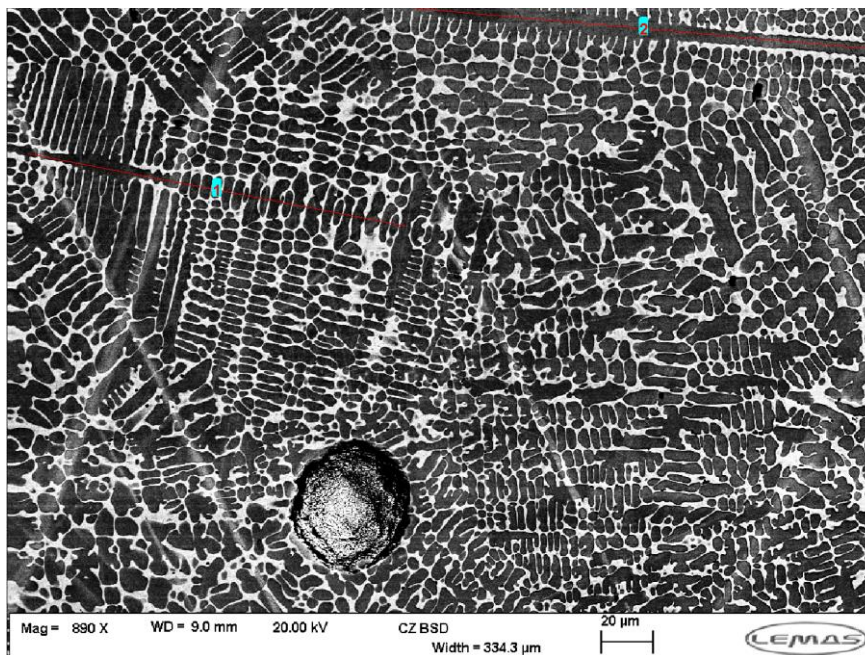
Figure 5.44 Sample measurement of SDAS in Cu – 68.5 at. % Co alloy by measuring the length of the dendrite trunk and dividing by the number of visible arms.
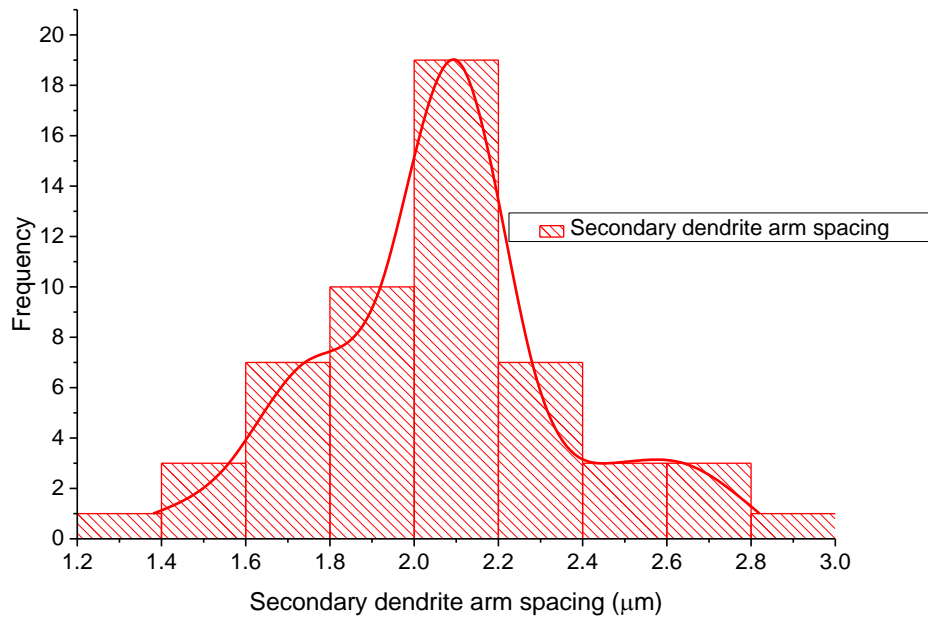
Figure 5.45 Frequency distribution of SDAS in 500 – 300 μm sieve size range of the Cu – 50 at. % Co alloy.

Table 5.11 SDAS measurements in different droplet size range in drop tube processed Co - Cu alloys.

Lower droplet diameter range (μm)	Mean SDAS (50 at. % Co alloy)	Error	Mean SDAS (68.5 at. % Co alloy)	Error
850	2.33	0.0620	4.47	0.224
500	1.94	0.0656	3.80	0.154
300	2.06	0.0417	3.23	0.202
212	1.72	0.0427		
150	1.69	0.0475		
106	1.25	0.0350		

An inverse relationship is said to exist between the SDAS and cooling rate according to equation (3.4). The fitted relationship between the cooling rate and the experimentally measured SDAS is given in equations (6.1 and 6.2) for the Cu – 50 at. % Co and Cu – 68.5 Co alloys respectively.

$$\lambda_{SDAS} = 8.2337(\dot{T})^{-0.184} \tag{6.1}$$

$$\lambda_{SDAS} = 22.411(\dot{T})^{-0.24} \qquad\qquad (6.2)$$

Contrary to literature that the exponent value is between 0.3 and 0.5, results for the Co – Cu system gave a value outside this range and it is approximately 0.2 in both alloys (0.184 for the 50 at. % Co alloy and 0.24 for the Cu – 68.5 at. % Co alloy).
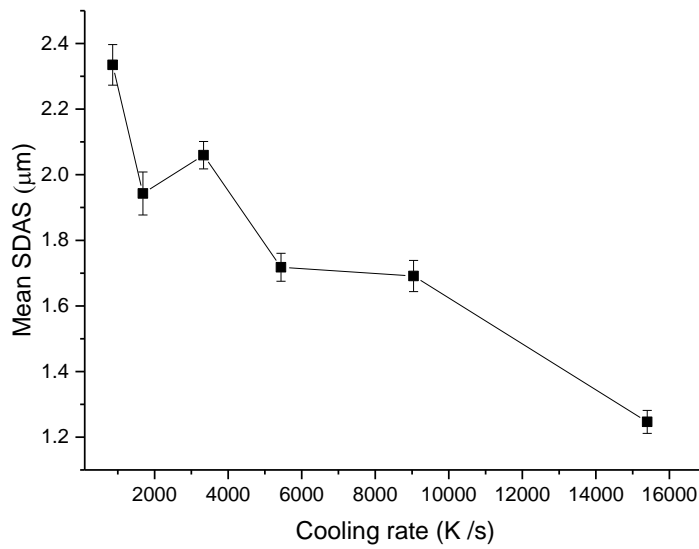
Figure 5.46 Secondary dendrite arm spacing (SDAS) variation with cooling rate for different diameter of Co – Cu drop tube powders of composition 50 at. % Co.
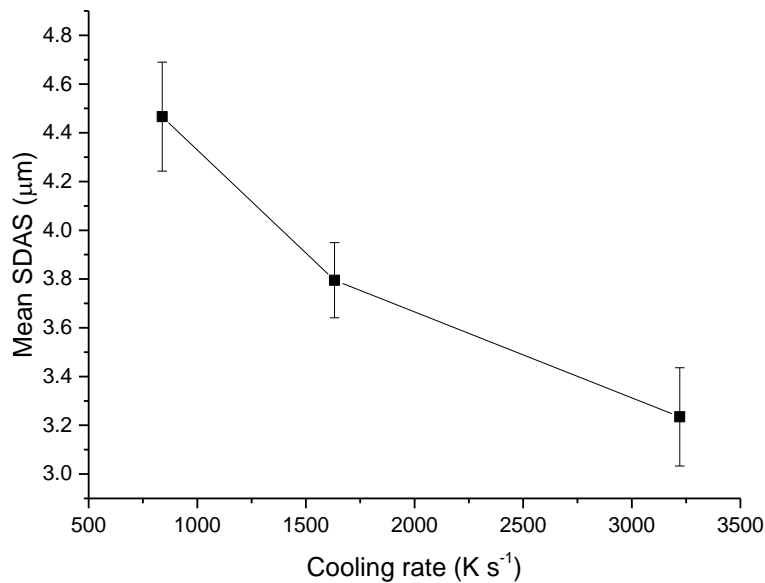
Figure 5.47 Secondary dendrite arm spacing (SDAS) variation with cooling rate for different diameter of Co – Cu drop tube powders of composition 68.5 at. % Co.

5.9   Thermal analysis

XRD analysis has established the presence of two phases in the alloys and these metastable LPS structures have been confirmed by microstructural evidence.

The drop tube powders as well as the starting arc melt sample were then subjected to DTA in order to determine the onset temperature of the metastable phase transformations that occurred. All samples were heated at the rate of 15 Kmin^{-1}.

The arc melt sample of the Cu – 50 at. % Co alloy has been excluded from this analysis due to its inhomogeneous appearance and difficulty in extracting the mixed section.

Also, due to the limited amounts of drop tube powder available for analysis, only droplets from the largest and smallest sieve size range were analysed (850+ and < 38 μm). As a result, the effects of heating rate on the alloys was not investigated. The retrieved powder samples from the DTA were black in

appearance probably due to release of Cu oxides which would explain some of the peaks in the second process cycle. Aside from oxide contamination, loss of homogeneity and non-rapid solidification, DTA curves from the second cycle upwards are most likely not representative of the starting alloy composition hence only the first process cycle is considered. The second cycle curves are in the appendix.

Baseline artefacts were observed on some of the DTA curves (figure 5.48), these are identified but not discussed as they are not part of the transformation details of the alloy but of the reference sample. The baseline was subsequently subtracted from all the curves.

5.9.1 DTA results of arc melt Cu – 68.5 at. % Co alloy

The DTA curves of the first heating and cooling cycle of arc melt sample of Cu – 68.5 at. % Co alloy is shown in figure 5.48. On the heating curve, the hump at around 400 K is clearly a baseline artefact while the cooling curve artefacts are observed at 1090.11 K and 1468 K.

There are two strong endothermic events on the heating curve. The first one is observed to have onset temperature of 1373 K which lies just above the peritectic temperature (1366.5 K). The composition at this temperature is majorly copper and as such taken as the melting temperature (T_m) of the Cu – rich phase (melting point of pure copper and cobalt is 1358 K and 1768 K respectively). As is expected all present solid transforms into liquid at the liquidus temperature. This is shown by the second endothermic peak of 1669.43 K. The temperature of this peak lies just above the liquidus line of the alloy however its onset temperature (1663.86 K) lies exactly on the liquidus hence is taken as the liquidus temperature. The observed peak of this event is probably due to latent heat of fusion.
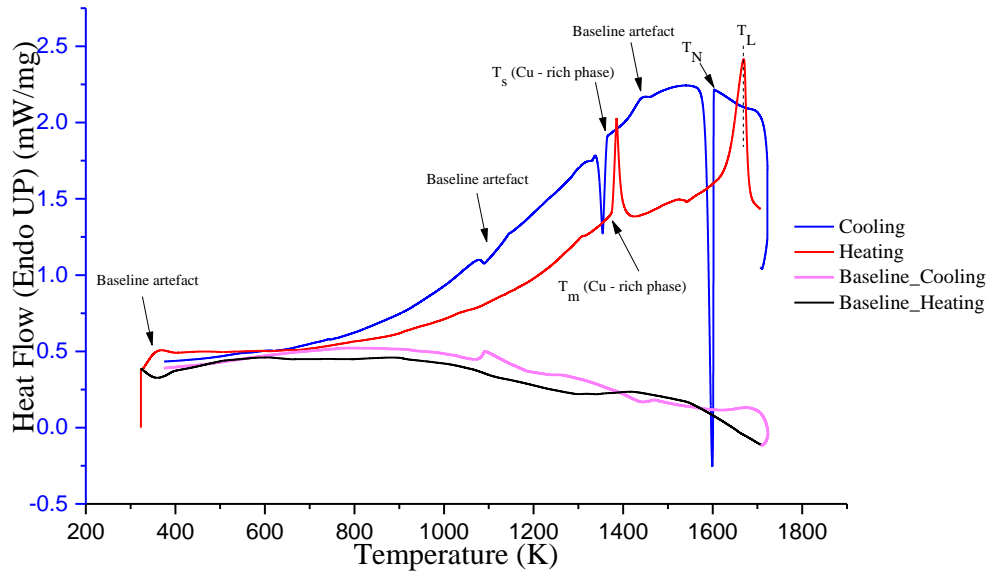
Figure 5.48 First cycle DTA curves of arc melt Cu − 68.5 at. % Co alloy showing the T_m of the Cu − rich phase and T_N of α − Co dendrites.

The first exothermic event on the cooling curve shown by a very strong peak occurred at 1599.05 K with an onset temperature of 1636 K which falls slightly below the liquidus. Using the equilibrium phase diagram, the alloy falls within the L + α region at this onset temperature and is characterised by a liquid phase volume fraction of 56.72 %. The alloy composition at this temperature was found to be 81.66 at. % Co, this explains the strong peak which is most likely due to the formation of α − Co hence the nucleation temperature, T_N = 1636 K for this alloy sample.

This is confirmed by microstructural image of the DTA sample (figure 5.49) below.
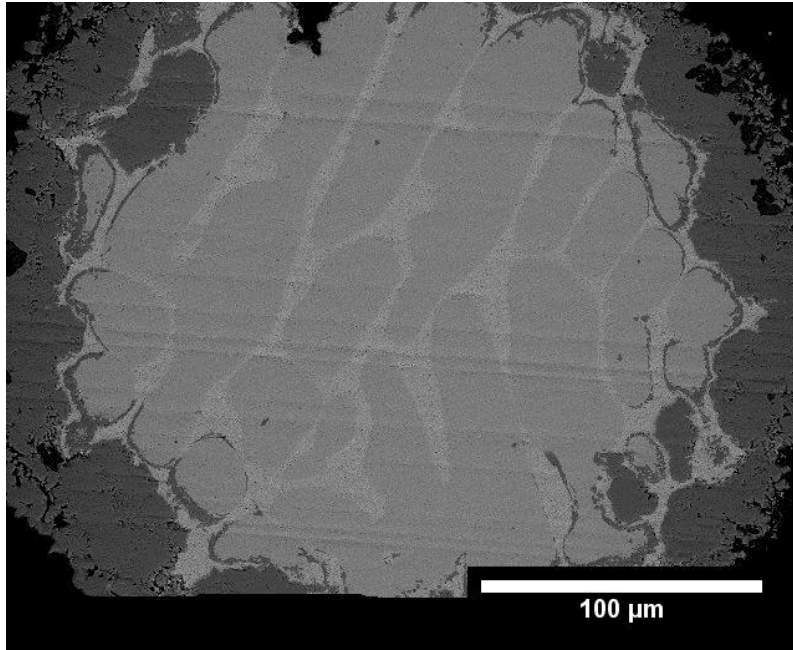
Figure 5.49 Back scattered SEM image of DTA sample of arc melt Cu –
68.5 at. % Co alloy.

The second exothermic event with onset temperature of 1375 K corresponds
to the solidification of the Cu – rich phase (in this case would be of the Cu –
rich inter dendritic space).

5.9.2 DTA results of Cu – 68.5 at. % Co alloy drop tube powders

5.9.2.1 850+ µm powder Cu – 68.5 at. % Co alloy

The DTA heating curve for this drop tube powder sample of the alloy (850+
µm) (figure 5.50) is not very different from that of the arc melt sample (figure
5.48). The only difference is that the peaks are slightly shifted. The T_m of the
Cu – rich phase for instance is 1372.71 K compared to 1373.00 K in the arc
melt sample. The onset temperature of the second endothermic peak is at
1631.60 K.

The DTA cooling curve of this powder sample also has some notable
difference compared to that of the arc melt sample. The baseline artefact
identified at 1090.11 K in the arc melt sample is shifted to 1097.59 K in this

powder sample. The interesting thing however is that the feature is considerably wider in this sample. The transformations occurring on the equilibrium phase diagram of the Co – Cu system at lower temperatures are the magnetic transformation which occurs at around 1323 K and eutectoid transformation at 695 K. There is no way of concluding if this feature is an artefact or a feature of the alloy however, it is suspected to be the magnetic transformation temperature which has been said to be lowered with increasing Cu content.

If the above is the case, it means the alloy went over the peritectic line and as such the use of the equilibrium phase diagram is justified.
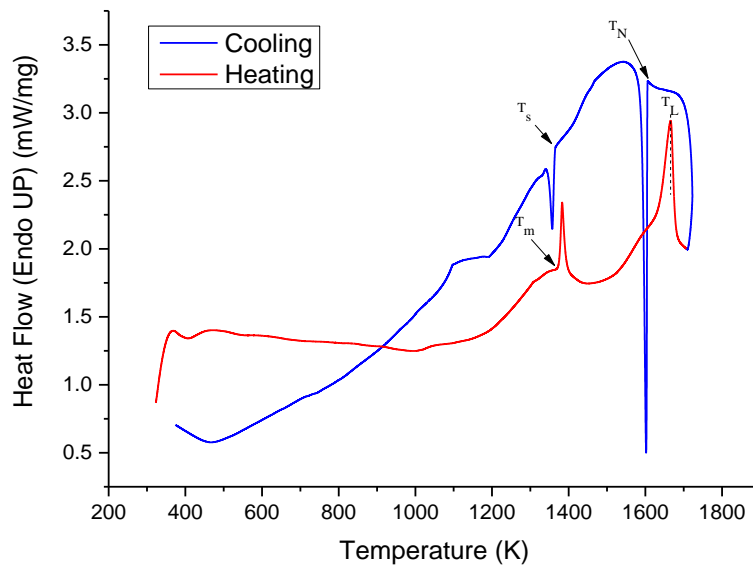
Figure 5.50 DTA plots of the 850+ μm drop tube powder of Cu – 68.5 at. % Co alloy showing melting temperature (T_m) of Cu – rich phase and nucleation temperature (T_N) of α – Co dendrites.

5.9.2.2   < 38 µm powder Cu – 68.5 at. % Co alloy

The DTA details of this alloy powder are very different from the two discussed so far. There are four endothermic and exothermic events each on the DTA curves (figure 5.51).

The T_m in this powder size is 1374.85 ($\pm$ 0.2℃) K which when compared with the arc melt sample differs by 1.85 K as against 0.26 K of the 850+ µm powder. Two small departures from the DTA baseline are also observed after the first endothermic event on the heating curve. These occurred at 1443.00 K and 1484.00 K. This suggests some sort of weak reactions occurred at these temperatures. It is rather interesting that when the temperature 1443.00 K was traced on the metastable phase diagram, it coincides with the binodal and spinodal curves. Due to the estimated high undercooling needed to bring this alloy into the spinodal region, it is highly unlikely to have spinodally decomposed during the DTA. On tracing it on the equilibrium phase diagram however, it touches the liquidus and also falls within α – Co region. The composition of the liquid is calculated to be 59.95 at. % Cu while the volume fraction of α – Co phase is given as 33%. The final endothermic event characterised by a very broad peak occurred at onset temperature of 1542.00 K. The lowest exothermic event on the cooling curve which is a small departure from the baseline occurred at 1176.00 K. Again this is thought to be the magnetic transformation temperature although the energy observed to be associated with it is rather low (-1. 3270 J/g). The onset temperatures of 1620.00 K, 1616.00 K and 1373.00 K are observed for the first, second and third exothermic peaks on the cooling curve respectively.
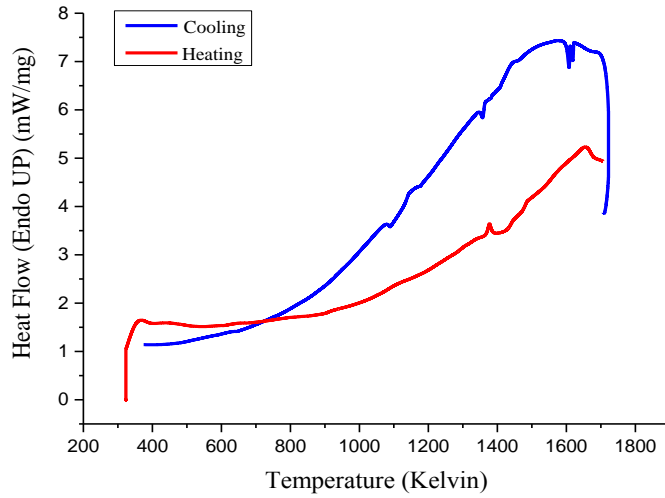
Figure 5.51 DTA plots of the < 38 μm drop tube powder of Cu – 68.5 at. % Co alloy.

5.9.3 DTA results of Cu – 50 at. % Co alloy drop tube powders

5.9.3.1 850+ μm powder Cu – 50 at. % Co alloy

The DTA curve for this powder size is presented in figure 5.52. The endothermic peaks on the heating curve at 1385.54 K and 1645.58 K have onset temperatures of 1294.80 K and 1522.00 K respectively.

The first onset on the equilibrium phase diagram falls in the (α + β) region with the Co – rich phase having a volume fraction of 50.66 at. %. The second onset temperature places the alloy in the L + α region with the composition of the liquid phase being 87.46 at. % Cu. The volume fraction of α – Co phase is 53 % and has a composition of 16.19 at. % Cu. The first exothermic onset on the cooling curve is at 1589.00 K and it also places the alloy in the L + α region but the composition of the liquid has reduced to 80.6 at. % Cu. This generally explains the shift between the heating curve endothermic and cooling curve exothermic peaks as during solidification the composition is constantly adjusting. The volume fraction of α – Co phase is 48.86 %. The second exothermic onset corresponds to the T_s of the Cu – rich phase.

193
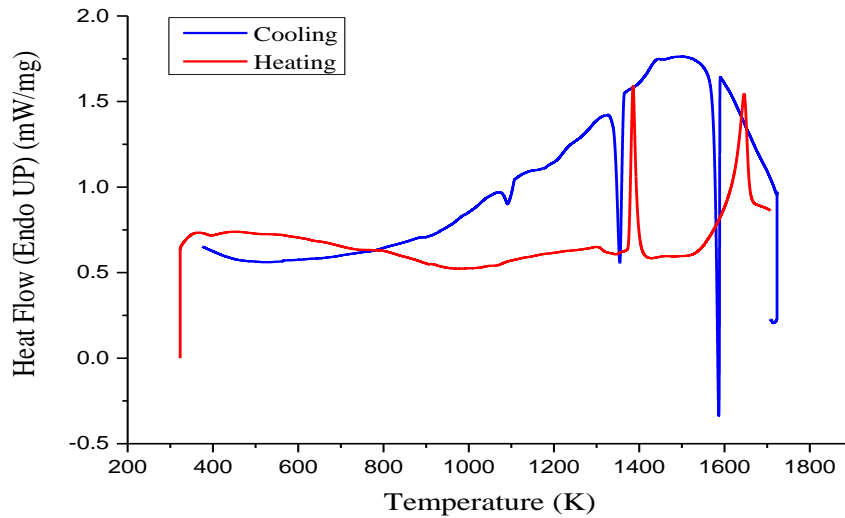
Figure 5.52 DTA plots of the 850+ μm drop tube powder of Cu – 50 at. % Co alloy.

5.9.3.2 < 38 μm powder Cu – 50 at. % Co alloy

The DTA plot of this powder size also showed two endothermic events on its heating curve (figure 5.53) with onset temperatures 1374.00 K and 1621.00 K. Since no indication of any metastable transformation, the equilibrium phase diagram is also used in analysing the plot. The first onset corresponds to the T_m of the Cu – rich phase having composition of 94.25 at. % Cu. The onset of the second endothermic peak places the alloy in the L + α region, the liquid having a composition of 71.60 at. % Cu which is lesser than observed in the 850+ μm drop tube powder of the alloy. The volume fraction of α – Co phase is calculated to be 40.6 %.

The composition of the alloy at the first exothermic onset temperature of 1613 K is found to be 74.80 at. % Cu which again is lesser than that observed in the larger powder size, the volume fraction of the Co – rich phase is also reduced to 49.9 at. %. The second exothermic peak on the cooling curve (onset temperature 1383.00 K) is higher than the T_s of the Cu – rich phase, the volume fraction of α – Co phase is noticed to have increased to 53 %.

194
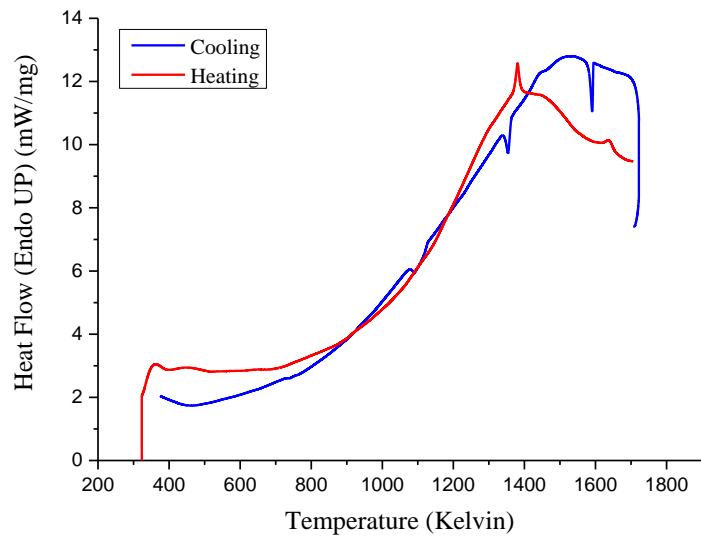
Figure 5.53 DTA plots of the < 38 μm drop tube powder of Cu – 50 at. % Co alloy.

6 Discussion

6.1   Phase diagram and transformations in Co – Cu alloys

According to the metastable phase diagram in Figure 5.1, the binodal boundary is from 12.2 – 91.7 at. % Cu. This is a much wider miscibility gap than that reported by Cao et al. [164]. Spinodal limit is from 26.7 – 82.2 at. % Cu.

The calculated miscibility gap is non symmetrical which is in agreement with the results of Munitz and Abbaschian [8]. The composition (X_c) and temperature (T_c) at the critical points are 58.7 at. % Cu and 1623 K respectively.

The value of the X_c obtained is higher than that of Davidoff et al. [176] but is the same as that obtained by Palumbo et al. [166] (58.5 at. % Cu), however, their T_c value was different (higher by 67 K) even though the same CALPHAD method was employed in calculation. The reason for the variance in the value of the Tc is most likely due to the inclusion of the Curie temperature in their calculation although they did point out that they had limited experimental data. Davidoff et al. obtained much lower value (1547 K).

After the calculated miscibility gap was superimposed on the equilibrium phase diagram of the Co – Cu system, it was observed that the peritectic temperature (T_p) was lower (1366.5 K) to that of the phase diagram by Cao et al. [164] and Robinson et al. [133] which was 1385 K. This newly obtained T_p is however not far off from that reported by Yamauchi et al. [165] who reported T_p of 1360 K.

The liquidus temperature of the Cu - 68.5 at. % Co alloy from figure 5.1 is 1662 K with estimated critical undercooling of 143 K and 256 K to cool into the binodal and spinodal regions. Cao et al. [210] in an alloy on the opposite

end on the phase diagram (Co – 68 at. % Cu) obtained a liquidus temperature of 1643 K and a critical undercooling of 263 K to cool into the binodal. Clearly, because of the compositional difference between the two alloys, the liquidus temperature and undercooling is expected to vary. According to the equilibrium phase diagram of the Co - Cu system, the liquidus temperature for their alloy should be and was less than that of the Cu – 68.5 at. % Co alloy.

However, on the basis of a non-symmetrical miscibility gap their estimated critical undercooling is too high as binodal decomposition should occur in the alloy at much lesser undercooling. The calculated miscibility gap in this research places the liquidus temperature of the alloy at 1632 K with critical undercooling of 28 K to access the binodal region while that of the spinodal is placed as 67 K. Their estimated undercooling of 263 K places the alloy well with the spinodal region.

The above seems to suggest that the higher the undercooling, the higher the liquidus temperature. This is perfectly reasonable due to the fact that as the undercooling increases, the composition of the alloy is constantly changing with the Co – rich phase becoming more enriched.

The Cu – 50 at. % Co alloy on the other hand had an estimated liquidus temperature of 1639 K and critical undercooling of 41 K and 52 K to cool into the binode and spinode respectively. These values are lower than those reported in literature, for instance Davidoff et al. [176] reported liquidus temperature of 1655 K for the alloy with critical undercooling of 106 K into the binodal region. These values are however confusing in that their phase diagram does not seem to support them. According to their calculations, their X_c was 52.7 at. % Cu and T_c was 1547 K, they also stated that their miscibility gap was symmetrical. If that is the case, the Cu – 50 at. % Co alloy is very close to the X_c and it is expected that it would contact the binode curve very close to the T_c.

The results of the thermal analysis gave insights into the phase transformation and accuracy of the calculated phase diagram of the Co – Cu system. In all the samples examined the onset temperature corresponding to the melting T_m, and temperature at which the Cu – rich phase starts to solidify T_s, are found to be within the range of 1372 – 1375 K.

In the arc melt sample of the Cu – 68.5 at. % Co alloy, the liquidus temperature determined from the DTA curves was 1663.86 K which is not far off from the phase diagram estimate of 1662 K. In the drop tube powder samples however, the values obtained from the DTA details are much lower (1631.6 K in the 850+ μm and 1616 K in the < 38 μm powder).

Using the phase diagram in combination with the onset temperatures it is seen that as the powder size decreased, the volume fraction of α – Co phase increased. This is also reflected by the T_m value which departs from that of pure copper as the sample size decreased. This implies that as the undercooling is increased (higher undercooling in smaller droplets), the Cu – rich phase content gradually starts to reduce which is in line with XRD results (figure 5.16).

The peak positions on the heating curve and second peak of the cooling curve of this powder sample are exactly 276 ℃ less than that of the arc melt sample while the first peak on the cooling curve of the powder sample differs from that of the arc melt sample by 275 ℃. However, the first exothermic event on the cooling curve in this powder sample has an onset temperature (that coincides with the temperature at which α – Co starts to form) that is higher than the arc melt sample (1607.66 K). The second exothermic peak was at 1357 K with an onset of 1375 K which when traced on the equilibrium phase diagram coincides with temperature at which the Cu – rich phase starts to solidify (T_s). Therefore the microstructure is expected to be α -Co dendrites with Cu – rich inter dendritic space. This is confirmed by the microstructure in figure 6.1 below.
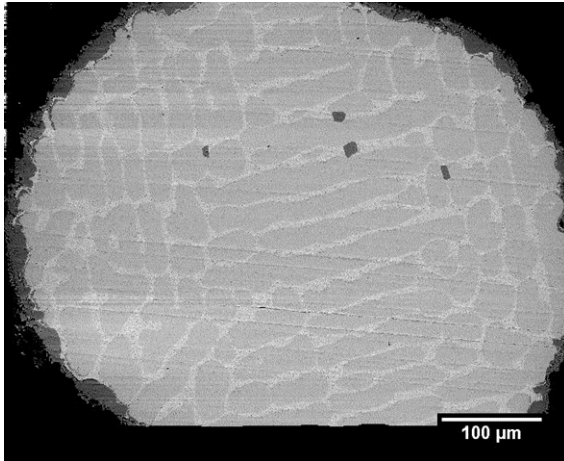
Figure 6.1 Back scattered SEM image of DTA sample of 850+ μm drop tube powder of the Cu − 68.5 at. % Co alloy.

The presence of a third exothermic peak on the DTA cooling plot of the Cu − 68.5 at. % Co alloy of < 38 μm is initially thought to be due to LPS based on its microstructure shown in figure 6.2. Clearly, the microstructure shows what looks like spherical particles but upon tracing out the temperatures on the metastable phase diagram, these coincide with the spinodal line. Since there is no evidence of spinodal decomposition in this microstructure and other microstructures of the alloy, the use of the equilibrium phase diagram in analysing it is justified. It is therefore concluded that the spherical particles are dendrite tips.
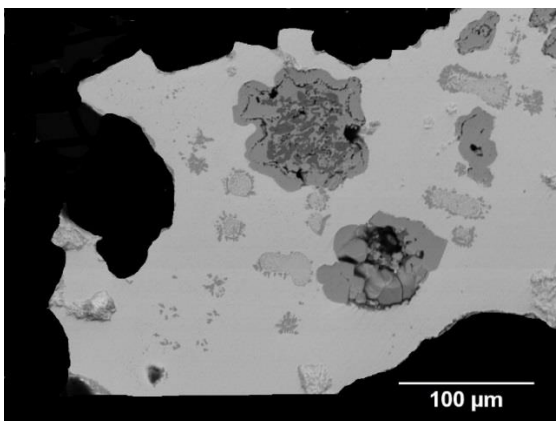
Figure 6.2 Back scattered SEM image of DTA sample of < 38 μm drop tube powder of the Cu − 68.5 at. % Co alloy.

The microstructure of the DTA samples of the Cu – 50 at. % Co alloy (figures 6.3a and b) is consistent with equilibrium phase diagram predictions as dendritic structures were observed in both powder sizes.
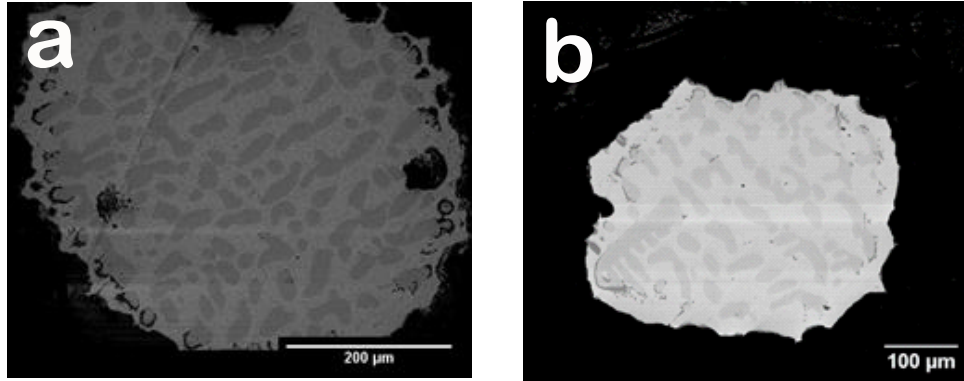
Figure 6.3 SEM microstructure of DTA samples of Cu – 50at. % Co powder of size range (a) < 38 μm and (b) 850+ μm.

6.2   Solidification pattern and behaviour in Co – Cu alloys

As already shown and discussed the solidification of the arc melt sample of the Cu – 68.5 at. % Co alloy follows the path of the equilibrium phase diagram with the formation of α – Co dendrites while that of the Cu – 50 at. % Co alloy does not. The micrographs of the Cu – 50 at. % Co alloy establishes that LPS occurred in the alloy evidenced by the dispersion of Co - rich L_1 particles in Cu - rich matrix. The apparent evidence of nucleation of the spherical particles (discussed in section 5.4.1) means that the alloy is in the binodal region of the miscibility gap since nucleation is not observed in the spinodal region.

In the binodal region, decomposition into $L_1 + L_2$ occurs by nucleation and growth; in this case of the spherical cobalt - rich particles. Migration and growth of particles in the region is by diffusion and this would explain the clustering noticed is as a result of high rate of diffusion in the matrix.

Migration of particles in the $L_1 + L_2$ region is usually due to temperature or concentration gradient but since there was no evidence of concentration gradient from etching micrographs (figures 4.5), it is assumed that the cobalt particles migration is due to the temperature variation which would explain the inhomogeneous distribution of the particles in the matrix.

Closer to the copper hearth temperature gradient is higher and as such Marangoni convection should be responsible for the upward movement of the particles (away from the colder end) however this may have been overwhelmed by flow induced by the arc's electric current. At the air side temperature difference is not as high and Stokes motion should dominate but since density difference between copper and cobalt is small ($8.92g/cm^3$ for copper and $8.90g/cm^3$ for cobalt), the Stokes effect is negligible. This explains why most of the clustered spherical particles are at the top of the sample.

The presence of the spherical particles in the arc melt sample is an indication that liquid phase separation occurred in the alloy composition. This is contrary to literature findings which indicate that the Cu -50 at. % Co alloy is dendritic unless at substantially high undercooling into the miscibility gap. Even though the temperature and cooling rate of the arc melter furnace is unknown, the fact that rapid cooling was able to cause liquid phase separation is an indication that the undercooling required to get the alloy into the miscibility gap is not as large which is in line with the calculated metastable phase diagram predictions.

Using the metastable phase diagram as a guide, solidification could occur in the drop tube powders with or without LPS depending upon the undercooling attained. The latter is more likely in the Cu − 68.5 at. % Co alloy and in larger droplets mainly because of the higher undercooling needed to get the alloy into the miscibility gap and lower undercooling in the larger droplets as a result of low cooling rates. Clearly these can be inferred from figure 5.34 with

low numbers of LPS structures in droplets with diameter, $d > 300$ μm. The observed microstructures in such a case of no LPS will predominantly be of α – Co dendrites (which may be in category NLPS_D or NLPS_F) in a Cu – rich matrix.

As the degree of undercooling increases, segregation may or not occur. Careful comparison of the microstructures of the two alloy suggests that the Cu – 68.5 at. % Co alloy is more prone to surface segregation. Upon accessing deeper undercooling enough to drop the droplet temperature below the binodal curve, LPS characterised by nucleation occurs. Even though hardly mentioned in literature, binodal decomposition characterised by multiple nucleation is more likely as alloys depart from the critical composition due to larger temperature difference between their binodal and spinodal curves. Multiple nucleation of more than one phase is also possible in the likelihood of segregation occurring before LPS. The implication of this is that solidification of microstructural features will occur at different times and temperatures and ultimately results in separated liquids of different compositions.

Microstructural evidence from this research suggests multiple nucleation events occurred in the binode. An example droplet thought to have undergone such multiple nucleation event is shown in figure 6.4. In this figure, over 16 isolated Co – rich regions are identified in the Cu – rich matrix. Although this type of structure could also be formed by coalescence, its appearance is considerably different from that of the ECS structures in figures 6.8a and b that it is considered unlikely and that the structure is as a result of multiple nucleation.
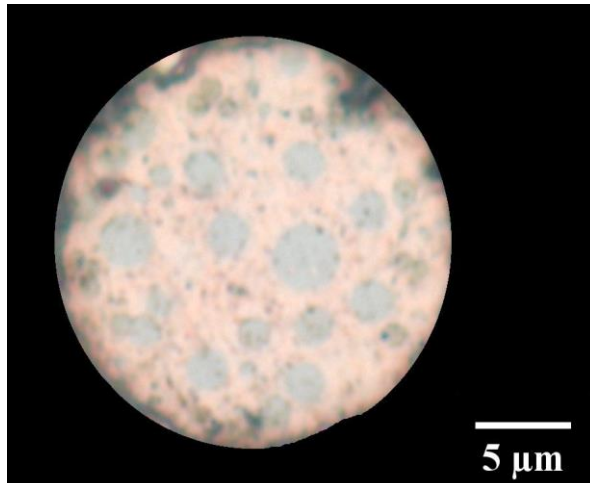
Figure 6.4 Droplet showing evidence of multiple nucleation events.

As the solidification process progresses and with higher cooling rates, undercooling below the spinodal curve becomes possible. This may occur with or without binodal decomposition occurring first as in the case of the critical composition in which nucleation is predicted to be suppressed and LPS occurs only spinodally.

In many of the SCS and ECS structures observed, two liquid phase separation events are identified. This would suggest binodal followed by spinodal decomposition. It is hypothesized that a primary LPS event (which happened in the binode) resulted in the formation of the distinct Co and Cu – rich regions. The second LPS event is thought to be spinodal decomposition. The microstructures in figures 6.5a and b from the Cu – 50 at. % Co alloy clearly shows the two separation events. As expected only artefacts of the primary LPS event is visible in the Cu – 68.5 at. % Co alloy.

Occurrence of spinodal decomposition is evidenced by the characteristic loop – like appearance of the microstructure similar to the structure (figure 3.17c) observed by Davidoff et al. [176] and predicted by Shi et al. [177] in their phase field model. However, contrary to the predictions of Shi et al., there were no microstructural evidence in this research to support a structure in which the two liquid phases segregated in opposite hemisphere of the parent

droplet (figure 3.21a). They had postulated that such a structure would be formed at equal volume fraction of phases.

In figure 6.5a, the spinodally decomposed Co – rich region contain very fine scale Cu – rich particles (shown more in the enlarged insert) just as predicted by Shi et al. The compelling scale difference between the bulk Cu – rich region (87 μm) and the dispersed Cu – rich particles (nano sized) within the loops of the Co – rich region further gives credence to the fact that two LPS events had occurred.

The side by side comparison of the SCS structure in both alloys offered in figure 5.42 clearly shows they are identical. If this is so, did spinodal decomposition then occur in the Cu – 68.5 at. % Co alloy? The answer to this is no. Referencing the metastable phase diagram, the calculated miscibility gap is asymmetrical being steeper on the Cu – rich side than on the Co – rich side. Also, the composition of the two demixed liquids (L_1 and L_2) is defined by two points on either side of the binodal curve and this corresponds to the temperature at which LPS structures are nucleated. The consequence of this is that following binodal decomposition, the undercooling needed to initiate spinodal decomposition varies in the two liquids with higher undercooling required in the Cu – rich liquid than in the Co – rich liquid. It then becomes clear that (1) the undercooling needed to get the two liquids in the Cu – 68.5 at. % Co alloy to spinodally decompose is likely unattainable before freezing occurs and (2) the alloy therefore spends longer time in the binode and as a result the primary LPS is prolonged which would explain the further LPS of the core and shell regions. It is also noted that the appearance of the core region in the alloy does not in any way appear loop – like as observed in the spinodal structures of the Cu – 50 at. % Co alloy.

The varying undercooling and composition of the two separated liquids also explains why SCS structures have different configurations ranging from dendritic to LPS to mixed core and shells. In randomly selected SCS structures across the whole sieve fraction size range in the Cu – 50 at. % Co alloy, the ratio of dendritic to LPS to mixed shells was found to be 3:6:1.

These findings while being consistent with the calculated asymmetrical miscibility gap in this research and that calculated by Palumbo et al. [166], are not consistent with the near symmetrical miscibility gap determined by Robinson et al. [133] and Cao et al. [164].

The ECS type droplets shown in figure 6.5a – c are believed to be at different stages along the solidification process path. Figures 6.5a - b are from the Cu – 50 at. % Co while figure 6.5c is from the Cu – 68.5 at. % Co alloy and these are all believed to be at the early stages of primary LPS as the regions are just evolving even though figure 6.8a has apparently decomposed spinodally. The droplet in figure 6.5c on the other hand is further along in the coalescence process and clearly migration of particles by Marangoni convection is much more advanced although not completed as evidenced by the irregular shape of the core which is also not centrally located in the parent droplet.

These structures illustrate the complexities of the dynamics between the evolving LPS structures and the freezing time in rapid solidification experiments of this kind resulting in a wide range of as solidified structures.
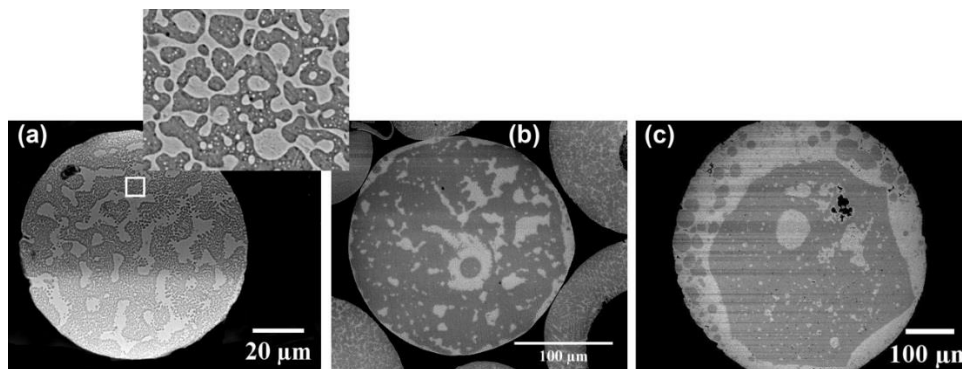
Figure 6.5 SEM backscatter images showing evolving core shell (ECS) structures at different stages along the solidification process. (a) is from the Cu - 50 at. % Co alloy while (b) and (c) are from the Cu - 68.5 at. % Co alloy. Dark particles are Co – rich while the light particles are Cu – rich. The insert shows spinodal decomposed region.

6.3 Core shell structures formation characteristics and mechanism in undercooled Co – Cu alloys

It has been established so far that the higher melting point component (which also has the higher surface energy) is the L_1 phase which eventually forms the core of the core shell structures (see discussion in section 5.6). In this section, the characteristics of the solidification of the core shell microstructures are discussed and based on microstructural evidence mechanism for their formation is proposed.

Nucleation of the higher surface energy droplets (referred to as HPD) in the homogeneous melt is initiated at the surface of the parent droplet where its temperature is lower compared to that at its centre as a result of contact with the inert gas of the drop tube environment. Figure 6.4 which had already been discussed as showing proof of multiple nucleation of the Co – rich particle and figure 5.64 are very good examples showing that surface nucleation occurred. The sizes of the Co – rich particles are observed to increase inwards signifying that they started at the tips. Also, figure 6.6a – c from the Cu – 68.5 at. % Co alloy shows segregated droplets with Co – rich particles observed to have nucleated at its edges.
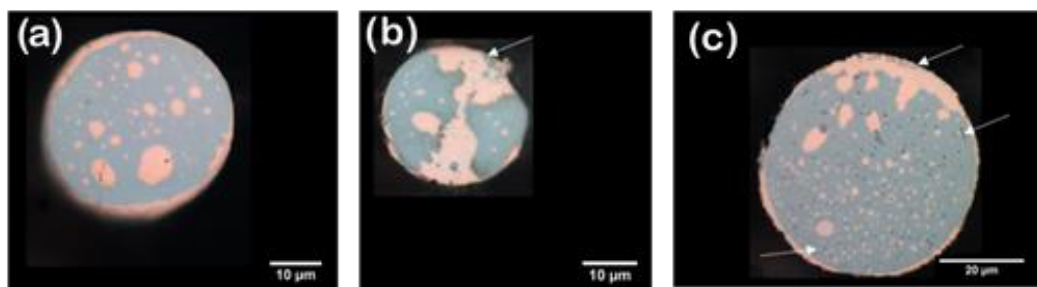
Figure 6.6 Segregated evolving core shell (ECS) structures from the Cu – 68.5 at. % Co alloy, all showing multiple nucleation events of more than one phase while droplets (b) and (c) show nucleation of L_1 particles (marked by arrows) at the edge of the droplet.

Following the nucleation, the L_1 particles under the forces of collision and in a bid to further reduce the energy of the system coalesce forming bigger particles away from the surface of the parent droplet. The thermal gradient

in the droplet then makes it possible for Marangoni effect to drive these coalesced Co – rich particles to the centre of the droplet thereby forming the core and completing the primary LPS process. If for any reason the Marangoni velocity was not high enough to get the coalesced particles to the centre or the time available for coalescence to complete is shortened, structures of the ECS types are formed.

This continuous process leads to the enrichment of the centre of the droplet with the L_1 phase and its depletion at the outer layer (shell) thereby creating a concentration gradient as well in the droplet. This concentration gradient then induces a solutal Marangoni effect which is in opposite direction to the thermal Marangoni motion (i.e. drives particles outward). The overall Marangoni direction then depends on the greater of the two.

Certainly there is a concentration difference between the shell and the core region but the presence of the Cu – rich (L_2) particles within the core necessitates that a concentration profile of the core be done to check whether solutal Marangoni is responsible for the movement of these L_2 particles as well since they are also observed to be capable of further growth. EDX analysis was then done by taking series of concentric circle spectrum of the core towards the centre of the droplet (figure 6.7). The result across two sieve size fractions (212 – 150 μm and 106 75 μm) is presented in figure 6.8. It shows that Co concentration of the core was fairly consistent (± 0.02) implying that another mechanism was responsible for the movement of the L_2 particles.
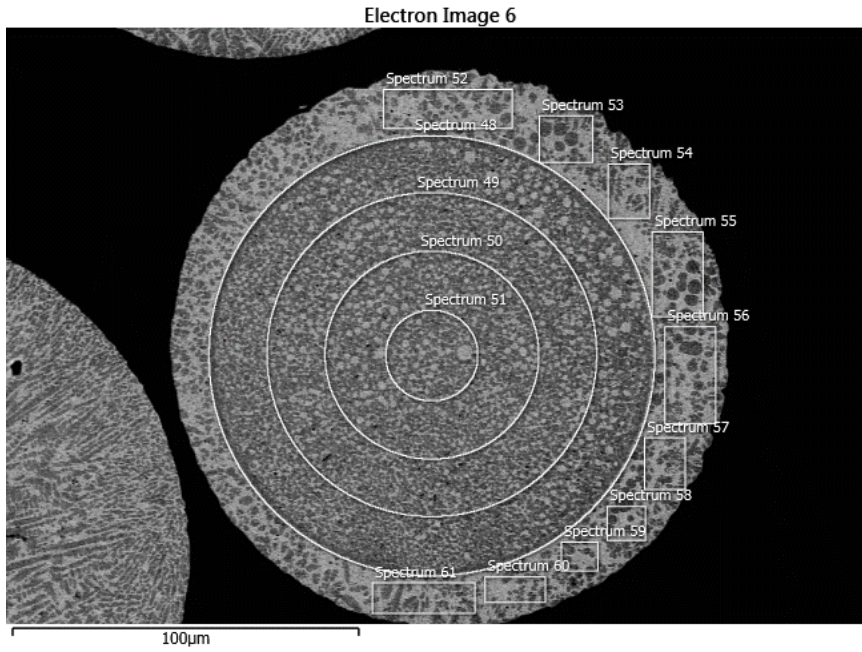
Figure 6.7 EDX sampling for the Co concentration within the core of a SCS structure with increasing distance from the centre.
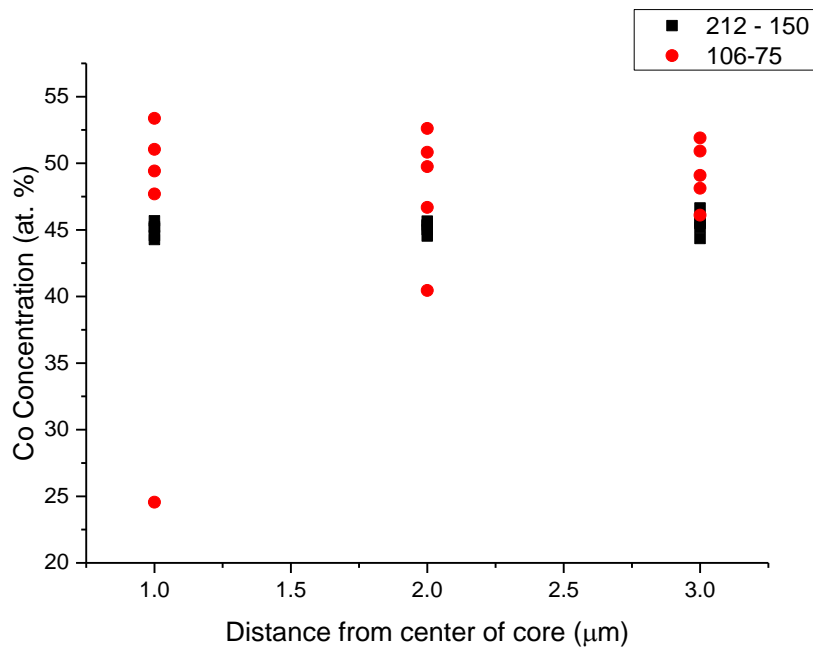
Figure 6.8 EDX results for Co concentration with distance from the centre of a SCS structure in two sieve fraction size.

It is believed that the mechanism responsible for the movement of the L_2 particles is Soret effect and that the Soret coefficient of the Cu – rich phase is positive. A positive Soret coefficient means that there is outward movement of the L_2 particles wherever they occurred (either in the core or in the coalescing L_1 particles in the shell) towards the surface of the droplet. This causes the Cu concentration to increase away from the centre of the droplet as reflected by the EDX results.

This argument for Soret effect in the alloy is very reasonable in the sense that within the core, the L_2 particles which is the phase with the lower surface energy has tendencies to want to wet the surface of the core (outward movement). They also strive to reduce the energy and in so doing collide and coalesce to form larger particles as seen in some SCS structures. Hypothetically, if Marangoni motion is strong enough in the core, a situation should occur where the L_2 particles would also converge at the centre of the established core thereby forming a triple layer core shell structure. But as earlier pointed out, Marangoni motion does not appear to be high enough in the alloys resulting in the inability of the L_2 particles to form larger regions / multi-layer core shell structures.

The above explanation applies only to the binodal route of LPS. In the occurrence of the secondary LPS process, the structure at whichever stage it is at along the solidification pathway further spontaneously separates and then coalesce into the characteristic loop – like structure (as already explained) which with time breaks up into tiny L_2 particles and a stable two layer core shell structure is formed.

In this research there are evidence that suggests the Cu – 68.5 at. % Co alloy is prone to surface segregation before LPS more than the other alloy (figures 6.6a - c). In line with the previous explanation, the Cu – rich phase continually moves to the surface of the parent droplet (figure 6.6a and b) which in turn created a layer deficient in the L_1 phase. In this instance, the nucleated HPDs are also the minority phase droplets (MPD).

Upon cooling into the binodal region, it takes time for the HPDs to attain a critical size in order for growth to occur. It is then postulated that within this time interval LPS also occurs concurrently in these HPDs as well as in the bulk liquid. This is evidenced by the presence of nano sized L_2 particles in figures 6.4 and 6.5c which are thought to be example of droplets in which this is clearly illustrated. This proves that multiple nucleation of more than one phase is possible in the Co - Cu alloy system.

By the time these HPDs attain critical size, the L_2 particles too have grown substantially in the core. This implies that the presence of the Cu – rich particles is first as a result of primary LPS which would further explain why the SCS structures in both alloys are identical.

As a result of Soret effect, nano sized L_2 particles in the L_1 structures in the shell then move into the bulk L_2 phase while those trapped within the larger Co – rich regions / core grows but since the thermal gradient is likely too small to effect Marangoni motion, these do not beyond a certain size.

Schematic diagram for the binodal and spinodal mechanism for the formation of the core shell and alternate structures along the solidification process is presented in figures 6.9 and 6.10 respectively.

Homogeneous melt.   Phase separation by nucleation.   Growth of separated particles via collision.   Movement of particles to center by Marangoni motion.   At time = t Primary phase separation ends with formation of spherical core shell structure .   At time = t +x Secondary phase separation is completed in the shell and core.
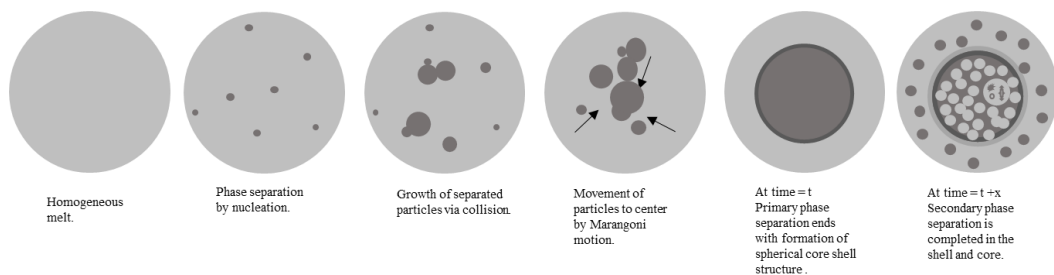
Figure 6.9 Binodal mechanism for the formation of a stable core shell structure. Starts with the homogeneous droplet followed by nucleation of the darker phase cobalt particles after cooling into the miscibility gap (MG). Growth of the nucleated phases then occurs by coalescence and due to the thermal gradient Marangoni movement occurs. This results in a stable core shell structure (SCS) at time = t. If the alloy remains in the MG, further liquid phase separation (LPS) occurs and as such the alloys have the same SCS structures.

The spinodal formation mechanism is quite difficult to predict, this is because the structure at any point along the solidification process could enter into the region. Figure 6.10 shows a typical scenario but the actual process is much more complex as evidenced by the numerous microstructures observed in this study.
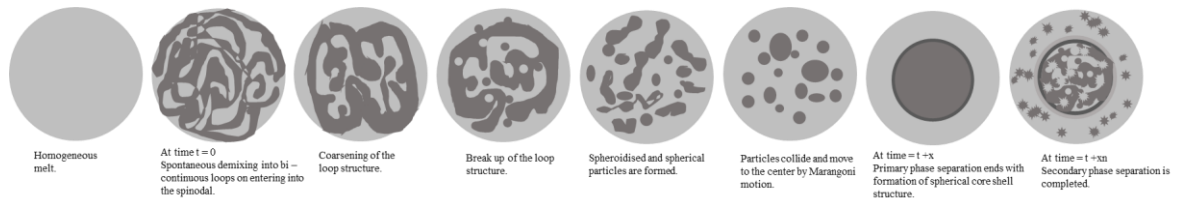
Figure 6.10 Spinodal mechanism at the critical composition for the formation of stable core shell structures. At the critical composition the alloy bypass the binode and enters straight into the spinodal. At every other composition evolving core shell (ECS) structures or even mixed structures can enter into the spinodal.

7 Conclusion

- 2 phases, a Co – rich and a Cu – rich phase are present in the arc melt and drop tube samples of the Cu – 50 at. % Co alloy and Cu – 68.5 at. % Co alloy.

- Core shell microstructures were observed in Cu - 50 at. % Co and Cu - 68.5 at. % Co alloys rapidly solidified in a drop tube.

- The microstructures are mainly formed as a result of primary liquid phase separation while a secondary liquid phase separation was observed in some droplets of the Cu - 50 at. % Co alloy. The secondary liquid phase separation is also believed to be viable for alloys at close proximity to the critical composition.

- The separation type was found to be greatly dependent on degree of undercooling, this is inferred from metastable phase diagram estimates since it is impossible to measure the undercooling in drop tube.

- Core / shell phase in the alloys is not dependent on volume fraction of the phases but rather on surface energies. The core was observed to always be formed by the phase with the higher melting point and surface energy.

- Failure of some of the smaller droplets in the 50 at. % Co alloy to form SCS structures is a direct consequence of the very high cooling rate due to insufficient time to coalesce while in the 68.5 at. % Co alloy it is as a result of high degree of undercooling needed to initiate the liquid phase separation process.

- Higher cooling rate yields fine scale core shell structures in the Cu - 50 at. % Co alloy while larger core shell particles are achieved in the Cu - 68.5 at. % Co alloy at lower cooling rate, opening the possibility for design of Co – Cu alloys with core shell microstructures at any composition.

- Optimum cooling rates exists in both alloys for peak formation of stable core shell microstructures.

8 Future work

Additions to the binary base alloy of metastable systems have been said to have effects on the miscibility gap, Marangoni velocity and volume fraction of the phases. Further study is proposed on the effects of this on the $Co - Cu$ system and how this affects the production of stable core shell structures.

Also, the impact of these additions on the mechanical properties especially the hardness is suggested for further study.

9 References

[1]   R.N. Singh, F. Sommer, Segregation and immiscibility in liquid

        binary alloys, Reports Prog. Phys. 60 (1997) 57–150.

[2]   Z.M. Zhou, J. Gao, F. Li, Y.K. Zhang, Y.P. Wang, M. Kolbe, On the

        metastable miscibility gap in liquid Cu--Cr alloys, J. Mater. Sci. 44

        (2009) 3793–3799.

[3]   L. Ratke, G. Korekt, S. Brück, F. Schmidt-Hohagen, G. Kasperovich,

        M. Köhler, Phase equilibria and phase separation processes in

        immiscible alloys, in: 2nd Sino - Ger. Symp., 2009.

[4]   W. Zhai, B. Wei, Liquid phase separation of ternary Al–In–Sn/Ge

        monotectic type alloys investigated with calorimetric method, J.

        Chem. Thermodyn. 86 (2015) 57–64.

[5]   A.E. Mironov, I.S. Gershman, E.I. Gershman, M.M. Zheleznov,

        Relationship between the tribological properties of experimental

        aluminum alloys and their chemical composition, J. Frict. Wear. 38

        (2017) 87–91.

[6]   X. Ji, Y. Chen, Y. Quan, Z. Shen, Tribological Performance of CuPb

        Alloy under Seawater Lubrication, Tribol. Trans. 59 (2016) 502–506.

[7]   Muthuchamy Ayyapan, Narendra Kumar Uttamchand, R.A.A. Rajan,

        Mechanical and wear properties of Copper - Lead alloy prepared by

        powder metallurgy processing technique, J. Chem. Technol. Metall.

        51 (2016) 726--734.

[8]   A. Munitz, R. Abbaschian, Microstructure of Cu-Co Alloys

Solidified at Various Supercoolings, Metall. Mater. Trans. A. 27 (1996) 4049–4059.

[9] X. Wei, J. Wang, Z. Yang, Z. Sun, D. Yu, X. Song, B. Ding, S. Yang, Liquid phase separation of Cu–Cr alloys during the vacuum breakdown, J. Alloys Compd. 509 (2011) 7116–7120.

[10] C.P. Wang, X.J. Liu, R. Kainuma, Y. Takaku, I. Ohnuma, K. Ishida, Formation of core-type macroscopic morphologies in Cu-Fe base alloys with liquid miscibility gap, Metall. Mater. Trans. A. 35 (2004) 1243--1253.

[11] D. V Cesar, C.A. Perez, M. Schmal, V.M.M. Salim, Quantitative XPS analysis of silica-supported Cu–Co oxides, Appl. Surf. Sci. 157 (2000) 159–166.

[12] G. Volkova, T. Yurieva, L. Plyasova, M. Naumova, V. Zaikovskii, Role of the Cu–Co alloy and cobalt carbide in higher alcohol synthesis, J. Mol. Catal. A Chem. 158 (2000) 389–393.

[13] R. Zhang, F. Liu, B. Wang, Co-decorated Cu alloy catalyst for C 2 oxygenate and ethanol formation from syngas on Cu-based catalyst: insight into the role of Co and Cu as well as the improved selectivity, Catal. Sci. Technol. 6 (2016) 8036–8054.

[14] R.T. Figueiredo, M.L. Granados, J.L.. Fierro, L. Vigas, P.R. de la Piscina, N. Homs, Preparation of alumina-supported CuCo catalysts from cyanide complexes and their performance in CO hydrogenation, Appl. Catal. A Gen. 170 (1998) 145–157.

[15]   J. Daughton, GMR applications, J. Magn. Magn. Mater. 192 (1999) 334–342.

[16]   Y. Nakagawa, Liquid immiscibility in copper-iron and copper-cobalt systems in the supercooled state, Acta Metall. 6 (1958) 704–711.

[17]   A.E. Berkowitz, J.R. Mitchell, M.J. Carey, A.P. Young, S. Zhang, F.E. Spada, F.T. Parker, A. Hutten, G. Thomas, Giant magnetoresistance in heterogeneous Cu-Co alloys, Phys. Rev. Lett. 68 (1992) 3745--3748.

[18]   J.Q. Xiao, J.S. Jiang, C.L. Chien, Giant magnetoresistance in nonmultilayer magnetic systems, Phys. Rev. Lett. 68 (1992) 3749–3752.

[19]   M. Kolbe, J. Brillo, I. Egry, D.M. Herlach, L. Ratke, D. Chatain, N. Tinet, C. Antion, L. Battezzati, S. Curiotto, E. Johnson, N. Pryds, Undercooling and demixing of copper-based alloys, Microgravity - Sci. Technol. 18 (2006) 174–177.

[20]   D. V. Ragone, Thermodynamics of Materials, Volume 2, John Wiley & Sons. Inc., 1995.

[21]   M.M. Kostic, The elusive nature of entropy and its physical meaning, Entropy. 16 (2014) 953–967.

[22]   D.A. Porter, K.E. Easterling, Phase transformations in metals and alloys, 2nd ed., CRC Press, 1992.

[23]   D.M. Herlach, Containerless undercooling and solidification of pure metals, Annu. Rev. Mater. Sci. 21 (1991) 23–44.

[24] D.M. Herlach, R.F. Cochrane, I. Egry, H.J. Fecht, A.L. Greer, Containerless processing in the study of metallic melts and their solidification, Int. Mater. Rev. 38 (1993) 273–347.

[25] D. Turnbull, R.E. Cech, Microscopic observation of the solidification of small metal droplets, J. Appl. Phys. 21 (1950) 804–810.

[26] J.H. Perepezko, J.S. Paik, Thermodynamic properties of undercooled liquid metals, J. Non. Cryst. Solids. 61 (1984) 113–118.

[27] K.S. Dubey, P. Ramachandrarao, On the free energy change accompanying crystallisation of undercooled melts, Acta Metall. 32 (1984) 91–96.

[28] W. Kauzmann, The nature of the glassy state and the behavior of liquids at low temperatures., Chem. Rev. 43 (1948) 219--256.

[29] H.J. Fecht, W.L. Johnson, Entropy and enthalpy catastrophe as a stability limit for crystalline material, Nature. 334 (1988) 50–51.

[30] W.L. Johnson, H.J. Fecht, Mechanisms of instability in crystalline alloys with respect to vitrification, J. Less-Common Met. 145 (1988) 63–80.

[31] B. Feuerbacher, Phase formation in metastable solidification of metals, Mater. Sci. Reports. 4 (1989) 1–40.

[32] B.S. Mitchell, An introduction to materials enmgineering and science for chemical and materials engineers, John Wiley & Sons, 2004.

[33] L. Ratke, S. Diefenbach, Liquid immiscible alloys, Mater. Sci. Eng.

R Reports. 15 (1995) 263–347.

[34] J. Wisniak, A new test for the thermodynamic consistency of vapor-liquid equilibrium, Ind. Eng. Chem. Res. 32 (1993) 1531–1533.

[35] D. Stefanescu, Science and Engineering of Casting Solidification, 2nd ed., Springer Science & Business Media, 2008.

[36] L. Ratke, G. Korekt, S. Bruck, M. Schmidt-Hohagen, F. Kohler, G. Kasperovich, Phase equilibria and phase separation processes in immiscible alloys, in: 2nd Sino-German Symp., 2009.

[37] J.Z. Zhao, T. Ahmed, H.X. Jiang, J. He, Q. Sun, Solidification of immiscible alloys: A review, Acta Metall. Sin. (English Lett. 30 (2017) 1–28.

[38] D.E. Laughlin, W.A. Soffa, Spinodal structures, ASM Handb. 9 (1985) 652–654.

[39] F. Findik, Improvements in spinodal alloys from past to present, Mater. Des. 42 (2012) 131–146.

[40] Novick-Cohen A, Segel Lee A., Nonlinear aspects of the Cahn-Hilliard equation, Phys. D Nonlinear Phenom. 10 (1984) 277–298.

[41] T. Lida, R.I.L. Guthrie, The physical properties of liquid metals, Clarendon Press, Oxford, 1988.

[42] C.J Smithells, Smithells Metal Reference Book, 7th ed., Butterworth-Heinemann, 1992.

[43] I. Egry, Thermophysical Property Measurements in Microgravity:

Chances and Challenges, Int. J. Thermophys. 24 (2003) 1313–1324.

[44]   J.J. Valencia, P.N Quested, Thermophysical properties, ASM Handb. Cast. 15 (2008) 468–481.

[45]   A.F. Crawley, Densities of Liquid Metals and Alloys, Int. Metall. Rev. 19 (1974) 32–48. doi:10.1179/imtlr.1974.19.1.32.

[46]   B. Predel, A. Emam, Excess volume of liquid alloys of Bi-Sn, Sn-Tl, Pb-Sn, Bi-Tl, Hg-In, Hg-Tl and Pb-Tl systems., Mater. Sci. Eng. 4 (1969) 287–296.

[47]   S. Tamaki, Ishiguro T., S. Takeda, Thermodynamic properties of liquid Na-Sn alloys, J. Phys. J. Phys. F Met. Phys. 12 (1982) 1613–1624.

[48]   K.C. Mills, Recommended Values of Thermophysical Properties for Selected Commercial Alloys, Woodhead Publishing, Cambridge, 2002.

[49]   ASM, ASM Ready Reference: Thermal properties of metals, ASM International, 2002.

[50]   Royal Society of Chemistry (Great Britain), Heat Capacities: Liquids, Solutions and Vapours, Royal Society of Chemistry, 2010.

[51]   N.E. Cusack, The electronic properties of liquid metals, Rep. Prog. Phys. 26 (1963) 361–409.

[52]   I. Kaban, W. Hoyer, M. Merkwitz, Experimental study of the liquid/liquid interfacial tension in immiscible Al–Bi system,

Zeitschrift Für Met. 94 (2003) 831–834.

[53]   I.G. Kaban, W. Hoyer, Characteristics of liquid-liquid immiscibility
       in Al-Bi-Cu, Al-Bi-Si, and Al-Bi-Sn monotectic alloys: Differential
       scanning calorimetry, interfacial tension, and density difference
       measurements, Phys. Rev. B - Condens. Matter Mater. Phys. 77
       (2008) 125426.

[54]   I. Kaban, M. Köhler, L. Ratke, W. Hoyer, N. Mattern, J. Eckert, A.L.
       Greer, Interfacial tension, wetting and nucleation in Al-Bi and Al-Pb
       monotectic alloys, Acta Mater. 59 (2011) 6880–6889.

[55]   W. Hoyer, I. Kaban, M. Merkwitz, Liquid-liquid interfacial tension in
       immiscible binary Al-based alloys, J. Optoelectron. Adv. Mater. 5
       (2003) 1069–1073.

[56]   J.A.V. Butler, The Thermodynamics of the Surfaces of Solutions,
       Math. Phys. Character. 13511174 (1932) 348–375.

[57]   T. Tanaka, T. Lida, Application of a thermodynamic database to the
       calculation of surface tension for iron-base liquid alloys, Steel Res.
       65 (1994) 21–28.

[58]   T. Tanaka, K. Hack, T. Lida, S. Hara, Application of Thermodynamic
       Databases to the Evaluation of Surface Tensions of Molten Alloys,
       Salt Mixtures and Oxide Mixtures, Zeitschrift Für Met. 87 (1996)
       380–389.

[59]   T. Tanaka, K. Hack, S. Hara, Use of Thermodynamic Data to
       Determine Surface Tension and Viscosity of Metallic Alloys, MRS

Bull. 24 (1999) 45–51.

[60]   J. Schmitz, J. Brillo, I. Egry, R. Schmid-Fetzer, Surface tension of
        liquid Al--Cu binary alloys, Int. J. Mater. Res. 100 (2009) 1529–
        1535.

[61]   R. Becker, On the formation of nuclei during precipitation, Proc.
        Phys. Soc. 52 (1940) 71–76.

[62]   J.W. Cahn, J.E. Hilliard, Free Energy of a Nonuniform System. I.
        Interfacial Free Energy, Chem. Phys. 28 (1958) 258–267.

[63]   D. Chatain, N.J. Eustathopoulos, Liquid-liquid interfacial tensions. II.
        Local chemical order. III. Comparison with Experimental Results,
        Chim. Phys. 81 (1984) 599–609.

[64]   G. Kaptay, Modelling Interfacial Energies in Metallic Systems,
        Mater. Sci. Forum . 473–474 (2005) 1–10.

[65]   J.S. Rowlinson, B. Widom, Molecular theory of capillarity,
        Clarendon Press, Oxford, 1982.

[66]   G. Kaptay, On the Temperature Gradient Induced Interfacial Gradient
        Force, Acting on Precipitated Liquid Droplets in Monotectic Liquid
        Alloys, Mater. Sci. Forum. 508 (2006) 269–274.

[67]   E.N.C. Andrade, A theory of the viscosity of liquids, London,
        Edinburgh, Dublin Philos. Mag. J. Sci. 17 (1934) 497–698.

[68]   T.E. Faber, Introduction to the theory of liquid metals, Cambridge
        University Press, Cambridge, 1972.

[69] L. Guang-Rong, B. Xiu-Fang, S. Min-Hua, Experimental Studies of Liquid Viscosity in Immiscible Al-In Alloys, Chinese Phys. Lett. 20 (2003) 1326–1328.

[70] S. Glasstone, K.J. Laidler, H. Eyring, The Theory of Rate Processess, McGraw-Hill, New - York, 1941.

[71] A. V Grosse, The viscosity of liuquid metals and an empirical relationship between their activation energy of viscosity and their melting points., J. Inorg. NucI. Chem. 23 (1961) 333–339.

[72] J. Vollmann, D. Riedel, The viscosity of liquid Bi–Ga alloy, J. Phys. Condens. Matter. 8 (1996) 6175–6184.

[73] Y. Wu, C. Li, Investigation of the phase separation of Al-Bi immiscible alloy melts by viscosity measurements, J. Appl. Phys. 111 (2012) 73521.

[74] S. Mudry, Y. Plevachuk, V. Sklyarchuk, A. Yakymovych, Viscosity of Bi-Zn liquid alloys, J. Non. Cryst. Solids. 354 (2008) 4415–4417.

[75] Y. Plevachuk, V. Sklyarchuk, O. Alekhin, O. Bilous, Viscosity of liquid binary Pb-Zn alloys in the miscibility gap region, J. Non. Cryst. Solids. 391 (2014) 12–16.

[76] Y. Plevachuk, V. Sklyarchuk, O. Alekhin, L. Bulavin}, O. Bilous}, Investigation of the critical region in monotectic systems by viscosity measurements, J. Phys. Conf. Ser. 98 (2008) 022007–022010.

[77] Y. Plevachuk, V. Sklyarchuk, O. Alekhin, L. Bulavin, Viscosity of liquid In - Se - Tl alloys in the miscibility gap region, J. Alloys

Compd. 452 (2008) 174–177.

[78]   Y.J. Lv, M. Chen, Thermophysical properties of undercooled alloys:
        An overview of the molecular simulation approaches, Int. J. Mol. Sci.
        12 (2011) 278–316.

[79]   A.K. Roy, R.P. Chhabra, Prediction of Solute Diffusion Coefficients
        in Liquid Metals, Metall. Mater. Trans. A. 19 (1988) 273–279.

[80]   S. Watanabe, M. Amatatu, T. Saito, Densities of Fe - Ni, Co - Ni, Co
        - Mo and Co - W Alloys in Liquid State, Trans. Japan Inst. Met.
        Mater. 12 (1971) 337–342.

[81]   S. Watanabe, T. Saito, Densities of Binary Copper Based Alloys in
        Liquid State, Trans. Japan Inst. Met. Mater. 13 (1972) 186–191.

[82]   I. Egry, L. Ratke, M. Kolbe, D. Chatain, S. Curiotto, L. Battezzati, E.
        Johnson, N. Pryds, Interfacial properties of immiscible Co-Cu alloys,
        J. Mater. Sci. 45 (2010) 1979–1985.

[83]   R.A. Eichel, I. Egry, Surface tension and surface segregation of liquid
        cobalt-iron and cobalt-copper alloys, Zeitschrift Fur Met. 90 (1999)
        371–375.

[84]   I. Egry, D. Herlach, M. Kolbe, L. Ratke, S. Reutzel, C. Perrin, D.
        Chatain, Surface Tension, Phase Separation, and Solidification of
        Undercooled Cobalt–Copper Alloys, Adv. Eng. Mater. 5 (2003) 819–
        823.

[85]   I. Egry, Brillo J., Surface tension and density of liquid metallic alloys
        measured by electromagnetic levitation, J. Chem. Eng. Data. 54

(2009) 2347–2352.

[86]   C. V. Thompson, F. Spaepen, Homogeneous crystal nucleation in binary metallic melts, Acta Metall. 31 (1983) 2021–2027.

[87]   N. Uebber, L. Ratke, Undercooling and nucleation within the liquid miscibility gap of Zn - Pb alloys., Scr. Metall. Mater. 25 (1991) 1133–1137.

[88]   L. Granasy, L. Ratke, Homogeneous nucleation within the liquid miscibility gap of Zn-Pb alloys, Scr. Metall. Mater. 28 (1993) 1329–1334.

[89]   Y. Zhang, C. Simon, T. Volkmann, M. Kolbe, D. Herlach, G. Wilde, Nucleation transitions in undercooled Cu70Co30 immiscible alloy, Appl. Phys. Lett. 105 (2014) 41908.

[90]   S. Karthika, T.K. Radhakrishnan, P. Kalaichelvi, A Review of Classical and Nonclassical Nucleation Theories, Cryst. Growth Des. 16 (2016) 6663–6681.

[91]   B.E. Wyslouzil, J. Wölk, Overview: Homogeneous nucleation from the vapor phase - The experimental science, J. Chem. Phys. 145 (2016) 211702.

[92]   L. Ratke, Simultaneous coarsening of dispersions by growth and coagulation, J. Colloid Interface Sci. 119 (1987) 391–397.

[93]   Zhao J.Z, Ratke L, Feuerbacher B, Microstructure evolution of immiscible alloys during cooling through the miscibility gap, Model. Simul. Mater. Sci. Eng. 6 (1998) 123–139.

[94] M. Kolbe, J.R. Gao, Liquid phase separation of Co-Cu alloys in the metastable miscibility gap, Mater. Sci. Eng. A. 413–414 (2005) 509–513.

[95] X. Lu, C. Cao, B. Wei, Microstructure evolution of undercooled iron–copper hypoperitectic alloy, Mater. Sci. Eng. A. 313 (2001) 198–206.

[96] C.D. Cao, B. Wei, D.M. Herlach, Disperse structures of undercooled Co-40 wt% Cu droplets processed in drop tube, J. Mater. Sci. Lett. 21 (2002) 341–343.

[97] J.R. Rogers, R.H. Davis, Modeling of collision and coalescence of droplets during microgravity processing of Zn-Bi immiscible alloys, Metall. Trans. A. 21 (1990) 59–68.

[98] J.Z. Zhao, L.L. Gao, J. He, Effect of Brownian coagulation on the microstructure evolution in rapidly solidified immiscible alloys, Appl. Phys. Lett. 87 (2005) 131905.

[99] H. Ahlborn, K. Lohberg, Influences Affecting Separation in Monotectic Alloys Under Microgravity, 1984.

[100] H. Ahlborn, S. Diefenbach, H. Neumann, B. Prinz, L. Ratke, A. Romero, Investigation of the Marangoni-motion on ternary A1-Si-Bi-alloys under microgravity conditions, Mater. Sci. Eng. 173 (1993) 133–135.

[101] J. Zhang, R.P. Behringer, A. Oron, Marangoni convection in binary mixtures, Phys. Rev. E. 76 (2007) 163061–163067.

[102] E.E. Michaelides, Particles, Bubbles & Drops: Their Motion, Heat and Mass Transfer, World Scientific, Singapore, 2006.

[103] W.Q. Lu, S.G. Zhang, J.G. Li, Macrosegregation driven by movement of minor phase in (Al0.345Bi0.655)90Sn10immiscible alloy, Appl. Phys. A Mater. Sci. Process. 117 (2014) 787–792.

[104] F. Huang, P. Chakraborty, C.C. Lundstrom, C. Holmden, J.J.G. Glessner, S.W. Kieffer, C.E. Lesher, Isotope fractionation in silicate melts by thermal diffusion, Nature. 464 (2010) 396–400.

[105] Y. Liu, C.T. Liu, E.P. George, X.Z. Wang, The Soret effect in bulk metallic glasses, Intermetallics. 15 (2007) 557–563.

[106] W.Q. Lu, S.G. Zhang, J.G. Li, Observation of Bi coarsening and dissolution behaviors in melting Al-Bi immiscible alloy, Acta Metall. Sin. (English Lett. 29 (2016) 800–803.

[107] S.C. Sarson, J.A. Charles, Monotectic systems, Mater. Sci. Technol. 9 (1993) 1049–1061.

[108] L. Ratke, Theoretical considerations and experiments on microstructural stability regimes in monotectic alloys, Mater. Sci. Eng. A. 413 (2005) 504–508.

[109] L. Ratke, A. Müller, On the destabilisation of fibrous growth in monotectic alloys, Scr. Mater. 54 (2006) 1217–1220.

[110] R. Dai, S. Zhang, X. Guo, J. Li, Formation of core-type microstructure in Al–Bi monotectic alloys, Mater. Lett. 65 (2011) 322–325.

[111] B. Ma, J. Li, Z. Peng, G. Zhang, Structural morphologies of Cu-Sn-Bi immiscible alloys with varied compositions, J. Alloys Compd. 535 (2012) 95–101.

[112] R. Dai, S.G. Zhang, Y.B. Li, X. Guo, J.G. Li, Phase separation and formation of core-type microstructure of Al-65.5 mass% Bi immiscible alloys, J. Alloys Compd. 509 (2011) 2289–2293.

[113] G.A. Chadwick, Monotectic solidification, Br. J. Appl. Phys. 16 (1965) 1095–1097.

[114] G.M. Schafer, M.B. Russel, The thermal method as as quantitative measure of clay mineral content, Soil Sci. 53 (1942) 353–364.

[115] R.N. Grugel, T.A. Lograsso, A. Hellawell, The solidification of monotectic alloys - Microstructures and phase spacings, Metall. Trans. A. 15 (1984) 1003--1012.

[116] R.N. Grugel, A. Hellawell, Alloy solidification in systems containing a liquid miscibility gap, Metall. Trans. A. 12 (1981) 669--681.

[117] W. Lu, S. Zhang, J. Li, Segregation driven by collision and coagulation of minor droplets in Al–Bi immiscible alloys under aerodynamic levitation condition, Mater. Lett. 107 (2013) 340–343.

[118] W. Lu, S. Zhang, Q. Hu, J.. Li, Interaction between L2 droplets and L1/L interface in solidifying Al–Bi immiscible alloy, Mater. Lett. 182 (2016) 351–354.

[119] Y. Liu, J. Guo, Y. Su, H. Ding, J. Jia, Microstructure of rapidly solidified Al-In immiscible alloy, Trans. Nonferrous Met. Soc. China.

11 (2001) 84–89.

[120] C. Potard, Structures of immiscible A1-In alloys solidified under microgravity conditions, Acta Astronaut. 9 (1982) 245–254.

[121] S. Gelles, A. Markworth, Microgravity studies in the liquid-phase immiscible system: Aluminum-indium, AIAA J. 16 (1978) 431–438.

[122] P. Morgand, C. Potard, "Immiscible alloys" experiment aboard Salyut 7: Results and interpretation of aluminium-indium emulsions solidified in microgravity, Adv. Sp. Res. 4 (1984) 53–56.

[123] S. Ozawa, T. Motegi, Solidification of hyper-monotectic Al–Pb alloy under microgravity using a 1000-m drop shaft, Mater. Lett. 58 (2004) 2548–2552.

[124] K. Moore, D. Zhang, B. Cantor, Solidification of Pb particles embedded in Al, Acta Metall. Mater. 38 (1990) 1327–1342.

[125] X. Luo, L. Chen, Investigation of microgravity effect on solidification of medium-low-melting-point alloy by drop tube experiment, Sci. China Ser. E Technol. Sci. 51 (2008) 1370–1379.

[126] W. Kim, D. Zhang, B. Cantor, Microstructure of rapidly solidified aluminium-based immiscible alloys, Mater. Sci. Eng. A. 134 (1991) 1133–1138.

[127] N. Wang, L. Zhang, Y.L. Peng, W.J. Yao, Composition-dependence of core-shell microstructure formation in monotectic alloys under reduced gravity conditions, J. Alloys Compd. 663 (2016) 379–386.

[128] C. Dong, B. Wei, Dendritic solidification of undercooled Cu-20%Pb hypomonotectic alloy, Scr. Mater. 34 (1996) 1523–1528.

[129] W. Kim, B. Cantor, Solidification behaviour of Pb droplets embedded in a Cu matrix, Acta Metall. Mater. 40 (1992) 3339–3347.

[130] N. Wang, B. Wei, Phase separation and structural evolution of undercooled Fe–Sn monotectic alloy, Mater. Sci. Eng. A. 345 (2003) 145–154.

[131] B. Luo, X. Liu, B. Wei, Macroscopic liquid phase separation of Fe–Sn immiscible alloy investigated by both experiment and simulation, J. Appl. Phys. 106 (2009) 0535231–0535238.

[132] X. Liu, X. Lu, B. Wei, Rapid monotectic solidification under free fall condition, Sci. China Ser. E Technol. Sci. 47 (2004) 409–420.

[133] M.B. Robinson, D. Li, T.J. Rathz, G. Williams, Undercooling, liquid separation and solidification of Cu-Co alloys, J. Mater. Sci. 34 (1999) 3747–3753.

[134] L. Zhang, E. Martinez, A. Caro, X.Y. Liu, M.J. Demkowicz, Liquid-phase thermodynamics and structures in the Cu–Nb binary system, Model. Simul. Mater. Sci. Eng. 21 (2013) 025005/1-22.

[135] D. Li, M.. Robinson, T. Rathz, G. Williams, Direct determination of the metastable liquid miscibility gap in undercooled Cu–Co alloys, Mater. Lett. 36 (1998) 152–156.

[136] D.J. Chakrabarti, D.E. Laughlin, The Cu−Nb (Copper-Niobium) system, J. Phase Equilibria. 2 (1982) 455–460.

[137] J.F. Smith, K.J. Lee, D.M. Bailey, Resolution of conflicting data: I. Temperature and equilibrium, Bull. Alloy Phase Diagrams. 5 (1984) 133–34.

[138] M. Hamalainen, K. Jääskeläinen, R. Luoma, M. Nuotio, P. Taskinen, O. Teppo, A thermodynamic analysis of the binary alloy systems Cu-Cr, Cu-Nb and Cu-V, Calphad. 14 (1990) 125–137.

[139] C. Allibert, J. Driole, E. Bonnier, C. R. Acad. Sci. Paris, C. R. Acad. Sci. Paris Ser. C. 268 (1969) 1579–1581.

[140] D. Li, M.B. Robinson, T.J. Rathz, Measurements of liquidus temperatures in the Cu-Nb and Cu-Cr systems, J. Phase Equilibria. 21 (2000) 136–140.

[141] A. Munitz, M. Bamberger, A. Venkert, P. Landau, R. Abbaschian, Phase selection in supercooled Cu--Nb alloys, J. Mater. Sci. 44 (2008) 64–73.

[142] J.L. Fihey, P. Nguyen-Duy, R. Roberge, On the solidification microstructure of copper-rich niobium alloys, J. Mater. Sci. 11 (1976) 2307–2311.

[143] R. Muller, Arc-Melted CuCr alloys as contact materials for vacuum interrupters, Siemens Forschungs- Und Entwicklungsberichte. 17 (1988) 105–111.

[144] G. Hindrichs, Metallographische Mitteilungen aus dem Institut für physikalische Chemie der Universität Göttingen. LXVII. Über einige Chrom- und Manganlegierungen, Zeitschrift Für Anorg. Chemie. 59

(1908) 414–449.

[145] M. Leonov, N. Bochvar, V. Ivanchenko, Chromium - Copper Phase Diagram, Dokl. Akad. Nauk SSSR. 290 (1986) 888–890.

[146] D.J. Chakrabarti, D.E. Laughlin, The Cr-Cu (Chromium-Copper) system, Bull. Alloy Phase Diagrams. 5 (1984) 59–68.

[147] G. Kuznetsov, V. Fedorov, A. Rodnyanskaya, Phase diagram of the Cu-Cr system, Izv. VUZ Tsvetn. Met. (1977) 84–86.

[148] K. Zeng, M. Hamalainen, Thermodynamic analysis of stable and metastable equilibria in the Cu-Cr system, Calphad. 19 (1995) 93–104.

[149] K.T. Jacob, S. Priya, Y. Waseda, A thermodynamic study of liquid Cu-Cr alloys and metastable liquid immiscibility, Zeitschrift Fur Met. 91 (2000) 594–600.

[150] C. Michaelsen, C. Gente, R. Bormann, Phase formation and thermodynamics of unstable Cu–Cr alloys, J. Mater. Res. 12 (1997) 1463–1467.

[151] Y. Wang, X. Song, Z. Sun, X. Zhou, J. Guo, The solidification of CuCr alloys under various cooling rates, Mater. Sci. Pol. 25 (2007) 199–207.

[152] Z. Sun, Y. Wang, G. Juan, Liquid phase separation of Cu-Cr alloys during rapid cooling, Trans. Nonferrous Met. Soc. China (English Ed. 16 (2006) 998–1002.

[153] J. Gao, Y.. Wang, Z. Zhou, M. Kolbe, Phase separation in undercooled Cu–Cr melts, Mater. Sci. Eng. A. 449–451 (2007) 654–657.

[154] J. He, J. Zhao, Behavior of Fe-rich phase during rapid solidification of Cu–Fe hypoperitectic alloy, Mater. Sci. Eng. A. 404 (2005) 85–90.

[155] Q. Chen, Z. Jin, The Fe-Cu system: A thermodynamic evaluation, Metall. Mater. Trans. A. 26 (1995) 417–426.

[156] G. Wilde, R. Willnecker, R.. Singh, F. Sommer, The metastable miscibility gap in the system Fe-Cu, Zeitschrift Fuer Met. Res. Adv. Tech. 88 (1997) 804–809.

[157] G. Wilde, J.. Perepezko, Critical-point wetting at the metastable chemical binodal in undercooled Fe–Cu alloys, Acta Mater. 47 (1999) 3009–3021.

[158] C.D. Cao, Z. Sun, X.J. Bai, L.B. Duan, J.B. Zheng, F. Wang, Metastable phase diagrams of Cu-based alloy systems with a miscibility gap in undercooled state, J. Mater. Sci. 46 (2011) 6203–6212.

[159] N. Liu, Investigation on the phase separation in undercooled Cu-Fe melts, J. Non. Cryst. Solids. 358 (2012) 196–199.

[160] S. Luo, W. Wang, J. Chang, Z. Xia, B. Wei, A comparative study of dendritic growth within undercooled liquid pure Fe and Fe50Cu50 alloy, Acta Mater. 69 (2014) 355–364.

[161] Y.Z. Chen, F. Liu, G.C. Yang, X.Q. Xu, Y.H. Zhou, Rapid

solidification of bulk undercooled hypoperitectic Fe–Cu alloy, J. Alloys Compd. 427 (2007) L1–L5.

[162] J.D. Verhoeven, E.D. Gibson, The monotectic reaction in Cu-Nb alloys, J. Mater. Sci. 13 (1978) 1576–1582.

[163] G. Elder, S.P. Munitz, A. Abbaschian, Metastable Liquid Immiscibility in Fe-Cu and Co-Cu Alloys, Mater. Sci. Forum. 50 (1989) 137–150.

[164] C. Cao, G. Görler, D. Herlach, B. Wei, Liquid–liquid phase separation in undercooled Co–Cu alloys, Mater. Sci. Eng. A. 325 (2002) 503–510.

[165] I. Yamauchi, N. Ueno, M. Shimaoka, I. Ohnaka, Undercooling in Co – Cu alloys and its effect on solidification structure, J. Mater. Sci. 33 (1998) 371–378.

[166] M. Palumbo, S. Curiotto, L. Battezzati, Thermodynamic analysis of the stable and metastable Co–Cu and Co–Cu–Fe phase diagrams, Calphad. 30 (2006) 171–178.

[167] A. Munitz, R. Abbaschian, Two-melt separation in supercooled Cu-Co alloys solidifying in a drop-tube, J. Mater. Sci. 26 (1991) 6458–6466.

[168] Y. Zhang, J. Gao, H. Yasuda, M. Kolbe, G. Wilde, Particle size distribution and composition in phase-separated Cu 75Co25 alloys under various magnetic fields, Scr. Mater. 82 (2014) 5–8.

[169] C. Cao, N. Wang, B. Wei, Containerless rapid solidification of

undercooled Cu-Co peritectic alloys, Sci. China Ser. A Math. 43 (2000) 1318–1326.

[170] X.Y. Lu, C.D. Cao, M. Kolbe, B. Wei, D.M. Herlach, Microstructure analysis of Co-Cu alloys undercooled prior to solidification, Mater. Sci. Eng. A. 375–377 (2004) 1101–1104.

[171] M.C. Flemings, Solidification Processing, McGraw-Hill, 1974.

[172] S. Curiotto, R. Greco, N. Pryds, E. Johnson, L. Battezzati, The liquid metastable miscibility gap in Cu-based systems, Fluid Phase Equilib. 256 (2007) 132–136.

[173] S. Curiotto, N.. Pryds, E. Johnson, L. Battezzati, Effect of cooling rate on the solidification of Cu58Co42, Mater. Sci. Eng. A. 449–451 (2007) 644–648.

[174] A. Munitz, R. Abbaschian, Liquid separation in Cu – Co and Cu – Co – Fe alloys solidified at high cooling rates, Mater. Sci. 33 (1998) 3639–3649.

[175] Y.K. Zhang, J. Gao, D. Nagamatsu, T. Fukuda, H. Yasuda, M. Kolbe, J.C. He, Reduced droplet coarsening in electromagnetically levitated and phase-separated Cu-Co alloys by imposition of a static magnetic field, Scr. Mater. 59 (2008) 1002–1005.

[176] E. Davidoff, P. Galenko, D. Herlach, M. Kolbe, N. Wanderka, Spinodally decomposed patterns in rapidly quenched Co–Cu melts, Acta Mater. 61 (2013) 1078–1092.

[177] R.P. Shi, C.P. Wang, D. Wheeler, X.J. Liu, Y. Wang, Formation

mechanisms of self-organized core/shell and core/shell/corona microstructures in liquid droplets of immiscible alloys, Acta Mater. 61 (2013) 1229–1243.

[178] A. V. Nomoev, S.P. Bardakhanov, M. Schreiber, D.G. Bazarova, N.A. Romanov, B.B. Baldanov, B.R. Radnaev, V. V. Syzrantsev, Structure and mechanism of the formation of core-shell nanoparticles obtained through a one-step gas-phase synthesis by electron beam evaporation, Beilstein J. Nanotechnol. 6 (2015) 874–880.

[179] R. Shi, Y. Wang, C. Wang, X. Liu, Self-organization of core-shell and core-shell-corona structures in small liquid droplets, Appl. Phys. Lett. 98 (2011) 204106.

[180] R. Dai, J.F. Zhang, S.G. Zhang, J.G. Li, Liquid immiscibility and core-shell morphology formation in ternary Al-Bi-Sn alloys, Mater. Charact. 81 (2013) 49–55.

[181] Y. Yu, X. Liu, Z. Jiang, C. Wang, R. Kainuma, K. Ishida, Thermodynamics and liquid phase separation in the Cu–Co–Nb ternary alloys, J. Mater. Res. 25 (2010) 1706–1717.

[182] M. Kolbe, C.D. Cao, X.Y. Lu, P.K. Galenko, B. Wei, D.M. Herlach, Solidification behaviour of undercooled Co-Cu alloys showing a metastable miscibility gap, Mater. Sci. Eng. A. 375–377 (2004) 520–523.

[183] C.P. Wang, X.J. Liu, R.P. Shi, C. Shen, Y. Wang, I. Ohnuma, R. Kainuma, K. Ishida, Design and formation mechanism of self-

organized core/shell structure composite powder in immiscible liquid system, Appl. Phys. Lett. 91 (2007) 1–4.

[184] J. Li, B. Ma, S. Min, J. Lee, Z. Yuan, L. Zang, Effect of Ce addition on macroscopic core-shell structure of Cu–Sn–Bi immiscible alloy, Mater. Lett. 64 (2010) 814–816.

[185] N. Wang, L. Zhang, Y.P. Zheng, W.J. Yao, Shell phase selection and layer numbers of core-shell structure in monotectic alloys with stable miscibility gap, J. Alloys Compd. 538 (2012) 224–229.

[186] C.P. Wang, X.J. Liu, I. Ohnuma, R. Kainuma, K. Ishida, Formation of immiscible alloy powders with egg-type microstructure, Science (80-.). 297 (2002) 990–993.

[187] Z. Sun, X. Song, Z. Hu, G. Liang, S. Yang, R.F. Cochrane, Effects of Ni addition on liquid phase separation of Cu–Co alloys, J. Alloys Compd. 319 (2001) 276–279.

[188] C. Xu, R. Du, X.J. Wang, S. Hanada, H. Yamagata, W.H. Wang, C.L. Ma, Effect of cooling rate on morphology of primary particles in Al-Sc-Zr master alloy, Trans. Nonferrous Met. Soc. China (English Ed. 24 (2014) 2420–2426.

[189] T. Qin, H. Wang, B. Wei, Simulated evolution process of core-shell microstructures, Sci. China Ser. G Physics, Mech. Astron. 50 (2007) 546–552.

[190] J.P. Heath, J.S. Dean, J.H. Harding, D.C. Sinclair, Simulation of impedance spectra for core-shell grain structures using finite element

modeling, J. Am. Ceram. Soc. 1931 (2015) 1925–1931.

[191] K. Wang, C. Cui, Q. Wang, S. Liu, C. Gu, The microstructure and formation mechanism of core–shell-like TiAl3/Ti2Al20Ce in melt-spun Al–Ti–B–Re grain refiner, Mater. Lett. 85 (2012) 153–156.

[192] B.C. Luo, H.P. Wang, B.B. Wei, Phase field simulation of monotectic transformation for liquid Ni-Cu-Pb alloys, Chinese Sci. Bull. 54 (2009) 183–188.

[193] D.M. Herlach, D. Holland-Moritz, P. Galenko, Metastable solids from undercooled melts, Elsevier, 2006.

[194] J. Zarling, Heat and mass transfer from freely falling drops at low temperatures, NASA STI/Recon Tech. Rep. N. (1980).

[195] R.B. Bird, W.E. Stewart, E.N. Lightfoot, Transport phenomena, Wiley, New York, 1960.

[196] D. Brandon, W.D. Kaplan, Microstructural Characterization of Materials, John Wiley and Sons Ltd., Sussex, 2008.

[197] R. Haynes, Optical Microscopy of Materials, International Textbook Co., Loughborough, 1984.

[198] S. Bradbury, B. Bracegirdle, Introduction to Light Microscopy, BIOS Scientific Publishers, Oxford, 1998.

[199] G.J. Van Dalen, M. Koster, 2D and 3D particle size analysis of micro-CT images, Http://bruker-microct.com/company/UM2012/31.pdf. (2012).

[200] H. Lipson, H. Steeple, Interpretation of X-ray powder Diffraction Patterns, Macmillan, London, 1970.

[201] D.J. Dyson, X-ray and Electron Diffraction Studies in Materials Science, Maney for the Institute of Materials, Minerals and Mining, London, 2004.

[202] B.D. Cullity, Elements of X-ray Diffraction, Addison - Wesley Publishing Co., Massachusetts, 1956.

[203] A.C. Larson, R.B. Von Dreele, Los Alamos National Laboratory Report No. laur 86-748, 2004.

[204] R.J. Hill, C.J. Howard, Quantitative phase analysis from neutron powder diffraction data using Rietveld method, Appl. Crystallogr. 20 (1987) 467–474.

[205] T.E.J. Wiedemann, Advances in Instrumentation, Birkhäuser, 2013.

[206] L.G. Berg, Estimation and determination of heats of reaction, Comptes Rendus L'Academie Des Sci. L'URSS. 49 (1945) 648–651.

[207] L.T. Alexander, S.B. Hendricks, R.A. Nelson, Minerals present in soil colloids II: Estimation in some representative soils, Soil Sci. 48 (1939) 273–279.

[208] F.C. Kracek, The polymorphism of Potassium Nitrate, Phys. Chem. 34 (1930) 225–247.

[209] S. Speil, Appllication of thermal analysis to clays and amorphous minerals, U.S Bur. Mines Rep. Inv 3764. (1944) 36.

[210] C. Cao, T. Letzig, G. Görler, D. Herlach, Liquid phase separation in undercooled Co–Cu alloys processed by electromagnetic levitation and differential thermal analysis, J. Alloys Compd. 325 (2001) 113–117.

Appendix

Cooling rate code

```
% Define universal constants

grav = 9.81 ;
stef = 5.670E-08 ;


% Define gas properties - Nitrogen


C_g = 1039.0 ; % Specific heat capacity J/kg/K
Mu_g = 1.76E-05 ; % Dynamic viscosity Pa s
K_g = 0.024 ; % Thermal Conductivity W/m/K
rho_g = 1.165 ; % Density kg/m^3


Press = 0.4 ;
rho_g = rho_g*Press ;
Nu_g = Mu_g/rho_g ;
T_g = 295.0 ;
Pr = C_g*Mu_g/K_g ;
Pr3 = Pr^(1/3) ;


% Define melt properties - CoCu


fCo = 0.685 ; % At. fraction of Co, adjust for different alloy compositions
C_l = fCo*690.0 + (1-fCo)*490.0 ; % Specific heat capacity J/kg/K (690 for Co, 490 for Cu)
% L = fCo*276000.0 + (1-fCo)*205000.0 ; % Latent heat of melting J/kg (276000 for Co, 205000 for Cu)
L = 0 ; % Latent heat of melting J/kg (Use 0 for liquid phase cooling for LPS)
rho_l = fCo*7750.0 + (1-fCo)*8020.0 ; ; % Density of liquid kg/m^3 (7750 for Co, 8020 for Cu)
T_l = 1662 ; % Melt temperature K (Use 1639 K for 50% Co and 1662 for 68% Co)
T_inv = 0.0 ; % Melting interval (liquidus-solidus) K (NB - Not used for liquid phase cooling)
eps = fCo*0.37 + (1-fCo)*0.15 ; % Emmisivity of melt (0.37 for Co, 0.15 for Cu)



% Basic droplet quantities
```

```matlab
% D = 35.0:5.0:850 ;
D = [38.0 53.0 75.0 106.0 150.0 212.0 300.0 500.0 850.0] ;
% D = [45.5 64.0 90.5 128.0 181.0 256.0 400.0 675.0] ;
D = D*1.0E-6 ;
R = D/2 ;
Cd = D ;
Cd = 1 ;
Area = 4*pi*(R.^2) ;
Vol = (4/3)*pi*(R.^3) ;
mass = Vol*rho_l ;


% Calculate drag coefficient & terminal velocity

CdRe2 = 4*mass*grav./(pi*rho_g*(Nu_g.^2)) ;
for i=1:5
    Re = sqrt(CdRe2./Cd) ;
    Cd = 2.0 - 0.5*log10(Re) ;
    if (Cd < 0.5)
        Cd = 0.5 ;
    end
end
u_term = sqrt(((4*grav*D)./(3*Cd))*(rho_l-rho_g)/rho_g) ;


% Calculate cooling rates
% C_eff = C_l + L/T_inv ;
C_eff = C_l ;
Re = rho_g*D.*u_term/Mu_g ;
h = K_g*(2.0 + 0.6*sqrt(Re)*Pr3)./D ;
dT = (6./(rho_l*C_eff*D)).*(h*(T_l-T_g) + eps*stef*(T_l^4-T_g^4)) ;
t_sol = (L/C_l)./dT ;
t_fal = 6.5./u_term ;



Monte Carlo simulation codes
a = 2/(1 + sqrt(2)) ;
b = 2*sqrt(2)/(1 + sqrt(2)) ;

Fsg = 0.4
```

```
weight = 0.4 ;
iter = 500 ;

for i = 1:iter,
  r(i) = a + (b-a)*rand ;
  Rcg(i) = r(i)*(1 - Fsg)^(1/3) ;
  z(i) = 1 + abs(weight*randn) ;
  d(i) = abs(z(i)-r(i)) ;
  rt(i) = sqrt(r(i)^2 - d(i)^2) ;
  rc(i) = Rcg(i)^2 - d(i)^2 ;
  if (rc(i) < 0)
    rc(i) = 0 ;
  else
    rc(i) = sqrt(rc(i)) ;
  end
  vt(i) = (4/3)*pi*rt(i)^3 ;
  vc(i) = (4/3)*pi*rc(i)^3 ;
  vs(i) = vt(i) - vc(i) ;
  fs(i) = vs(i)/vt(i) ;
end
mean(fs)
```
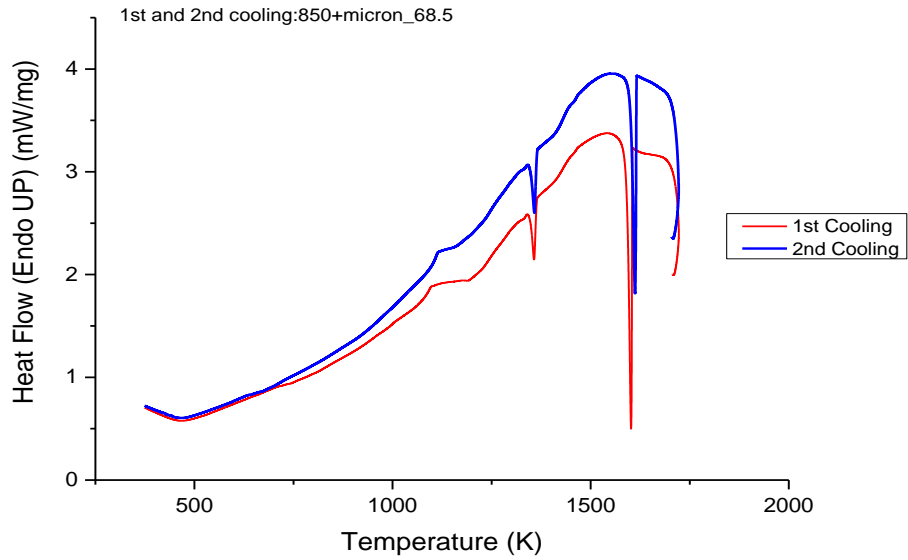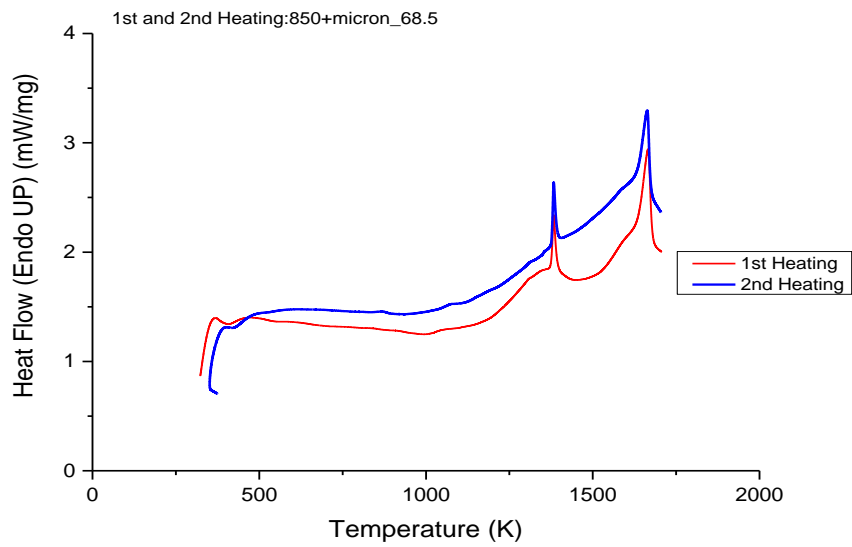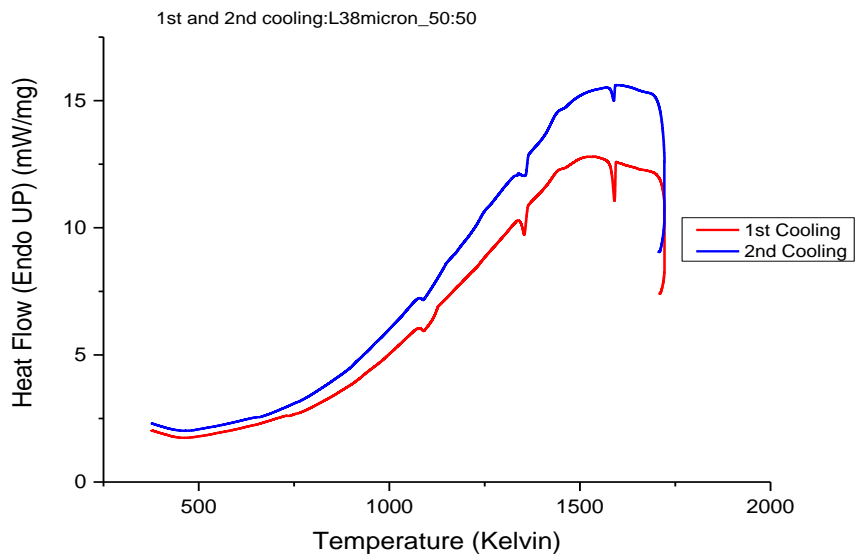

First and second cooling cycle of 38 μm powder of Cu – 68.5 at. % Co alloy.

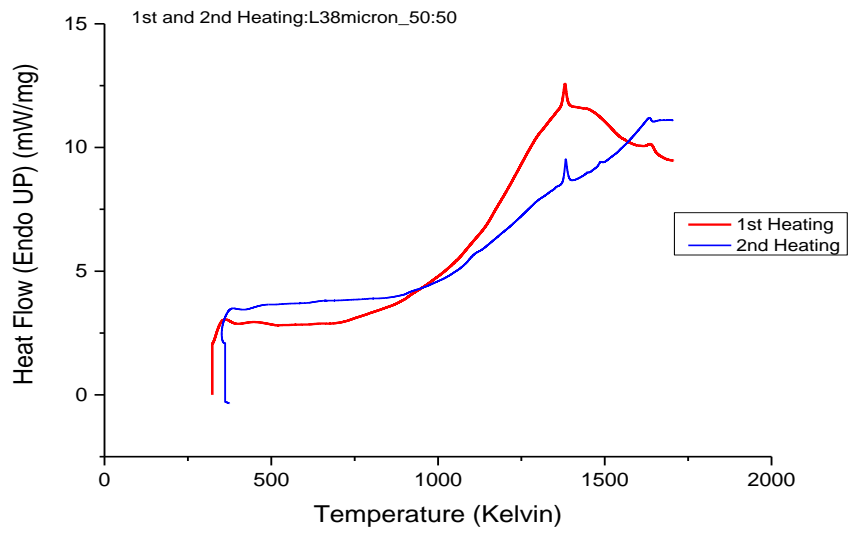First and second heating cycle of 38 μm powder of Cu – 68.5 at. % Co alloy.

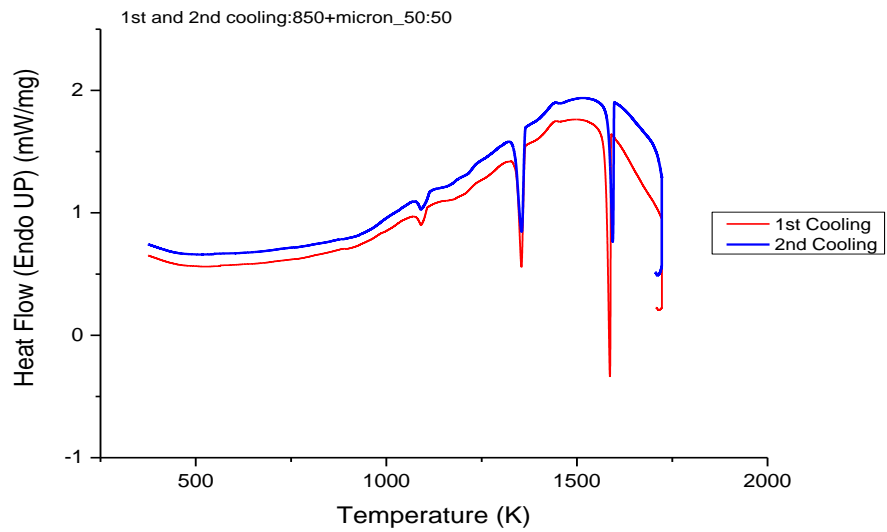First and second cooling cycle of 850 μm powder of Cu – 68.5 at. % Co alloy.

First and second heating cycle of 850 μm powder of Cu – 68.5 at. % Co alloy.
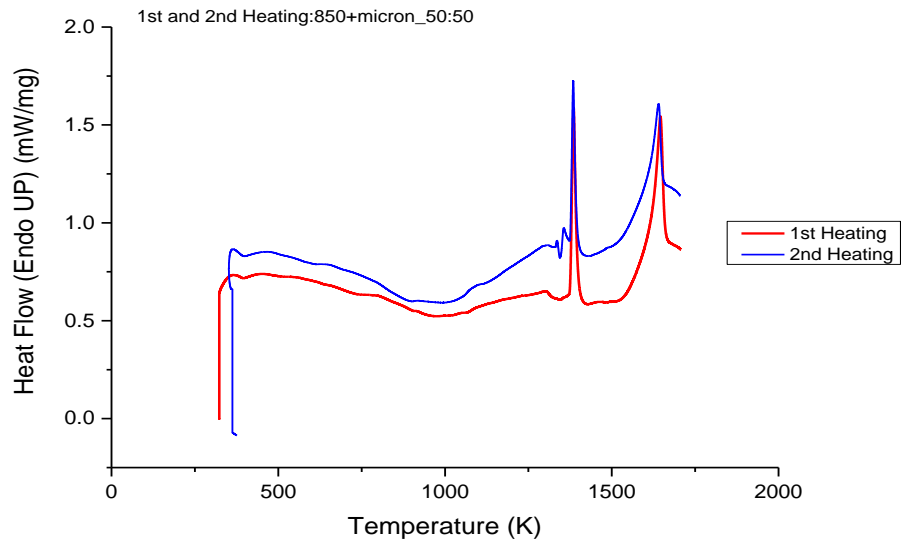

First and second cooling cycle of 38 μm powder of Cu – 50 at. % Co alloy.

First and second heating cycle of 38 μm powder of Cu – 50 at. % Co alloy.

First and second cooling cycle of 850 μm powder of Cu – 50 at. % Co alloy.

First and second heating cycle of 850 μm powder of Cu – 50 at. % Co alloy.